BIOMIMETIC ANTIFREEZE MATERIALS FOR INHIBITION OF ICE GROWTH AND ICE

RECRYSTALLIZATION IN ORDINARY PORTLAND CEMENT PASTE

by

Shane Frazier

B.S., Indiana University-Purdue University Indianapolis, 2012

B.A., Indiana University-Purdue University Indianapolis, 2012

M.S., University of Colorado Boulder, 2017

A thesis submitted to the

Faculty of the Graduate School of the

University of Colorado in partial fulfillment

Of the requirement for the degree of

Doctor of Philosophy

Materials Science and Engineering Program

2021

Committee Members:

Wil V. Srubar III

Prannoy Suraneni

Yifu Ding

Mija Hubler

Virginia Ferguson

Yunping Xi

i

ABSTRACT

Frazier, Shane Davis (Ph.D., Materials Science and Engineering)

Biomimetic Antifreeze Materials for Inhibition of Ice Growth and Ice Recrystallization in

Ordinary Portland Cement Paste

Thesis directed by Associate Professor Wil V. Srubar III

Freeze-thaw damage is a major deterioration mechanism for cementitious materials exposed to cyclic freezing and thawing temperatures. The formation and growth of ice crystals within the pores of cementitious materials can create pressures high enough to induce cracking. Cracking accelerates deterioration by reducing bulk mechanical properties, increasing water and ion penetration, and increasing susceptibility to damage upon exposure to subsequent freeze-thaw cycles.

The incorporation of air entraining agents (AEAs) to create an air void network is the most common method for freeze-thaw mitigation of cementitious materials. High-quality air void networks are obtainable, especially in a laboratory setting. However, it is difficult to produce consistent high-quality air void systems in the field. Furthermore, freeze-thaw resistance is not guaranteed when a properly entrained air void network is present, and performance can vary based on the AEA used.

An alternative approach for freeze-thaw mitigation that does not rely on the creation of an air void network is described in this work. Biomimetic ice recrystallization inhibition (IRI) active materials are studied as alternatives to traditional AEAs for freeze-thaw mitigation within ordinary portland cement (OPC) paste. It is hypothesized that when ice begins to form in the

cementitious pores, these biomimetic antifreeze materials interact with the ice-water interface and slow ice crystal growth.

Polyethylene glycol-polyvinyl alcohol graft copolymer (PEG-PVA), polyvinyl alcohol (PVA), and folic acid were screened for biomimetic antifreeze properties in neutral and pH > 12 solutions. Based on the IRI results, the materials were added as water-solubilized admixtures to OPC paste and tested for freeze-thaw resistance. Hardened state air contents were determined utilizing micro X-ray computed tomography (MXCT). The results demonstrate that highly IRI-active polymers PEG-PVA and PVA enhance the freeze-thaw resistance of OPC paste without producing a properly entrained air void system (< 1% air and spacing factor > 0.2 mm). Folic acid which is moderately IRI active only provided resistance to surface damage.

The water absorption characteristics and quantities of ice formed during freezing were investigated for PVA-modified pastes. The results indicate that the presence of PVA with appropriate molecular weight and degree of hydrolysis lead to nearly identical water absorption characteristics compared to a control paste while lower amounts of ice form during freezing.

In a final study, the IRI activities of commonly used AEA surfactants were investigated. It was hypothesized that surfactant molecules in better-performing AEAs displayed higher IRI activity than AEAs that yield moderate or low freeze-thaw resistance. Interestingly, the IRI activity of sodium oleate, vinsol resin, sodium lauryl sulfate, and a phenol ethoxylate, displayed varying levels of IRI activity that correlate with previously reported freeze-thaw performance results (*i.e.*, higher IRI activity equates to better freeze-thaw performance). The results demonstrate that surfactant molecules, including those commonly used as AEA admixtures, can display IRI activity and could provide insight into a new design parameter for AEAs.

Taken together, these results substantiate that highly IRI-active materials, like PEG-PVA and PVA, can provide freeze-thaw resistance *via* a mechanism alternative to air entrainment. The incorporation of IRI-active materials provides a unique approach for freeze-thaw mitigation in cementitious materials that could displace the use of AEAs. In cement paste, an air void network of proper size and spacing factor is not required when biomimetic antifreeze materials are utilized, which could result in a more effective strategy for freeze-thaw mitigation as the creation of a proper air void network under field conditions is difficult to produce.

DEDICATION

To my wife Emily and my daughter Natalie. Without your love and support, none of this would

be possible.

ACKNOWLEDGEMENTS

Graduate school, like many things in life, cannot be accomplished without the support of others. Many colleagues, lab mates, mentors, teachers, friends, and family members helped me through this process. Thank you to all of you.

I am so thankful for my family and the support they provided during my time as a graduate student. I love all of you.

To all my lab mates and colleagues, thank you. The list is long, but a few played especially important roles. Anastasia Aday and Jorge Osio-Norgaard, you started as my lab mates and became great friends. I cannot thank you enough. You provided my introduction to the worlds of cement and concrete. I truly could not have done most of the work in this dissertation without your input, conversations, and help with experiments. Mohammad Matar the same can be said about you, except you provided my introduction to mixing concrete and testing its fresh and hardened state properties. Elle Delesky, Jacqueline Wallat, and Aparna Lobo I am glad the three of you were around to struggle through all the headaches and frustrations with the nanoliter osmometer. Thank you, Jay Arehart, for allowing me to stay at your place during my occasional visits to Boulder during the last two years of my Ph.D. work.

Table of Contents

List of Tables

List of Figures

xviii

Chapter 1 Introduction

1.1 Problem Statement

Cementitious materials in environments that reach near or subzero temperatures are susceptible to freeze-thaw damage (also referred to as frost damage). Freeze-thaw damage is a significant deterioration mechanism that contributes to the $2+ trillion needed to repair and improve the transportation infrastructure in the United States.[1] The damage can be generalized into two categories: surface damage and internal damage. Surface damage is most often characterized by spalling and scaling. Internal damage is characterized by loss of mass, exposure of aggregate, and visible cracks. Freeze-thaw damage can be observed in structures such as roads, bridges, hydraulic dams, and spillways.

Since the 1930s, the *de facto* mechanism to mitigate freeze-thaw damage of concrete has been through the creation of an air void network. Air voids are introduced into cementitious materials using surface-active air entraining agents (AEAs). AEAs can provide freeze-thaw resistance however, the resultant air void network must meet a variety of parameters including air void sizes, spacing factors, and specific surface area. Although successful implementation is certainly feasible, it is difficult to produce consistent, high-quality air void systems in the field.[2]

Researchers have utilized a variety of other materials and methods, almost exclusively in conjunction with AEAs, to enhance the freeze-thaw resistance of cementitious materials. These alternative strategies include (1) densifying and strengthening cement paste using nanoparticles or supplementary cementitious materials (SCMs),[3–6] (2) incorporating superabsorbent hydrogel particles as a non-surfactant method to achieve an air void system,[7,8] (3) using macroscale polymeric fibers for mitigating crack propagation due to freeze-thaw damage,[9,10] and (4) surface treatment or direct incorporation of hydrophobic materials to reduce water ingress.[11,12] Despite

some success, all of these methods aim at mitigating deleterious symptoms of ice expansion in cement paste, mortar, and concrete rather than inhibiting the source—ice crystal growth.

1.2 Purpose of the Research

The main objectives of the work were (1) to investigate the ability of biomimetic antifreeze polymers to provide freeze-thaw resistance to ordinary portland cement (OPC) paste, (2) to investigate the effect of biomimetic antifreeze polymers on fresh and hardened state properties of OPC paste, (3) to investigate a small molecule for biomimetic antifreeze properties and its ability to provide freeze-thaw resistance to hardened OPC paste, (4) to investigate surfactants used in commercially available AEAs for ice recrystallization inhibition (IRI) activity, and (5) explore the structure-property relationships of surfactants with IRI activity. Objectives 1-3 aim to provide an alternative to AEAs for freeze-thaw resistant cementitious materials. Objectives 4 and 5 and aim to further the understanding of surfactant and small molecule IRI activity.

1.3 Background

1.3.1 What are Cement and Concrete?

Concrete is the second most consumed material in the world behind water.[13] The reasons for its widespread use include 1) low cost, 2) abundance, and 3) moldability, Often concrete is the cheapest option, primarily due to the abundance of its components, with cost in the United States typically $113/yd^3 to $120/yd^3 in 2019.[14,15] Concrete components can easily be molded (or cast) into a variety of shapes such as pipes, accropodes, vaults, walls, components of parking structures, and many others.[16] Additionally, concrete requires little maintenance in many applications and is fire resistant.

Concrete is composed of cement, fine aggerates, coarse aggregates, and water. Cement is the key component of concrete as it acts as the binder. If cement is mixed only with water and sand (*i.e.*, fine aggregate), then a mortar is produced. If cement is mixed with only water, then cement paste is produced. The water used in concrete, mortar, and cement paste is from local potable sources.[17] Fine aggregates generally include sand and crushed stone and have particle sizes smaller than 4.75 mm. Coarse aggregates usually consist of gravel and have particle sizes greater than 4.75 mm.[18,19] Concrete is typically composed of 60-75% aggregate, 10-15% cement, and 15-20% water by volume.[17,20]

There are many types of cementitious binders, but ordinary portland cement (OPC) is by far the most widely used. OPC is a fine powder composed primarily of C_3S (tricalcium silicate or alite), C_2S (dicalcium silicate or belite), C_3A (tricalcium aluminate), C_4AF (tetracalcium aluminoferrite), and $C\check{S}H_2$ (gypsum) where the standard cement notation is used: $C = CaO$, $S = SiO_2$, $A = Al_2O_3$, $F = Fe_2O_3$, $\check{S} = SO_3$, and $H = H_2O$. These compounds react with water, referred to as cement hydration, to form the primary products shown in **Equations 1.1-1.5**

$$(1.1) \qquad 2C_3S + 11H \rightarrow C_3\text{-}S_2\text{-}H_8 + 3CH$$

$$(1.2) \qquad 2C_2S + 9H \rightarrow C_3\text{-}S_2\text{-}H_8 + CH$$

$$(1.3) \qquad C_3A + 3C\check{S}H_2 + 26H \rightarrow C_6A\check{S}_3H_{32}$$

$$(1.4) \qquad 2C_3A + C_6A\check{S}_3H_{32} + 4H \rightarrow 3C_4A\check{S}H_{12}$$

$$(1.5) \qquad C_4AF + 2CH + 10H \rightarrow C_3AH_6 + C_3FH_6$$
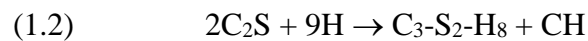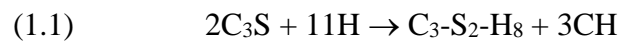
The resulting structure contains crystalline and semi-crystalline phases and additional hydration products. Calcium silicate hydrate (C-S-H) is a disordered semi-crystalline phase with a variable composition, as indicated by the hyphens, which is the main product of cement hydration.

1.3.2 The Importance of Durability

Due to the ubiquity of cement, the economic and environmental consequences are significant. The production of OPC alone accounts for 4%–8% of global CO_2 emissions, and its use places a burdensome toll on potable water resources.[21–24] Cement production is estimated to increase ~50% by 2050 to keep pace with new and aging infrastructure needs in all parts of the world.[13] The long-term durability of cementitious materials remains critical to minimizing economic and environmental costs associated with unplanned damage and maintenance, especially in light of a changing climate that may exacerbate exposure conditions and lead to premature deterioration.

Concrete is remarkably durable but varying material sources, design and construction practices, and exposure conditions can limit the aesthetic, functional, and/or structural longevity. The causes of concrete deterioration can be classified as physical and chemical.[25] Physical deterioration includes surface wear from abrasion, erosion, cavitation, cracking due to temperature and humidity gradients, structural loading, exposure to fire, and cyclic exposure to freeze-thaw temperatures.

Freeze-thaw damage can be considered one of the major types of deterioration leading to reduced durability. Roadways, facades, exposed concrete, parking structures, sidewalks, driveways, and lock and dam structures are susceptible to freeze-thaw damage and it is estimated that the annual cost for repairs and maintenance exceeds $7 billion annually in the US alone.[26] This demonstrates the criticality of ensuring cementitious materials are resistant to freeze-thaw

4

damage. When considering freeze-thaw deterioration of hardened cement paste and concrete, the pore system and water content play key roles in the material's durability.

1.3.3 Pore Systems Within Cementitious Materials

Cement paste and concrete are porous materials. The pore structure itself makes cement paste and concrete susceptible to damage from freezing and thawing temperatures. In fact, the porosity of cementitious materials greatly impacts the overall durability. The pores of cement paste and concrete can be categorized as followed based on size: gel pores (0.5 nm to 10 nm), capillary pores (5 nm to 10 μm), entrained air voids (10 μm to 1 mm), and entrapped air voids (> 1 mm).[27,28] It should be noted that the actual porosity is a continuous spectrum of sizes across all categories and that most pores are connected within the microstructure.

The gel pores are the interlayer porosity of C-S-H. The capillary pores are spaces that are not occupied by cement grains or hydration products.[29] Capillary pores are connected, and their connectivity plays a critical role in freeze-thaw resistance and directly affects the durability of cementitious materials.[30,31] Entrained air voids are spherical voids that can be both intentionally and unintentionally introduced during mixing. The entrained air voids are also connected to capillary pores.[32,33] Entrapped air voids are usually less spherical than entrained air voids and are a result of poor compaction procedures.[19]

The pore sizes and distributions within cementitious materials are influenced by the water to cement (w/c) ratio, age, compaction, and the temperature and humidity during curing.[34] As cement hydration continues with time, or at higher degrees of hydration, the overall pore distribution shifts to smaller sizes.[35] At higher w/c ratios the occurrence of larger pores increases

in concrete,[34,36] including in cement paste.[37] Additionally, poor compaction can result in an increased number of macropores.

1.3.4 Water in Cementitious Materials

Water exists in multiple states within hardened cement paste, which is primarily governed by the location within the pore system. The states can be defined as free water, water held by capillary tension, adsorbed water, interlayer water, and chemically bound water.[19,38,39] Alternatively, the states of water could be grouped as capillary water, gel water, and chemically bound water.[40] The difficulty of water to exit hardened cement paste is the primary differentiator between each category (*i.e.*, bound vs. free water). Also, it is important to note that the water contained within the hardened cement paste is not pure as it contains a variety of dissolved alkali species.

(1) Capillary, or free water, exists within the capillary pores that are of sizes > 50 nm. In capillary pores < 50 nm, water is held by capillary tension. Water held by capillary tension is often grouped with capillary water.[40,41] Capillary water is evaporable between 50 °C and 105 °C.[40]

(2) Adsorbed water, sometimes referred to as gel water, is held near the surfaces of both capillary pores and gel pores throughout the hardened cement paste. Hydrogen bonding and other attractive forces are responsible for water adsorbing to the surfaces. Adsorbed water can mostly be removed from the hardened cement paste with a change in humidity and is evaporable at 105 °C.[40]

(3) Interlayer water exists within the C-S-H structure. It is held by hydrogen bonding and is difficult to evaporate. It only evaporates at a relative humidity below 20%.[42]

(4) Chemically combined water, sometimes referred to as hydrate water, exists as part of the hydration products (see **Equations 1.1-1.5**) and is chemically bound. This water is non-evaporable.

1.3.5 Freeze-Thaw Damage Mechanisms

The process of liquid water undergoing a phase change to ice results in a 9% increase in volume. The formation of ice within cement binder is well accepted to be the cause of internal freeze-thaw damage. However, the underlying mechanism of the damage has proven to be complex. The damage induced by cyclic freezing and thawing in concrete has been explained by the Hydraulic Pressure Theory,[43,44] Osmotic Pressure Theory,[45] Litvan's work,[46–48] and Crystallization Pressure Theory.[49] All of these theories have only been partially validated. Several researchers have stated that most likely, different aspects of each theory occur simultaneously.[49,50] A brief description of each theory follows. This thesis does not include a discussion on freeze-thaw damage of aggregates or salt scaling, as they are outside the scope of this work.

1.3.5.1 Hydraulic Pressure Theory

The hydraulic pressure theory was introduced by Powers in 1949.[44,51] Powers proposed that as water freezes in saturated capillary pores, the increase in volume can either result in the pore expanding or the water being pushed from the pore as shown in **Figure 1.1**. When the water is pushed away from the newly formed ice and flows through the pore system hydraulic pressure is generated.[44,45] This would explain how air voids could reduce the generated pressure by allowing a location for the water to flow to. Powers generated an equation to estimate the developed

pressure using Darcy's Law. According to Darcy's Law, a given amount of water traveling a distance through porous media over a time period will generate pressure.[52,53] If the pressure were to exceed the tensile strength of cement paste, then damage occurs. A sufficiently large distance of travel for water or sufficiently high freezing rate could result in high enough pressures to develop that result in damage.

Powers developed **Equation 1.6** to calculate the maximum distance, L_{max}, for water to travel before the hydraulic pressure causes damage.[50] In developing the equation, Powers considered a single air void surrounded by cement paste of thickness L as shown in **Figure 1.2.**

$$(1.6) \qquad \frac{L_{max}^3}{r_b} + \frac{3L_{max}^3}{2} = \frac{KT}{UR} \times C$$

where L is the thickness of cement paste, r_b is the radius of the air void, K is the permeability coefficient of cement paste, T is the tensile strength of cement paste, U is the quantity of freezable water, R is the freezing rate, and C is a constant. Powers expanded on **Equation 1.6** and provided a method to estimate the maximum distance of water travel for all voids within a cement paste. The equation to estimate the maximum distance of water travel for all voids is used today in ASTM C457 to calculate the spacing factor.[54]
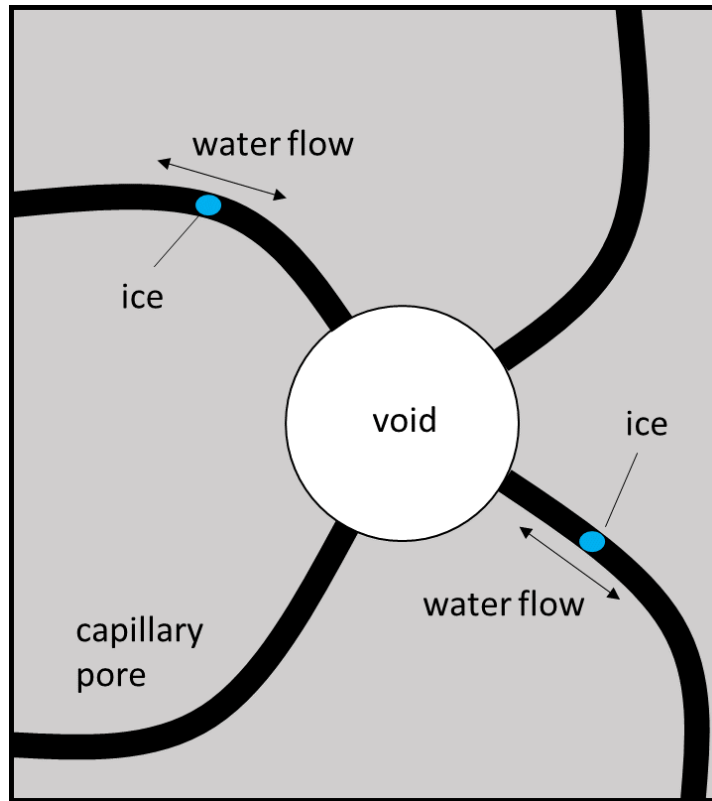
Figure 1.1. Schematic diagram of ice formation within capillary pores of cement paste. The formation of ice results in water near the ice crystal being pushed away and creating hydraulic pressure. Adapted from Mehta and Monteiro.[19]
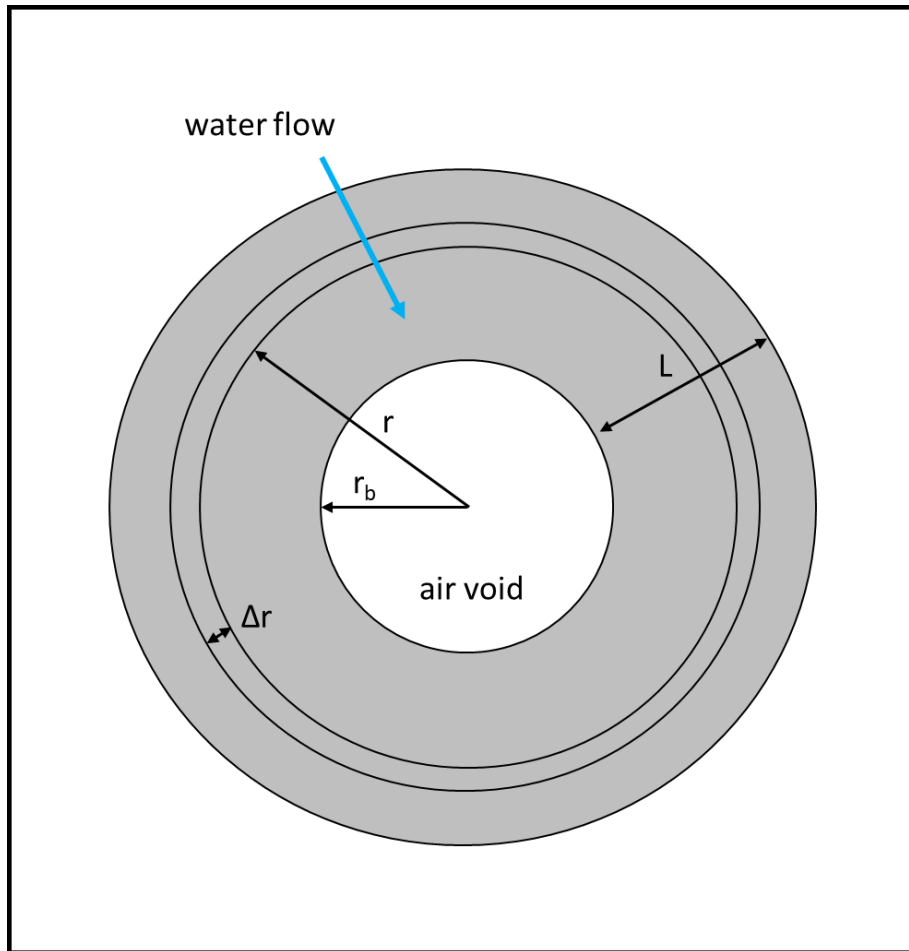
Figure 1.2. Schematic of single air void surrounded by paste with parameters used by Powers to develop the maximum distance, L_{max}, for water to travel before the hydraulic pressure causes damage, Equation 1.[44,50]

The Hydraulic Pressure Theory is not completely valid, as Powers himself later published.[55] Experiments have shown that water flows to capillary pores and not from them.[50] Additionally, the theory could not explain why concrete with entrained air shrunk after being exposed to cyclic freezing and thawing temperatures instead of expanding. Even if invalid, aspects of the Hydraulic Pressure Theory are likely accurate.[50]

1.3.5.2 Diffusion and Osmotic Pressure Theories

The Diffusion and Osmotic Pressure Theories are comprised of the work by Powers and Helmuth from 1953 to 1975.[45,55] The Diffusion Theory was not named as such by Powers but has been given the title herein. The work was developed to account for experimental discrepancies that could not be explained by the Hydraulic Pressure Theory.[45,55] The central discrepancy was experimental observations indicating that water moved towards capillary pores during freezing. The Diffusion and Osmotic Pressure Theories explain observations of AEA-modified concrete contracting as opposed to expanding during freezing. The works were meant to be an addition to the Hydraulic Pressure Theory.

Given the size of gel pores, <10 nm, it was assumed that water could not freeze within them but would become supercooled. Additionally, it was assumed that all the water within the gel pores was adsorbed onto the pore surface which also would prevent freezing. At temperatures below 0 °C, ice that forms within capillary pores or air voids would have lower free energy than the unfrozen water within the gel pores. Due to the higher chemical potential energy of the unfrozen water in the gel pores, it will flow to the ice within the capillary pores as depicted in **Figure 1.3**.[56,57] The movement of water from the gel pores to the capillary pores creates shrinkage stresses. Once the water reaches the capillary pores it will freeze, creating a larger volume of ice resulting in pressure development.

Another driving force for water movement from gel pores to capillary pores results from the presence of an ion concentration gradient. As ice forms, the ions present in the pore solution are excluded from the ice crystal structure. The exclusion of the ions in the ice crystals causes the local concentration of the ions in the pore solution to increase, creating a concentration gradient. Water will move from the gel pores to the capillary pores to remove the gradient but during this movement generate pressure.[45]
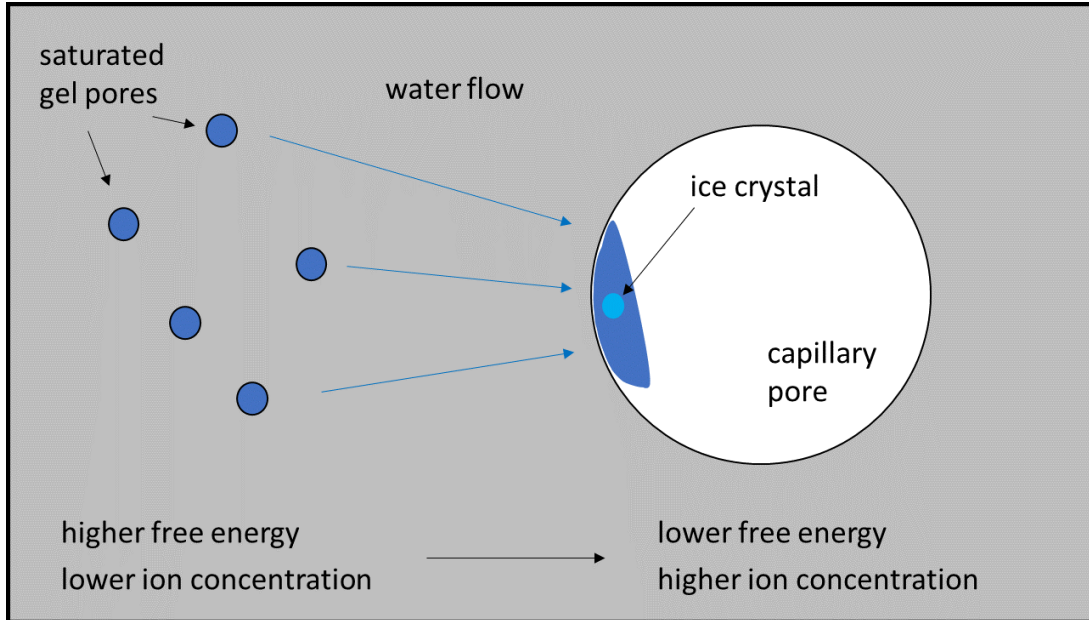
Figure 1.3. Schematic diagram of the Diffusion and Osmotic Pressure Theories. Water in gel pores does not freeze but rather becomes supercooled. Supercooled water has a higher free energy than ice which has formed within capillary pores. Water flows from a region of high to low free energy. When ice forms it creates localized regions of higher ion concentration because the ions are excluded from the ice crystal structure. The higher ion concentrations create a concentration gradient which results in water flow from gel pores to capillary pores where it also freezes.

1.3.5.3 Litvan's Work

Litvan developed a theory to describe freeze-thaw damage primarily based on the idea that water within capillary pores and absorbed to surfaces becomes supercooled.[46,48,58,59] The vapor pressure of supercooled water is higher than the vapor pressure of ice causing the migration of water to a location where it can freeze. The mass transport of water results in the cement paste partially drying and ice accumulating at larger voids.

Consider a piece of cement paste that is saturated and exposed to freezing temperatures. Water on the external surfaces and within air void surfaces freezes. The vapor pressure at these locations is lower than that of capillary pores creating a non-equilibrium state. The vapor

pressure of the supercooled water-containing regions can be lowered by the movement of water away from these regions. According to Litvan, damage occurs when mass transport (*i.e.*, movement of water) is not allowed to proceed at an appropriate rate due to low permeability, degree of saturation, or high freezing rates.[48]

1.3.5.4 Crystallization Pressure Theory

Scherer argued that the primary cause of freeze-thaw damage in concrete is crystallization pressure.[49,60] Crystallization pressure is created by a repulsive force between ice crystals and minerals in pore walls. An ice crystal is surrounded by a film of liquid water. Therefore, an ice-water-mineral interface exists. Because the refractive index of water is higher than ice, van der Waals forces between the ice crystal and mineral surface are repulsive.[49,61] For the ice crystal to come in contact with the pore wall (*i.e.*, mineral surface), a pressure the magnitude of concrete's strength is needed.[60]

When an ice crystal grows within a capillary pore, it will do so until the liquid surrounding the crystal encounters a pore wall (or other obstruction). If an opening exists on that pore wall, the ice can penetrate that opening if the crystallization pressure is large enough. This is dictated by the radius of curvature of the pore entries, temperature, interfacial energies, pore size distribution, size of the pore that the ice crystal currently resides in, and shape of the ice crystal. Without air voids, crystals nucleate in smaller pores (*i.e.*, capillary pores) and generate stresses on pore walls.

If ice nucleates in an air void, the ice crystal can grow within the larger void allowing for lower crystallization pressures to develop. Scherer hypothesized that this is the role of air voids, to behave as preferential sites of ice nucleation. Once the ice nucleates within an air void, water

would be sucked from nearby capillary pores allowing for further growth. The nucleation of ice within air voids would explain the experimental observations of water flowing from capillary pores and air entrained concrete contracting under freeze-thaw cycles.

1.3.6 Factors Affecting Freeze-Thaw Performance

There are a multitude of factors that influence the resistance of a cementitious materials to freeze-thaw damage including the rate of cooling, tensile strength, air entrainment, the degree of saturation, w/c ratio, and the pore system structure. Research on the effect of freezing rate on freeze-thaw damage has been conflicting.[62–65] Generally, it appears that internal cracking from freeze-thaw cycling (not salt scaling) increases with increased rates of freezing.[62,64,65] The tensile strength of the cement paste dictates the level of pressure that can be developed from ice formation before damage occurs. The most important factors influencing resistance to freeze-thaw damage are the degree of saturation, the pore structure, and air entrainment.

It is well studied that when saturated, concrete is highly susceptible to freeze-thaw damage.[66–69] Saturation is the ratio of the volume of water absorbed to the total pore volume (*i.e.*, the total volume of absorbable water). It has become apparent that a critical degree of saturation, DOS_{cr}, of 70-91% exists.[68,70,71] Once the DOS_{cr} is reached, freeze-thaw damage is unavoidable even with the use of proper air entrainment.[68]

The overall pore size distribution influences how quickly water ingress occurs and ultimately the time to reach DOS_{cr}. Smaller pores generate larger capillary pressure than large pores (*i.e.*, air voids) according to the Young-Laplace equation.[72] Due to the capillary pressure, capillary pores become saturated before larger air voids as illustrated in **Figure 1.4**.[68,73,74]
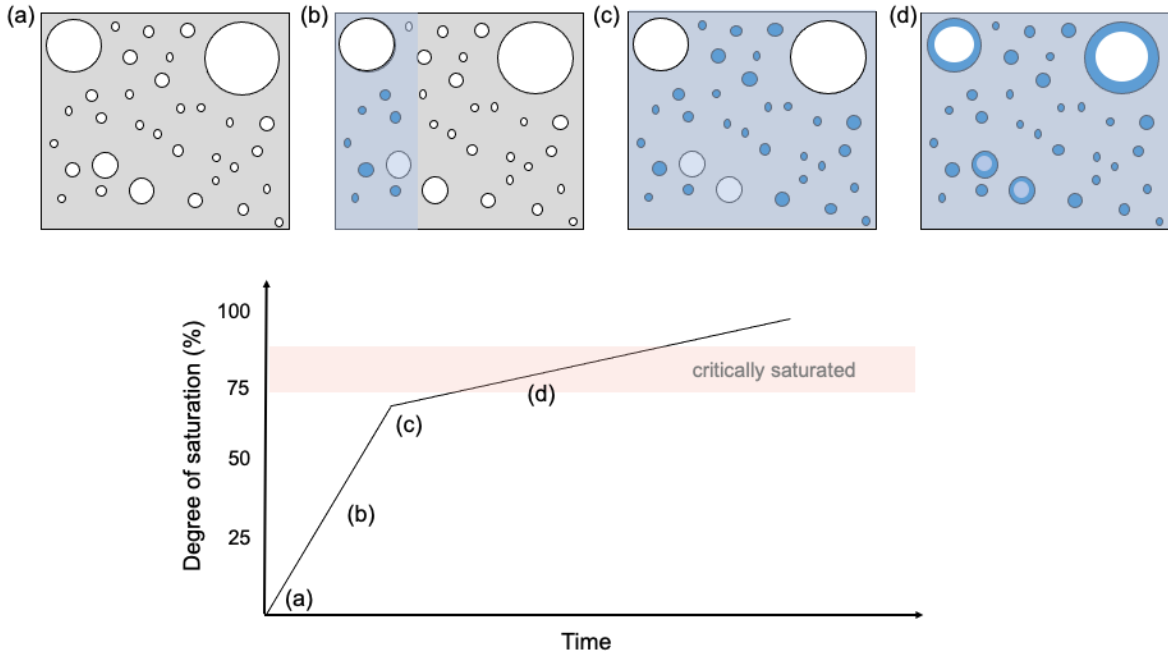
Figure 1.4. Illustration of water absorption with time. (a) – (c) the gel and capillary pores fill with water. (d) the entrained and entrapped air voids become filled with water. As the air voids become water-filled, the critical degree of saturation, DOS_{cr}, is approached. Figure adapted from Weiss, 2014.[74]

Air entrainment is the *de facto* method to providing freeze-thaw resistance in cementitious materials. Air voids provide freeze-thaw resistance by effectively providing pressure relief sites for developing hydraulic, osmotic, and crystallization pressures and likely serve as sites for preferential nucleation. To be effective, air voids must be of specific sizes and distributions and exhibit proper spacing.[8-10] **Chapter 2** will discuss air entrainment in greater detail.

1.3.7 Methods to Mitigate Freeze-Thaw Damage

Researchers have utilized a variety of materials and methods to enhance the freeze-thaw resistance of cementitious materials. The prevailing strategy to enhance the freeze-thaw resistance of OPC concrete is to entrain an air void system in the paste that effectively reduces the pressures that develop during cyclic freezing and thawing. Conventional air-entraining

admixtures (AEAs) create stabilized air void systems within cementitious matrices. Other materials and strategies include the incorporation or application of nanoparticles, SCMs, superabsorbent polymers, fibers, and hydrophobic agents.[3–12] **Chapter 2** will discuss each approach in more detail. No material or method currently used for mitigation of freeze-thaw damage in cementitious materials directly prevents or slows the nucleation and growth of ice.

1.3.8 Ice and Ice Recrystallization

The formation of ice from liquid water is unique in that in the solid state, ice, has a lower density than the liquid state which corresponds to a 9% larger volume.[75] The vast majority of ice on earth occurs as the hexagonal crystal structure or ice 1h.[76] The hexagonal crystal structure can be seen in **Figure 1.5a** with the c- and a-axis, basal plane, primary prismatic, and secondary prismatic planes labeled. **Figure 1.5b** shows a structural representation of ice with the lattice constants for hexagonal ice along the basal plane a=4.52 Å and along the primary prism plane c = 7.36 Å labelled.[75,77]
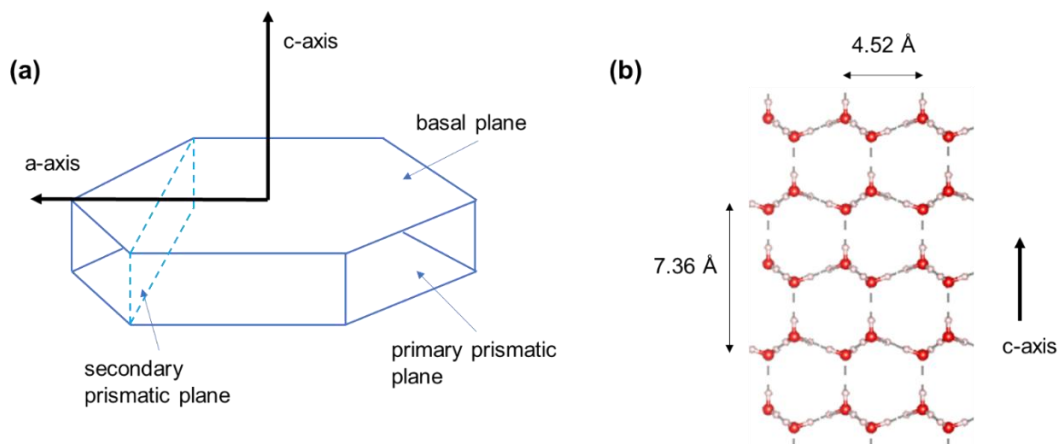
Figure 1.5. (a) Hexagonal crystal structure of ice with c-axis, a-axis, basal, primary prismatic, and secondary prismatic planes labeled. (b) Schematic representation of ice. The red circles represent oxygen atoms, the white circles represent hydrogen atoms, and the dashed lines represent hydrogen bonding. The structure was created using VESTA software.[78] Lattice

constants for hexagonal ice along the basal plane a=4.52 Å and the primary prism plane c = 7.36 Å.[75,77]

The formation of ice consists of nucleation, growth, and recrystallization. Nucleation can be both homogeneous and heterogeneous. Homogeneous nucleation occurs spontaneously and randomly under the conditions of supercooling. Homogeneous nucleation does not occur in pure water till nearly -40 °C.[79] Heterogeneous nucleation occurs at surfaces, particles, or other impurities in contact with liquid water. In most cases, nucleation of ice occurs heterogeneously due to the presence of impurities, and because heterogeneous nucleation has a lower free energy barrier to overcome in the crystallization process compared to homogenous nucleation.[80] Once nucleation occurs, water molecules add to ice crystals allowing them to grow. At rapid rates of cooling an amorphous glass forms without crystalline ice formation, a process known as vitrification.

Ice recrystallization plays a critical role in cryopreservation,[81–83] food storage,[84–86] climate and glacier sciences, [87–89] among other natural phenomena and technological processes. Ice recrystallization is a thermodynamically driven process where large ice crystals (*i.e.*, grains) grow at the expense of smaller ice crystals (*i.e.*, Ostwald ripening).[90] Ice recrystallization is shown in the micrographs of **Figure 1.6**. The grains, or ice crystals, which are highlighted in color can be seen to grow larger over time in **Figure 1.6**. Water molecules transfer from the surface of smaller ice crystals to the surface of large ice crystals. The reduction in the surface area to volume ratio with the growth of larger ice crystals results in lower free energy.

larger surface area to volume ratio   smaller surface area to volume ratio
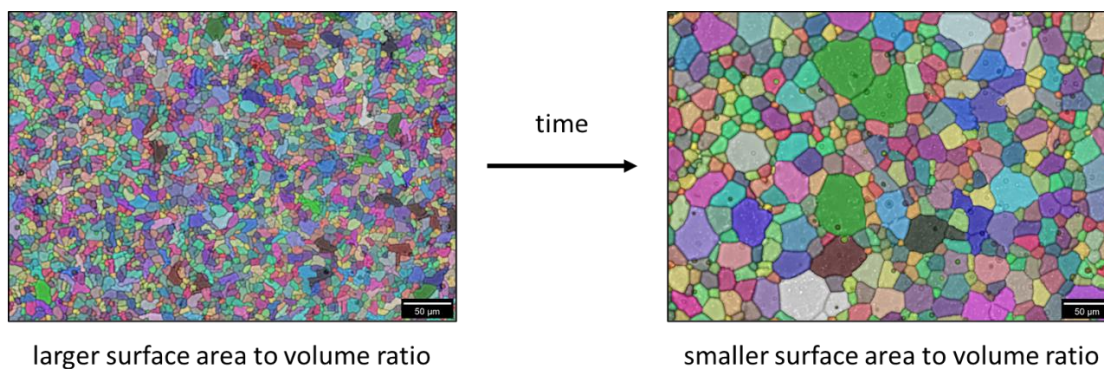
Figure 1.6. Ice recrystallization is shown on micrographs of a monolayer of ice. Each grain is highlighted in color for enhanced visualization. The ice grain, or crystals, grow over time to reduce the free energy.

The transition between the ice crystal surface and the liquid water phase is not abrupt, but rather a semi-ordered phase exists between them which is referred to as the quasi-liquid layer (QLL). The exact characteristics of the QLL are the subject of ongoing research.[91–94] However, significant evidence has shown the presence of the QLL and that it plays a critical role in the growth of ice crystals.[95–98] For example, disruption of the QLL region is used to explain how amphiphilic anti-ice coatings function.[99,100] **Figure 1.7** provides a simplified schematic representation of the bulk or liquid water, QLL, and ice crystal phases.
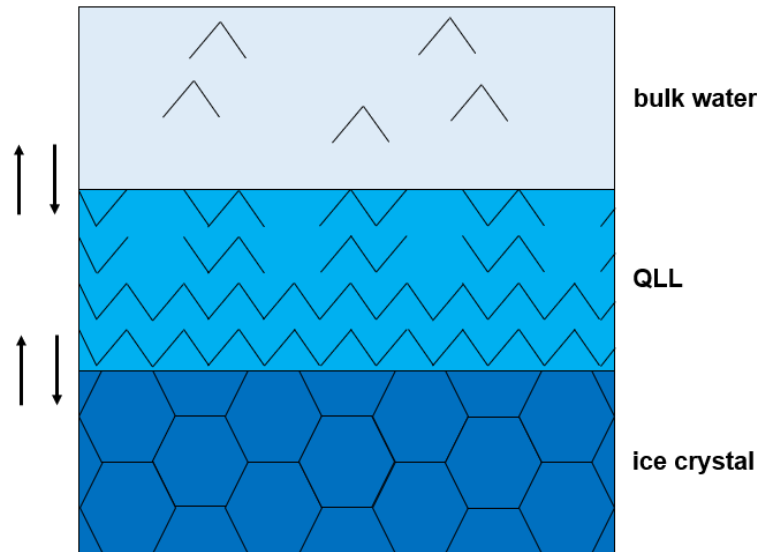
Figure 1.7. Schematic representation of the interfaces between bulk or liquid water (▪), QLL (▪), and ice crystal phases (▪). The black lines represent water molecules and hydrogen bonding between water molecules. The arrows on the left side of the figure indicate the movement of water molecules between all three phases.

1.3.9 Antifreeze Proteins – Nature's Solution to Ice Crystal Growth

The nucleation, growth, and recrystallization of ice can be detrimental to life in cold climates. For example, the formation and growth of ice within a cell or blood vessel could be lethal. Nature has developed ice-binding proteins (IBPs) as a means to survive freezing temperatures. IBPs serve various functions[101] including freeze avoidance by thermal hysteresis (TH),[102–104] freeze tolerance by ice recrystallization inhibition (IRI),[105–107] ice adhesion,[108–110] structuring of external ice,[111,112] and ice nucleation.[113–115] It is widely accepted that IBPs function by adsorbing to the surface of ice allowing them to control the growth of ice.[116]

Antifreeze proteins (AFPs) and antifreeze glycoproteins (AFGPs) are a subset of IBPs produced by plants,[117–119] fish,[120–122] insects,[123] fungi,[117,124,125] diatoms,[126–128] and bacteria.[129–131] AFPs and AFGPs specifically allow for freeze avoidance and freeze tolerance *via* TH and IRI activity respectively. By binding to the surface of ice, AFPs and AFGPs can inhibit the growth

and recrystallization of ice crystals (*i.e.*, Ostwald ripening) *via* IRI. AFPs and AFGPs also induce dynamic ice shaping (DIS) and reduce the freezing point of ice below the equilibrium freezing point (*i.e.*, TH).[132] Recent work suggests that ice-binding and antifreeze properties are a result of anchored clathrate and ice-like motifs in AFPs and IBPs.[133,134] However, the underlying mechanisms are yet to be fully explicated.[135]

Researchers have successfully isolated AFPs and AFGPs from a multitude of freeze-tolerant organisms. However, the production cost of AFPs is high which limits their application.[136,137] High costs render AFP incorporation into cementitious materials impractical at the current time. Additionally, proteins are well known to restructure in non-native environments.[138] Given that the structure of AFPs drives their function, the high alkalinity (pH >12.5) of concrete pore solution is unfavorable for protein stability.[139]

To overcome economic limitations and instabilities of proteins in non-native environments, researchers have synthesized a variety of non-proteinaceous materials that mimic the IRI and DIS activity of AFPs and AFGPs.[140–144] The most widely studied material displaying IRI and DIS activity is the polymer polyvinyl alcohol (PVA). The pendant hydroxyl groups along the polymer backbone of PVA mimic the highly hydroxylated carbohydrates of AFGPs.[140] A more thorough review of biomimetic antifreeze materials will be presented in **Chapter 3**.

1.4 Overview of Work and Organization of Dissertation

Chapter 2 is a review of methods used to mitigate freeze-thaw damage in OPC paste, mortar, and concrete. This review focuses on the underlying mechanisms that allow for freeze-thaw resistance, materials that are used in each approach, and the shortcomings of each method. Specifically, air entrainment, methods for densification, use of superabsorbent polymers, the

addition of polymeric fibers, and application of hydrophobic agents are examined. This review demonstrated a clear need for investigating materials that either directly prevent the nucleation or slow the growth and recrystallization of ice within cementitious materials.

Chapter 3 is a review of biomimetic antifreeze materials. This review starts with a description of the current understanding of antifreeze protein (AFP) and antifreeze glycol protein (AFGP) function and performance in ice recrystallization inhibition (IRI) and thermal hysteresis (TH). A variety of materials that mimic AFPs and AFGPs are discussed including synthetic peptides, self-assembling molecules, polymers, nanoparticles, and small molecules. The structural components that allow for the biomimetic activity of these materials are discussed. This review demonstrated that polyvinyl alcohol is the most IRI active synthetic material researched and the most widely studied, which makes it an ideal candidate for study within hardened cement paste.

Chapter 4 investigates the performance of polyethylene glycol-polyvinyl alcohol graft copolymer (PEG-PVA) to inhibit ice recrystallization and induce dynamic ice shaping in both neutral and pH 13 solutions and as an additive to OPC paste for freeze-thaw performance. The purpose of this work was to determine if an IRI active polymer can provide freeze-thaw resistance to hardened cement paste without the use of traditional AEAs. The results for Chapter 5 have been published in Cell Reports Physical Science.[145]

Chapter 5 investigates the role that both molecular weight and degree of hydrolysis play in the performance of PVA as an additive to OPC paste for freeze-thaw mitigation. The purpose of this work was to determine the molecular weight and degree of hydrolysis requirements for PVA to be effective at providing freeze-thaw resistance in hardened cement paste. Additionally, this

work demonstrated that the presence of IRI active polymers results in reduced ice contents during freezing temperatures.

Chapter 6 investigates the performance of folic acid, which mimics Type IV AFPs, to inhibit ice recrystallization, display thermal hysteresis, and induce dynamic ice shaping. The ability of folic acid to self-assembly at concentrations between 0.01-0.5 mg/mL was investigated. Lastly, folic acid was tested as an additive to OPC paste for freeze-thaw mitigation. This work demonstrates for the first time that folic acid displays IRI activity. Although folic acid shows promise as an IRI active material, further investigation is required to fully explicate its use as an additive to cementitious materials. Folic acid-modified paste displayed greater resistance to surface damage than internal damage during freeze-thaw cycling.

Chapter 7 focuses on the IRI activity of surfactants used in commercially available AEAs. Sodium oleate, vinsol resin, sodium lauryl sulfate, and a phenol ethoxylate IRI activity were compared to previously published concrete freeze-thaw results to determine if a correlation between IRI activity and freeze-thaw resistance exists. Additionally, the role of hydrophobicity, topological polar surface area, molecular volume, and molecular weight on IRI activity was explored. For the surfactants studied, higher levels of IRI activity correlated with higher freeze-thaw performance in concrete. The surfactants studied herein do not appear to follow the same structure-property relationships regarding IRI activity when compared to other small molecules.

Chapter 8 presents a summary of scientific contributions within this thesis to the fields of biomimetic antifreeze materials and freeze-thaw resistance of cementitious materials. Suggestions for future research directions are discussed with a focus on broadening the application of biomimetic antifreeze materials to OPC concrete.

Chapter 2 Methods for Enhanced Freeze-Thaw Resistance in Cementitious Materials – A Review

2.1 Introduction

The primary aim of this chapter is to present the methods by which the freeze-thaw resistance of cementitious materials is enhanced and present brief a state-of-the-art review of the field. Researchers have utilized a variety of materials and methods to enhance the freeze-thaw resistance of cementitious materials. These materials and strategies include (1) creation of an air void system with the use of AEAs,[2] (2) densifying and strengthening cement paste using nanoparticles or supplementary cementitious materials,[3–6] (3) incorporating superabsorbent polymer particles (SAPs) as a non-surfactant method to achieve an entrained air void system,[7] (4) using macroscale polymeric fibers for mitigating crack propagation due to frost-induced damage,[9,10] (5) and decreasing water absorption using hydrophobic agents.[146–148]

In concrete, the most common method in the USA of evaluating freeze-thaw performance is outlined in ASTM C666 Procedure A.[149] and AASHTO T 161 Procedure A.[150] Concrete specimen undergo cyclic exposure to freezing and thawing temperatures while fully submerged in water. After 300 freeze-thaw cycles, a specimen is considered to pass if it maintains a relative dynamic modulus of elasticity or durability factor greater than 60% of the initial.

To compare the strategies discussed within this chapter, the published durability factors (%) from previous work are graphed in **Figure 2.1**. All results within **Figure 2.1** are for concrete specimen that were exposed to cyclic freeze-thaw conditions outlined in ASTM C666 Procedure A. As can be seen in **Figure 2.1**, a variety of the strategies do not result in a durability factor greater than 60%. It should be noted that a wide variety of other test methods exists[151,152] and published research often modifies either ASTM C666 or another standardized test.

Figure 2.1. Previously reported results from ASTM C666 Procedure A. The durability factor (%) is the reported value at 300 cycles.[153–158]

2.2 Air Entraining Agents (AEAs)

AEAs provide freeze-thaw resistance by allowing for the formation of an air void system within cementitious materials. Air void systems are believed to provide freeze-thaw resistance by acting as a pressure relief reservoir for the hydraulic, osmotic, and crystallization pressures that develop during freeze-thaw cycling. Air voids intersect the network of capillary pores and because the air voids are larger than capillary pores, water and ice can move from the capillary pores to the air voids during freezing.[159] Scherer and Valenza proposed in the Crystallization Pressure Theory that air voids provide a preferential site for ice nucleation and growth.[49] The air voids reduce the ingress of water and increase the time to reach critical saturation as it takes a longer amount of time for water to enter air voids.[68] Additionally, AEAs that coagulate with Ca^{2+} have been shown to provide a protective layer around the air void.[160,161]

Air bubbles within cement paste are inherently unstable due to their surface energy. AEAs reduce the surface tension of water which stabilizes the air bubbles. The vast majority of AEAs are surfactants. As shown in **Figure 2.2 a**, surfactants contain both a hydrophilic (*i.e.*, water loving) and hydrophobic (*i.e.*, water hating) portion and therefore are amphiphilic. When placed into a solution of water followed by agitation, the AEAs orient themselves such that the hydrophilic head is pointed toward the water and the hydrophobic tail is pointed inward toward the air as shown in **Figure 2.2 c**. Without the presence of AEAs, the air bubbles would thermodynamically be driven to agglomerate and form larger size air voids as shown in **Figure 2.2 b**.
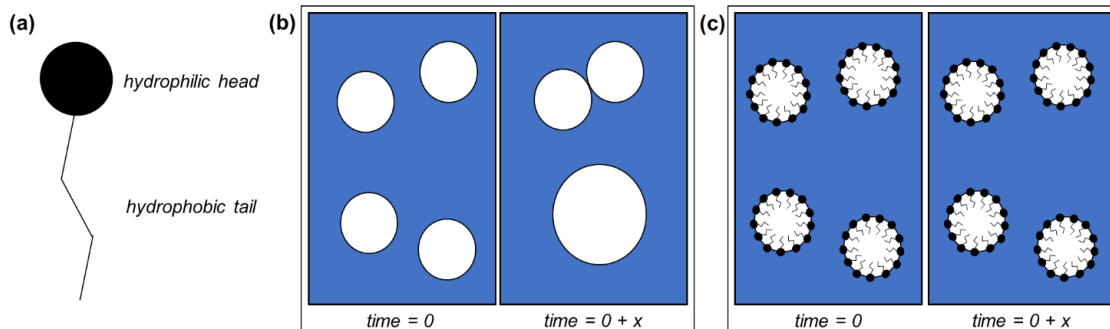
Figure 2.2. (a) Basic chemical structure of a surfactant molecule; (b) unstabilized air bubbles coalescing with time; (c) stabilized air bubbles through the incorporation of AEAs.

AEAs can be classified in several ways. Here, they will be broadly classified in two ways: (1) ability to coagulate in the presence of calcium (*i.e.*, insoluble vs soluble), and (2) by the type of ionic compound: anionic, cationic, zwitterionic, and non-ionic. The interaction of an AEA molecule with calcium is important. Vinsol resin and sodium oleate are two examples of AEAs that coagulate with calcium, and they do not significantly change the surface tension of water.[162] An insoluble calcium salt (or soap) is formed when two anionic surfactant molecules interact with Ca^{2+}. It is believed that the collection of these calcium salts forms a hydrophobic layer around an air void (*i.e.*, an insoluble calcium salt).[2,163] and evidence suggests that AEAs provide freeze-thaw resistance when such a shell is formed.[164] Examples of AEAs that coagulate with Ca^{2+} include sodium lauryl sulfate, sodium oleate,[163] and vinsol resin.[160,162,163]

Table 2.1 provides the classification of common AEAs. Synthetic AEAs are generally aliphatic chains with head groups containing either SO_4^{2-}, CO_3^{2-}, or OH^-. Anionic surfactants are the most heavily used type of AEA,[165] and examples include sodium dodecyl benzene sulfonate, sodium lauryl sulfate, sodium oleate, and sodium alkane hydroxy sulfonic acids. Vinsol resin and saponified rosin are among the most commonly used nonionic surfactants.[166] Cationic and

zwitterionic surfactants have been shown to result in poor freeze-thaw performance.[164] Additionally, commercial AEAs tend to contain multiple surfactants.[162]

Several physical parameters are utilized to predict the efficacy of an air void system to provide freeze-thaw resistance including fresh state air content, hardened state air content, spacing factor, and specific surface area. Fresh state air content is most commonly determined following the pressure method outlined in ASTM C231.[167] An air meter device is used to measure the air content and the air content of aggregate is accounted for. Alternatively, ASTM C173 or C183 can be utilized for the determination of fresh state air content. To be effective, AEAs need to entrain ~4%–10% air by volume of concrete, or ~16%–25% air by volume of cement paste.[163,168]

The hardened state air content is typically determined using petrographic methods outlined in ASTM C457.[54] A recent modification to the method outlined in ASTM C457 utilizes cross-sectional images obtained using micro X-ray computed tomography.[169,170] The measured fresh state air content is typically 0.5 to 1.5% higher than the hardened state content due to the opportunity for the voids to coalesce in the fresh state.[171] The actual difference depends on the surface activity of AEA used, transportation, placement, and consolidation practices.[159] In general, a hardened-state air content of ~4%–10% ensures adequate resistance to freeze-thaw damage.[168,172]

The same petrographic methods outlined in ASTM C457 are used to determine the spacing factor and specific surface area.[54] Spacing factor is a measure that estimates the maximum distance from any point within the cement paste to an air void. Generally, it is recommended that the spacing factor be less than <200 μm with some literature suggesting a maximum up to 250 μm.[44,159,173] It has become accepted that the spacing factor is a more accurate means of predicting

freeze-thaw performance compared to air content.[174,175] Specific surface, α, is the ratio of the surface area of voids to volume (mm^2/mm^3). Specific surface is recommended to be at least 25 mm^2/mm^3.[168]

The above parameters can only be used as guidelines, as there are a multitude of examples where freeze-thaw resistance is not obtained when recommendations are met and *vice versa*. Despite enhancing freeze-thaw resistance, the introduction of an air void system results in reduced mechanical strength, which can be as high as 5% per 1% entrained air, and an increase in permeability that is proportional to the amount of introduced air.[176]

2.3 Densification of Cementitious Materials

A denser concrete has reduced permeability and higher strength. Given this, one strategy to improve freeze-thaw resistance of cementitious materials is through densification. The primary strategies for densification are through the addition of nanoparticles and supplementary cementitious materials (SCMs).[3–6]

A variety of nanomaterials have been shown to improve the microstructure of cementitious materials which led to reduced permeability and enhanced freeze-thaw resistance including SiO_2 nanoparticles[5,177,178] and carbon nanotubes (CNTs) [179–181]. The improvement in microstructure is believed to be a result of 1) the nanoparticles behaving as a nucleating agent for hydration products which accelerates cement hydration, 2) reduction of $Ca(OH)_2$ phase when nanoparticle has pozzolanic reactivity,[182] and 3) behaving as a filler material in pores.[183,184] Issues with nanoparticles include increased water demand and agglomeration of the nanoparticles. [185,186] Agglomeration is a major challenge as previous research has shown that poor distribution can result in no property enhancements or even be detrimental to performance.[184,187,188] Proper

dispersion is often achieved through the use of surfactants or sonification.[188–192] For CNTs specifically, the source and quality of the material can also play a role in how well they perform.[179] Lastly, the cost of CNTs, and other nanomaterials, can be cost prohibitive.

Fly ash,[193,194] silica fume,[193,195] metakaolin,[4,193] and ground granulated blast furnace slag[4] have all been studied for enhancing freeze-thaw resistance, including at an early age.[196] Generally, the observed freeze-thaw performance is not sufficient to meet the 60% durability factor requirements of ASTM C666 unless AEAs are also utilized. Fly ash modified cementitious materials have mixed results regarding freeze-thaw resistance and require a properly entrained air void system.[197,198] Silica fume, metakaolin, and ground granulated blast furnace slag[4] have all shown the ability to provide freeze-thaw resistance without the use of air entraining agents, with silica fume being the most promising.[193,195] The freeze-thaw performance can be attributed to the SCMs behaving as a filler and a pozzolan leading to densification.[3,195,199] Additionally, the quality and availability of SCMs is becoming an ever-increasing problem.[200,201]

2.4 Superabsorbent Polymers

Superabsorbent polymers (SAPs) can be utilized to create voids in concrete akin to air voids. In fact, previous work has shown that the spacing factor of SAP voids, and all other voids, can be used as an indicator for freeze-thaw performance of SAP modified concrete.[7] When SAPs are added to a mix, the SAP particles absorb water which results in their swelling. The absorbed water behaves as an internal curing agent as it releases water during curing.[202] As cement hydration continues, the water surrounding the SAP particle is consumed creating a void between the cement paste and the SAP particle. This process is shown schematically in **Figure 2.3**. The

voids created by SAP particles have been attributed to observed freeze-thaw resistance when

SAPs are added to concrete.[7,8,153,202–204]
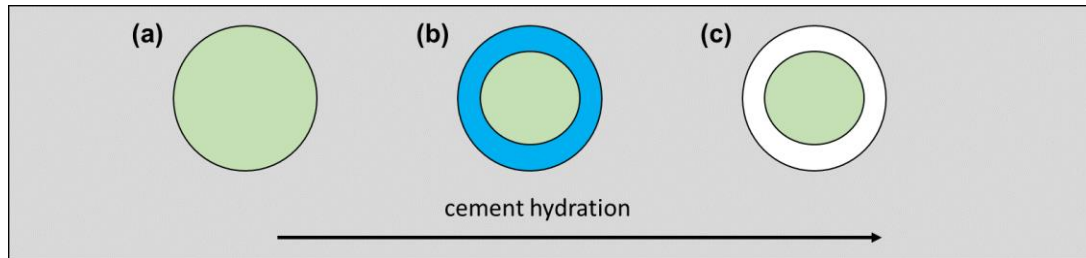
Figure 2.3. Schematic representation of SAP void creation process during cement hydration. SAP particle is green. (a) Swollen SAP particle after initially being placed in mix. (b) De-swollen SAP particle still surrounded by water. (c) De-swollen SAP particle where water surrounding particle is consumed by cement hydration.

Although SAPs have been shown to provide freeze-thaw resistance, the results are not always

satisfactory. For example, Jones and Weiss showed that concrete with SAP but no AEA did not

pass ASTM C666 Procedure A.[153] An extensive interlaboratory study found that traditionally air

entrained concrete displayed better freeze-thaw performance than concrete modified with

SAP.[205] Furthermore, SAP particles made *via* suspension polymerization often contain surfactant

molecules on their surface which can result in both the SAP voids and entrained air voids.[7]

Suspension polymerization is one of the two major techniques used to create SAPs with the other

being bulk polymerization.

Several parameters related to SAPs play a critical role in their freeze-thaw performance

including particle size and particle shape. Like air voids, the size of particles is critical to freeze-

thaw performance and other properties. Finer SAP particle sizes result in better freeze-thaw

performance.[205]

30

2.5 Polymeric Fibers

Fibers can be added to cementitious materials to help prevent cracking and improve strength and toughness.[19] The fiber modified materials are referred to as fiber-reinforced concrete (FRC) or fiber-reinforced cement-based composites (FRCCs). The fibers are discontinuous, randomly dispersed, can be a variety of shapes and sizes, and are typically steel, glass, natural materials (*i.e.*, cellulose or wool), or polymeric fibers.[19,206] The resulting properties of FRCs are dependent on the size, type, geometry, dispersion, bond with paste, and content of fibers.

Polymeric fibers are widely used in FRCs and several commercial products exist. In addition to observed enhancements to mechanical properties, enhanced freeze-thaw durability has been reported and attributed to mitigation of crack formation. The polymers most widely studied for freeze-thaw performance in FRCs include propropylene[9,207,208], polyethylene, and PVA.[9,154,209,210] The fibers vary in size with reported lengths of 12 to 51 mm and diameters of 0.012 to 0.806 mm.

Although it is believed that the polymeric fibers provide freeze-thaw resistance by mitigating crack propagation, work has indicated that entrained air is still required.[211] Similar to nanomaterials, the fibers need to be dispersed appropriately to provide enhancements.[210,211] Furthermore, polymeric fibers have been shown to entrain air.[207] Fibers typically have a negative impact on fresh state properties including reduced workability and increased mixing and placement times.

2.6 Hydrophobic Agents

The degree of water saturation is a critical factor influencing the freeze-thaw resistance of cementitious materials. Previous work has shown that once a critical degree of saturation

between 86-88% is reached, freeze-thaw damage is unavoidable even with a properly entrained air void system.[68] Hydrophobic treatments have been utilized to reduce the amount of water ingress. The hydrophobicity of cementitious materials can be increased by either surface treatment[148,212–214] or the addition of a hydrophobic agent added as part of the mix design.[147,215] Silanes and siloxanes are the most commonly used hydrophobic agents for both surface and internal treatment.[146–148,215–217] Hydrophobic surface treatment is the more prevalent strategy of the two.

Surface treatment is generally classified into three categories: coatings, pore blockers, and pore liners. The three categories of hydrophobic surface treatment are schematically shown in **Figure 2.4**. If the surface applied hydrophobic agent is unable to penetrate the pores and only forms a film on the surface, it is a coating (**Figure 2.4 a**). If the molecule size of the surface applied hydrophobic agent is sufficiently small, it can penetrate the capillary pores. Once the material has penetrated the pores, it is considered a pore liner if it adheres to the surfaces (**Figure 2.4 b**). The third type of surface treatment, pore blocker, forms insoluble products within the pores (**Figure 2.4 c**).[218]

(a) coating   (b) pore liner   (c) pore blocker
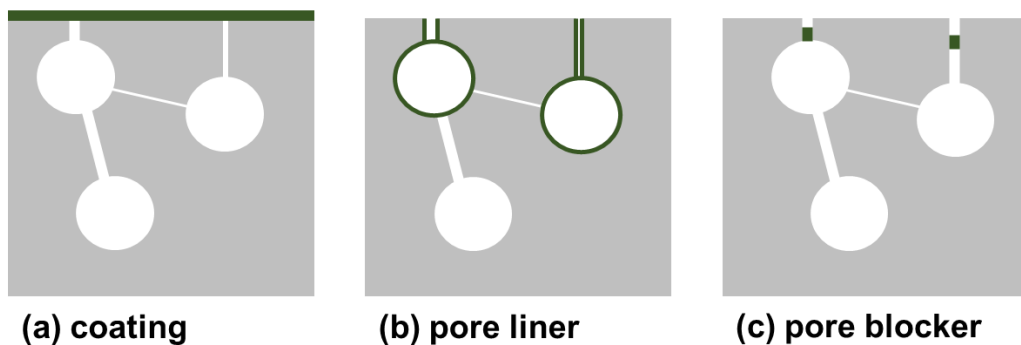
Figure 2.4. Categories of hydrophobic surface treatments. (a) Application of hydrophobic agent generating a surface coating. (b) Penetration of hydrophobic agent from surface to capillary pores, known as a pore liner. (c) Penetration of hydrophobic agent from surface to capillary pores and generation of insoluble product referred to as a pore blocker. Green color represents the hydrophobic material. White color represent pore. Grey color represents hardened cement.

Although hydrophobic surface treatments have been shown to reduce the ingress of water and reduce ionic species ingress,[213] they cannot be a replacement for an air void network to mitigate internal cracking from freeze-thaw damage. Instead, the application of hydrophobic agents is done in conjunction with AEAs.[219] Hydrophobic surface treatment appears to be a more effective strategy for reducing surface scaling than internal cracking from freeze-thaw cycling.[148]

Chapter 3 Biomimetic Antifreeze Materials – A Review

3.1 Introduction

Nature has developed a unique strategy to survive cold climates. A multitude of organisms produce ice binding proteins (IBPs), a broad classification of proteins that can provide freeze tolerance, freeze avoidance, ice recrystallization inhibition, ice adhesion, and ice nucleation.[116] Antifreeze proteins (AFPs) and antifreeze glycoproteins (AFGPs) are a subset of IBPs which allow species to survive freezing temperatures. AFPs and AFGPs inhibit the recrystallization of ice (*i.e.*, Ostwald ripening), induce dynamic ice shaping, and reduce the freezing point of ice below the equilibrium freezing point *(i.e.*, thermal hysteresis).[132]

In this chapter, a brief overview of AFPs and AFGPs will be presented. First, definitions of ice recrystallization inhibition (IRI), thermal hysteresis (TH), and dynamic ice shaping (DIS) activities are presented. The current understanding of the mechanisms for each observable interaction along with measurement techniques is discussed. Second, the structure-property relationships of AFPs and AFGPs are explored. A review of biomimetic antifreeze materials including polymers, synthetic peptides and molecular analogs, nanostructures and self-assembling molecules, and small molecules focusing on structure-property relationships and IRI activity is presented. Finally, the chapter is concluded with a discussion of the applications for IRI active materials.

3.1.1 Biomimetic Antifreeze Properties

3.1.1.1 Thermal Hysteresis

TH activity is a strategy for freezing avoidance. TH results from the non-colligative reduction in the freezing temperature of a solution while the melting is maintained or elevated,

thus a hysteresis gap is developed between the freezing and melting temperatures. Due to the reduction in the freezing point, it becomes more difficult for a solution to freeze. AFPs can produce TH activities from 1°C to 5°C (moderate to hyperactive).[101,116]

TH is most often measured using a nanoliter osmometer. A nanoliter-sized drop of an aqueous sample is placed in microscopy immersion oil. The sample is rapidly cooled to form polycrystalline ice (-20°C or lower). Next, the sample is slowly melted to form a single ice crystal (*e.g.*, heating at a rate of 5°C/min). The temperature is kept constant for 3 – 15 minutes to ensure the ice crystal is stable, and this is taken as the melting temperature of the sample. Last, the sample is cooled at 0.01°C/min until crystal growth is observed. **Figure 3.1** provides representative micrographic images of the polycrystalline ice, stable single ice crystal, and the single ice crystal beginning to grow. The temperature at which growth is observed is reported as the freezing temperature and the difference between the observed melting and freezing temperatures is taken as the TH.
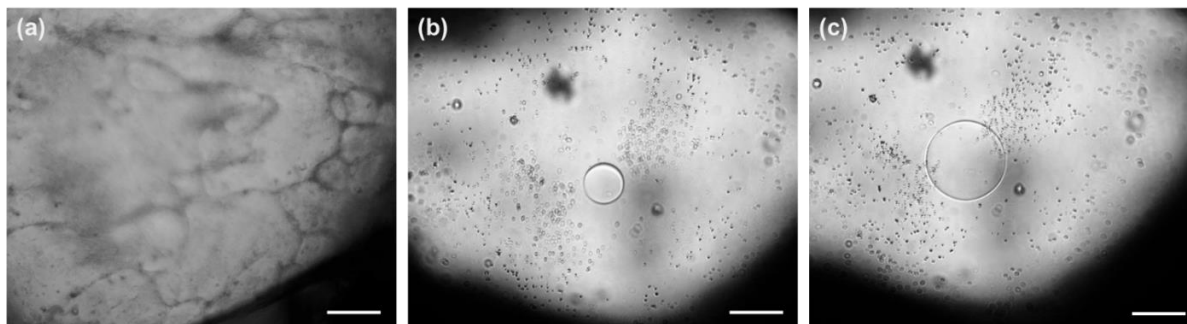
Figure 3.1. Representative micrographs of ice formation, melting, and growth during thermal hysteresis (TH) measurement using nanoliter osmometry. (a) polycrystalline ice, (b) stable single ice crystal, and (c) growing single ice crystal as the temperature is decreased. Scale bars are 50 µm.

Depending on the specific interaction of the material being tested with the ice crystal during TH measurement, the crystal shape can vary during growth (freezing). This reshaping of the ice crystal is referred to as dynamic ice shaping (DIS). The shape is dependent on which

crystallographic plane of 1h ice the material interacts with. **Figure 3.2** provides a summary of the ice crystal shapes that result from interaction with the crystallographic planes of ice. DIS is likely not a strategy to survive cold climates but rather a side-effect of AFPs adsorbing to the ice crystals.
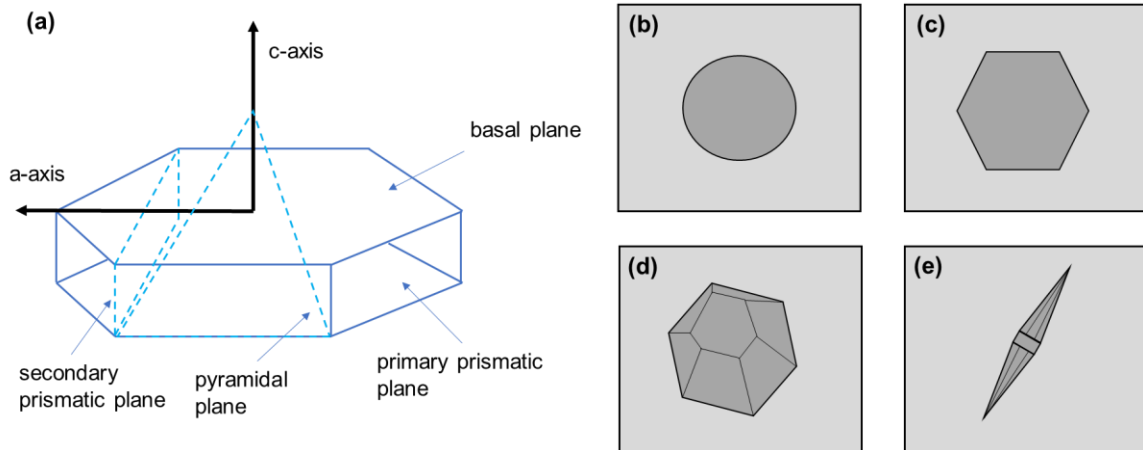
Figure 3.2. Crystallographic planes of 1h ice and commonly observed shapes of single ice crystals in DIS assay. (a) Ice crystal planes which AFPs are known to adsorb to, including the basal plane, primary prismatic plane, pyramidal plane, and secondary prismatic plane. (b) The circular shape of ice crystal with no material adsorbing to a crystallographic plane. C-axis is normal to the paper plane. (c) Hexagonal shape of ice crystal when material is adsorbed on the primary prismatic plane.[106] C-axis is normal to the paper plane. As ice continues to add to the basal plane, the hexagonal shape elongates along the c-axis. (d) Lemon-shaped ice crystal resulting from adsorption on the primary prismatic plane and basal plane.[220] Note that the lemon-shape often has less well defined edges as shown here. (e) Bipyramidal-shaped ice crystal can result from adsorption onto the prism, basal, and/or the pyramidal planes.[132] In the example shown here, the c-axis is along the points of the pyramidal structures.

3.1.1.2 Ice Recrystallization Inhibition (IRI)

Instead of avoiding freezing, IRI activity allows for freezing tolerance. Ice recrystallization is a thermodynamically driven process where large ice crystals (*i.e.*, grains) grow at the expense of smaller ice crystals (*i.e.*, Ostwald ripening).[90] Water molecules transfer from the surface of smaller ice crystals to the surface of large ice crystals. The reduction in the surface area to

36

volume ratio with the growth of larger ice crystals results in a lower free energy. IRI is believed

to result from the adsorption of material onto the surface of an ice crystal. The adsorption results

in regions of local surface curvature that slow the growth of ice. The curvature of the crystal

surface reduces the local melting point according to the Gibbs-Thompson equation.[221–223]

The predominant method for measuring IRI activity is the splat assay which was initially

developed by Knight and Dumani.[82] A 10-20 µL volume of sample is dropped from 1.5-3 m onto

a glass slide (thickness of 1 mm). The glass slide is typically located on an aluminum block

precooled with dry ice (-78°C). Once the sample hits the glass slide it forms a monolayer of

polycrystalline ice. The slide is then immediately transferred to a cold stage and annealed at a

temperature below the melting point for a prescribed amount of time. The annealing temperature

is often between -4°C and -10°C and the annealing time is typically 30 minutes. Images are

collected immediately after the sample was placed on the cold stage and again at the prescribed

endpoint to observe ice recrystallization. The samples can be both qualitatively and

quantitatively compared. Comparing the micrographs at the endpoint allows for qualitative

comparison. The Feret diameter of the individual ice grains of the micrographs can be measured.

Often the diameters, or sizes, of the grains are compared to a control (*i.e.*, the aqueous solvent)

and reported as the percent mean largest grain size (MLGS). A smaller % MLGS indicates a

more IRI active material. Typically, the 10 largest grains are measured from three replicates for

the determination of the MLGS.

When considering IRI activity, a clear definition of what constitutes negligible vs. moderate

vs. highly active is still not widely agreed upon.[224] It is clear that AFPs and AFGPs are highly

active as they typically result in an MLGS 20% or lower compared to a control solution at

concentrations below 0.1 mg/mL.[77,224] Biggs *et al.* proposed using four zones based on

previously studied materials. The most active materials would display IRI activity similar to

AFGPs and function at concentrations below 0.1 mg/mL. Next are materials that display IRI

activity up to 1 mg/mL followed by materials that display IRI activity up to 10 mg/mL. Lastly,

are weak inhibitors which essentially display little to no IRI activity.[224] One problem with the

four zones guide is that it does not provide recommendations on the MLGSs. Briard *et al.*

classified activity based on MLGS where >70% indicated inactive and <70% indicated

activity.[225] Delesky proposed a similar grouping of MLGS where >80% indicated negligible IRI

activity and <30% indicated potent IRI activity.[226] In this work the definitions outlined in **Table
3.1** will be used to define the IRI activity.

Table 3.1. Definitions of IRI activity used in this work. Highly, moderately, and negligible IRI
activity is defined by both the percent mean largest grain size (% MLGS) and the concentration
the material was tested at.

Category	% MLGS limits	Concentration limits
Highly IRI active	$\leq 20\%$	up to 0.1 mg/mL
Moderately IRI active	$> 20\%$ and $\leq 70\%$	≤ 1 mg/mL
Negligible IRI active	$>70\%$	≥ 1 mg/mL

3.1.2 Antifreeze Proteins and Antifreeze Glycoproteins

Antifreeze proteins (AFPs) function to inhibit ice growth and recrystallization within various

organisms *via* IRI and TH activity. AFPs are believed to adsorb onto the surface of ice nuclei to

stop ice growth.[223] The adsorption of the AFP to the ice surface creates micro-curvature that

lowers the local freezing temperature through the Kelvin effect.[227,228] The exact mechanism has

not been fully explicated, but recent work suggests that ice-binding and antifreeze properties are

a result of anchored clathrate and ice-like motifs in AFPs.[16,17] This is different than traditional

antifreeze materials (*i.e.*, ethylene glycol, glycerol, dimethyl sulfoxide) which prevent ice

formation in a colligative manner.

The size and structure of AFPs vary significantly which is likely to be a result of independent evolution.[116] **Figure 3.3** provides examples of Type I, Type II, Type III, and Type IV from fish. Characteristic features including size, amino acid bias, and structural features are highlighted in **Figure 3.3**. Across all four types of fish AFP, the size varies drastically from ~ 3 kDa to 24 kDa.[229–231] The same can be said about structural features such as the α-helix structure of Type I AFPs vs the globular, β-strand containing structure of Type III AFPs and the amino acid bias that is observed. This same diversity in protein structure and composition can be seen in insect AFPs and plant AFPs which themselves are quite different than fish AFPs.[116,230–232]
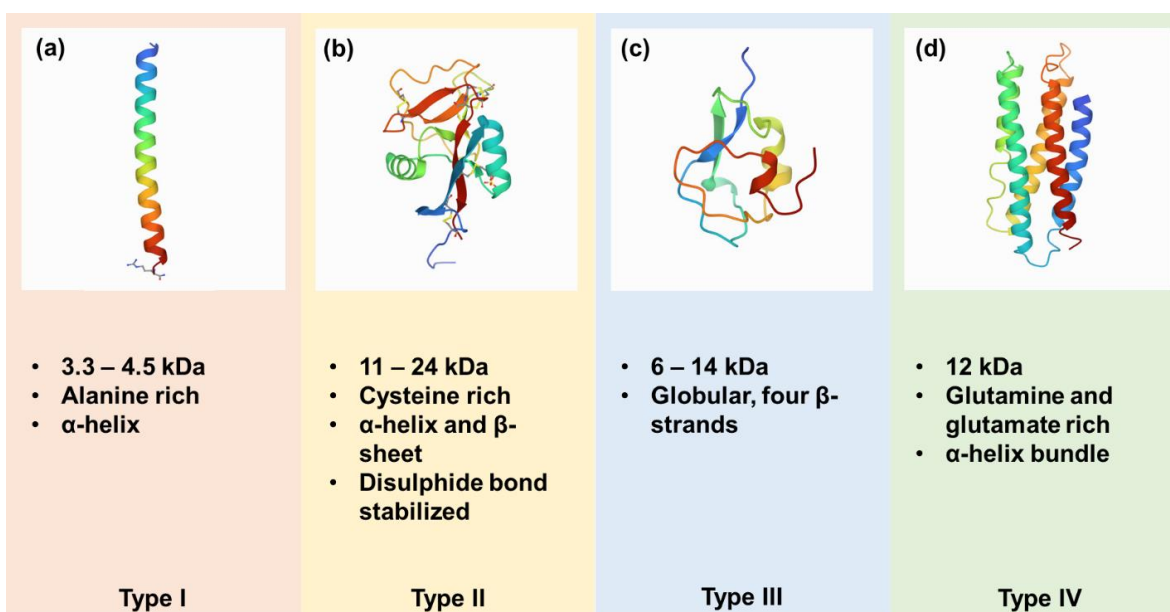
Figure 3.3. Representative fish antifreeze proteins (AFPs) and distinguishing features. (a) Type I AFPs have a size of 3.3-4.5 kDa, are alanine rich, and α-helical.[86,229,233] (b) Type II AFPs have a size of 11-24 kDa, are cysteine rich, generally made up of 2 α-helices and 2 β-sheets, and are stabilized by disulfide bonds.[229,231,232] (c) Type III AFPs have a size of 6-14 kDa, no amino acid bias, and are globular with β-strands.[229,231,232] (d) Type IV AFP has a size of 12 kDa, are glutamine and glutamate rich, and contain α-helical bundles.[86,229,230] The protein structures were taken from images on the RCSB Protein Data Bank (PDB) (rcsb.org). (a) PDB id: 1WFA,[234] (b) PDB id: 2ZIB,[235] (c) PDB id: 1AME,[236] and (d) PDB id: 1AEP.[237] Note that 1AEP is just representative and not from a fish.

The specific site of AFPs that interacts with ice is referred to as the ice binding site (IBS) or ice binding face. The IBS tends to be comparatively flat, hydrophobic, lacking charged residues, and generally containing repeating motifs.[116] The amino acid threonine is one particular motif that often is found in a repeating pattern on the IBS.[238–241] Asparagine and aspartic acid are also common among other polar mildly hydrophobic residues.[131]

Antifreeze glycoproteins (AFGPs) are found in the blood serum of cold weather marine fish.[144,242] The structure of a typical AFGP is shown in **Figure 3.4**. The repeating tripeptide sequence is often Alanine-Alanine-Threonine and the disaccharide, β-D-galactosyl(1-3)-α-N-acetyl-D-galactosamine, is attached to the hydroxyl oxygen of the threonine residue. Compared to AFPs which have defined secondary structures, AFGPs are unstructured[243] and are flexible molecules.[244,245] AFGPs are grouped into eight classes based on size, with AFGP1 being the largest (33 kDa) to AFGP8 being the smallest (2.6 kDa).[242,246]
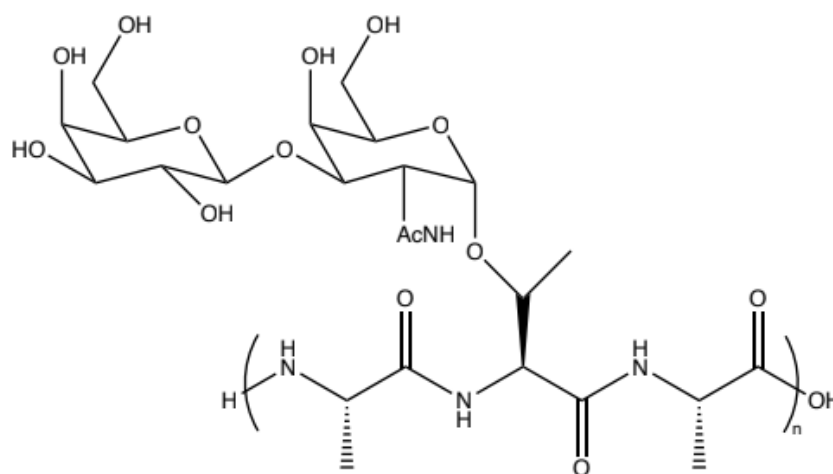
Figure 3.4. Typical structure of antifreeze glycoprotein (AFGP). The repeating peptide sequence is shown here is Alanine-Threonine-Alanine. The β-D-galactosyl(1-3)-α-N-acetyl-D-galactosamine sugar is attached to the threonine residue.

AFGPs, like AFPs, have also been shown to bind to the surface of ice.[247–249] The binding of AFGPs appears to occur on the primary prismatic planes and be reversible.[245,250] Furthermore, molecular dynamics simulations indicate that adsorption occurs *via* the hydrophobic methyl groups of both the peptide and sugar of the AFGPs,[245] which is supported by experimental mutation studies.[251] Compared to AFPs, AFGPs have weak TH activity.[242] However, AFGPs display the most potent IRI activity.[252]

Researchers have successfully isolated AFPs and AFGPs from a multitude of freeze-tolerant fish, plant, insect, algae, fungal, and bacterial species.[116,119,120,122,124,128,253,254] The highly alkaline (pH > 12) and ionic environment of ordinary portland cement (OPC) solution, however, pose significant challenges for AFPs as they are well known to restructure in non-native environments.[138,139] Additionally, the production of AFPs and AFGPs comes with significant economic limitations.[137,255] Non-proteinaceous synthetic alternatives to AFPs and AFGPs displaying IRI activity having been identified and characterized. These synthetic alternatives provide means to potentially overcome the economic limitations and physical and chemical instabilities of proteins in non-native environments. The following sections will highlight a selection of materials shown to have biomimetic antifreeze properties.

3.3 Biomimetic Antifreeze Polymers

Polymers have much lower barriers to scalability than proteins. Polymers can be produced with nearly any chemical moiety, a multitude of architectures, and a wide range of sizes, with some control over the sequence of monomers. Given these advantages, a variety of polymers having chemical moieties that mimic those found on the IBS of AFPs or the highly hydroxylated carbohydrates of AFGPs have been studied for TH, DH, and IRI activities.[224,256–258] PVA is the

most widely studied polymer to date and the most IRI-active synthetic material studied.[77,140,259–268] Other polymers displaying IRI activity include polyampholytes[256,257,269,270] and Nylon-3 polymers.[258] **Figure 3.5** provides a quick overview of the reported IRI activities of synthetic polymers based on the concentration they were tested at and molecular weight. No polymer studied to date has shown appreciable TH activity and only PVA has demonstrated DIS activity at relatively high concentrations (10 mg/mL).[145,271]

From **Figure 3.5** it is evident that of the synthetic polymers selected, PVA has the highest IRI activity. The only other polymer to display high levels of IRI activity (*i.e.*, <20% MLGS) are nylon-3 polymers. Additionally, PVA displays high levels of IRI activity across a range of molecular weights, 2,000-115,500 g/mol, and concentrations, 0.04-10 mg/mL.
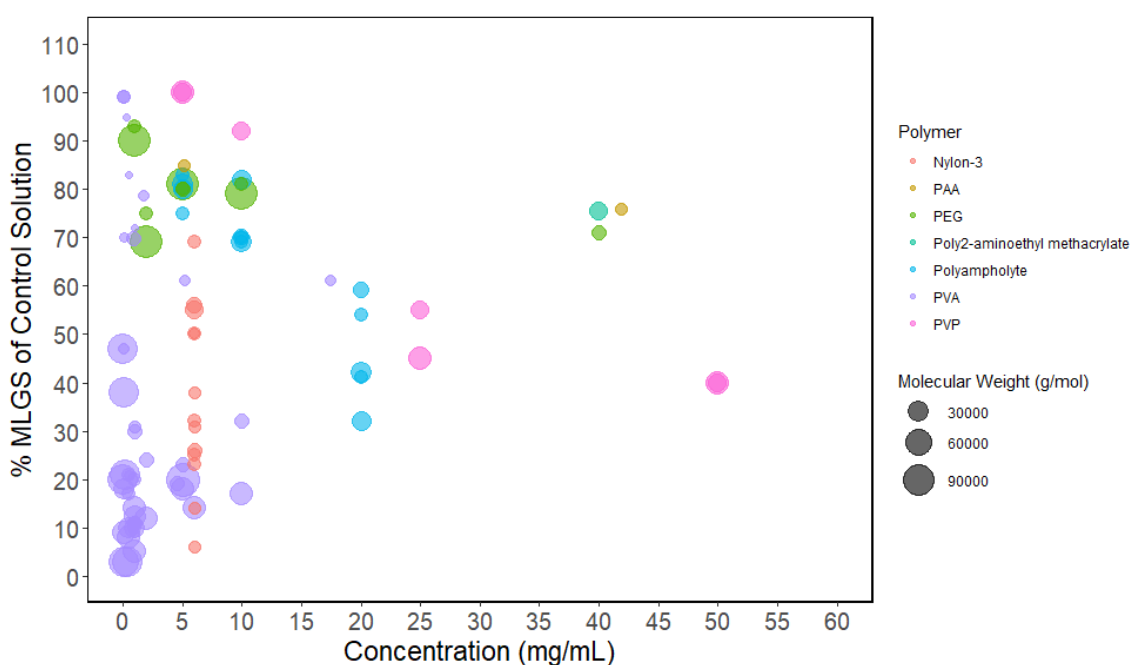
Figure 3.5. Ice recrystallization inhibition (IRI) activity of select synthetic polymers. Activity is reported as % mean largest grain size (MLGS) compared to control solution. All polymers in plot were tested in PBS solution. The size of the data point represents molecular weight (g/mol). Color of data point indicates type of polymer: nylon-3 polymers,[258] polyacrylic acid (PAA),[243] polyethylene glycol (PEG),[243,265] poly2-aminoethyl methacrylate,[243] polyampholytes,[272] polyvinyl alcohol (PVA),[140,243,255,265,268] and polyvinyl pyrrolidone (PVP).[140]

Significant effort has been placed on understanding the underlying mechanism which allows PVA to inhibit ice recrystallization.[77,140,259–268] Although the underlying mechanism is still to be fully elucidated, it has been shown that PVA does bind to ice.[264] The binding is believed to result from hydrogen bonding of hydroxyl groups which are spaced at a distance that closely matches the lattice spacing of ice with water molecules.[77,264]

Previous work has explored the effect of architecture,[140,261,268] copolymerization,[145,261] pH,[266] and degree of polymerization[140] on IRI activity of PVA. PVA bottlebrushes[261] and 3-arm star PVA polymers[268] were shown to maintain IRI activity when compared to linear PVA which demonstrate the ability of PVA to maintain activity in complex architectures. Random incorporation of hydrophobic groups on the PVA chain was shown to reduce IRI activity which indicates proper placement of hydrophobic groups is critical.[140] IRI activity of PVA was shown to be pH-dependent, and increasing pH results in greater activity. In the same study, the effect of anion and cation species in solution was also studied but no real influence on IRI activity was observed.[266] The minimum chain length of PVA for IRI activity was found to be 10 repeat units.[140]

3.4 Synthetic Peptides and Molecular Analogs

Synthetic peptides and molecular analogs have been produced primarily to mimic AFPs with repetitive amino acid sequences, simple secondary structures, and small sizes such as Type I AFPs and AFGP(8).[144] Making synthetic versions of Type I AFPs and AFGP(8) allow for the use of solution-phase synthesis and solid-phase peptide synthesis which are readily available techniques. Synthetic peptides have been studied more for TH and DIS activity than IRI

activity.[144,226,273,274] Surís-Valls and Voets provide a more in-depth review than is provided here[144], but a brief overview of select work is presented.

A 43 residue lysine-alanine rich polypeptide was synthesized to mimic Type I AFP from shorthorn sculpin.[273] The 43 residue polypeptide exhibited both TH and DIS activity and was used to better understand the structure-property relationships. Similarly, a series of polypeptides were synthesized to mimic a Type I AFP from winter flounder with regularly spaced lysine residues.[274] The polypeptides with regularly spaced lysine residues were found to display both TH and DIS activity while polypeptides with randomly space lysine residues displayed no TH or DIS activity demonstrating the importance of residue sequences or location. In this case, when the lysine resides were all oriented on one side of the helix structure, activity was observe.

Several synthetic peptides and homo-polypeptides including poly-L-histidine, poly-L-hydroxyproline, poly-L-lysine, poly-L-asparagine, L-threonine, poly-L-threonine, L-arginine, poly-L-arginine, L-glutamic acid, poly-L-glutamic acid have all been studied for IRI activity.[226,243] Poly-L-histidine and poly-L-glutamic acid in PBS were shown to have similar IRI-activity to PVA with a molecular weight (Mw) of 3,500 g/mol.[243] It is worth noting that poly-L-histidine and poly-L-glutamic acid all had molecular weights exceeding the 3,500 g/mol PVA and did not perform as well as PVA with a larger molecular weight (*i.e.*, >9,000 g/mol). Alternatively, in the same study, poly-L-hydroxyproline outperformed the 3,500 g/mol PVA but still was not displaying IRI activity on par with higher molecular weight PVA. The amino acids L-threonine, L-arginine, and L-glutamic acid were tested for IRI activity in PBS solution along with their corresponding homo-polypeptides poly-L-threonine, poly-L-arginine, and poly-L-glutamic acid.[226] In all cases, the amino acids displayed no appreciable IRI activity up to 10 mg/mL while the poly-L-threonine displayed significant IRI activity, 40% MLGS compared to

control, at concentrations ≥ 0.1 mg/mL. **Figure 3.6** provides a summary of the reported IRI activity from these two studies.

Analogs of AFGPs have also been produced.[275–278] Much of the research with AFGP analogs has focused on synthetic pathways and DIS and TH activity, with less of a focus on IRI activity. Analogs with as low as two alanine-threonine-alanine (ATA) repeats, see **Figure 3.4**, have been shown to display TH activity, but TH activity increased with increasing chain length.[278–280] Wilkinson *et al.* synthesized a series of synthetic AFGPs with sizes of 1.2 kDa to 19.5 kDa, and found that the synthetic AFGPs outperformed a native AFGP (AFGP8) in IRI activity when amino acid chain length exceeded 24.[278] Additionally, the synthetic AFGPs displayed TH and DIS activity when amino acid chain length exceeded 24 amino acids. **Figure 3.6** provides a summary of the reported IRI activity of the synthetic AFGPs compared to synthetic peptides and homo-polypeptides.

As can be seen in **Figure 3.6**, only the synthetic AFGP12 and AFGP32 are highly IRI active (*i.e.*, <20% MLGS).[278] The other synthetic AFGPs display moderate IRI activity. The only other materials to display moderate IRI activity (*i.e.*, 20%-70% MLGS at ≤ 1 mg/mL) was poly(L-threonine). L-glutamic acid, poly(L-glutamic acid), and poly(L-hydroxyproline) display moderate IRI activity at concentrations exceeding 10 mg/mL.
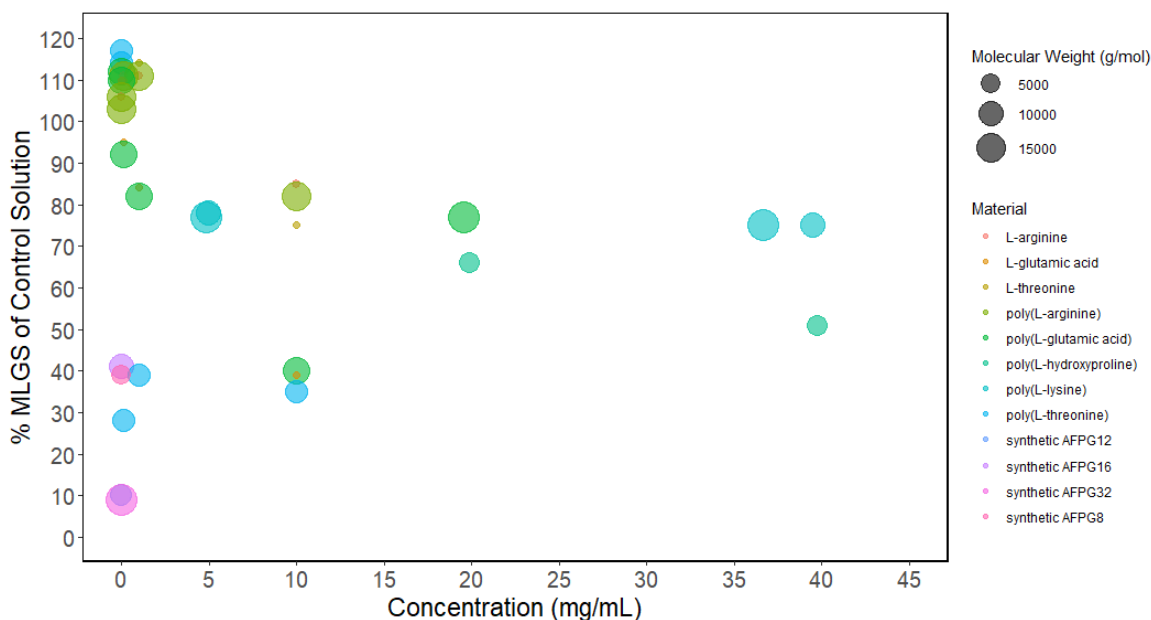
Figure 3.6. Ice recrystallization inhibition (IRI) activity of select synthetic peptides and molecular analogs of AFPs and AFGPs. Activity is reported as % mean largest grain size (MLGS) compared to control solution. All materials in plot were tested in PBS solution. The size of the data point represents molecular weight (g/mol). Color of data point indicates material: L-arginine,[226] L-glutamic acid,[226] L-threonine,[226] poly(L-arginine),[226] poly(L-glutamic acid),[226,243] poly(L-hydroxypropline),[243] poly(L-lysine),[243] poly(L-threonine),[226] synthetic AFGP12,[278] synthetic AFGP16,[278] synthetic AFGP 32,[278] and syntheticAFPG8.[278]

3.5 Nanostructures and Self-Assembling Molecules

Nanomaterials[141,255,281,282] and self-assembling molecules,[142,283–285] which generate nanoscale structures, that display IRI and TH activity have generated interest because of their unique properties and potential applications. For nearly every material, IRI activity is attributed to amphiphilicity. **Figure 3.7** provides a summary of the reported IRI activity of selected nanomaterials and self-assembling molecules. Note that not all the materials discussed here were screened for IRI activity with the splat assay. Materials screened with the sucrose sandwich method are not included in **Figure 3.7** due to differences in the methods.

Gold nanoparticles were coated with PVA exhibited IRI activity that matched that of the free PVA polymer.[281] Graphene oxide, which is a 2D material, was shown to adsorb on ice crystal

46

surfaces resulting in significant IRI activity and DIS activity.[282] The adsorption is believed to be a result of hydrogen bonding by oxidized groups on the basal plane of graphene oxide. At a concentration of 0.55 mg/mL in an 8.0 mg/mL NaCl solution, MLGS was reduced by ~75 %. Bai *et al*. synthesized a series of oxidized quasi-carbon nitride quantum dots (OQCNs) which displayed both IRI and DIS activity.[141] The OQCNs were only able to reduce the MLGS by ~ 20-34% at a concentration of 1 mg/mL, but concentrations of 10 mg/mL were able to achieve reductions > 50% compared to the PBS control. The IRI activity was attributed to the spacing of tertiary N atoms on the OQCNs which allow for adsorption onto the ice crystal surface through hydrogen bonding. Cellulose nanocrystals and 2,2,6,6-tetramethylpiperidine-1-oxyl (TEMPO) oxidized cellulose nanofibrils were shown to display excellent IRI activity at concentrations of 4 and 1.5 mg/mL in a 0.01 M NaCl solution.[255] The nanocellulose materials, like the graphene oxide materials, are believed to display IRI activity as a result of their amphiphilic nature.

Safranine O, a synthetic dye, self assembles into fibers that demonstrates comparable IRI activity to that of AFGPs at millimolar concentrations.[142] The authors attribute ordered waters along the self-assembled structure for the IRI activity. In the same study, 26 other synthetic dyes were studied but all failed to show IRI activity. Zirconium acetate (ZRA) and zirconium acetate hydroxide (ZRAH) assemble into polymer-like structures that are bridged together by hydrogen bonding of hydroxyl groups.[286,287] Both ZRA and ZRAH have acetate and hydroxyl group functionalities that are believed to bind to ice *via* hydrogen bonding allowing for TH, DIS, and IRI activity depending on pH. It was proposed that ZRA arranges itself such that one side of the polymer contains both acetate groups and hydroxyl groups and is believed to interact with ice while the other side contains only hydroxyl groups and interacts with water. Similarly, ZRAH arranges itself with one side of the polymer containing acetate groups, the ice interacting side,

and the other side containing only hydroxyl groups, the water interacting side.[286] Triplex

metallohelices were shown to display IRI activity down to concentrations of 20 µM in PBS[284]

These metallohelices resemble α-helices, common in Type I AFPS, in diameter and charge.[288,289]

Furthermore, they are amphiphilic which is believed to be the primary reason for their activity

given that the metallohelices do not have the chemical functionalities commonly attributed with

IRI activity (*e.g.* OH).

Figure 3.7. Ice recrystallization inhibition (IRI) activity of select nanomaterials and self-assembling molecules. Activity is reported as % mean largest grain size (MLGS) compared to control solution. All materials in plot were tested in PBS solution unless indicated with * or **. * indicates material was tested in 0.01 M NaCl. ** indicates material was tested in 0.5 mg/mL NaCl. Color of data point indicates material AFGP functionalized perylene bisimide,[283] AFGP tripeptide,[283] carboxyl functionalized graphene,[282] cellulose nanocrystals,[255] cellulose nanofibrils,[255] graphene oxide,[282] metallohelix,[284] oxidized quasi-carbon nitride quantum dots (OQCNs),[141] PVA gold nanoparticle hybrids,[281] TEMPO oxidized cellulose nanofibrils.[255]

3.6 Small Molecules

A variety of small molecules have been shown to display IRI activity including surfactants,[290,291] sugars (*i.e.*, monosaccharides and disaccharides),[290,292,293] lysine derivates,[294] aryl-aldonamides,[225] and synthetic carbohydrate molecules.[143,290,295] Small molecules with IRI activity are desirable for cryopreservation because materials with larger sizes having IRI activity such as PVA generally show poor cell recovery after cryopreservation.[294] When considering application to other fields, small molecules might be an attractive alternative to natural AFPs, AFGPs, polymers, and synthetic peptides because of the synthetic efficiencies and large-scale production that can be obtained.[295] Much of the research focus has centered around sugars and carbohydrate-based molecules due to biocompatibility and structural similarities to AFGPs. **Figure 3.8** provides a summary of the reported IRI activity of select small molecules. The 3D-QSAR model was created to predict the IRI activity of molecules.[225]
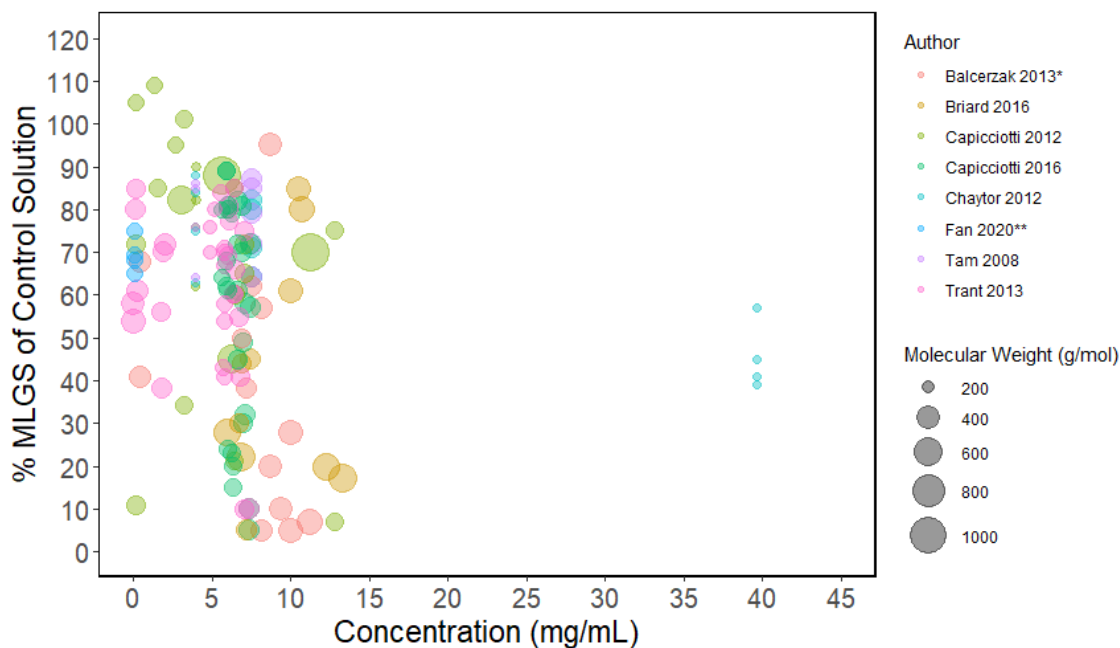
Figure 3.8. Ice recrystallization inhibition (IRI) activity of select small molecules. Activity is reported as % mean largest grain size (MLGS) compared to control solution. All materials in plot

were tested in PBS solution unless indicated with * or **. * indicates material was tested in 0.5 M NaCl. ** indicates material was tested in DI water. Color of data point indicates source.[143,225,290–295]

Small molecules differ mechanistically from AFPs and AFGPs in how they inhibit ice recrystallization. Small molecules do not actually bind to the surface of ice like AFPs and AFGPs. The exact mechanism leading to small molecule IRI activity is still to be fully explicated. However, several reports have shown a correlation between hydration index and hydrophobicity to IRI activity.

For carbohydrate-based molecules including monosaccharides and disaccharides, the hydration index was shown to have a linear correlation to IRI activity where a larger hydration index results in increased activity.[293,296] Hydration index is the ratio of the hydration number to the molar volume of a molecule.[293] The hydration number represents how many water molecules are tightly bound (hydrogen-bonded) to the molecule,[297] and therefore the hydration index represents the number of tightly bound waters per volume. It was proposed that a carbohydrate molecule with a higher level of hydration (*i.e.*, higher hydration index) would more strongly disrupt the bulk water phase at the quasi liquid layer (QLL) thus making it energetically more difficult for water molecules to add to the growing ice crystal resulting in IRI activity.[293,297] See **Chapter 1** for a description of the QLL.

Amphiphilicity and hydrophobicity appear to be important parameters for small molecule IRI activity, as is the case for other materials including AFPs and AFGPs.[294] For a series of lysine surfactants and hydrogelators, greater IRI activity was observed with greater hydrophobicity (alkyl chain length).[294] Alkylated galactose derivatives did not a correlation with increased hydrophobicity and IRI activity but did display significant IRI activity (>85% reduction in MLGS compared to control solution) when alkyl chains were longest or most hydrophobic.[143] A

50

series of photoswitchable carbohydrate-based surfactants were synthesized and tested for IRI activity.[298] Exposure to UV light vs. visible light-induced a cis to trans conformational change in azobenzene moiety on the alkyl chains that results in a change in hydrophobicity, the trans isomer is more hydrophobic than the cis isomer.[298,299] The trans isomer for a D-mannose based surfactant resulted in higher levels of IRI activity. A study focusing on surfactants, which are inherently amphiphilic, ability to inhibit ice recrystallization found that ionic surfactants display IRI activity while non-ionic surfactants do not.[291] Molecular dynamic simulations and ice affinity experiments with the surfactants show that the surfactants do not bind to ice, but instead the IRI activity is a result of an interaction with the QLL.

3.7 Applications

The inhibition of ice recrystallization is important to a variety of industries that deal with the unique chemical and physical properties of ice. AFPs, AFGPs, and biomimetic antifreeze materials have drawn tremendous interest for use in cryopreservation.[265,292,300–304] During the freeze and thawing of cryopreserved tissues, organs, and other biomaterials, ice growth and recrystallization occurs which can result in damage.[304,305] IRI active materials have shown some initial promise in limiting damage in cryopreservation. AFPs and AFGPs are currently used in the food industry to ensure that ice crystal size is limited, maintaining an appropriate texture in frozen foods.[84,306–308] IRI active materials have been utilized to tune the pore size in the production of porous materials.[309,310] Many material systems could have extended service life with the prevention of ice-induced damage. Concrete is susceptible to cyclic freeze-thaw damage and preliminary work has shown IRI active materials could provide resistance to the freeze-thaw damage.[145,311]

Chapter 4 Biomimetic Antifreeze Polyethylene Glycol-Polyvinyl Alcohol Graft Copolymer for Enhanced Freeze-Thaw Resistance of Ordinary Portland Cement Paste

4.1 Introduction

4.1.1 Freeze-Thaw Damage and Air Entrainment

Second only to water, concrete—a mixture of water, aggregates, and ordinary portland cement (OPC)—is one of the most consumed materials on Earth,[13] and the economic and environmental consequences of its worldwide ubiquity are significant. The production of OPC alone accounts for 4 to 8.6% of global CO_2 emissions[21,22,23] and places a burdensome toll on water resources, especially in water-scarce communities[24]. As the global population continues to rise, cement production is estimated to increase ~50% by 2050[13] to address new and aging infrastructure needs in both developing and developed countries. In all parts of the world, the long-term resilience of cementitious materials is critical to minimizing lifecycle economic and environmental costs associated with unplanned damage and maintenance, especially in light of a changing climate that may exacerbate environmental exposure conditions and lead to premature deterioration.

Cementitious materials exposed to cyclic freezing and thawing are highly susceptible to damage. It is well known that the formation and growth of ice crystals within the pores of cementitious materials can create hydraulic, osmotic, and crystallization pressures high enough to induce microscale cracks[45]. Cracking results in increased damage under further freeze-thaw cycles due to reduced mechanical integrity and increased water and ion penetration.

4.1.1 Freeze-Thaw Damage and Air Entrainment

The prevailing strategy to enhance the freeze-thaw resistance of OPC concrete is to entrain an air void system in the paste that effectively reduces the pressures that develop during cyclic freezing and thawing of water in capillary pores. Conventional air-entraining admixtures (AEAs) create stabilized air void systems within cementitious matrices *via* surfactant mechanisms. AEAs must produce air voids of specific sizes and distributions and exhibit proper spacing.[43,163,312] It remains commonplace to report the effectiveness of an AEA based solely on the volume of air in the paste—typically ~ 16-25% by volume of cement paste (or ~ 4-10% by volume of concrete).[163,168] Interestingly, however, despite meeting all parameters to be considered effective, some AEAs do not necessarily mitigate freeze-thaw damage—a result that suggests the chemical properties of AEAs play a critical role in their effectiveness.[163]

Stabilized air void structures mitigate freeze-thaw damage in concrete but introduce notable weaknesses, including reductions in mechanical strength (typically 5% per 1% entrained air)[57], increased permeability proportional to the amount of incorporated air, and retardation of set time.[176,313] Additionally, it is difficult to produce consistent and high quality air void systems in the field.[2] Given the difficulty to create and maintain entrained air void system and the inevitable side effects of AEAs, alternative approaches to mitigate damage due to cyclic freezing and thawing temperatures in cement paste are of particular interest.

Researchers have utilized a variety of other materials and methods, often in tandem with AEAs, to enhance the freeze-thaw resistance of cementitious materials. These strategies include (1) densifying and strengthening cement paste using nanoparticles or supplementary cementitious materials,[3–6] (2) incorporating superabsorbent hydrogel particles as a non-surfactant method to achieve an entrained air void system,[7,8] and (3) using macroscale polymeric fibers for

mitigating crack propagation due to frost-induced damage,[9,10] Despite some success, all of these methods aim at mitigating deleterious symptoms of ice expansion in cement paste and concrete rather than inhibiting the source—ice crystal growth.

4.1.2 Nature's Antifreeze

Antifreeze proteins (AFPs) and antifreeze glycoproteins (AFGPs) are a subset of ice-binding proteins (IBPs) produced by organisms across the biological kingdom classifications to survive freezing temperatures.[116] By binding to the surface of ice, AFPs and AFGPs can inhibit the growth and coalescence of ice crystals (*i.e.*, Ostwald ripening) *via* a process called ice recrystallization inhibition (IRI). AFPs and AFGPs also induce dynamic ice shaping (DIS) and reduce the freezing point of ice below the equilibrium freezing point (*i.e.*, thermal hysteresis).[132] While recent work suggests that ice-binding and antifreeze properties are a result of anchored clathrate and ice-like motifs in AFPs,[133,134] specific mechanisms by which AFPs inhibit ice recrystallization have yet to be fully explicated.[135]

Researchers have successfully isolated AFPs and AFGPs from a multitude of freeze-tolerant fish, plant, and insect species,[116,122,123,128,231,314] which renders their incorporation into cementitious materials feasible. However, proteins are well known to restructure in non-native environments,[138] yielding the highly alkaline (pH > 12.5) and ionic environment of OPC paste pore solution unfavorable for protein stability.[139] Other studies have shown that proteinaceous materials behave like set-retarding admixtures in fresh concrete,[315] and behave as air entrainers and foamers.[316]

4.1.3 Biomimetic Antifreeze Polymers

To overcome the economic limitations and physical and chemical instabilities of proteins in non-native environments, researchers have synthesized polymers that mimic the structure and functionality (*i.e.*, IRI and DIS activity) of AFPs and AFGPs.[140,258,269] The most widely studied polymer that displays IRI and DIS activity is polyvinyl alcohol (PVA). The pendant hydroxyl groups along the polymer backbone of PVA mimic the highly hydroxylated carbohydrates of AFGPs.[140]

Although PVA displays IRI and DIS activity, two potential disadvantages exist when considering its use in cementitious systems, namely (1) although it is soluble in water, mild heating is needed for it to solubilize, and (2) PVA is known to readily form hydrogels when exposed to cyclic freezing and thawing temperatures.[317,318] To this end, it was hypothesized using polyethylene glycol-polyvinyl alcohol graft copolymer (PEG-PVA), a commercially available polymer commonly used as a pharmaceutical excipient,[319] would combine the IRI activity of PVA with the higher solubility of PEG so that it would inhibit frost-induced damage when used as a polymeric additive to cement paste.

4.2 Experimental Procedure

4.2.1 Materials

PEG-PVA (CAS # 96734-39-3), polyethylene glycol (PEG) (CAS # 25322-68-3), and PVA (CAS # 9002-89-5) were purchased from Sigma-Aldrich and used without any modification. **Figure 4.1** and **Table 4.1** show the chemical structure and molecular weight used in this study of PEG, PVA, and PEG-PVA respectively. Research grade $Ca(OH)_2$ and 1x phosphate buffered saline (PBS) solution were purchased from Fisher Scientific. The cement used in this study was a

commercially available Type I/II OPC (Quikrete®) that complies with ASTM C150.[320] The

chemical composition of the OPC is reported in **Appendix A**.
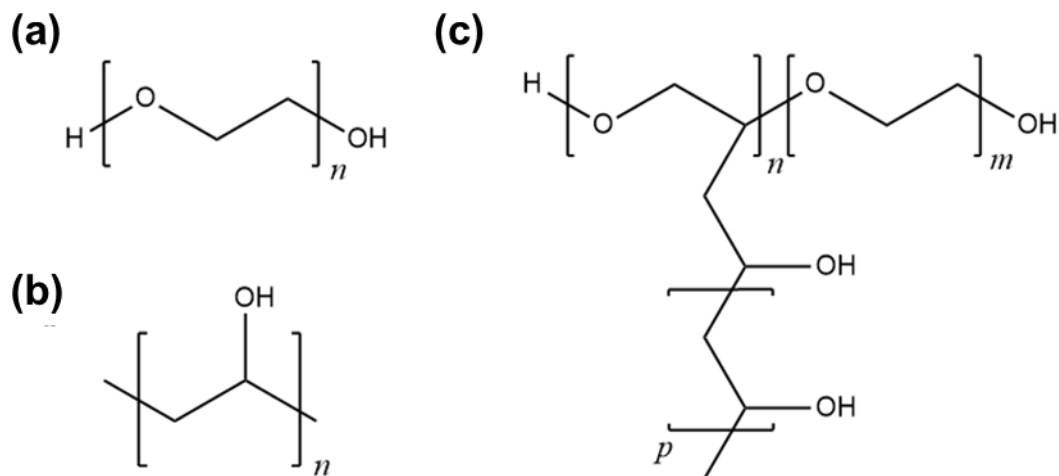
Figure 4.1. The chemical structure of polymers in this study. (**a**) polyethylene glycol (PEG) (**b**) polyvinyl alcohol (PVA) (**c**) polyvinyl alcohol-polyethylene glycol graft copolymer (PEG-PVA).

4.2.2 Antifreeze Properties

4.2.2.1 Ice Recrystallization Inhibition

The IRI activities of PEG, PVA, and PEG-PVA were tested at a concentration of 0.25 and

0.5 mg/mL in PBS. A modified IRI assay was performed to observe IRI activity.[321] 10 μL of

sample was dropped from 1.7 m onto a glass slide (thickness of 1 mm). The glass slide was pre-

cooled on an aluminum block at -78°C. The slide was then immediately transferred to an Otago

nanoliter osmometer cold stage and annealed at -4°C (air temperature) for 30 mins. Images were

collected immediately after the sample was placed on the cold stage and again at 30 min to

observe ice recrystallization. For all samples, images were obtained using an Olympus BX41

microscope with ELWD U Plan 20×/0.45 objective and crossed polarizers, equipped with an

OMAX A35140U camera on a 0.5× C-mount adaptor. ImageJ 1.48v software (National Institutes

of Health) was used to estimate the mean (n=10) largest grain size of three micrographs for each sample.

4.2.2.2 Dynamic Ice Shaping

DIS occurs when a material interacts with one or more crystallographic planes of ice resulting in a change to the morphology of a single ice crystal.[322] To observe DIS, a nanoliter-sized drop of sample was placed in microscopy immersion oil (Sigma) where both are in a hole of ~0.5 mm diameter within an aluminum disk. The aluminum disk was placed on an Otago nanoliter osmometer cold stage, where the temperature of the cold stage was rapidly cooled to -20°C to form polycrystalline ice. Next, the sample was slowly melted to form a single ice crystal by heating at a rate of approximately 5°C/min. Once a single ice crystal was obtained the temperature was kept constant for 3 min to ensure stability. Last, the sample was cooled at 0.01°C/min until crystal growth and/or ice shaping was observed. Samples were tested in DI water and a saturated $Ca(OH)_2$ solution. A concentration of 10 mg/mL was tested for all polymers due to previous studies of the DIS abilities of PVA.[271]

4.2.3 Sample Preparation

Table 4.1 provides the sample compositions of OPC paste samples. Samples were hand mixed for 3 min with a 0.42 water to cement ratio (w/c) and cured for 14 days in a 99% relative humidity chamber prepared according to ASTM C192 at 20°C ± 2°C.[323] Freeze-thaw resistance, air content, and compressive strength samples were cast in cylindrical polyethylene molds 32 mm in height and 16 mm in diameter complying with the ratios of height to diameter provided in ASTM C39.[324] The amounts of PEG, PVA, and PEG-PVA chosen in the mix design were based

on the concentrations used for IRI testing (*i.e.*, 0.25 mg/mL = 0.010 wt.% polymer in mixing

water).

Table 4.1. Cement Paste Mix Designs.

Sample	Polymer MW* (g/mol)	w/c Ratio	Polymer (wt.% of cement)
Control	-	0.42	-
PEG-L	3,350 (M_n)	0.42	0.010%
PVA-L	13,000-23,000 (M_w)	0.42	0.010%
PEG-PVA-L	45,000	0.42	0.010%
PEG-H	3,350 (M_n)	0.42	0.021%
PVA-H	13,000-23,000 (M_w)	0.42	0.021%
PEG-PVA-H	45,000	0.42	0.021%

* Values reported by manufacturer.

4.2.4 Fresh State Properties

4.2.4.1 Mini-Slump Cone

To test the flowability, or consistency, of cement pastes, a mini slump cone test was

performed.[325] Samples were prepared following the compositions shown in **Table 4.1**. After

mixing the miniature slump cone (height = 58 mm, top diameter = 19 mm, bottom diameter = 37

mm) was filled approximately one-third of the way and tamped no more than 25 times to remove

entrapped air. This procedure was repeated twice more to fill the cone. Finally, the top of the

cone was screeded. The cone was removed from the sample and the diameter of the base (at two

locations) was measured immediately and at 5 mins, 15 mins, 30 mins, 45 mins, 60 mins, and 24

hours. The diameter was used to calculate the average spread area at each time point. Each

mixture composition was tested in triplicate.

4.2.4.2 Isothermal Conduction Calorimetry

Isothermal conduction calorimetry (ICC) was performed to understand the impact of the

polymeric admixtures on both the heat of hydration and time of set. A TAM Air 8-Channel Isothermal Calorimeter from TA instruments was set at 21°C and allowed to equilibrate for 24 hours. All samples were mixed for 3 minutes in glass ICC vials, with a water to cement (w/c) ratio of 0.5, and immediately placed in the calorimeter and allowed to equilibrate for 1 hour before the calorimeter signal was considered stable. Data was measured for 60 hours. The peak thermal power at 50% was used to approximate the time of set.[326]

4.2.5 Hardened State Properties

4.2.5.1 X-ray Diffraction

X-ray diffraction (XRD) was performed on all samples to qualitatively determine mineralogy. After 14 days of curing samples were placed in acetone for a minimum of 24 hours to stop hydration reactions. Samples were crushed into a fine powder and suspended in ethanol (200 proof) to homogenize the powder. The suspension was pipetted onto a silica zero background plate and placed on a heated plate to allow for ethanol evaporation resulting in a thin film of sample. Diffractograms were collected using a Bruker D8 Advance XRD equipped with a Cu Kα radiation source. Data were recorded in the range of $2\theta = 5°$ to $65°$ with a step size of $0.02°$ and a dwell time of 2 sec/step.

4.2.5.2 Hardened State Air Content

Micro X-ray computed tomography (MXCT) enabled 3D visualization of internal air void systems. The MXCT (ZEISS Xradia 520 Versa) source voltage was set to 140 kV and the power to 10 W. An objective with an optical magnification of 0.4× was used. The source and detector locations were varied to obtain the desired resolution (voxel size) of approximately 4.6 – 5.0 μm.

Samples were scanned using MXCT before and after freeze-thaw cycling. The scans performed before freeze-thaw cycling were used to ensure cracking was not occurring due to other phenomena (*e.g.*, shrinkage). Internal cracks present in the samples post-freeze-thaw cycling indicated damage due to freeze-thaw cycling.

The volume of air in hardened paste, or air content, was determined from the volume of all voids with diameters greater than 15 μm for 2 replicates of each sample. These diameters were chosen based on the accepted size range of air voids,[19] previous research,[327] and resolution capabilities of MXCT. Dragonfly 2021.1 software (Object Research Systems) was used to generate the 3D reconstructions, to calculate the scanned volume of sample, and volume of all voids.

The MXCT data were first segmented within Dragonfly 2021.1 to identify voxels that are associated with air voids (*i.e.*, region of interest, ROI). Following segmentation, a multi-ROI analysis was performed. The multi-ROI analysis groups the labeled voxels and calculates a variety of properties including volume. The resulting volumes were exported and used to generate histograms of air void sizes (diameters).

4.2.5.3 Compressive Strength

Compressive strength of 16 mm x 32 mm (diameter x height) cylinders was measured on an INSTRON 5889 compression load frame with a 50-kN load cell. Samples were loaded at a rate of 0.025mm/s. Due to the size of the samples, no preloading was attempted. The average compressive strength of six trials is reported.

4.2.5.4 Freeze-Thaw Resistance

Freeze-thaw cycling of OPC paste samples was performed in a custom-built chamber following a modified version of ASTM C666 procedure A.[149] Details of the chamber may be found in **Appendix B**. All samples were tested for a total of 30 cycles in which the freezing lasted for 1.5 hours and thawing for 2.5 hours, respectively. During freezing cycles, the temperature reached -15°C ± 2°C and thawing cycles 16.5°C ± 2°C, as measured with a DHT-22 temperature sensor (SparkFun Electronics, USA). A water level that kept ~1/3 of the samples submerged was maintained in the sealed sample chamber to ensure the samples remained saturated.

4.3 Results

4.3.1 Antifreeze Properties

4.3.1.1 Ice Recrystallization Inhibition

Splat-assay micrographs showing the IRI activity of polymers PEG, PVA, and PEG-PVA at low and high concentrations in neutral pH PBS solution are shown in **Figures 4.2 and 4.3** respectively. As expected PVA[140] exhibits IRI activity, while PEG[328] displays no IRI activity. PEG-PVA exhibited IRI activity and reduced the average ice crystal grain size up to 90% when compared to a phosphate-buffered solution (PBS) control—an interesting result, given that the IRI activity of PEG-PVA has not yet been reported.
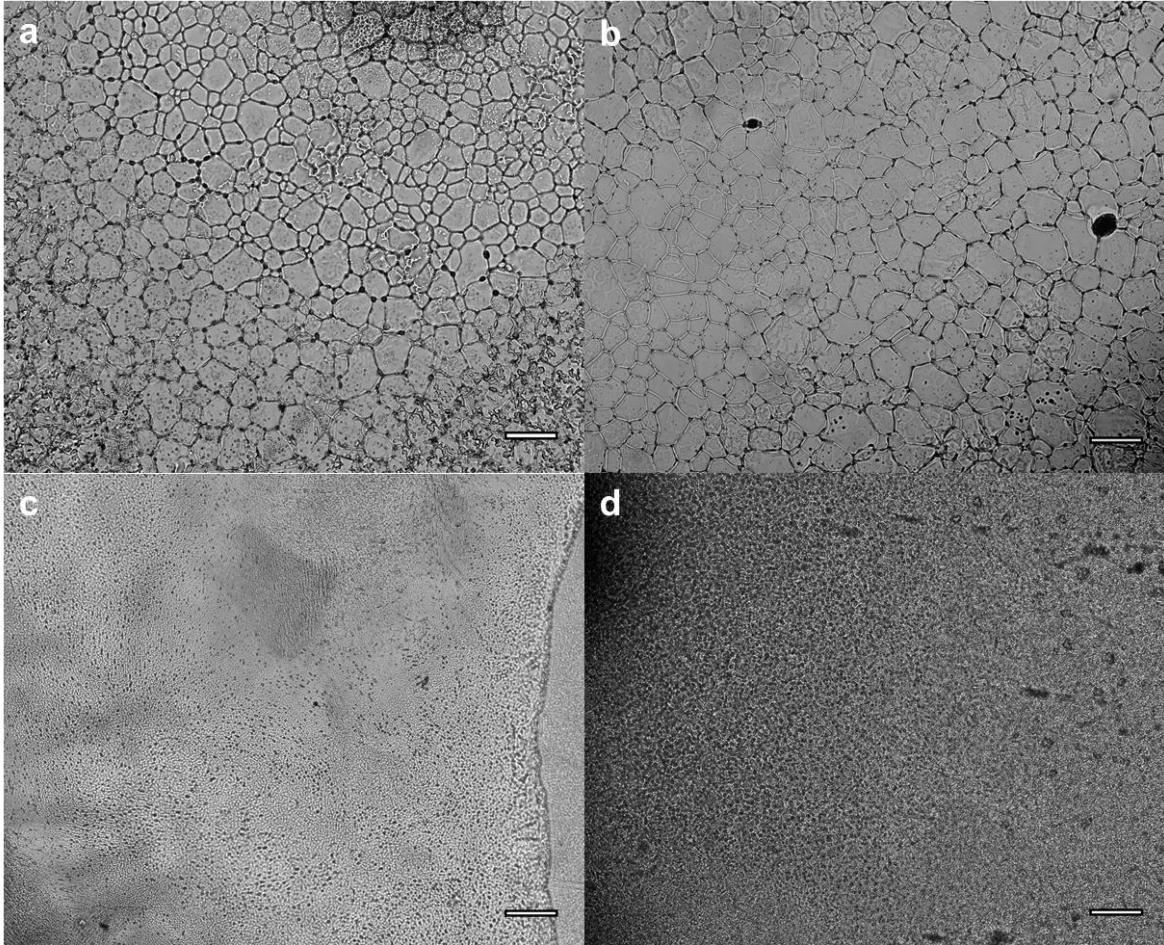
Figure 4.2. Optical Micrographs of IRI Splat Assay of PEG, PVA, and PEG-PVA at low concentrations (L) in neutral PBS solution. Images show individual ice crystal grains that form in (**a**) PBS control solution, (**b**) 0.25 mg/mL PEG (PEG-L), (**c**) 0.25 mg/mL PVA (PVA-L), and (**d**) 0.25 mg/mL PEG-PVA (PEG-PVA-L) in PBS after 30 min of annealing at −4°C. Scale bars are 100 μm.
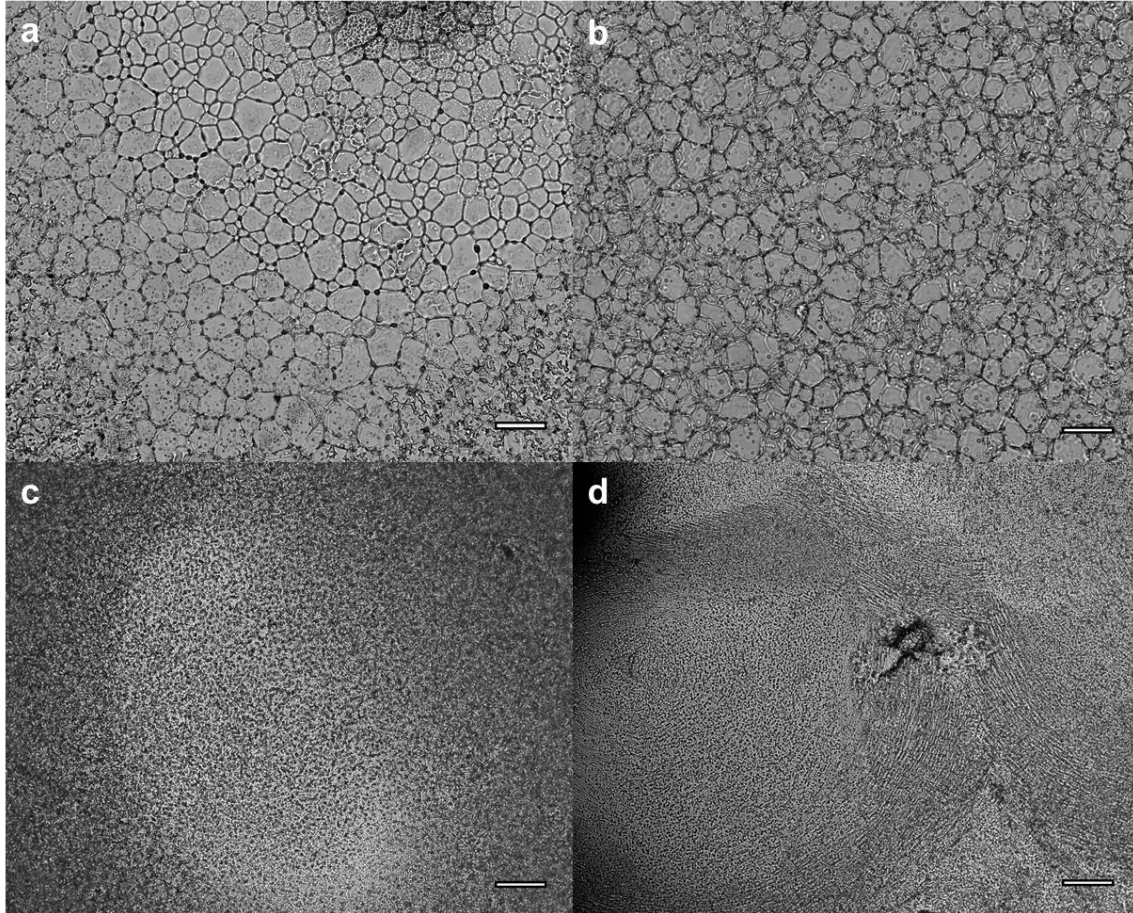
Figure 4.3. Optical Micrographs of IRI Splat Assay of PEG, PVA, and PEG-PVA at high concentrations (H) in neutral PBS solution. Images show individual ice crystal grains that form in (**a**) PBS control solution, (**b**) 0.50 mg/mL PEG (PEG-H), (**c**) 0.50 mg/mL PVA (PVA-H), and (**d**) 0.50 mg/mL PEG-PVA (PEG-PVA-H) in PBS after 30 min of annealing at −4°C. Scale bars are 100 μm.

The IRI activities of all polymers were also screened in pH 13 solutions to determine whether their IRI activities would be affected by the highly alkaline environment characteristic of OPC pore solution. The IRI activities of both PVA and PEG-PVA, however, were unaffected by the pH 13 solution, **Figures 4.4 and 4.5**. The results for PVA were anticipated, as Burkey *et al.* previously demonstrated that the IRI activity of PVA increases in pH 13 solutions when compared to pH 1 and pH 7 solutions.[266] Similarly, PEG-PVA retains the IRI activity in a highly

alkaline solution, showing an ~88% reduction in the mean largest size of ice grains compared to

the control pH 13 solution.
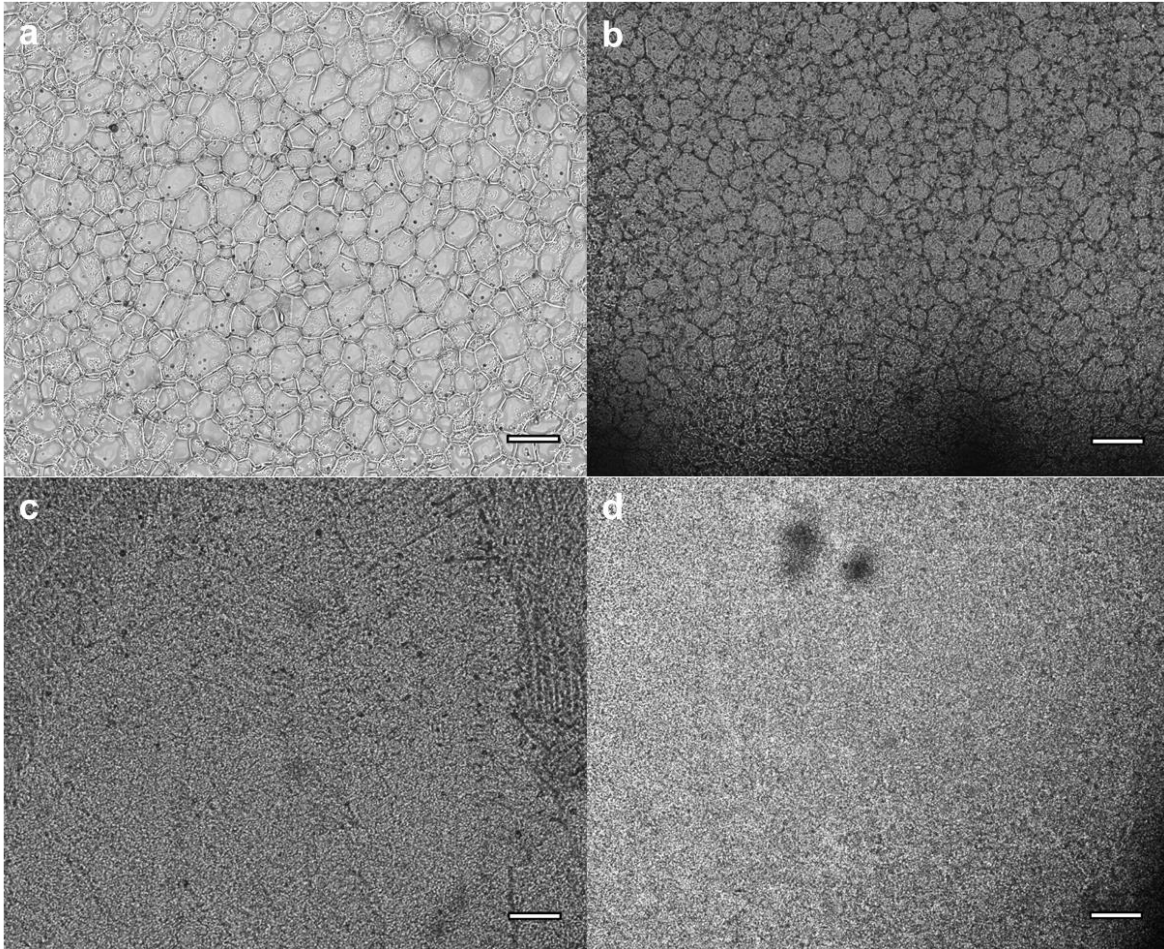
Figure 4.4. Optical Micrographs of IRI Splat Assay of PEG, PVA, and PEG-PVA at low concentration (L) in pH 13 adjusted PBS solution. Images show individual ice crystal grains that form in (**a**) pH 13 control solution, (**b**) 0.25 mg/mL PEG (PEG-L), (**c**) 0.25 mg/mL PVA (PVA-L), and (**d**) 0.25 mg/mL PEG-PVA (PEG-PVA-L) in pH 13 adjusted PBS solution after 30 min of annealing at −4°C. Scale bars are 100 μm.
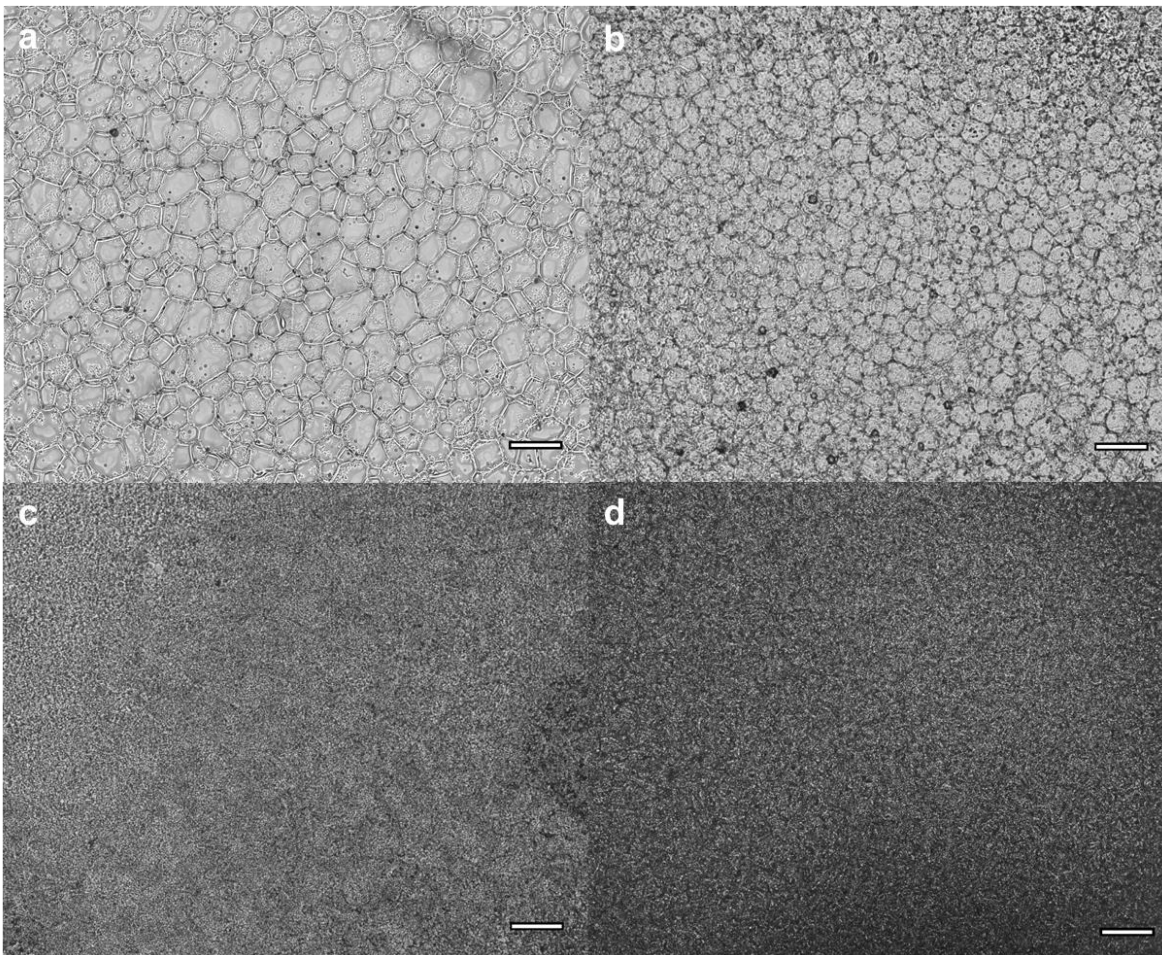
Figure 4.5. Optical Micrographs of IRI Splat Assay of PEG, PVA, and PEG-PVA at high concentration (H) in pH 13 adjusted PBS solution. Images show individual ice crystal grains that form in (**a**) pH 13 control solution, (**b**) 0.50 mg/mL PEG (PEG-H), (**c**) 0.50 mg/mL PVA (PVA-H), and (**d**) 0.50 mg/mL PEG-PVA (PEG-PVA-H) in pH 13 adjusted PBS solution after 30 min of annealing at −4°C. Scale bars are 100 μm.

4.3.1.2 Dynamic Ice Shaping

Figure 4.6 shows the DIS micrographs of each polymer in DI water and saturated $Ca(OH)_2$ solution at a concentration of 10 mg/mL. Both PVA and PEG-PVA induced hexagonal shaping, indicating evidence of interaction of these molecules with ice crystal surfaces. Recent work has shown that the IRI activity of PVA is a result of hydroxyl group interaction with the prismatic faces of 1h (hexagonal) ice.[263,264] Together, the IRI and DIS results indicated PVA and PEG-

PVA maintain their ability to interact with ice in the highly alkaline, highly ionic, and Ca^{2+} rich environment of cement pore solution.
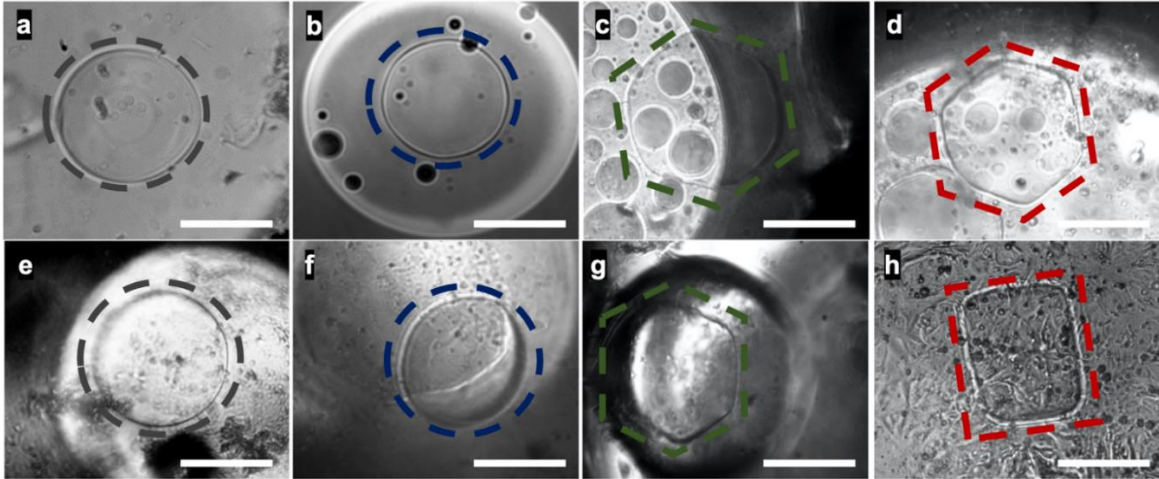
Figure 4.6. Optical Micrographs of DIS. Single ice crystals for (**a**) DI water, (**b**) 10 mg/mL PEG in DI, (**c**) 10 mg/mL PVA in DI, and (**d**) PEG-PVA at 10 mg/mL in DI. Both PVA and PEG-PVA display hexagonal ice shaping. Single ice crystals for (**e**) saturated $Ca(OH)_2$ solution. (**f**) 10 mg/mL PEG in sat. $Ca(OH)_2$ solution. (**g**) 10 mg/mL PVA in sat. $Ca(OH)_2$ solution. (**h**) 10 mg/mL PEG-PVA in sat. $Ca(OH)_2$ solution. Both PVA and PEG-PVA maintain their ability to shape ice in the presence of saturated $Ca(OH)_2$ solution. Note that in (**c**), (**d**), and (**g**) the c-axis of hexagonal ice crystal is perpendicular to the plane of image and in (**h**) it is in plane of the image. Scale bars are 50 μm.

4.3.2 Fresh State Properties

4.3.2.1 Mini-Slump Cone

All polymers increased the initial fluidity when compared to the control regardless of concentration. As can be seen in **Figure 4.7**, all polymer additions resulted in ≥ 20% increase in the initial area (*i.e.*, t = 0) except PVA-L. After 60 mins, the observed areas are only 3-17% greater than the control as shown in **Figure 4.8**.
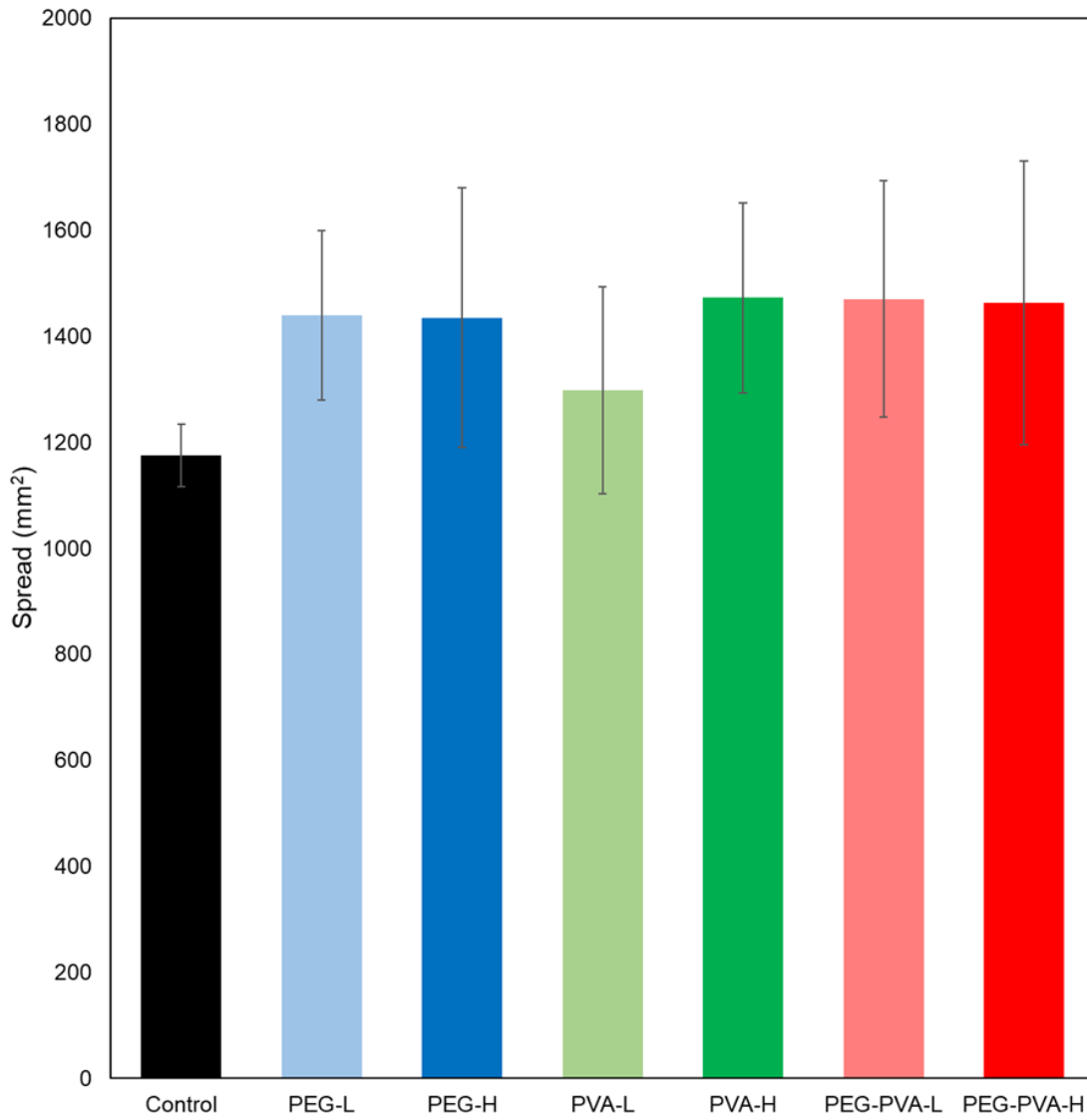
Figure 4.7. Flowability (mini-slump cone) results for all samples at t = 0. Values presented are the average and one standard deviation of three replicates.
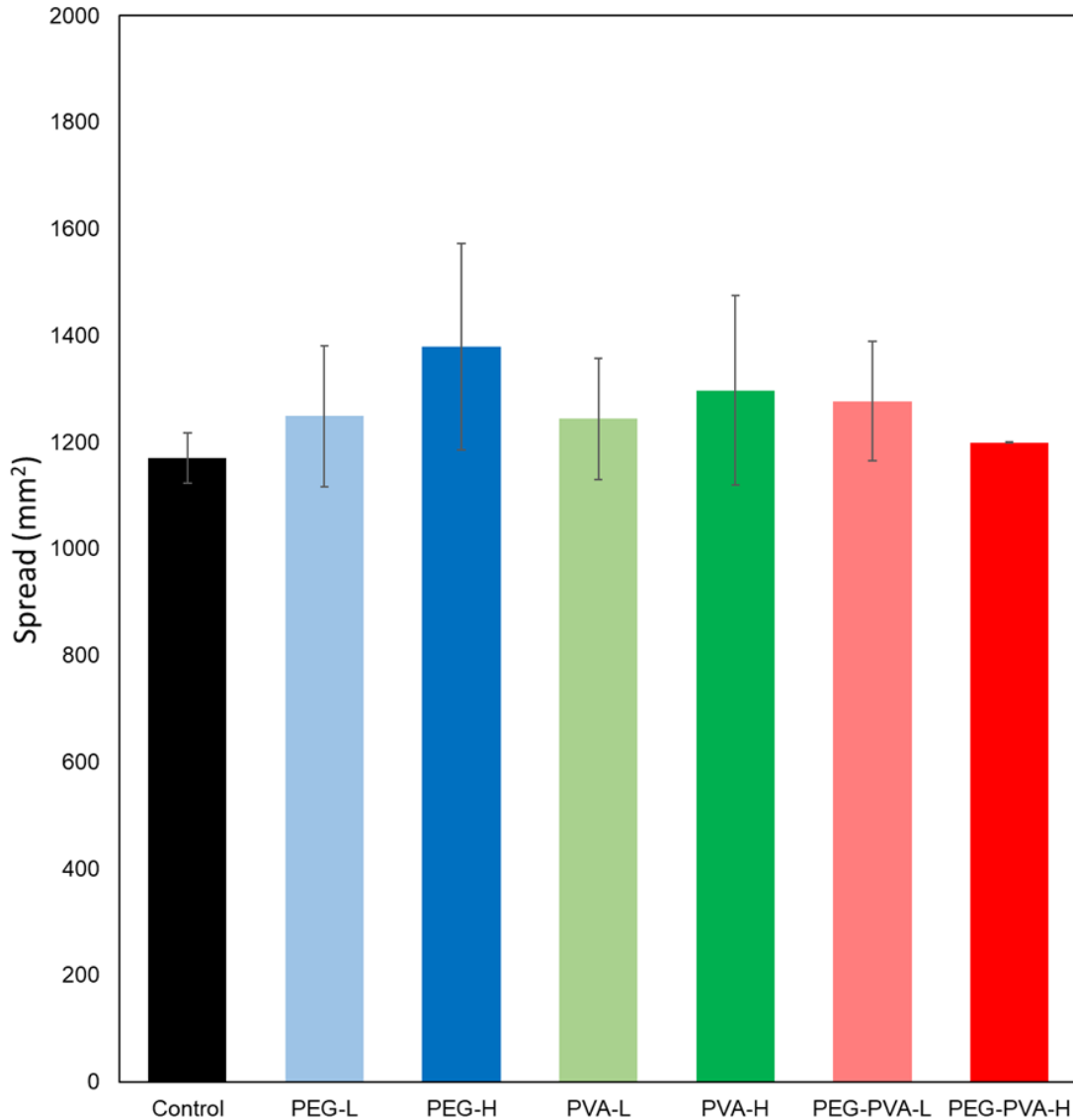
Figure 4.8. Flowability (mini-slump cone) results for all samples at t = 60 mins. Values presented are the average and one standard deviation of three replicates.

4.3.2.2 Isothermal Conduction Calorimetry

ICC results in **Figures 4.9-4.12** show that time of set and heat of hydration were minimally impacted at low concentrations of polymer, whereas no change was observed in high concentrations of polymer. **Figure 4.9** shows that the addition of PEG-L results in slightly higher total heat compared to the control and all other polymer additions. **Figure 4.11** shows that for all polymer additions at low concentrations (0.010% by wt. of cement) there is a marginal

acceleration in hydration. **Figures 4.10** and **4.12** show no observable difference in normalized

total heat or heat flow for polymer additions at high concentrations (0.021% by wt. of cement)

compared to the control. Generally, the addition of water-soluble polymers, including PVA,[329,330]

reduces the heat of hydration and retards set, however this behavior is typically observed when

the polymeric additions are $\geq 0.1\%$ by weight of cement.[331] Many polymeric materials help to

impede flocculation of cement grains, including PVA, which can result in accelerated

hydration.[332,333] It appears that the ability of the polymers to impede flocculation is dependent on

polymer concentration. However, the high concentrations in this study appear to not retard time

of set.
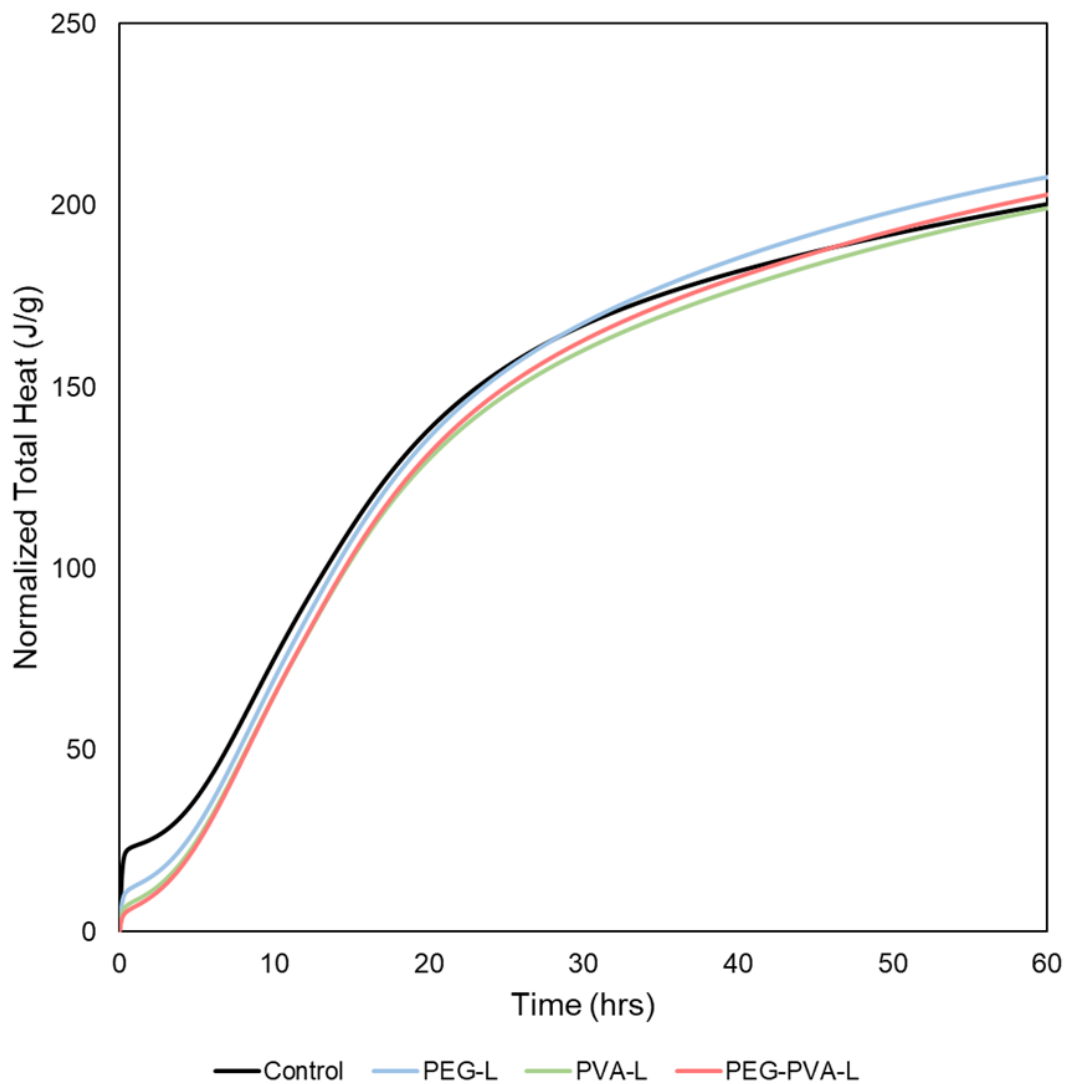
Figure 4.9. Normalized total heat plots for (a) low concentrations: control (—), PEG-L (—), PVA-L (—), PEG-PVA-L (—) up to 60 hrs.
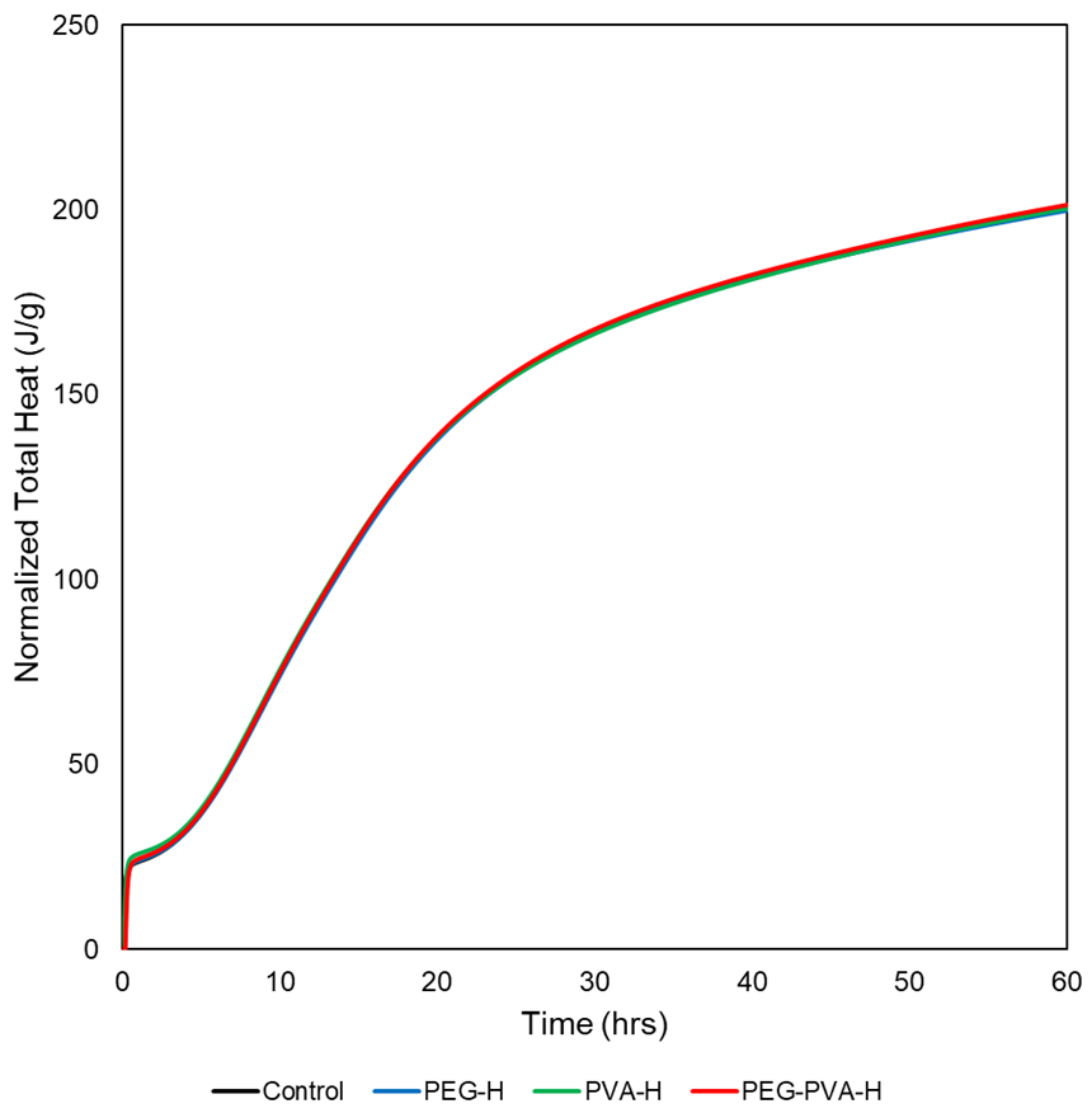
Figure 4.10. Normalized total heat plots for control (━), PEG-H (━), PVA-H (━), PEG-PVA-H (━) for up to 60 hrs.
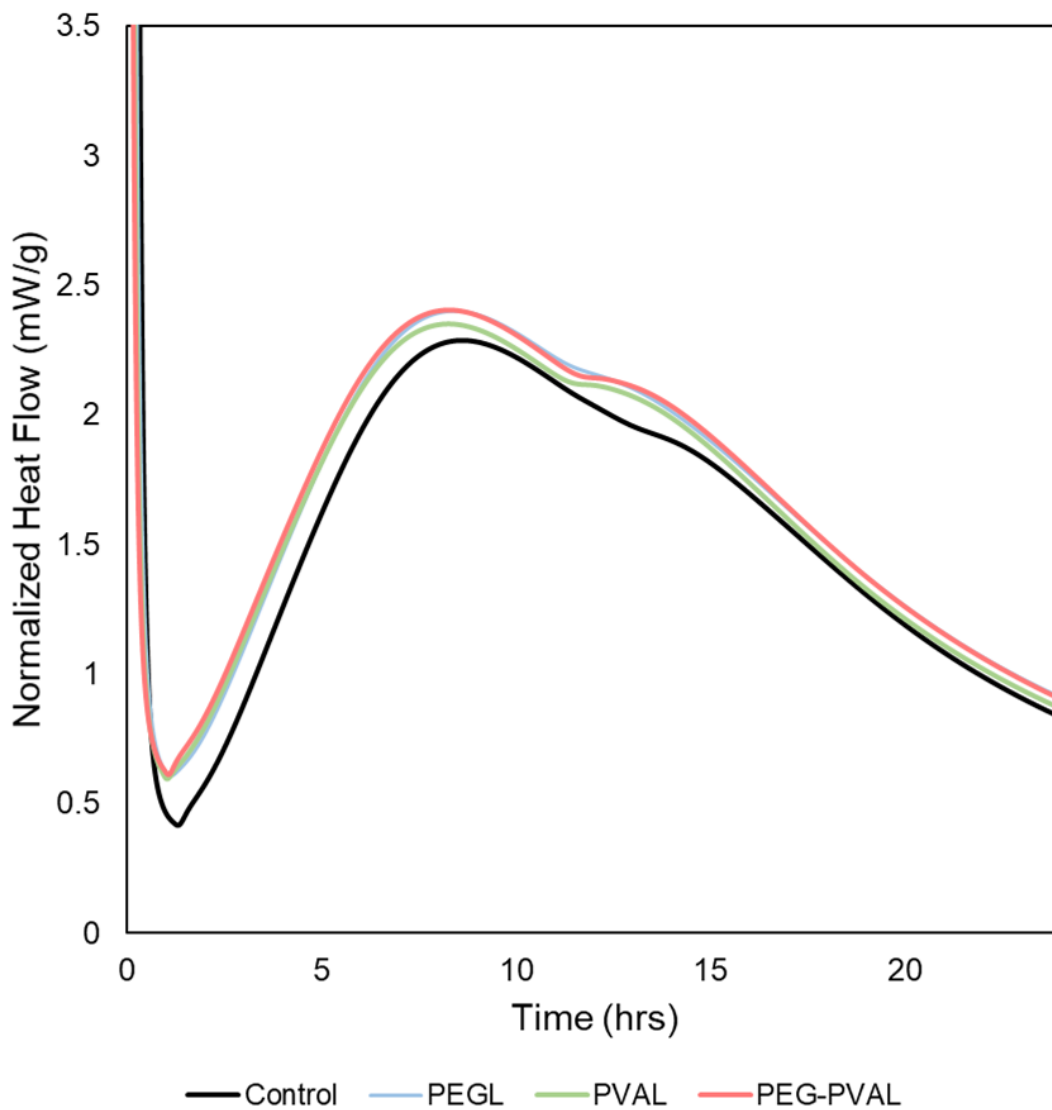
Figure 4.11. Normalized heat flow plots for control (━), PEG-L (━), PVA-L (━), PEG-PVA-L (━) up to 24 hrs.
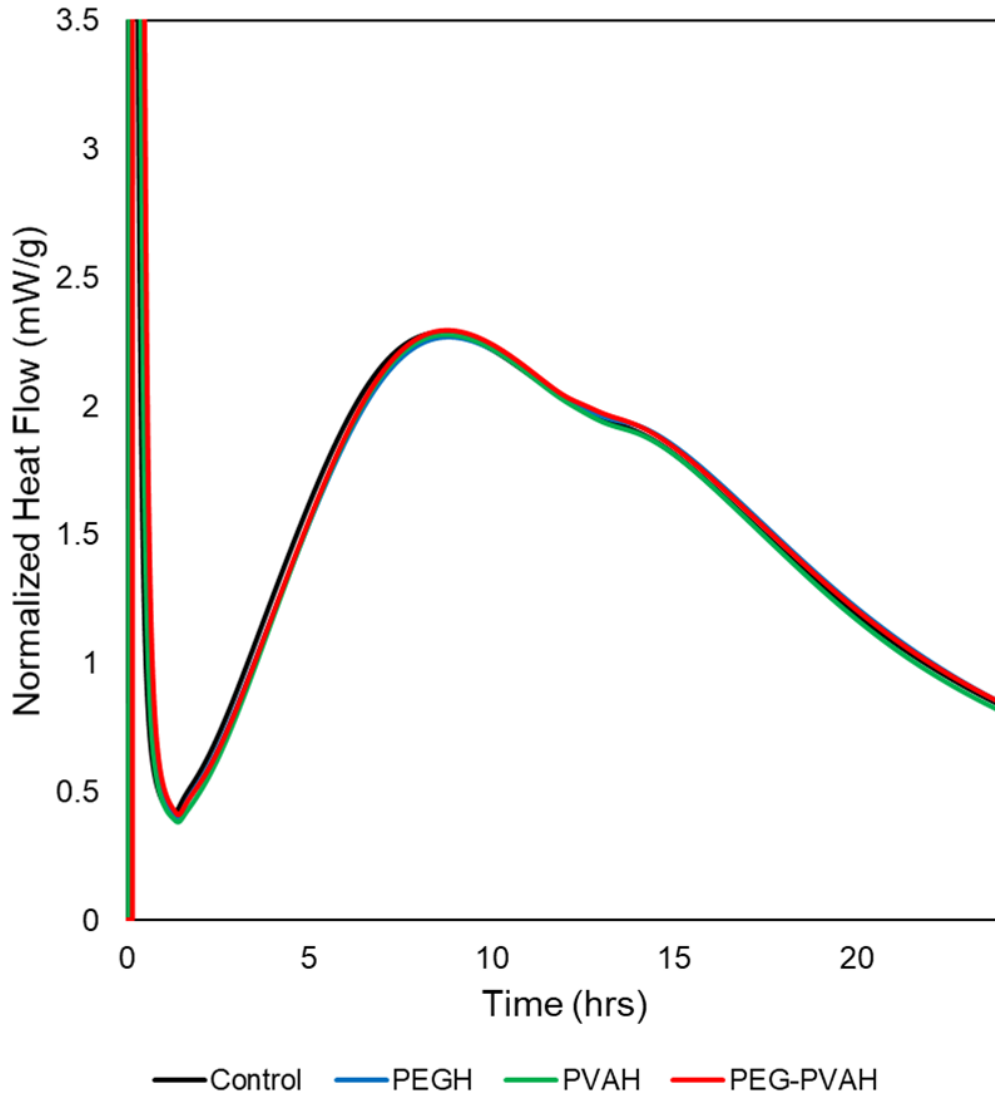
Figure 4.12. Normalized heat flow plots for control (━), PEG-H (━), PVA-H (━), PEG-PVA-H (━) for up to 24 hrs.

4.3.3 Hardened State Properties

4.3.3.1 X-ray Diffraction

Figure 4.13 and Figure 4.14 show XRD diffractograms for low and high concentration polymer additions, respectively. Regardless of polymer concentration the main constituent minerals (*i.e.*, portlandite, calcite, and calcium silicate hydrate) are present. Additionally, ettringite, brownmillerite, larnite (belite), and alite were present in all samples. The presence of

these minerals in hardened ordinary portland cement paste was expected.[334,335] **Table 4.2** summarizes the peaks identified in **Figures 4.13 and 4.14** and the corresponding mineral.
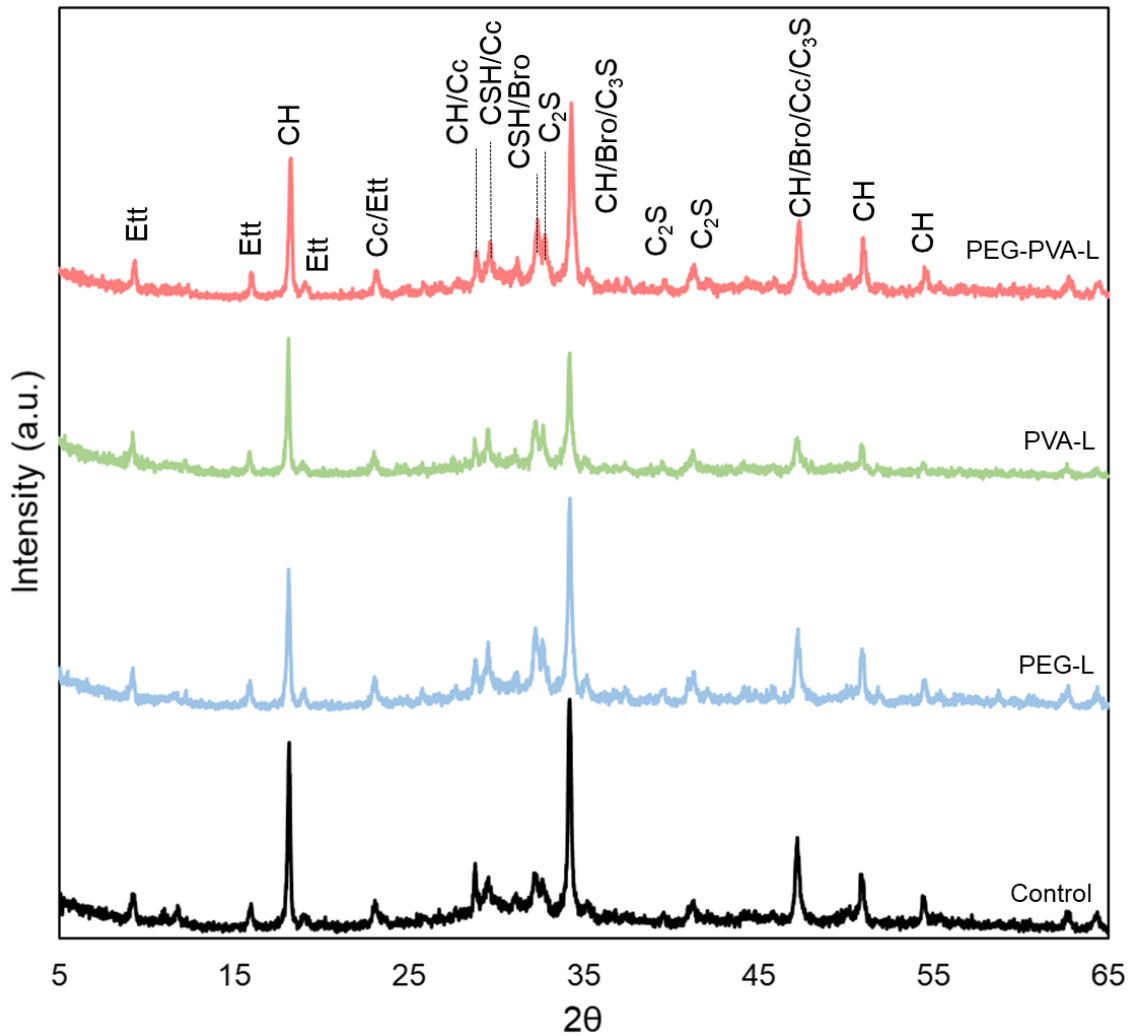
Figure 4.13. XRD diffractograms of samples after 14-day cure. Diffractograms of OPC control (—), PEG-L (—), PVA-L (—), PEG-PVA-L (—). Bro: Brownmillerite; Cc: calcite; CH: portlandite; C-S-H: calcium silicate hydrate; Ett: Ettringite; C_2S: Larnite (Belite); C_3S: Alite.
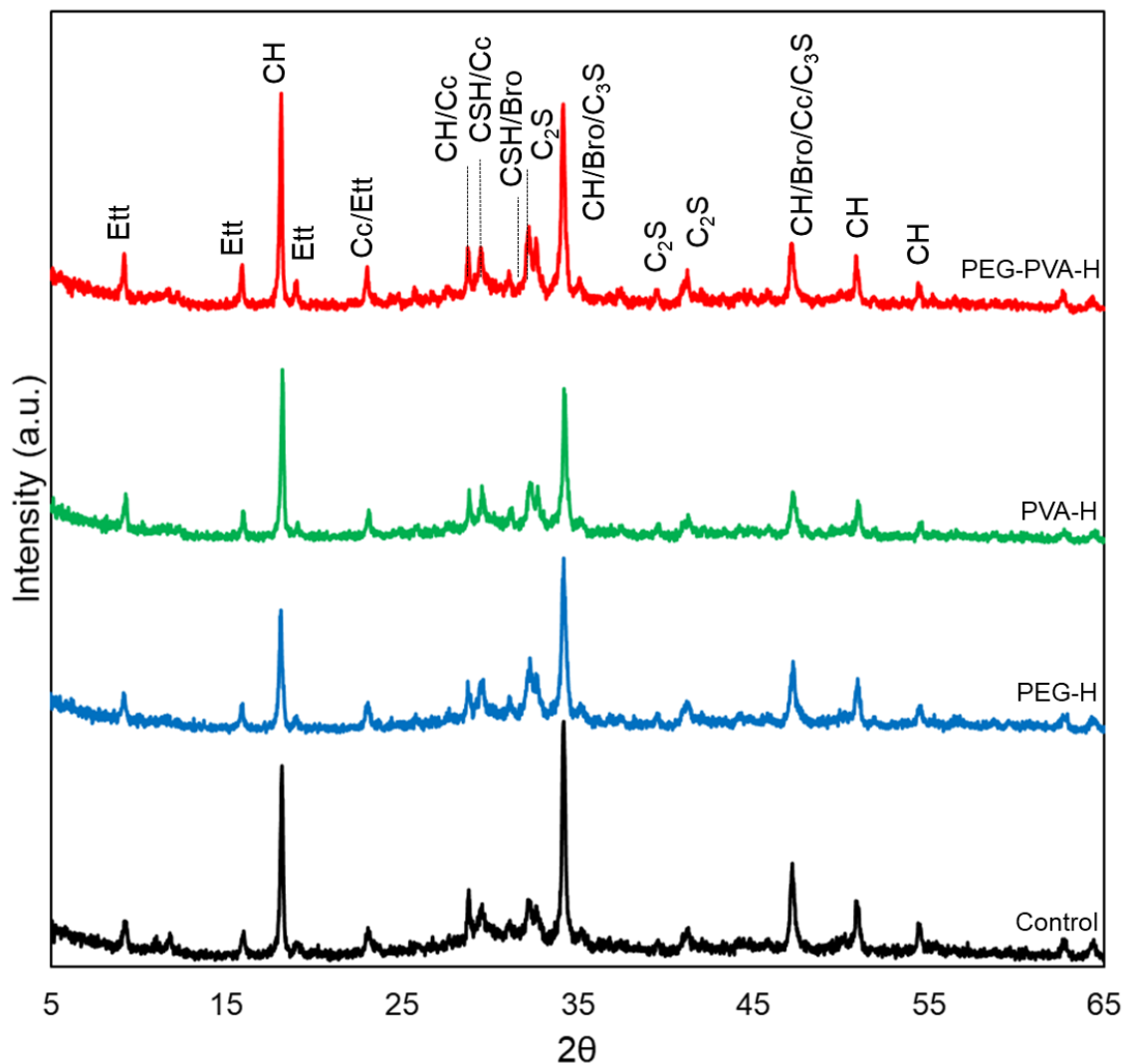
Figure 4.14. XRD diffractograms of samples after 14-day cure. Diffractograms of OPC control (━), PEG-H (━), PVA-H (━), PEG-PVA-H (━). Bro: Brownmillerite; Cc: calcite; CH: portlandite; C-S-H: calcium silicate hydrate; Ett: Ettringite; C_2S: Larnite (Belite); C_3S: Alite.

Table 4.2. Summary of peaks identified in XRD diffractograms.

Symbol	Mineral	2θ	Reference
Bro	Brownmillerite	32.1	334
Cc	Calcite	23, 29.3	334,336,335
CH	Portlandite	18.1, 29, 34.1, 47.2, 51, 54.5	334,336,335,337,338
C-S-H	Calcium silicate hydrate	29.6, 32.2	335,339
C_2S	Larnite (Belite)	32.2, 32.6, 39.5, 41.2	334,340
C_3S	Alite	34.1, 47.2	334,340
Ett	Ettringite	9.1, 15.8, 23	334,336,335,337,338

4.3.3.2 Hardened State Air Content

The percent volume of air, or air content, of samples was determined by measuring the volume of pores with a diameter larger than 15 μm. This volume was determined from MXCT scans of samples after curing and before freeze-thaw cycling. **Figure 4.15** provides representative MXCT 2D cross-sections of the air void systems, colored red, and the average air content for all samples. PEG, PVA, and PEG-PVA at both concentrations used in this study introduce less than 0.7% air content. In the case of PEG-PVA-H, less than 0.7% air was entrained while freeze-thaw resistance was increased. These observed air contents are much lower than the industry accepted air contents of ~ 16 to 25% air by volume of cement paste, or ~ 4 to 10% by volume of concrete.[163,312]
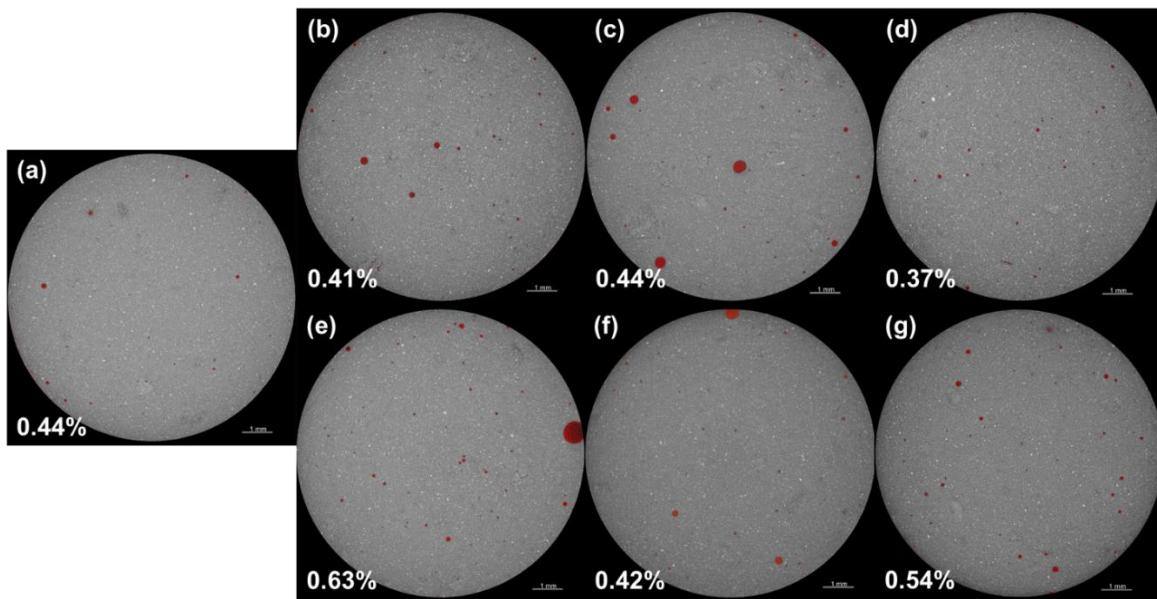
Figure 4.15. Representative MXCT 2D cross-section with air voids highlighted red for (**a**) control, (**b**) PEG-L, (**c**) PVA-L, (**d**) PEG-PVA-L, (**e**) PEG-H, (**f**) PVA-H, and (**g**) PEG-PVA-H. Scale bars are 1 mm. The average (n = 2) air content is shown in the lower left corner of each cross-section image.

Although the air content is low, a higher number of small air voids could explain higher freeze-thaw resistance. However, as can be seen in **Figures 4.16 and 4.17** the polymer modified

samples do not contain higher numbers of air voids with diameters $< 60\ \mu$m compared to the control. **Table 4.3** summarizes details of the air void size histograms including the minimum air void diameter, maximum air void diameter, average air void diameter, and the number of air voids identified.
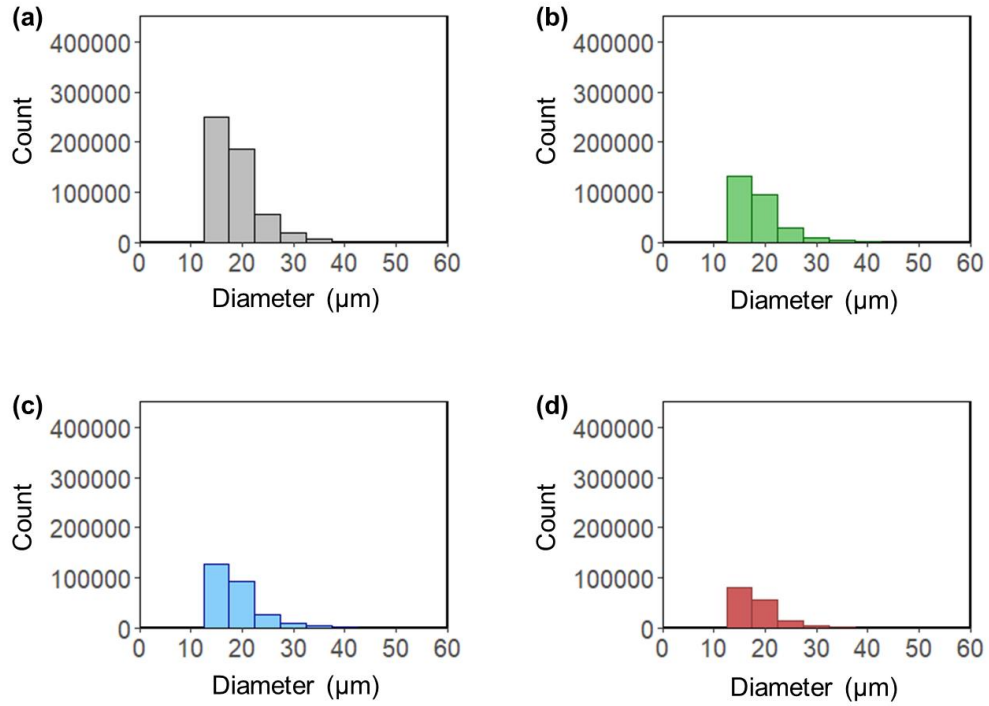
Figure 4.16. Histograms of air voids with diameters <60 µm for (a) control, (b) PEG-L, (c) PVA-L, and (d) PEG-PVA-L hardened paste samples.
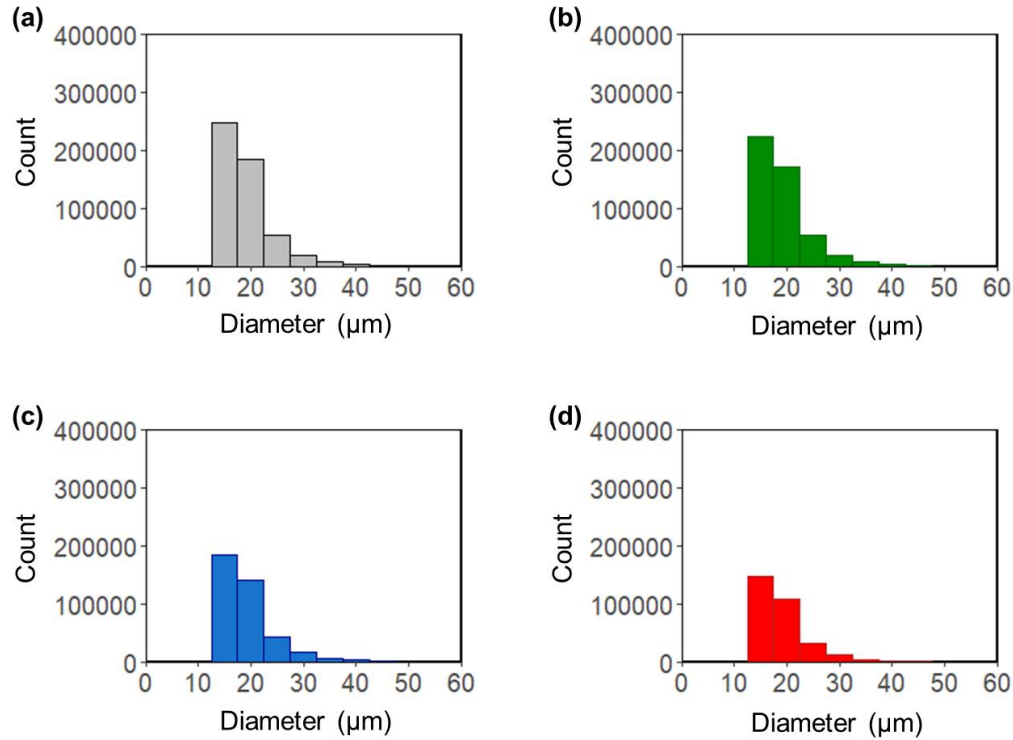
Figure 4.17. Histograms of air voids with diameters <60 µm for (a) control, (b) PEG-H, (c) PVA-H, and (d) PEG-PVA-H hardened paste samples.

Table 4.3. Summary of air void analysis. Values in parentheses represent the second replicate.

	Minimum Air Void Size (µm)	Maximum Air Void Size (µm)	Average Air Void Size (µm)	Number of Air Voids
Control	15.09 (15.09)	960.58 (754.47)	19.52 (20.05)	528,018 (452,768)
PEG-L	15.09 (15.07)	809.98 (740.28)	20.00 (21.00)	270,399 (232,067)
PVA-L	15.07 (15.09)	921.31 (854.18)	20.85 (20.29)	280,200 (410,406)
PEG-PVA-L	15.07 (15.09)	656.83 (968.50)	20.70 (20.03)	164,917 (236,839)
PEG-H	15.09 (15.09)	1,557.56 (913.16)	19.88 (20.42)	404,637 (421,970)
PVA-H	15.09 (15.10)	790.42 (749.53)	21.17 (20.57)	489,733 (91,183)
PEG-PVA-H	15.09 (15.09)	831.22 (941.49)	21.02 (20.31)	317,645 (436,986)

4.3.3.3 Compressive Strength

Initial compressive strengths of all samples, **Figure 4.18**, show that there are no significant effects due to polymer addition, regardless of concentration. These results further indicate that minimal air was entrained, given that air entrainment is well known to decrease compressive strength by ~ 5% per 1% entrained air.[57] Previous research has shown that higher additions of

PEG and PVA (0.1 to 3 wt.% of cement) can lead to denser microstructures and increased compressive strength by retarding flocculation during hydration, thereby enabling higher reactivity of cement particles.[341,342] However, the low wt.% additions investigated herein neither increased nor decreased the compressive strength of the hardened cement paste.
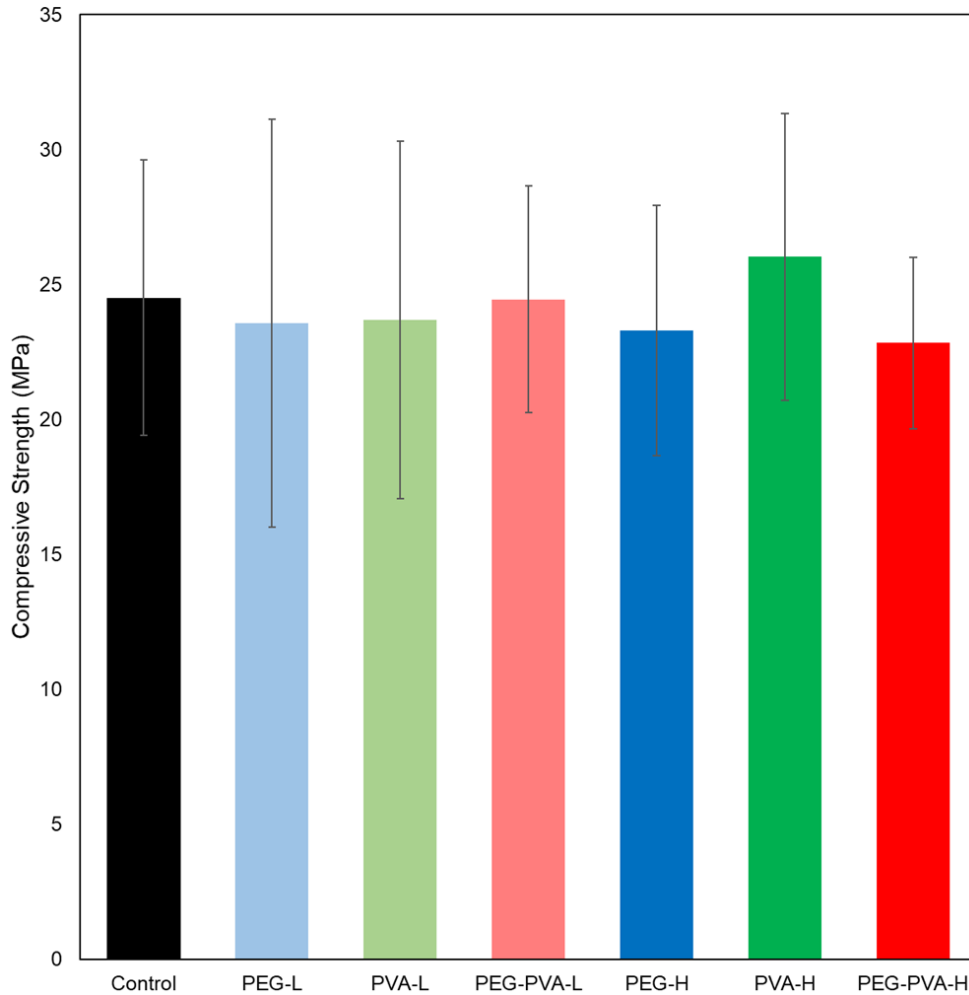
Figure 4.18. Initial compressive strength results of all paste formulations. Compressive strength of all samples with one standard deviation reported for six results (n = 6).

4.3.3.4 Freeze-Thaw Resistance

   Figures 4.18 and 4.19 provide representative images from multiple trials of the bulk paste samples post 30 freeze-thaw cycles. As can be seen in **Figure 4.18**, the control paste and paste

modified with low concentrations of polymer all display significant external damage including cracking and spalling. The same is seen in **Figure 4.19** for all samples except PEG-PVA-H which display no visible external damage. **Figures 4.20 and 4.21** provide representative 2D cross-sectional MXCT images of paste samples after 30 freeze-thaw cycles. Control paste and pastes modified with PEG and PVA at both low (L) (0.010 wt.% cement) and high (H) (0.021 wt.% cement) concentrations display clear signs of internal crack formation. OPC paste containing PEG-PVA at an addition of 0.021 wt.% of cement (PEG-PVA-H) exhibited no damage.
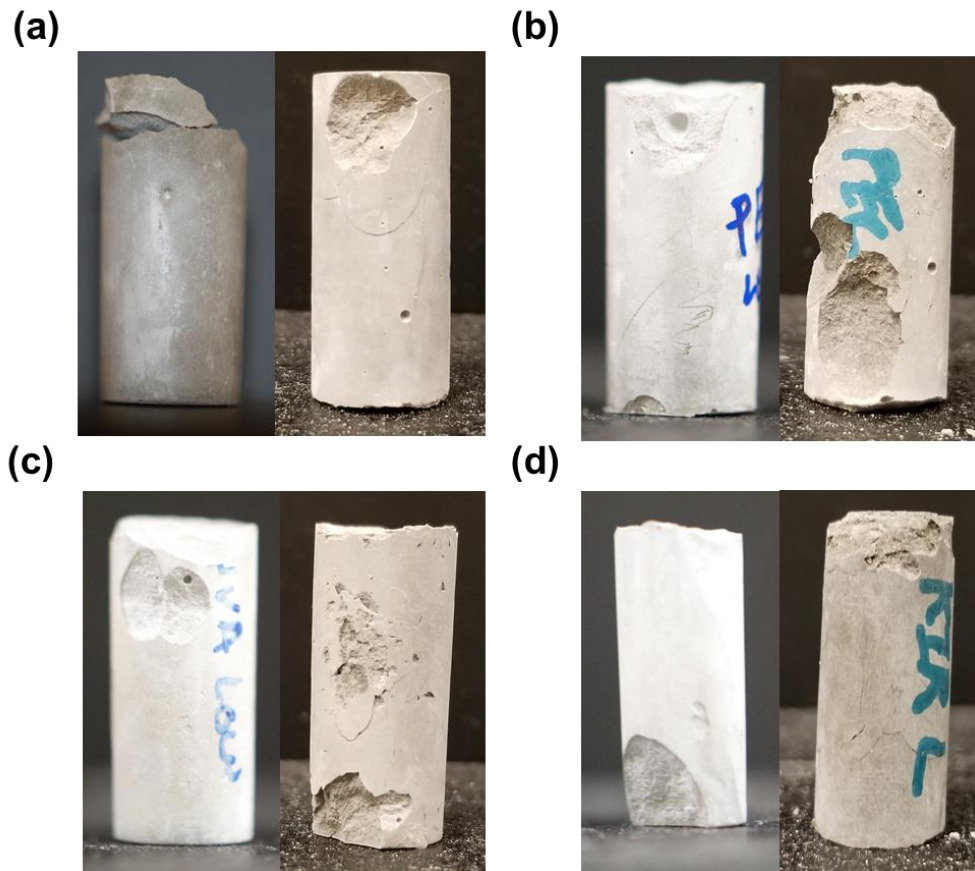
Figure 4.19. Post freeze-thaw bulk sample images from two trials. (**a**) control, (**b**) PEG-L, (**c**) PVA-L, and (**d**) PEG-PVA-L. Bulk samples are 16 mm in diameter by 32 mm in height.
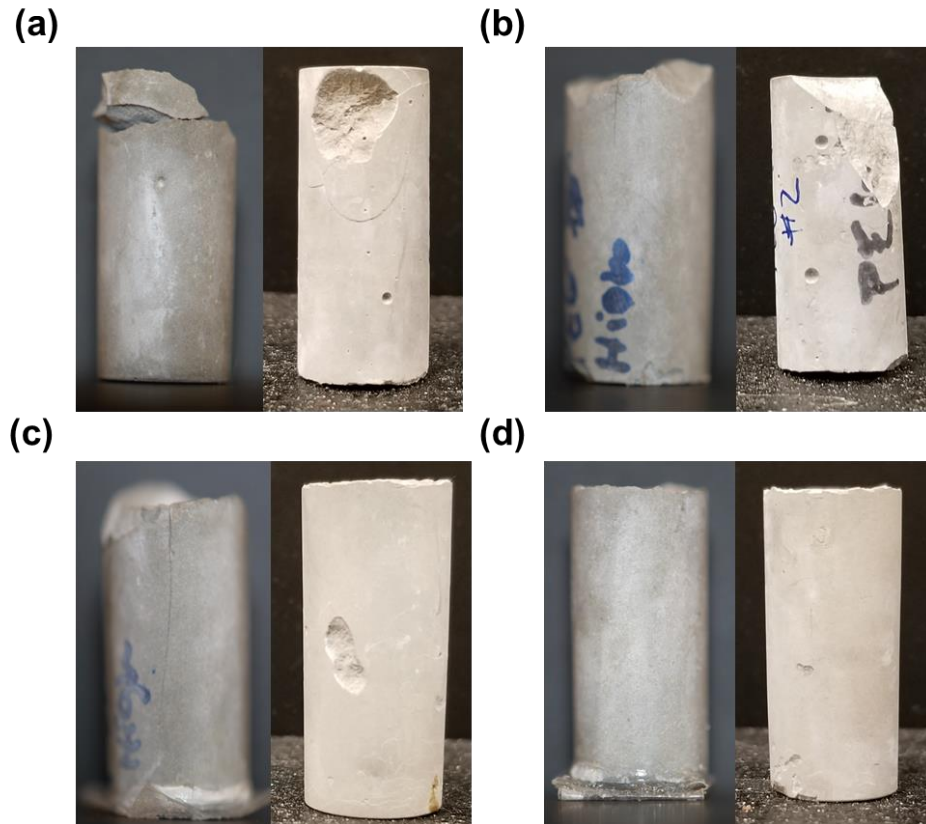
Figure 4.20. Post freeze-thaw bulk sample images from two trials. (**a**) control, (**b**) PEG-H, (**c**) PVA-H, and (**d**) PEG-PVA-H. Bulk samples are 16 mm in diameter by 32 mm in height.
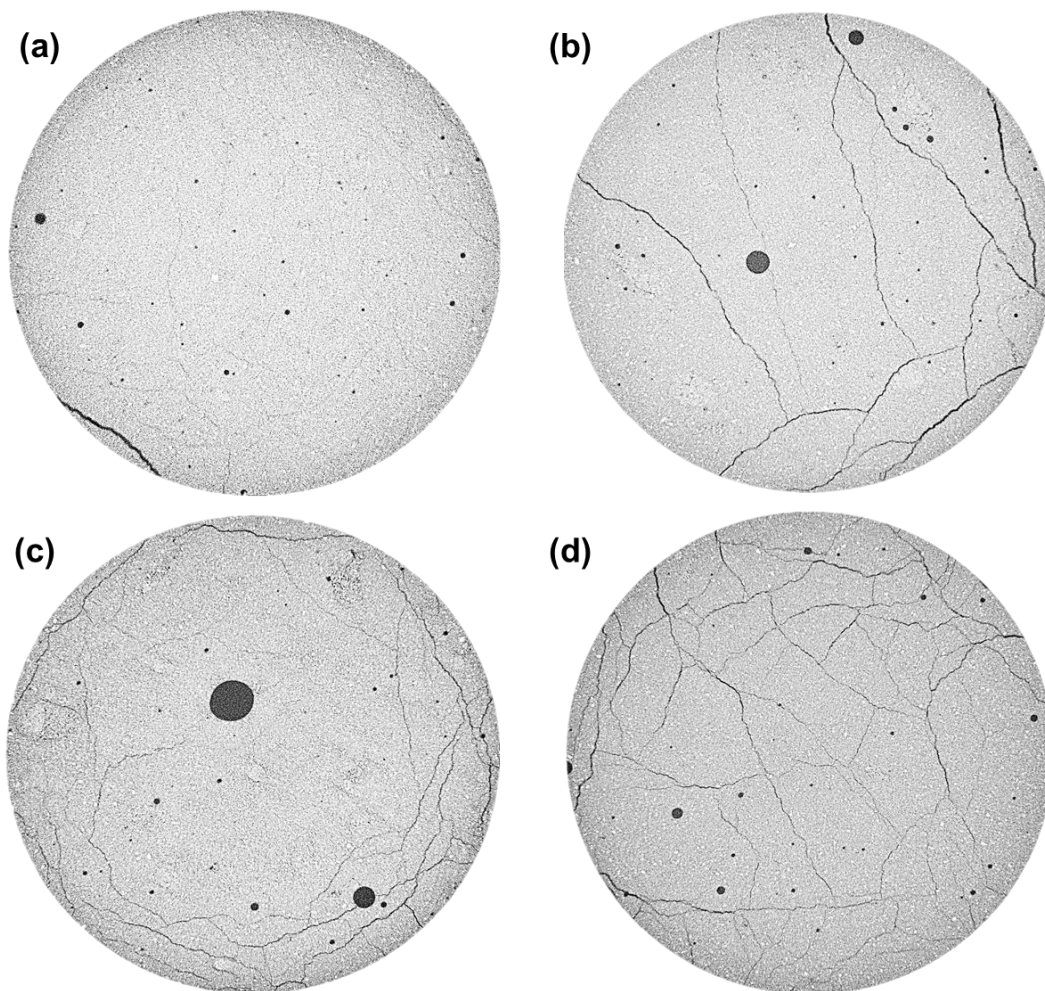
Figure 4.21. Post freeze-thaw MXCT 2D cross-sectional images. (**a**) control, (**b**) PEG-L, (**c**) PVA-L, and (**d**) PEG-PVA-L. MXCT cross-sections are ~9 mm in diameter.
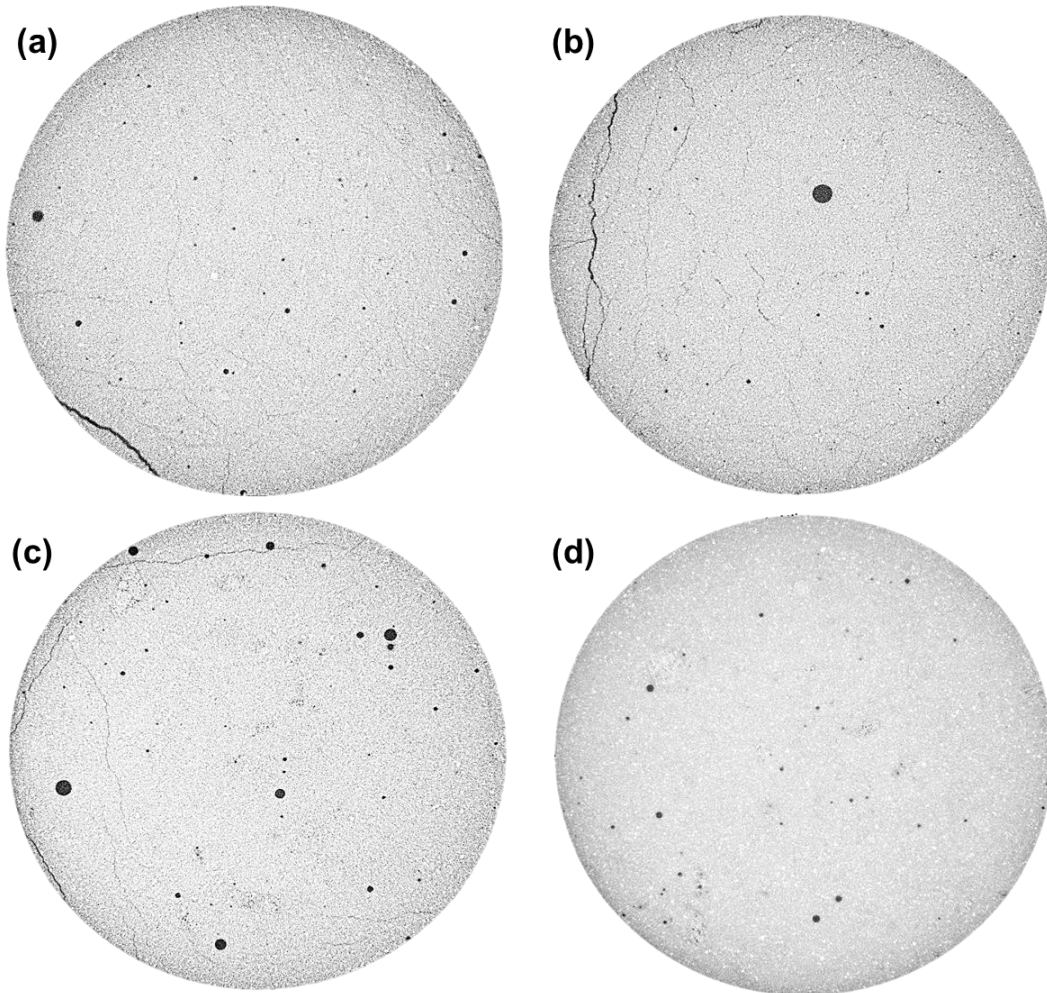
Figure 4.22. Post freeze-thaw MXCT 2D cross-sectional images. (**a**) control, (**b**) PEG-H, (**c**) PVA-H, and (**d**) PEG-PVA-H. MXCT cross-sections are ~9 mm in diameter.

4.4 Discussion

Together with the IRI and DIS data, the freeze-thaw resistance testing and air void content analysis reveals that, with sufficient dosage, PEG-PVA can provide resistance to freeze-thaw damage in OPC paste by a mechanism that is distinct from AEAs. While AEAs stabilize an air void system that helps dissipate hydraulic and osmotic pressures that are generated by ice crystal growth and coalescence, the results presented herein indicate that PEG-PVA imparts freeze-thaw resistance to paste *via* IRI activity. Given that PEG-PVA exhibited IRI and DIS activity in high-

pH solutions characteristic of OPC pore solution, the resistance of PEG-PVA-modified paste to resist freeze-thaw damage is mechanistically attributable to the ability of PEG-PVA to inhibit ice crystal growth.

These results suggest that biomimetic antifreeze molecules, like PEG-PVA, can inhibit freeze-thaw damage in cement paste. The use of these molecules may help counter other deleterious disadvantages that coincide with the use of AEAs. For example, despite achieving target air void contents, some AEAs do not necessarily mitigate freeze-thaw damage—a result that suggests the chemical properties of AEAs may play a critical role in their effectiveness.[163] In addition, it is well known that reductions in compressive strength, increased permeability, and retardation of setting time can occur with the use of AEAs[176,313]—behaviors that were not exhibited herein by the use of PEG-PVA in cement paste. Furthermore, recent research has indicated that, if a critical water saturation level is reached in air-entrained concrete (∼86%–88%), entrained air void systems are rendered ineffective and freeze-thaw damage is inevitable.[68,70] While the time to reach this critical water saturation level can be years,[68,72] the propensity for unavoidable damage in saturated air-entrained concrete is a limitation to the use of AEAs.

4.5 Conclusions

The results presented herein substantiate that a polymer that displays biomimetic antifreeze behavior (*i.e.*, IRI and DIS) enhances the freeze-thaw resistance of OPC paste without producing an entrained air void system or negatively affecting the fresh- or hardened-state properties of the paste. By providing an alternative to traditional surfactant air-entraining agents, biomimetic antifreeze polymers represent a new class of admixture biotechnologies for cement and concrete

that could enhance long-term durability in cyclic freeze-thaw environments. In summary, the results from this work indicate that robust IRI- and DIS-active molecules with an ability to interact directly with ice and prevent its continued growth and coalescence can provide an alternative mechanistic approach to freeze-thaw mitigation in cement paste—a finding that motivates further research and development into biomimetic antifreeze admixture technologies.

Chapter 5 Biomimetic Antifreeze Polyvinyl Alcohol for Enhanced Freeze-Thaw Resistance of Ordinary Portland Cement Paste

5.1 Introduction

Concrete placed in environments that reach near or subzero temperatures is susceptible to freeze-thaw damage. Freeze-thaw damage affects numerous concrete structures including roads, bridges, hydraulic dams, and spillways. The formation (*i.e.*, nucleation) and growth of ice crystals within the pores of cementitious materials can create hydraulic, osmotic, and crystallization pressures high enough to induce microscale cracks.[45,49] Cracking accelerates deterioration by reducing bulk mechanical integrity, exacerbating water and ion penetration, and increasing susceptibility to damage upon exposure to subsequent freeze-thaw cycles. The damage can be generalized into two categories: surface damage and internal damage. Surface damage is most often characterized by spalling and scaling. Internal damage is characterized by loss of mass, exposed aggregate, and visible cracks.

The *de facto* approach to freeze-thaw resistance in concrete has relied upon the creation of a stabilized air void network. Air voids are stabilized in fresh concrete by the use of surface-active air-entraining agents (AEAs). While air voids can provide freeze-thaw resistance, the resultant void network must meet a variety of parameters, including proper air void sizes, spacing factors, and specific surface area. While adequate air void networks are easily achievable in controlled laboratory settings, in practice, it is difficult to produce consistent, high quality air void systems.[2,312] Additionally, previous research has shown that once a critical degree of saturation is reached, 70-91%, an adequate air void network cannot prevent freeze-thaw damage.[68,71,343]

Researchers have utilized a variety of other materials and methods to enhance the freeze-thaw resistance of cementitious materials. These strategies include densifying and strengthening

cement paste using nanoparticles and supplementary cementitious materials,[5,198] reduction of water ingress through the use of hydrophobic agents,[147,148] and incorporating superabsorbent polymers as a non-surfactant method to achieve a void system.[7,344] In addition, researchers have used polymeric fibers for mitigating crack propagation due to frost-induced damage.[9,10] Each of these strategies is often deployed in conjunction with traditional air entrainment.[153,197,219] All of these methods aim at mitigating deleterious symptoms of ice formation in cement paste and concrete rather than inhibiting the source, ice crystal growth.

Recently, a new strategy for providing freeze-thaw resistance in cement paste, mortar, and concrete based on the biomimetic antifreeze properties of water-soluble polymers has been introduced.[145,311] It is proposed that when ice begins to form within the pores of cement paste and concrete, these biomimetic antifreeze polymers interact with the ice-water interface and slow ice crystal growth. Polyethylene glycol-polyvinyl alcohol graft-copolymer (PEG-PVA), which is 75% PVA, was shown by Frazier *et al*. to provide freeze-thaw resistance to both cement paste and concrete at dosages of 0.021% and 0.066% by wt. of cement respectively.[145] However, in that same study PVA was also tested and shown to provide no freeze-thaw resistance at the same dosage in cement paste. In another study, Qu *et al*. showed that PVA can provide scaling resistance to mortar at dosages as low as 0.0089% by wt. of cement.[311] When comparing the PVA used in these two studies, the only difference was the molecular weight and dosages of PVA. Additionally, neither study used a PVA with a degree of hydrolysis below 98%.

In other fields, biomimetic antifreeze polymers, such as PVA and PEG-PVA, have been studied as alternatives to antifreeze proteins (AFPs) and antifreeze glycoproteins (AFGPs). AFPs and AFGPs are directly linked to the survival of a multitude of species in sub-zero conditions.[132] Specifically, AFPs and AFGPs can directly bind to ice and inhibit the growth and coalescence of

ice crystals *via* a process called ice recrystallization inhibition (IRI). When considering PVA, the hydroxyl groups along the backbone of the polymer mimic highly hydroxylated AFGPs.[140] Recent work suggests that the interaction of PVA hydroxyl groups, whose spacing closely matches lattice constants of the ice crystal structure, with the basal and prismatic faces of ice results in IRI activity.[77,263,264]

The IRI activity of PVA has been well studied.[77,140,259,261–266,268,345] Researchers have found that, at molecular weights exceeding 21,000 g/mol, PVA exhibits significant IRI activity, which we define as reducing the mean largest grain size of ice crystals by >80% at concentrations of 0.1 mg/mL or lower.[140,224] At molecular weights below 21,000 g/mol PVA has minimal to no IRI activity at concentrations of 0.1 mg/mL and lower. This led us to hypothesize that a molecular weight of PVA that exceeds 21,000 g/mol would be needed to provide freeze-thaw resistance to cement paste.

PVA has been utilized in cementitious materials primarily as a solid fiber[9,154,210] and as a water-soluble polymer additive.[329,346,347] When added as a polymeric fiber, PVA helps prevent crack migration. PVA has also been used as a water-soluble polymer additive. When used in dosages ~1% by wt. of cement, soluble PVA can improve flexural strength,[348] increase aggregate-paste bond strength,[346] and improve workability[349] due to the formation of polymer films and the interaction of PVA with $Ca(OH)_2$. Although PVA can lead to beneficial property enhancements, it has also previously been shown to interact with cement grains resulting in retardation of hydration.[329,330] Additionally, PVA is known to entrain air at dosages >1% by wt. of cement.[347] No previous studies have investigated the effect of PVA added as a water-soluble admixture on the freeze-thaw resistance of cement paste.

The objectives of this work were (1) to determine if the presence of IRI-active PVA in hardened cement paste yields lower quantities of ice when frozen, (2) to study the effect of PVA molecular weight and degree of hydrolysis on freeze-thaw resistance of cement paste, and (3) to analyze the effect of PVA molecular weight and degree of hydrolysis on hydration kinetics and mineralogy at a dosage of 0.021% by wt. of cement.

5.2 Experimental Procedure

5.2.1 Materials

PVA of three molecular weights, namely M_w=13,000-23,000 g/mol (PVA 1), M_w=31,000-50,000 g/mol (PVA 2), and M_w=130,000 g/mol (PVA 3) having degrees of hydrolyses of 98%, 98-99%, and >99%, respectively, were purchased from Sigma Aldrich (St. Louis, MO, USA) and used without further modification. Polyethylene glycol (PEG) having an M_n of 3,350 g/mol was Sigma Aldrich and used without further modification. PVA of molecular weights M_w=75,000 g/mol (PVA 4) and M_w=214,500 g/mol (PVA 5) having degrees of hydrolyses of 86.5-89% and 87-89% respectively were generously provided by Kuraray American (Houston, TX, USA). A commercially available AEA with active ingredients of sulfonic acids (1-3%) and rosin (<1%) was used without modification. The cement used in this study was Type I/II OPC (Quickrete®) that complies with ASTM C150.[350] The chemical composition of the OPC is reported in **Appendix A**.

5.2.2 Ice Recrystallization Inhibition

The IRI activities of PEG, PVA 1, PVA 2, PVA 3, PVA 4, and PVA 5 were tested at a concentration of 0.5 mg/mL in PBS. This concentration was chosen based on previous research

in cement paste.[145] A modified IRI assay was performed to observe IRI activity.[321] 10 μL of sample was dropped from 1.7 m onto a glass slide (thickness of 1 mm). The glass slide was pre-cooled on an aluminum block at −78°C. The slide was then immediately transferred to an Otago nanoliter osmometer cold stage and annealed at −4°C (air temperature) for 30 min. Images were collected immediately after the sample was placed on the cold stage and again at 30 min to observe ice recrystallization. For all samples, images were obtained using an Olympus BX41 microscope with ELWD U Plan 20×/0.45 objective and crossed polarizers, equipped with an OMAX A35140U camera on a 0.5× C-mount adaptor. ImageJ 1.48v software (National Institutes of Health) was used to estimate the grain sizes.

5.2.3 Sample Preparation

Cement paste samples were hand-mixed for 3 min at a water to cement ratio (w/c) of 0.42 and cast into cylindrical polyethylene molds 32 mm in height and 16 mm in diameter. Cast samples were cured for 14 days in a 99% relative humidity chamber according to ASTM C192 at 20°C ±2°C.[323] **Table 5.1** provides the sample compositions. The amount of PVA chosen in the mix design was based on previous work,[145] and is equivalent to the 0.5 mg/mL concentration used in the IRI assay. An AEA-modified sample was prepared for testing in differential scanning calorimetry only. The AEA dosage of 1.4% by wt. of cement was found to entrain 18% air in the fresh state. See **Appendix C** for details of the AEA dosage and fresh state air content measurements.

Table 5.1. Cement Paste Mix Designs.

Sample	Polymer M_w* (g/mol)	Degree of Hydrolysis* (%)	w/c Ratio	Polymer (wt.% of cement)

Control	-	-	0.42	-
PVA 1	13,000-23,000	98	0.42	0.021%
PVA 2	31,000-50,000	98-99	0.42	0.021%
PVA 3	130,000	>99	0.42	0.021%
PVA 4	75,200	86.5-89	0.42	0.021%
PVA 5	214,500	87-89	0.42	0.021%
AEA	-	-	0.42	1.4%

* Values reported by manufacturer.

5.2.4 Isothermal Conduction Calorimetry

Isothermal conduction calorimetry (ICC) was performed to understand the impact of the

polymeric admixtures on both the heat of hydration and time of set. A TAM Air 8-Channel

Isothermal Calorimeter from TA instruments was set at 21°C and allowed to equilibrate for 24

hours. All samples were mixed for 3 minutes in glass ICC vials, with a w/c ratio of 0.5, and

immediately placed in the calorimeter and allowed to equilibrate for 1 hour before the

calorimeter signal was considered stable. Data was measured for 72 hours to capture the peak

thermal power. The peak thermal power at 50% was used to approximate the time of set.[326]

5.2.5 X-ray Diffraction

X-ray diffraction (XRD) was performed on all samples to qualitatively determine

mineralogy. After 14 days of curing samples were placed in acetone for a minimum of 24 hours

to stop hydration reactions. Samples were crushed into a fine powder and suspended in ethanol

(200 proof) to homogenize the powder. The suspension was pipetted onto a silica zero

background plate and placed on a heated plate to allow for ethanol evaporation resulting in a thin film of sample. Diffractograms were collected using a Bruker D8 Advance XRD equipped with a Cu Kα radiation source. Data were recorded in the range of $2\theta = 5°$ to $65°$ with a step size of $0.02°$ and a dwell time of 2 sec/step. Crystalline phases were identified using Bruker DIFFRAC.EVA software and the International Center for Diffraction Data (ICDD) PDF-4 AXIOM 2019 database.[351]

5.2.6 Freeze-Thaw Resistance

Freeze-thaw cycling of OPC paste samples was performed in a custom-built chamber. Details of the chamber may be found in **Appendix B**. All samples were tested in triplicate and exposed to a total of 30 cycles in which the freezing lasted for 1.5 h and thawing for 2.5 h, respectively. During freezing cycles, the temperature reached $-15°C \pm 2°C$ and thawing cycles $16.5°C \pm 2°C$. To ensure samples remained saturated, a minimal water level was maintained at the bottom of the chamber.

Freeze-thaw damage was assessed by visual inspection for spalling of bulk samples and by scanning with micro X-ray computed tomography (MXCT) to observe internal microcracking. The MXCT (ZEISS Xradia 520 Versa) source voltage was set to 140 kV and the power to 10 W. An objective with an optical magnification of $0.4\times$ was used. The source and detector locations were varied to obtain the desired resolution (voxel size) of approximately 5 µm. Dragonfly 3.9 software (Object Research Systems) was used to generate reconstructions from MXCT scans that were analyzed for microcracking.

5.2.7 Differential Scanning Calorimetry

Differential Scanning Calorimeter (DSC) was used to quantify the ice content formed within hardened cement paste. Samples were prepared as outlined in section 5.2.3. Samples were chipped from the cylindrical samples and trimmed to ensure they both fit within the DSC pans and had a flat surface to contact the bottom of the DSC pan. Thermal data were collected using a TA Instruments Q2000 DSC in a nitrogen environment using a purge rate of 50 mL/min. 15-45 mg samples of saturated surface dried (SSD) paste samples were placed in hermetically sealed aluminum pans. The SSD masses were recorded before sealing the pans. The samples were first equilibrated to 15 °C followed by cooling at a rate of 5 °C/min to -60 °C. The samples were then heated at a rate of 5 °C/min to 5°C.

Figure 5.1 shows a representative DSC thermogram for the freezing and thawing cycles. The four characteristic peaks are identified in **Figure 5.1**. Peak 1 is a supercooling event that results from water freezing in macropores (*i.e.*, capillary pores and air voids).[352] Due to the nature of supercooling, this DSC peak cannot be directly analyzed. Peaks 2 and 3 can be attributed to ice formation within mesopores, 2-50 nm, (*i.e.*, capillary pores) and micropores, <2 nm, (*i.e.*, gel pores) respectively.[352,353]
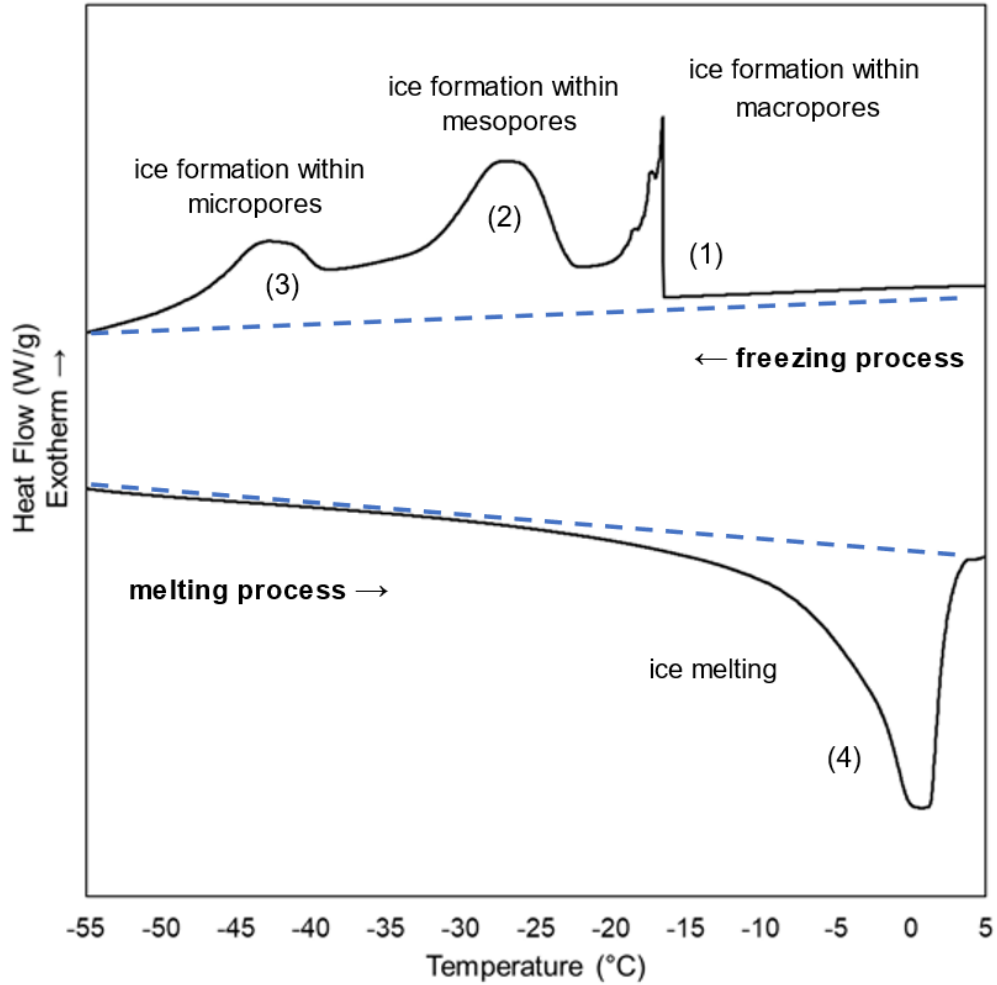
Figure 5.1. Representative DSC thermogram of hardened OPC paste showing characteristics peaks.

The amount of ice formed or melted within the hardened cement paste was estimated using a method adapted from Sun and Scherer.[354] First, the enthalpy of DSC peaks 2, 3, and 4 were calculated by integration of the heat flow curves using the software package Universal Analysis 2000 Version 4.5A (TA Instruments). A representative enthalpy calculation is shown in **Figure 5.2**. The enthalpy is determined by using a sigmoidal tangent baseline for integration to account for the baseline having a slope before and/or after a thermal event. Second, the enthalpy was then divided by a corrected heat of fusion, H' (J/g), to calculate the ice content, m_c (g):

$$(5.1) \qquad m_c = \frac{h}{H'}$$

For freezing events, the corrected heat of fusion is H' = 332.4 J/g [354,355]. The same corrected heat

of fusion is also valid for melting if pores are assumed to be spherical. For this analysis, the

corrected heat of fusion, H' = 332.4 J/g, is used for both heating and cooling.
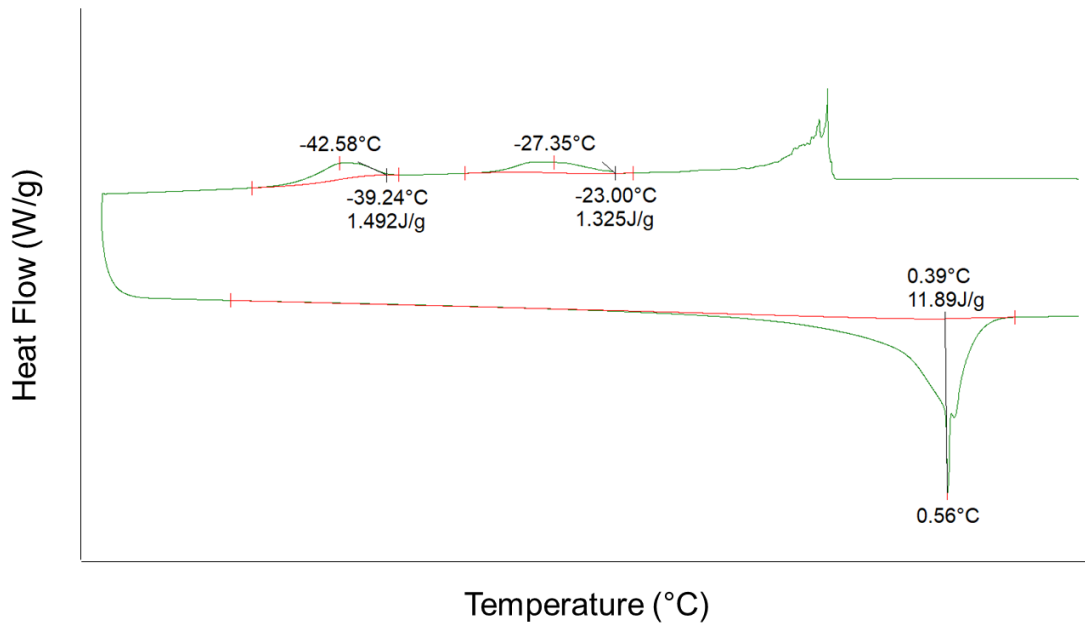
Figure 5.2. Representative enthalpy calculations using software package Universal Analysis.
The green line represents the DSC data, and the red line represents the baseline
programmatically placed for the determination of the enthalpy. The small vertical red lines
indicate the beginning and endpoints for the enthalpy calculation.

The m_c was calculated for peaks 2, 3, and 4 of **Figure 5.1** using Equation 1. It was assumed

that all the ice formed during the freezing events of peaks 1, 2, and 3 melted during the melting

event, or peak 4. Therefore, the amount of ice that formed during peak 1, or the supercooling

event, can be estimated using Equation 5.2. Note that the supercooling event occurs at a

temperature near the freezing temperature used in the freeze-thaw cycles used within this study.

$$(5.2) \qquad m_{c,peak\ 1} = m_{c,peak\ 4} - (m_{c,peak\ 2} + m_{c,peak\ 3})$$

5.2.8 Water Absorption

The water absorption behaviors of the Control, PVA 1, PVA 2, PVA 3, PVA 4, and PVA 5

modified pastes were characterized by testing 3 cylinder specimens after a 14-day cure as

described in section 5.2.3 and 3 samples with masses between 0.15 mg and 0.45 mg to match the

sample size used in the DSC experiments. The specimen were placed in an oven at 170 °F (77

°C) to remove free water. The specimen masses were monitored until negligible mass loss was

observed (<2%).

After oven-drying, the specimen were placed in room temperature tap water. The mass was

monitored for 600 mins at intervals of 5, 10, 40, 70, 120, 180, 290, and 600 mins. The water

absorbed, WA, was calculated according to the following:

$$(5.3) \qquad WA = \frac{m_t - m_o}{m_o} \times 100\%$$

Where m_t is the mass of the sample at a given time, and m_o is the initial mass of the sample after

oven drying.

5.2.9 Air Void Parameters

The air content, spacing factor, void frequency, and specific surface were calculated using

equations provided in the linear traverse method of ASTM C457 for 1 of the 3 replicates used in

freeze-thaw cycling of each sample [54]. The methods described in ASTM C457 were applied to

MXCT 2D cross-sectional images as opposed to using light microscopy. This general approach

has previously been used [170,356]. Here 18 cross-sectional images per sample were analyzed.

Figure 5.3 visually summarizes the approach used. The cross-sectional images were opened

in ImageJ 1.48v software (National Institutes of Health), **Figure 5.3a**. The images were then

thresholded to create a binary image such that the cement paste and air voids were divided into two classes of pixels. This can be seen in **Figure 5.3b** where the cement paste pixels are assigned white and the air void pixels are assigned black. An equally sized grid was applied to all images as shown in **Figure 5.3c**. Ten horizontal lines were placed on the grid and the plot profile tool was used to measure the distance of paste (*i.e.*, white pixels) and air voids (*i.e.*, black pixels) traversed. A minimum of 1,000 mm length was traversed per sample.
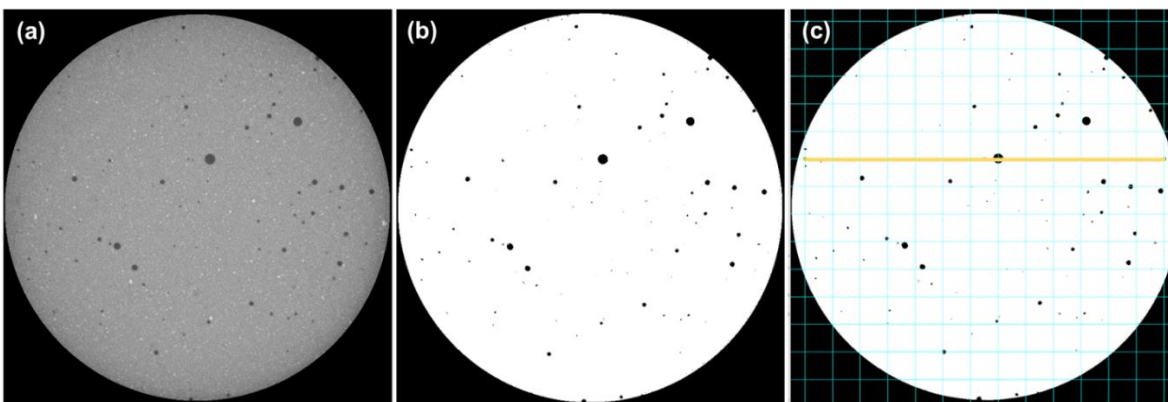
Figure 5.3. Image processing of MXCT 2D cross-sectional images within ImageJ for determination of air void parameters. (a) unmodified MXCT 2D cross-sectional image. (b) image after undergoing thresholding where the paste is assigned white and the air is assigned black. (c) grid applied to an image and 10 horizontal lines were placed on the grid to measure grey values (i.e., white and black pixels) using the plot profile tool.

5.3 Results

5.3.1 Ice Recrystallization Inhibition

Figure 5.4 shows the splat assay micrographs for the PBS control, PEG, PVA 1, PVA 2, PVA 3, PVA 4, and PVA 5 at 0.5 mg/mL in PBS. Based on visual comparison of grain sizes, at 30 mins PVA 1, PVA 2, PVA 3, PVA 4, and PVA 5 all exhibited significant IRI activity when compared to the negative control, PEG, and the PBS control. The mean largest grain size (MLGS) of the PBS control sample was 105 ± 12 µm. The reduction in grain size for all PVA

samples easily exceed 80% compared to the control PBS solution with MLGS ≤ 10 μm. These

results were expected at a concentration of 0.5 mg/mL.[140]
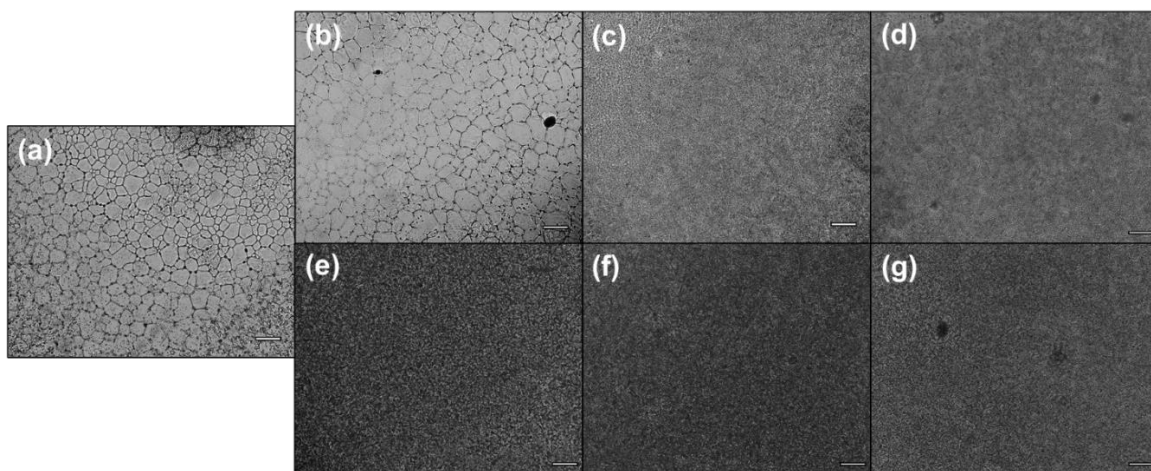
Figure 5.4. Optical micrographs of IRI splat assay. (a) PBS control solution, (b) 0.5 mg/mL PEG, (c) 0.5mg/mL PVA 1, (d) 0.5 mg/mL PVA 2, (e) 0.5 mg/mL PVA 3, (f) 0.5 mg/mL PVA 4, and (g) 0.5 mg/mL PVA 5 in PBS after 30 min of annealing at -4°C. Scale bars are 100 μm.

5.3.2 Isothermal Conduction Calorimetry

Figures 5.5 and **5.6** provide the normalized total heat and normalized heat flow for PVA 1,

PVA 2, and PVA 3, while **Figures 5.7** and **5.8** provide the normalized total heat and normalized

heat flow for PVA 4 and PVA 5. The data were normalized with respect to the sample masses

used in the ICC. As shown in **Figure 5.5** the normalized total heat was minimally affected up to

24 hours by the addition of 0.021wt% PVA at all three molecular weights where the degree of

hydrolysis exceeded 98%. After 40 hours, PVA 1, PVA 2, and PVA 3 modified paste had

cumulative heats that were 97.7%, 98.0%, and 99.1% of the control, respectively. After 60 hours,

PVA 1, PVA 2, and PVA 3 modified paste had cumulative heats that were 96.9%, 97.1%, and

98.0% of the control, respectively. PVA 4 and PVA 5 with lower degrees of hydrolysis also

resulted in minimal impact to the total heat as shown in **Figure 5.6**. After 24 hours, PVA 4 and

PVA 5 modified paste had cumulative heats that were 102 and 103% of the control.

Figure 5.7 and **Figure 5.8** show the normalized heat flow for the first 24 hours. The start of

the acceleration period is delayed by approximately 30 mins for PVA 1, PVA 2, and PVA 3

modified paste. At 50% peak thermal power the setting time can be estimated.[326] The presence of

PVA 1, PVA 2, and PVA 3 resulted in delayed set times of 0.56 hrs, 0.67 hrs, and 0.69 hrs

compared to the Control. The start of the acceleration period is delayed by approximately 12

mins for PVA 4 and PVA5 modified paste and the set times were delayed by less than 10 mins

compared to the Control.
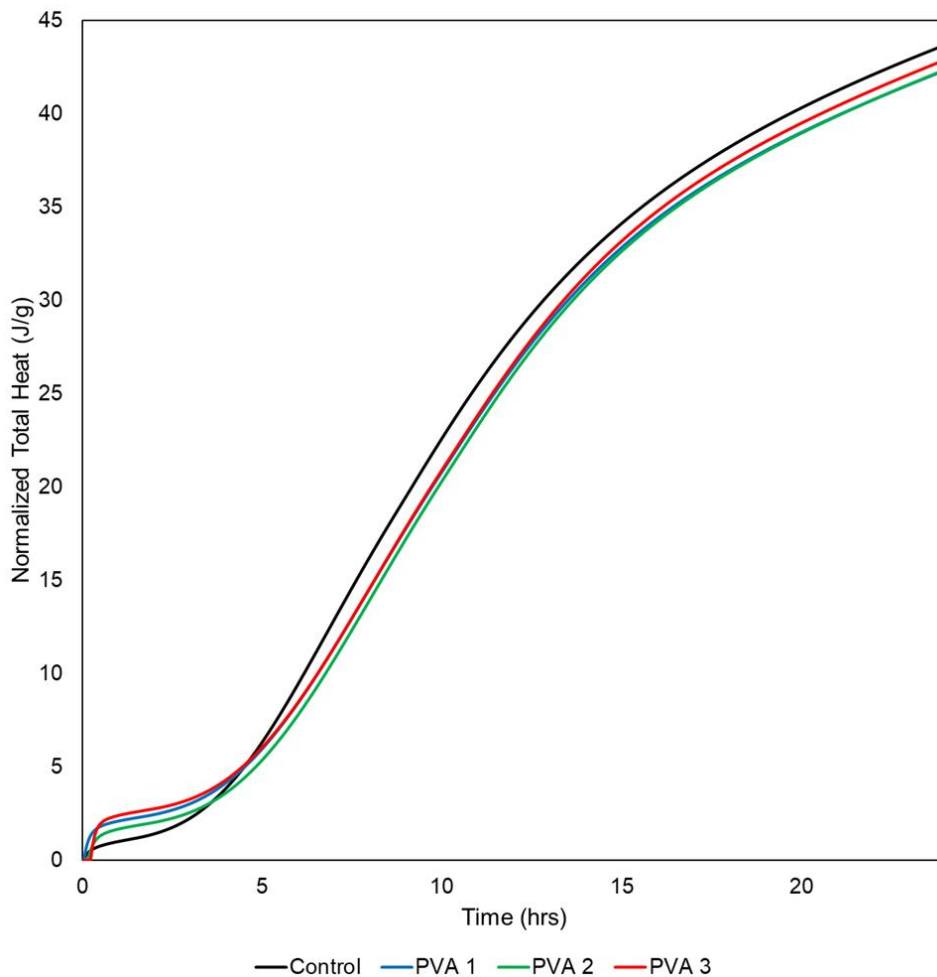
Figure 5.5. Isothermal conduction calorimetry normalized total heat plots for Control (black),
PVA 1 (blue), PVA 2 (green), and PVA 3 (red).
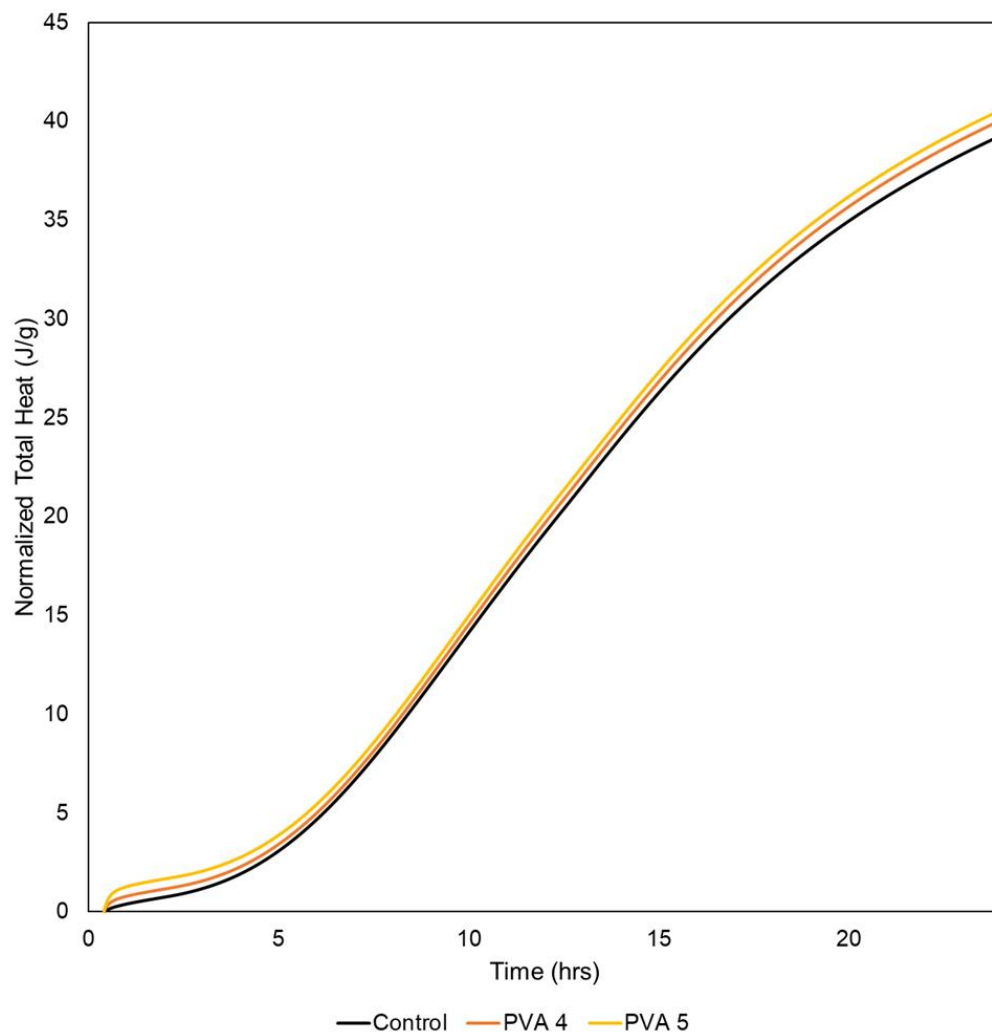
Figure 5.6. Isothermal conduction calorimetry normalized total heat plots for Control (black), PVA 4 (orange), and PVA 5 (yellow).
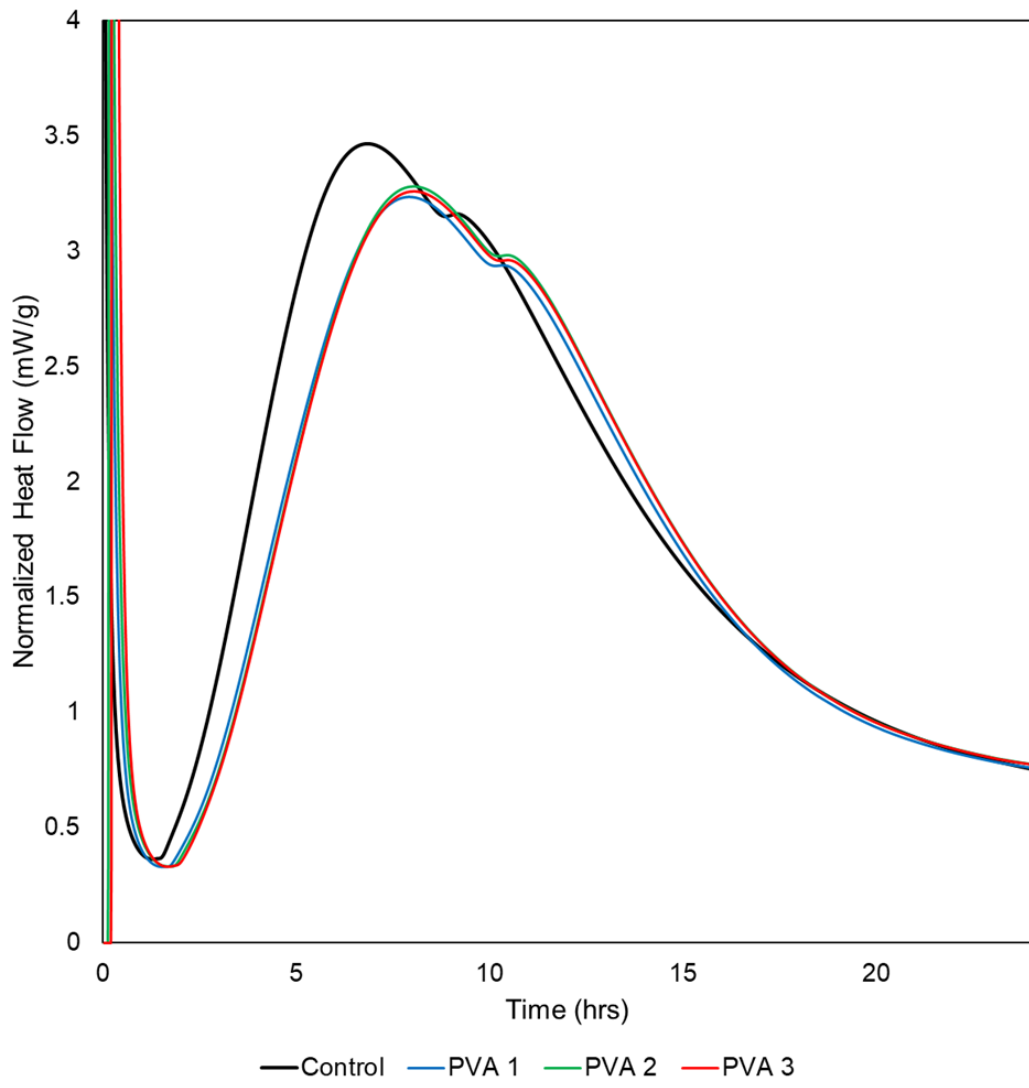
Figure 5.7. Isothermal conduction calorimetry normalized heat flow plots for Control (black), PVA 1 (blue), PVA 2 (green), and PVA 3 (red).
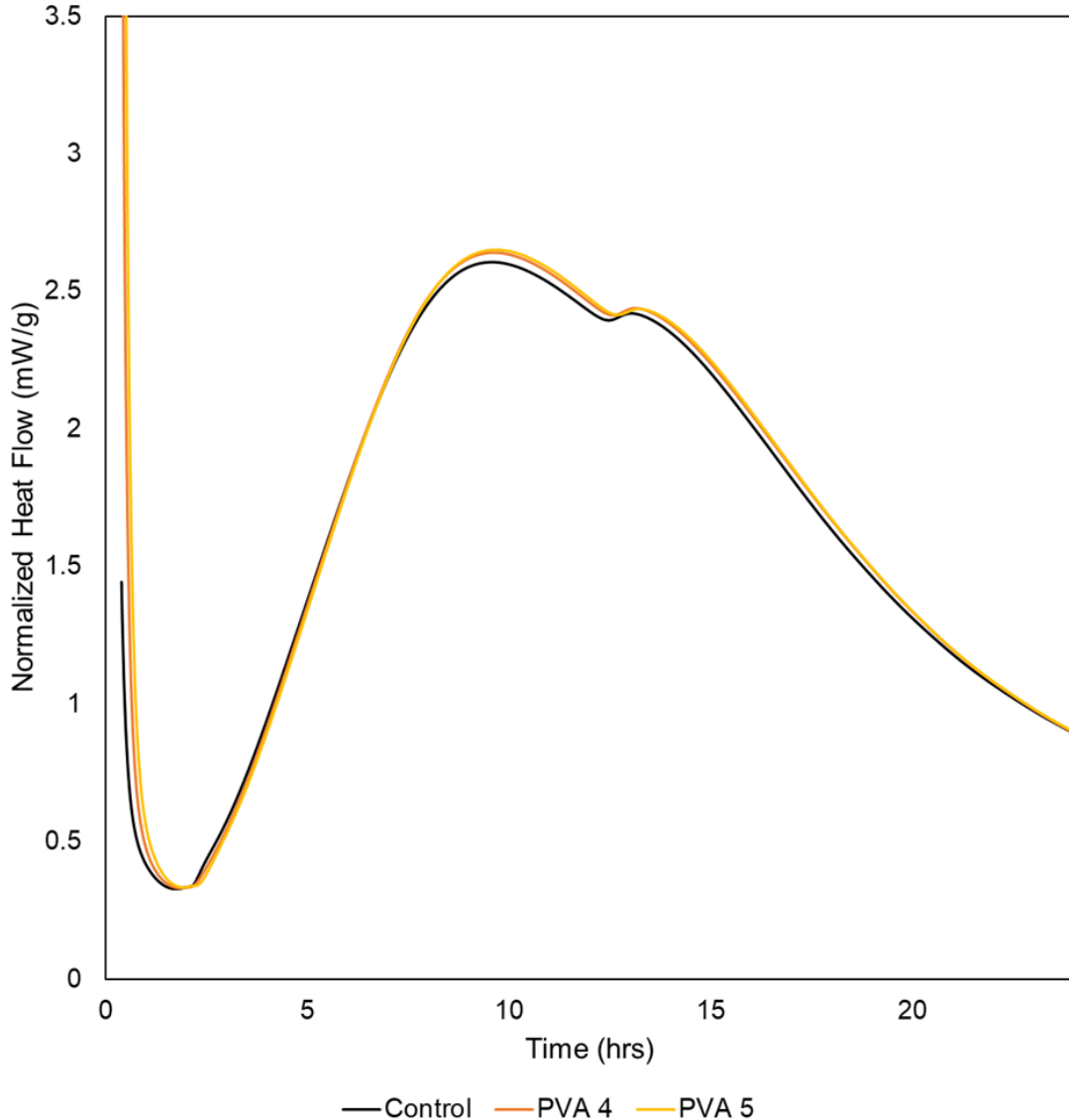
Figure 5.8. Isothermal conduction calorimetry normalized heat flow plots for Control (black), PVA 4 (orange), and PVA 5 (yellow).

5.3.3 X-ray Diffraction

Figure 5.9 shows XRD diffractograms of the control, PVA 1, PVA 2, and PVA 3 modified paste samples with identified minerals. **Table 5.2** summarized the identified peaks, all of which are anticipated for hardened OPC paste. The primary difference between the unmodified and PVA modified paste where the degree of hydrolysis >98% can be seen at $2\theta = 50.8°$ and $54.4°$, both of which have been identified as $Ca(OH)_2$.[334,335] The peak at $50.8°$ is not present for PVA 3,

the highest molecular weight PVA. The peak at 54.4° appears to disappear for both PVA 2 and

PVA 3. **Figure 5.10** shows XRD diffractograms of the control, PVA 4, and PVA 5 modified

paste samples with identified minerals. PVA 4 and PVA 5 both have a degree of hydrolysis <

90%. Unlike PVA 2 and PVA 3, the $Ca(OH)_2$ at 54.4° does not disappear for PVA 4 or PVA 5.
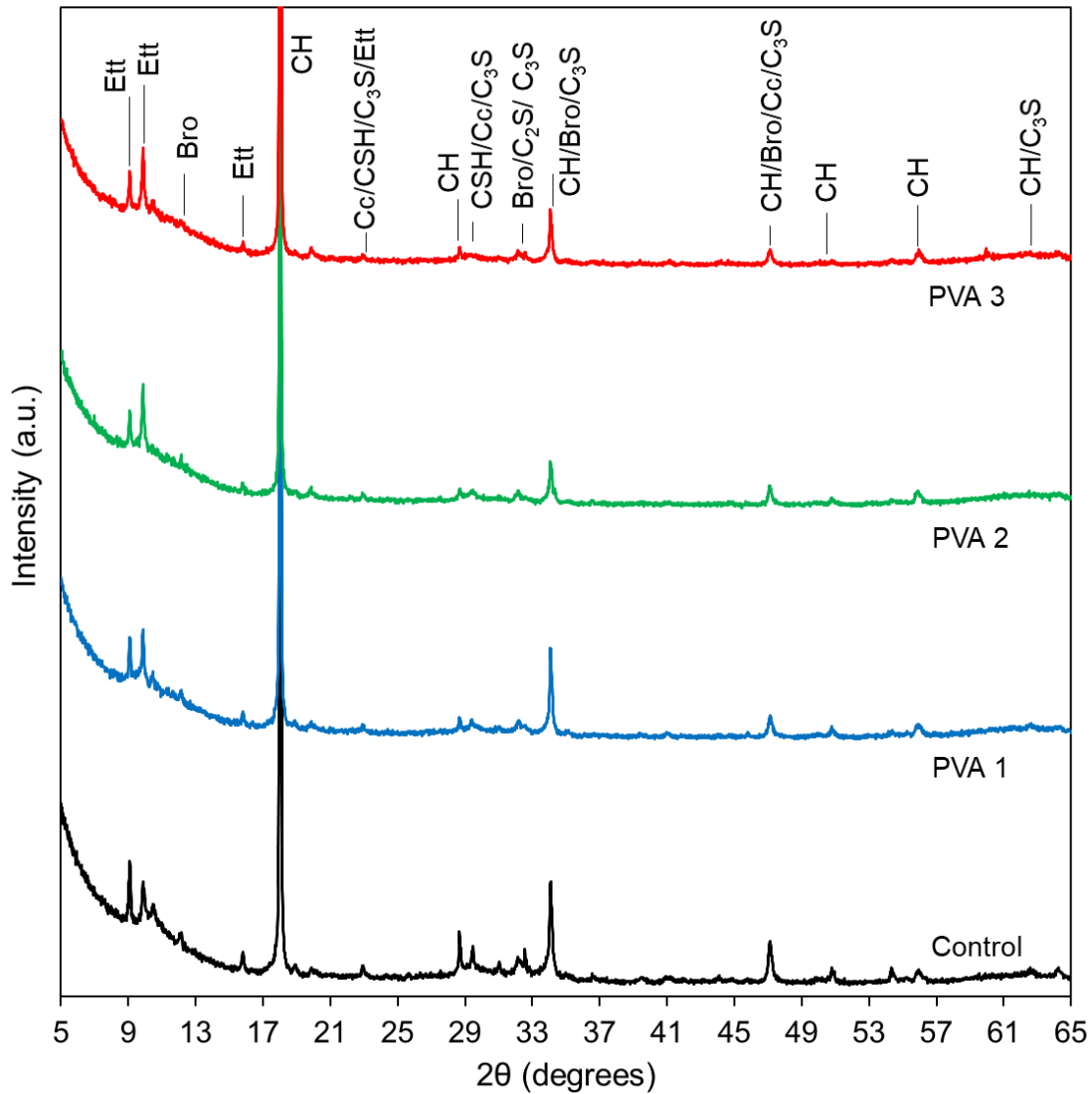
Figure 5.9. XRD diffractograms of control, PVA 1, PVA 2, and PVA 3 modified paste samples after 14-day cure. Bro: Brownmillerite; Cc calcite; CH: $Ca(OH)_2$/portlandite; C-S-H: calcium silicate hydrate; Ett: Ettringite, C_2S: belite; C_3S: alite.
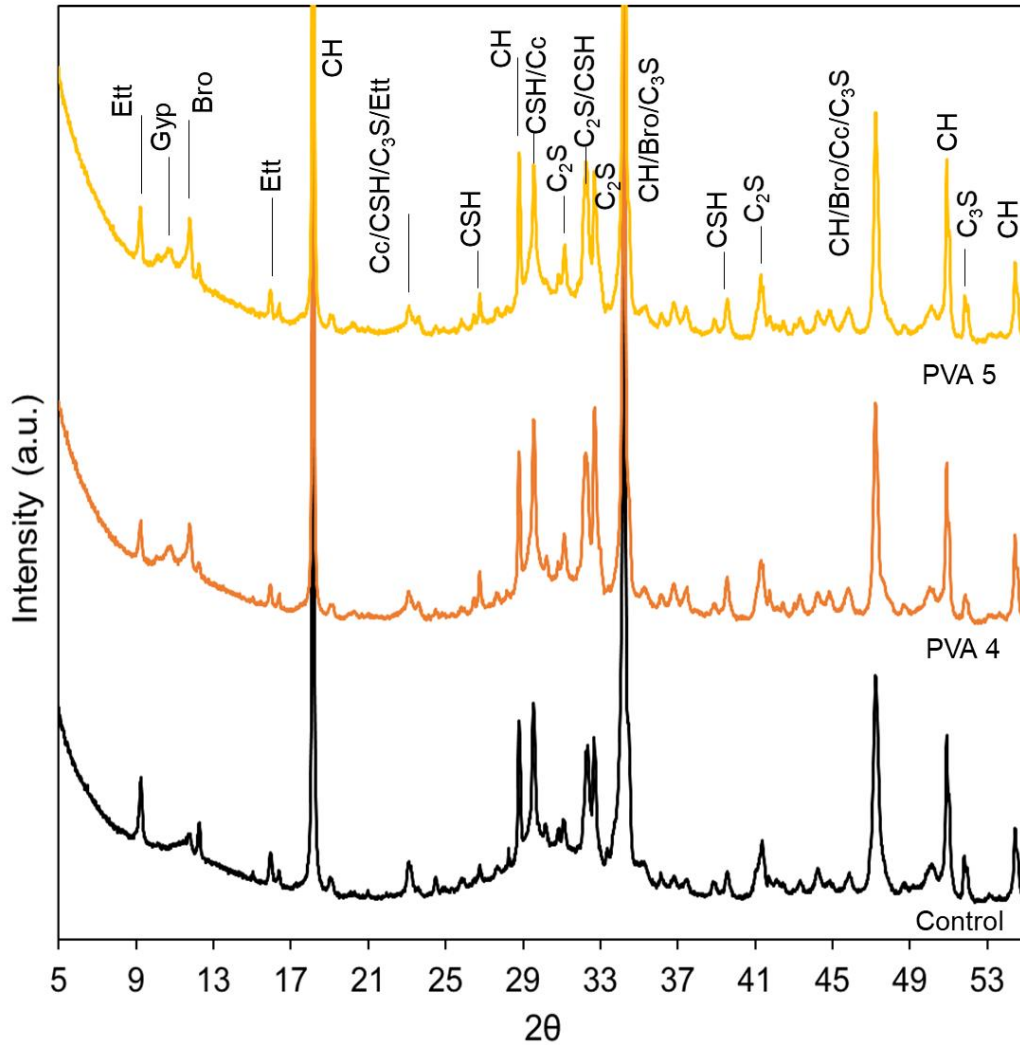
Figure 5.10. XRD diffractograms of control, PVA 1, PVA 2, and PVA 3 modified paste samples after 14-day cure. Bro: Brownmillerite; Cc calcite; CH: $Ca(OH)_2$/portlandite; C-S-H: calcium silicate hydrate; Ett: Ettringite, C_2S: belite; C_3S: alite; Gyp: gypsum.

5.3.4 Freeze-Thaw Resistance

Figure 5.11 provides representative 2D cross-sectional MXCT images of paste samples after exposure to 30 freeze-thaw cycles. Control pastes and pastes containing 0.021 wt% additions of PVA 1 exhibited signs of internal crack formation as highlighted by the red arrows. **Figure 5.12** provides images of the bulk samples paste samples after exposure to 30 freeze-thaw cycles. Control pastes and PVA 1 and PVA 5 modified pastes exhibited clear external damage. OPC

paste containing PVA 2 displayed minor spalling near the top of the samples. OPC paste

containing PVA 3 and PVA 4 at an addition of 0.021 wt.% of cement exhibited no internal or

external damage.
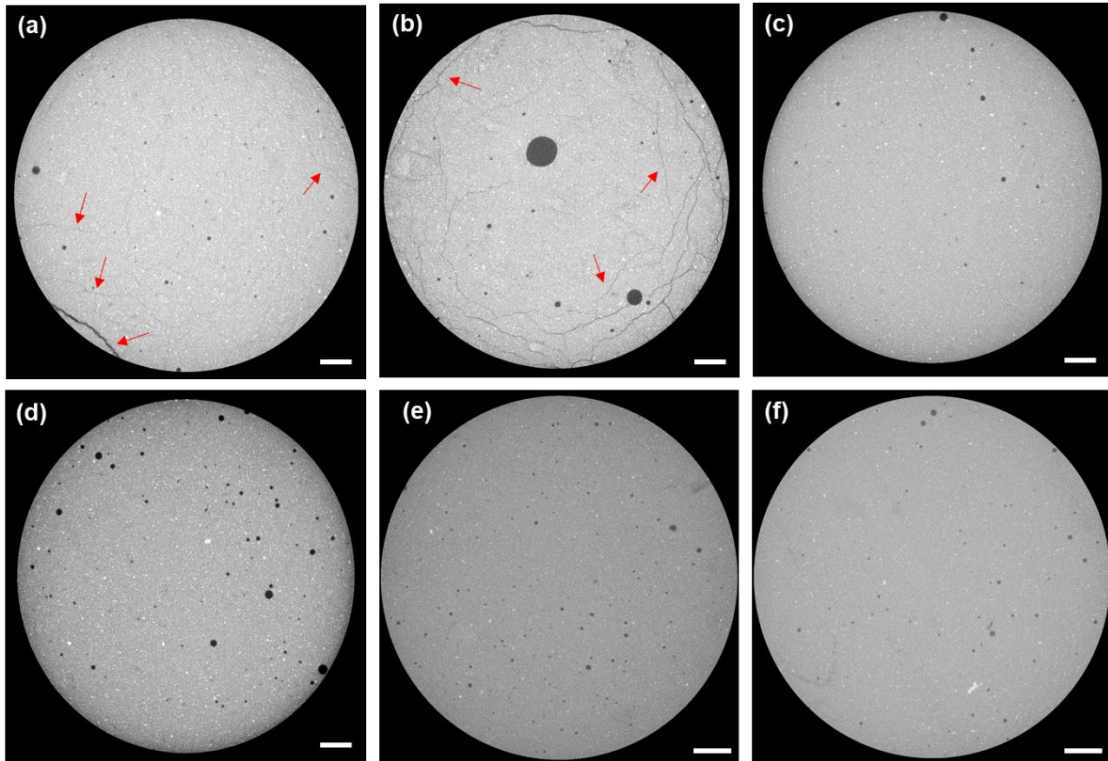
Figure 5.11. Representative post-freeze-thaw MXCT 2D cross-sectional images of (a) control, (b) PVA 1, (c) PVA 2, (d) PVA 3, (e) PVA 4, and (f) PVA 5 cement paste formulations. Red arrows indicate microcracks. Scale bars are 1 mm.
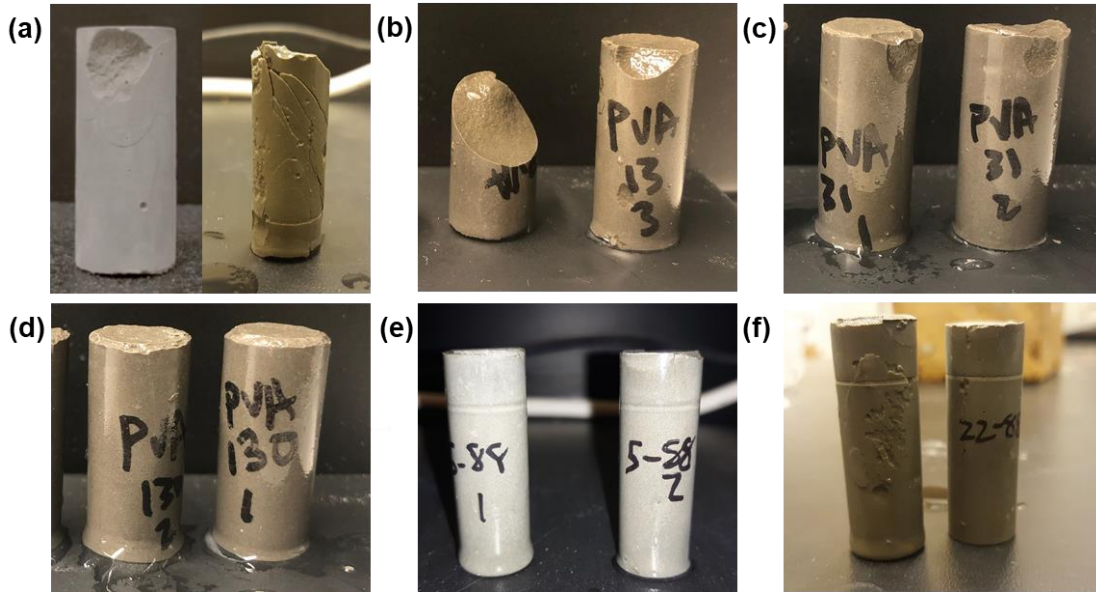
Figure 5.12. Post-freeze-thaw images of bulk samples. (a) control, (b) PVA 1, (c) PVA 2, (d) PVA 3, (e) PVA 4, and (f) PVA 5 cement paste formulations. Bulk samples are ~16 mm diameter by 32 mm in height.

5.3.5 Differential Scanning Calorimetry

The calculated ice contents for the freezing events (peaks 1, 2, and 3) and melting event (peak 4) are shown in **Figure 5.13**. PVA 1, PVA 2, PVA 3 and PVA 4 modified pastes had lower ice contents during the supercooling event (*i.e.*, peak 1), which were 64%, 44%, 39%, and 57% of the control respectively. PVA 5 and AEA modified pastes had resulted in minor reductions in ice contents, 87% and 86% respectively. All PVA-modified paste samples have significantly higher ice contents within mesopores (*i.e.*, peak 2) where ice was observed to form between -25 °C and -40 °C. The PVA 1, PVA 2, PVA 3, PVA 4, and PVA 5 modified pastes have ice contents of 258%, 219%, 197%, 269%, and 248% respectively but with significant variability. The AEA modified had essentially the same ice content within the mesopores. Within the micropores (*i.e.*, peak 3) ice contents of 100%, 75%, 90%, 34%, and 40% of the control were observed for PVA 1, PVA 2, PVA3, PVA 4, and PVA 5 modified paste samples where ice forms between the temperatures of -40 °C and -55 °C. The PVA modified samples all had lower

calculated ice contents during the melting event (*i.e.*, peak 4). The melting event is representative

of the overall ice that formed during the freezing process. The ice contents for PVA 1, PVA 2,

PVA 3, PVA 4, and PVA 5 were 86%, 64%, 59%, 73%, and 96% of the control. The AEA

modified paste ice content during the melting event was 87% of the control.
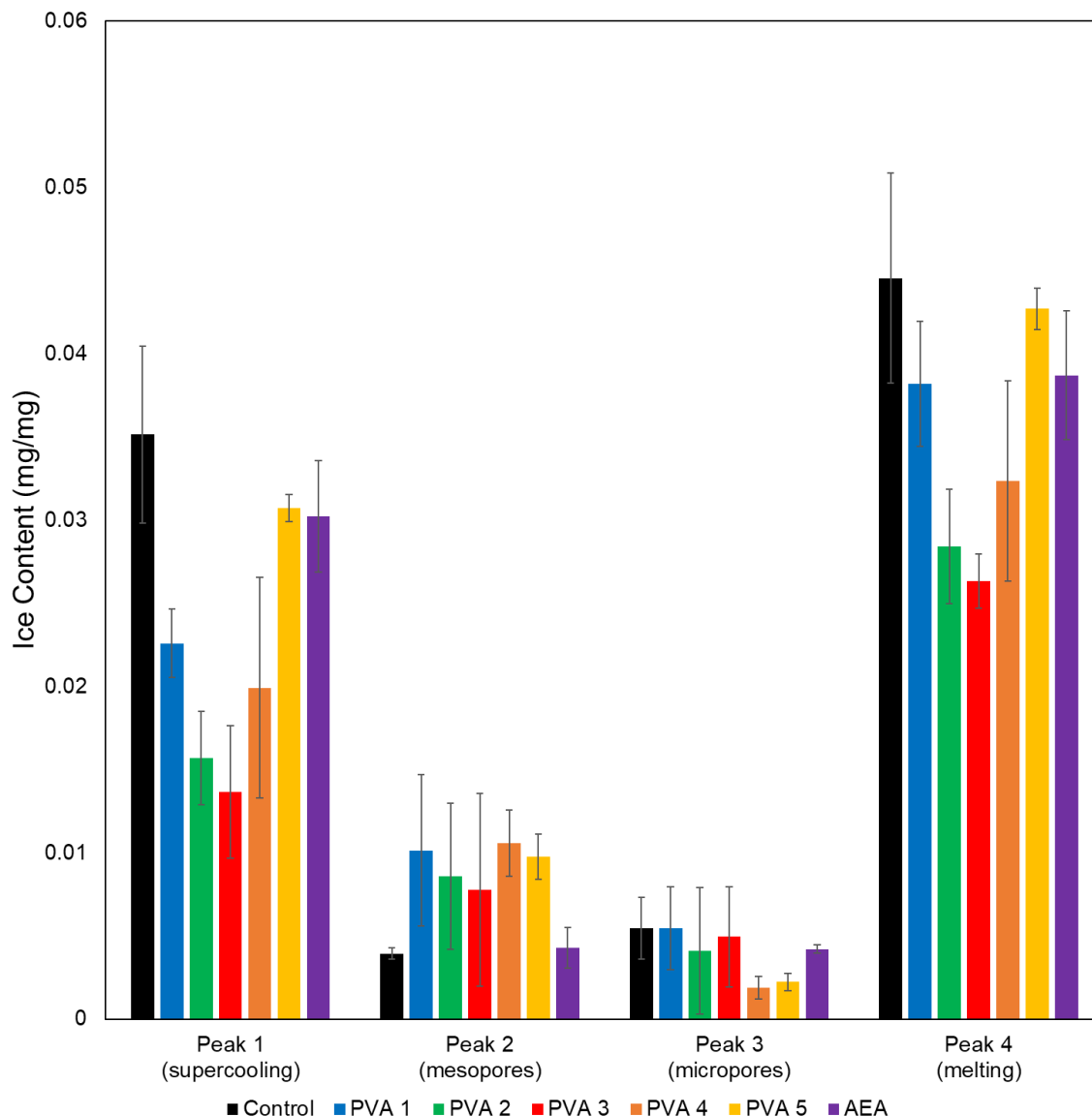
Figure 5.13. Calculated ice contents of each freezing and melting event for control (black), PVA 1 (blue), PVA 2 (green), PVA 3 (red), PVA 4 (orange), PVA 5 (yellow), and AEA (purple) from DSC. Error bars represent one standard deviation of 3 replicates.

5.3.6 Water Absorption

Figure 5.14 shows the water absorption behavior in percent mass gained of the control, PVA 1, PVA 2, PVA 3, PVA 4, and PVA 5 modified pastes after oven-drying at 120 mins in tap water. In **Figure 5.14 a**, the samples are equivalent in dimension to samples used in freeze-thaw cycling, 16 mm x 32 mm cylindrical samples. In **Figure 5.14 b** the samples are 0.15 – 0.45 mg of hardened paste to match the size of samples used in the DSC analysis.

As can be seen in **Figure 5.14 a**, all cylindrical PVA modified paste have approximately the same amount of water absorption compared to control. The DSC-sized PVA 1 and PVA 5 modified pastes had slightly lower water absorption while the other PVA modified pastes have approximately the same amount of water absorption compared to the control. Additionally, the results in **Figure 5.15** indicate that the samples reach maximum water absorption by ~80 minutes. **Figure 5.15** provides the time dependent water absorption behavior of the cylindrical Control, PVA 1, PVA 2, PVA 3, PVA 4, and PVA 5 modified pastes after oven-drying up to 600 mins in tap water.
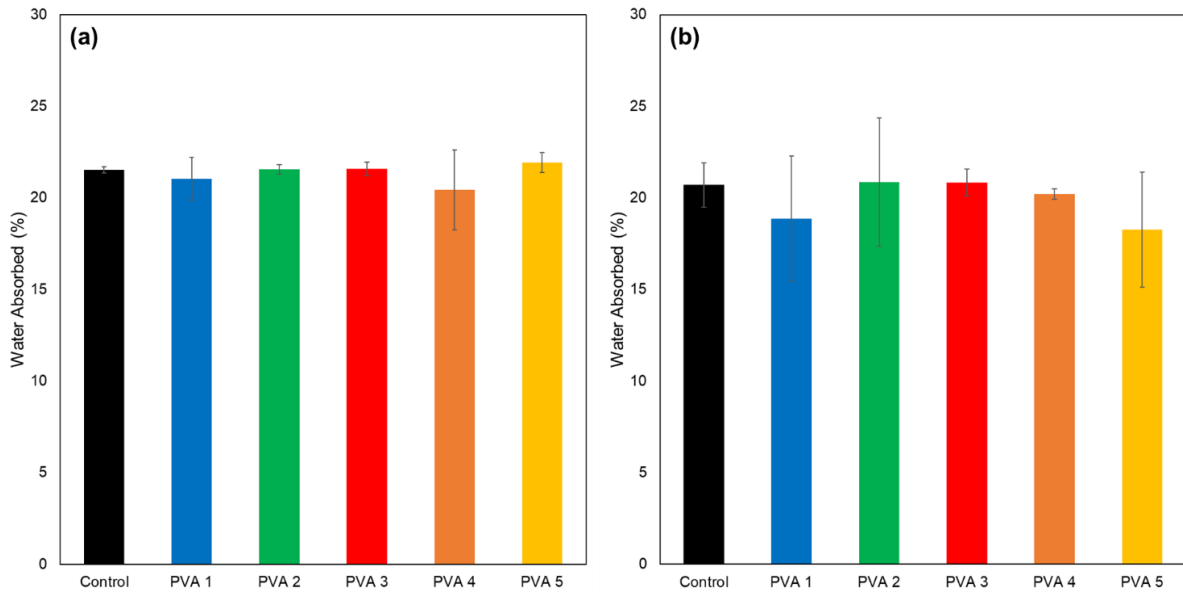
Figure 5.14. Water absorption for Control, PVA 1, PVA 2, PVA 3, PVA 4, and PVA 5 modified paste samples reported as percent mass gained compared to oven dry mass. (a) Water absorption for 16 mm x 32 mm cylindrical samples at 120 mins. (b) Water absorption for samples with masses between 0.15 mg and 0.45 mg at 120 mins. Error bars represent one standard deviation of 3 replicates.
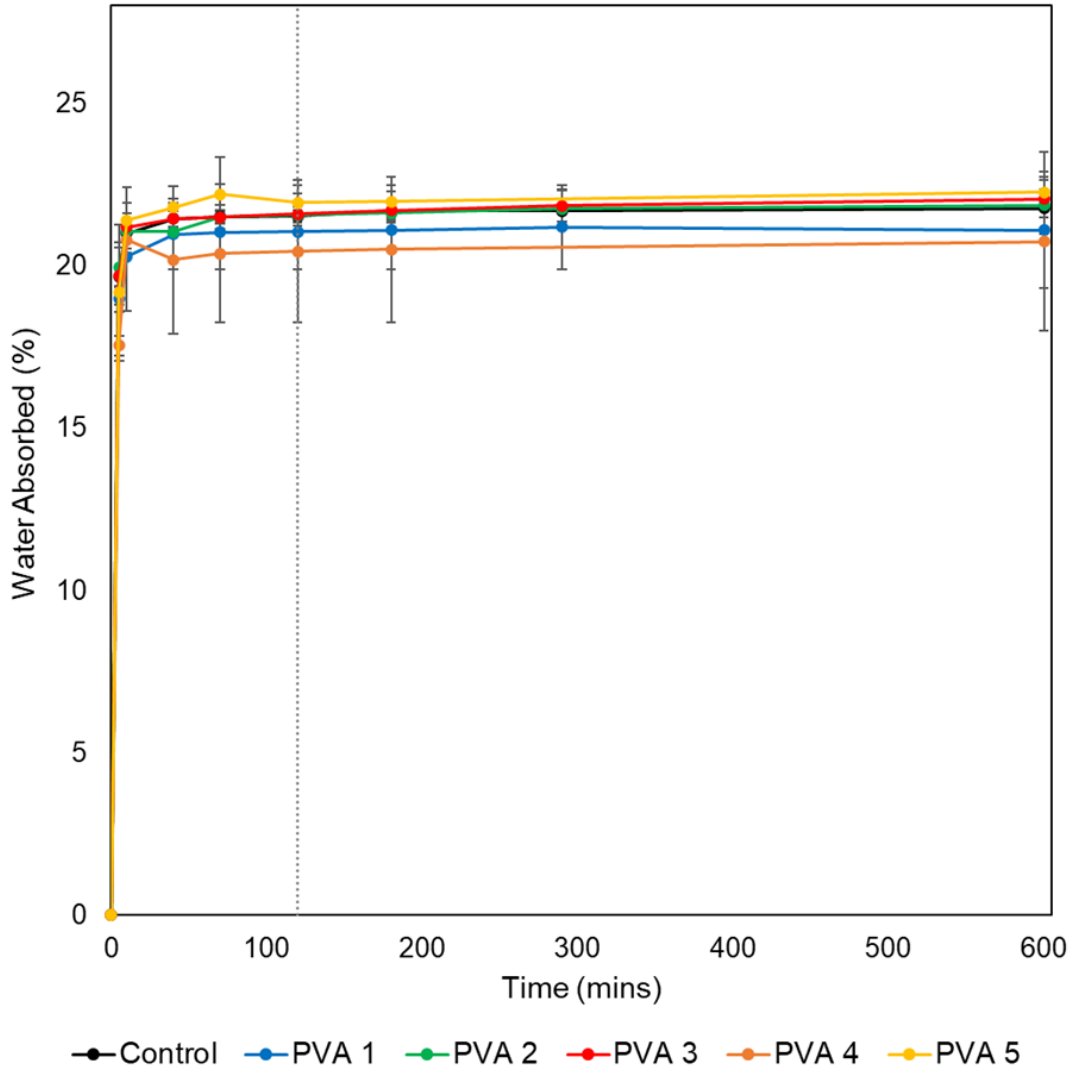
Figure 5.15. Water absorption curves for Control, PVA 1, PVA 2, PVA 3, PVA 4, and PVA 5 modified paste samples. All samples were 16 mm x 32 mm cylindrical samples. Error bars represent one standard deviation of 3 replicates. Vertical grey line indicates 120 mins.

5.3.7 Air Void Parameters

The hardened state air content was evaluated to determine how the molecular weight of PVA influenced air entrainment. **Table 5.3** summarizes the hardened state air contents and spacing factor of all samples. PVA 1, PVA 2, PVA 3, PVA 4, and PVA 5 at 0.021wt% of cement introduce <1.0% air content in the paste. The observed air contents are lower than the industry accepted air contents of ~16-25% air by volume of cement paste, or 4-10% by volume of

concrete, which are recommended for freeze-thaw resistance.[163] The spacing factors all exceed

the recommended 200 µm maximum.[168] Interestingly, all samples meet the recommended

minimum specific surface of 25 mm^{-1} except PVA 2 modified paste which was calculated at 24

mm^{-1}.[168] Higher values of specific surface indicate smaller air voids. However, the void

frequency is well below the 0.3/mm recommended value.[54]

Table 5.2. The air void parameters of Control, PVA 1, PVA 2, PVA 3, PVA 4, and PVA 5
modified paste samples. Results for oven dry density were calculated from three replicates. Air
void parameters were calculated using the linear traverse method of ASTM C457 applied to
MXCT 2D cross-sectional images.

Sample	Length Traversed (mm)	Number of Voids	Void Frequency (mm^{-1})	Hardened State Air Content (%)	Specific Surface (mm^2/mm^3)	Spacing Factor (µm)
Control	1311	52	0.040	0.25	62	445
PVA 1	1337	67	0.050	0.54	37	567
PVA 2	1405	50	0.036	0.59	24	835
PVA 3	1260	98	0.078	0.60	52	389
PVA 4	1034	108	0.10	0.59	71	285
PVA 5	1278	91	0.071	0.98	29	573

5.4 Discussion

This work, along with previous studies,[145,311] demonstrate that biomimetic antifreeze

polymers such as PVA can provide freeze-thaw resistance to cementitious materials due to their

interaction with ice. Taken together, these studies suggest the IRI activity of biomimetic

polymers can be exploited as an alternative, mechanistic approach to air entrainment. In **Chapter

4**, PEG-PVA, which is 75% PVA, was shown to be effective at providing freeze-thaw resistance

in cement paste while PVA having a molecular weight of 13,000-23,000 g/mol was not.[145] In a

separate study, PVA with a molecular weight of 146,000 g/mol was shown to provide scaling resistance in mortar.[311] In these previous works, PVA having a degree of hydrolysis $\geq$ 98% was used. Therefore, the only difference between the types of PVA was molecular weight.

Understanding the PVA molecular weights and degree of hydrolyses that are effective at providing freeze-thaw resistance is critical for the application of the polymer as a water solubilized additive for freeze-thaw resistance. Both molecular weight and degree of hydrolysis affect solubility, viscosity, adhesive strength, and IRI activity.[140,357] Generally, solubility is increased with a reduced degree of hydrolysis or reduced molecular weight. Viscosity increases with increased molecular weight and increased degree of hydrolysis. From the results herein and those in Frazier et al. and Qu et al.,[145,311] a molecular weight (Mw) of ~31,000 g/mol to ~146,000 g/mol is required to impart freeze-thaw resistance to cement paste. PVA having a molecular weight of 214,000 (*i.e.*, PVA 5) failed to provide freeze-thaw resistance to cement paste. PVA 5 might have failed to provide freeze-thaw resistance in the study because of a higher viscosity. PVA 5 has a reported viscosity ~4x greater than that of PVA 4. This increased viscosity could result in reduced distribution of the polymer throughout the cement matrix. Additionally, a degree of hydrolysis between 87% and 99% appears to be acceptable within the recommended range of molecular weights.

Based on a significant amount of previous literature,[132,140,224,252,345] it can be stated that PVA 2 (M_w = 31,000-50,000 g/mol), PVA 3 (M_w = 130,000 g/mol), PVA 4 (M_w = 75,200), and PVA 5 (M_w = 214,500 g/mol) used in this study and PVA with a molecular weight of 146,000 g/mol used by Qu *et al.* are highly IRI active while PVA 1 (M_w = 13,000-23,000 g/mol) is not highly IRI active. More specifically, PVA 1 is the only polymer that does not provide reported IRI activity exceeding 80% MLGS reduction at a concentration of 0.1 mg/mL.[140] As can be seen in

Figure 5.11 and **Figure 5.12**, PVA 2, PVA 3, and PVA 4 provided freeze-thaw resistance to the hardened cement paste samples while PVA 1 and PVA 5 provided no to limited freeze-thaw resistance.

Although PVA and a PVA-containing copolymer have been shown to provide freeze-thaw resistance in cementitious materials, no direct evidence of the polymer interacting with ice within cement paste, mortar, or concrete has been reported prior to this work. Previous work has only shown IRI activity and resulting freeze-thaw resistance. The DSC results shown in **Figure 5.13** provide direct evidence that PVA results in lower ice contents during freezing temperatures. While the overall amount of ice that formed in PVA-modified pastes was reduced (*i.e.*, ice content of peak 4), PVA-modified pastes did exhibit up to 258% higher ice contents in peak 2 alone, which corresponds to mesopores or 2 to 50 nm in diameter. This result indicates that a larger number of capillary pores, sizes 2–50 nm, likely exist in these samples compared to the control. Given that (1) the temperatures used in this study for freeze-thaw cycling (*i.e.*, -15 °C) was well above the -25 °C to -40 °C required to form ice within these pores and (2) we observed lower ice contents during melting, we conclude that freeze-thaw resistance is not a result of an increased number of capillary pores but rather due to the interaction of PVA with ice.

Relatedly, PVA 2, PVA 3, and PVA 4 modified paste exhibited nearly identical water absorption characteristics, indicating that the lower observed ice contents were not a result of lower water contents. PVA 2, PVA 3, and PVA 4 modified paste exhibited ~27-41% lower overall ice contents, **Figure 5.13**, but nearly identical water contents at 2 hours, **Figure 5.14** and **Figure 5.15** (*i.e.*, time at which DSC testing began after submersion in water). The 0.15 mg – 0.45 mg samples exhibited 1% higher water contents for PVA 2 and PVA 3 and 2.5% lower water content for PVA 4 compared to the control.

113

One drawback of using PVA in cement paste and concrete is the susceptibility of PVA to delay cement hydration and entrain air.[329,341,358,359] As shown in **Figure 5.7**, the acceleration stage of the hydration reactions is delayed by approximately 30 mins, which is relatively minor, regardless of PVA molecular weight when the degree of hydrolysis exceeds 98%. Similar results have been previously reported for a variety of molecular weights and explained by the interaction of PVA with cement particles and adsorption onto C_3S, nucleation sites of $Ca(OH)_2$ and CSH.[329,330,359] XRD diffractograms in **Figure 5.9** indicate that PVA with >98% degree of hydrolysis does have a propensity to interact with $Ca(OH)_2$. The peaks at $2\theta = 50.8$ and 54.4, which can be attributed to $Ca(OH)_2$, disappear with increasing molecular weight of PVA. The interaction of PVA with $Ca(OH)_2$ is believed to result from hydrogen bonding between hydroxyl groups.[329] This result is substantiated by the XRD diffractograms in **Figure 5.10** showing the negligible effect of PVA 4 and PVA 5, which have a lower degree of hydrolysis, on the peaks at $2\theta = 50.8$ and 54.4. Additionally, a negligible effect of PVA 4 and PVA 5 on the acceleration stage is observed as shown in **Figure 5.8**. The decreased degree of hydrolysis results in a reduced number of pendant hydroxyl groups that can interact with cement particles, adsorb onto C_3S, $Ca(OH)_2$, and C-S-H.

PVA and other water-soluble polymers are known to be surface-active and, therefore, can stabilize air voids within cement paste.[347,358,360] In fact, PVA has amphipathic characteristics as a result of hydrophilic hydroxyl groups and hydrophobic methylene groups. Therefore, it is no surprise that PVA has been reported on numerous occasions as an additive that entrains air, but typically this observation occurs at doses of 1% by weight of cement or greater.[347,358] In this study, the concentration or dosage of PVA used is considerably lower (0.021% by weight of cement). Thus, it was anticipated that the amount of air entrained would be relatively low, which

was confirmed *via* MXCT. As can be seen in **Table 5.3**, the hardened state air contents are all below 1%, considerably lower than standard recommendations of 4-10% in concrete. However, it is worth noting that the PVA modified samples had double the hardened state air content of the control. Additionally, the spacing factors were all above the recommended value of 0.2 mm and the void frequency below the recommended value of 0.3 mm^{-1}.[54,168] The specific surface areas were at or above the recommended value of 0.25 mm^{-1} though, indicating that the voids that are present are relatively small.[157]

Taken together, these results substantiate that IRI-active polymers, like PVA, can provide freeze-thaw resistance *via* a mechanism alternative to air entrainment. The use of IRI-active polymers provides a unique approach to provide freeze-thaw resistance to cementitious materials that could supplant AEAs. In cement paste, an air void network of proper size and with a small enough spacing factor is not required when biomimetic antifreeze polymers are utilized, which could result in a more effective strategy for freeze-thaw mitigation as the creation of a proper air void network under field conditions is difficult to produce. Additionally, there is a possibility that biomimetic antifreeze polymers work in conjunction with traditional air entrainment.

5.5 Conclusions

This work presents experimental evidence that the molecular weight of PVA is a critical parameter for the IRI-active polymer to provide freeze-thaw resistance to cement paste. Furthermore, the molecular weight should be sufficiently high such that the PVA is IRI active at concentrations below 0.1 mg/mL (*i.e.*, highly IRI active). Results from freeze-thaw testing indicate that a molecular weight of 31,000 g/mol to 130,000 g/mol is required to provide freeze-thaw resistance. DSC results indicate that cement paste modified with higher molecular weights,

PVA 2 (M_w=31,000-50,000 g/mol), PVA 3 (M_w=130,000 g/mol), and PVA 4 (M_w=75,200 g/mol) result in lower amounts of ice developing during freezing temperatures when water contents are nearly identical to control pastes. The air contents of all PVA modified samples were less than 1% and spacing factors were greater than 200 µm. In summary, these results suggest that PVA provides freeze-thaw resistance through its biomimetic antifreeze properties, mainly IRI activity, rather than its ability to form a stabilized air void system.

Chapter 6 Biomimetic Antifreeze Properties of Folic Acid and Application for Freeze-Thaw Resistance in Ordinary Portland Cement Paste

6.1 Introduction

A multitude of organisms produce ice binding proteins (IBPs), a broad classification of proteins that can provide freeze tolerance, freeze avoidance, ice recrystallization inhibition, ice adhesion, and ice nucleation.[116] Antifreeze proteins (AFPs) and antifreeze glycoproteins (AFGPs) are a subset of IBPs which allow species to survive freezing temperatures. AFPs and AFGPs inhibit the recrystallization of ice (*i.e.*, Ostwald ripening), induce dynamic ice shaping, and reduce the freezing point of ice below the equilibrium freezing point (*i.e.*, thermal hysteresis).[132] Ice recrystallization inhibition (IRI), dynamic ice shaping (DIS), and thermal hysteresis (TH) activity are macroscopic effects resulting from the microscopic interactions of AFPs and AFGPs with ice.

Fish AFPs are classified as Type I, Type II, Type III, and Type IV. Each type of fish AFP has characteristic features including size, amino acid bias, and structural features. Across all four types of fish AFP, the size varies drastically from ~ 3 kDa to 24 kDa.[229–231] The same can be said about structural features such as the α-helix structure of Type I AFPs *vs* the globular, β-strand containing structure of Type III AFPs.

A variety of molecules have been shown to mimic the IRI activity of AFPs and AFGPs including synthetic peptides,[144,226,273,274] self-assembling molecules,[142,283–285] polymers,[224,256–258], nanomaterials,[141,255,281] and small molecules.[143,286,292,293] The diverse structure and chemical functionalities resulting in IRI activity parallels the observed diversity in AFPs and AFGPs

which they mimic. The IRI activity is generally attributed to (1) chemical moieties that mimic those of AFPs and AFGPs that are believed to bind with ice (*e.g.*, threonine and hydroxyl groups), (2) spacing of chemical moieties that match the lattice spacing of 1h ice crystal structure, and (3) amphiphilic nature.

Type IV AFPs are unique in that they have particularly high contents of glutamate and glutamine.[86,230,361] Glutamate is the ionic form of glutamic acid. As shown in **Figure 6.1**, folic acid contains a glutamic acid group. Folic acid is a vitamin which in solution self-assembles into disk-like tetramers induced by hydrogen bonding between hoogsteen-type bases,[362,363] **Figure 6.2a**. Furthermore, the tetramers have been shown to stack and form a columnar rod-shaped mesophase,[362,364] **Figure 6.2b**. Once an appropriate concentration is reached, the formation of a hexagonal mesophase composed of the columnar structures forms, **Figure 6.2c**.[363,364]

Intermolecular spacing between glutamic acid groups of the disk-like tetramer has been proposed to be 7.28 Å.[365] The diameter of the rod-like structures has previously been reported to be 14.5 – 15.5 Å and spacing between tetramers to be 3.3 – 4.0 Å.[363–365] These distances are particularly interesting when considering the lattice spacing of 1h ice. The intermolecular spacing of the glutamic acid groups, 7.28 Å, is close to the 7.36 Å primary prism plane spacing of 1h ice.[75,77] Additionally, the diameter of the rod-like structures, 14.5 – 15.5 Å, closes matches the 2x the primary prism plane spacing, 14.72 Å. Lastly, 4x spacing between tetramers, 13.2 – 16.0 Å, closes matches the 2x the primary prism plane spacing.
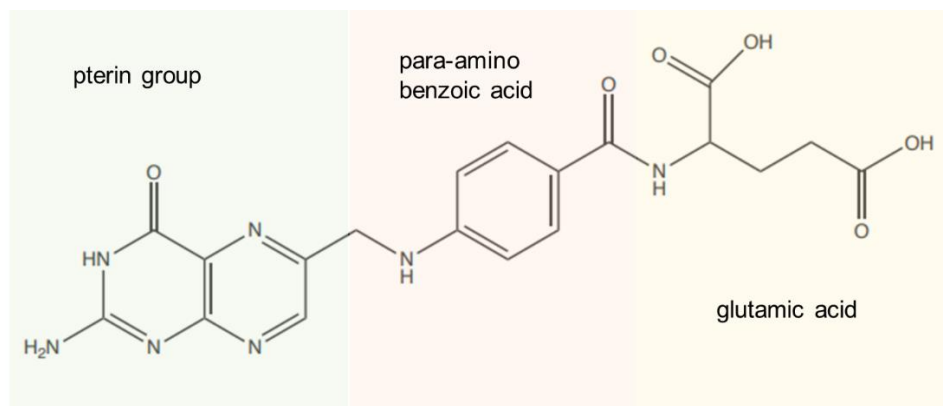
Figure 6.1. Chemical structure of folic acid. (●) pterin group. (●) para-amino benzoic acid. (●) glutamic acid.
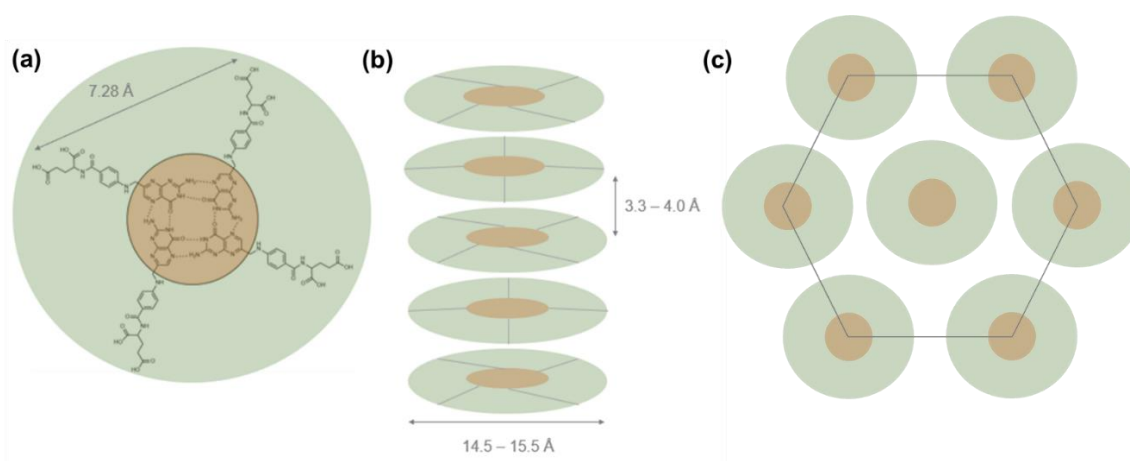
Figure 6.2. Self-assembly of folic acid. (a) formation of tetramers via hydrogen bonding between hoogsten-type bases highlighted orange. Intermolecular spacing between glutamic acid groups of the disk-like tetramer has been proposed to be 7.28 Å.[365] (b) stacking of tetramers into columnar mesophase. Diameter of columnar structures previously reported to be 14.5 – 15.5 Å and spacing between tetramers to be 3.3 – 4.0 Å.[363–365] (c) top view of hexagonal mesophase composed of columnar structures.

Based on the similar chemical moieties to Type IV AFPs (*i.e.*, glutamic acid), spacing of intra- and intermolecular spacing within self-assembled structures, and known amphiphilic characteristics at higher pHs[362], folic acid was hypothesized to display biomimetic antifreeze properties. The IRI, TH, and DIS activities of folic acid have not been previously reported. The objectives of this work were (1) to determine if folic acid displays IRI, TH, and DIS activity, (2) to determine the extent that folic acid self-assembles at concentrations less than 1 mg/mL (0.1

wt%), and (3) to determine if folic acid can provide freeze-thaw resistance to hardened cement paste.

6.2 Experimental Procedure

6.2.1 Materials

Folic acid (CAS # 59-30-3) was purchased from Sigma-Aldrich (St. Louis, MO, USA) and used without modification. A 1x phosphate buffered saline (PBS) solution was purchased from Fisher Scientific. The cement used in this study was Type I/II OPC (Quickrete®) that complies with ASTM C150.[350] The chemical composition of the OPC is reported in **Appendix A**.

6.2.2 Antifreeze Properties

6.2.2.1 Ice Recrystallization Inhibition

A modified IRI assay was performed to observe IRI activity.[321] 10 µL of sample was dropped from 1.7 m onto a glass slide (thickness of 1 mm). The glass slide was pre-cooled on an aluminum block at −78°C. The slide was then immediately transferred to an Otago nanoliter osmometer cold stage and annealed at −4°C (air temperature) for 30 min. Images were collected immediately after the sample was placed on the cold stage and again at 30 min to observe ice recrystallization. For all samples, images were obtained using an Olympus BX41 microscope with ELWD U Plan 20×/0.45 objective and crossed polarizers, equipped with an OMAX A35140U camera on a 0.5× C-mount adaptor. ImageJ 1.48v software (National Institutes of Health) was used to measure the grain sizes.

The IRI activity of folic acid was tested at concentrations of 0.01 mg/mL, 0.05 mg/mL, and 0.5 mg/mL in DI, PBS, 0.41 mM NaCl, and 4.1 mM NaCl. Additionally, IRI activity was tested

in 0.86 mg/mL Ca(OH)$_2$ PBS solution. The concentration of 0.5 mg/mL folic acid was chosen to match the research in **Chapters 4 and 5**.

6.2.2.2 Thermal Hysteresis and Dynamic Ice Shaping

TH results from the non-colligative reduction in the freezing temperature of a solution while the melting temperature is maintained or elevated, thus a hysteresis gap is developed between the two temperatures. DIS occurs when a material interacts with one or more crystallographic planes of ice resulting in a change to the morphology of a single ice crystal and occurs in tandem with TH. To observe TH and DIS, a nanoliter-sized drop of sample was placed in microscopy immersion oil (Sigma-Aldrich) where both are in a hole of ~0.5 mm diameter within an aluminum disk. The aluminum disk was placed on an Otago nanoliter osmometer cold stage, where the temperature of the cold stage was rapidly cooled to -20°C to form polycrystalline ice. Next, the sample was slowly melted to form a single ice crystal by heating at a rate of approximately 5°C/min. Once a single ice crystal was obtained, the temperature was kept constant for 3 min to ensure stability. Last, the sample was cooled at 0.01°C/min until crystal growth and/or ice shaping was observed. Samples were tested in DI water at a concentration of 0.05 mg/mL, 0.5 mg/mL, and 5 mg/mL. Additionally, the samples were tested in a 0.75 M NaOH at concentrations of 5 mg/mL and 10 mg/mL.

6.2.3 X-Ray Diffraction Studies

X-ray diffraction (XRD) patterns were performed on liquid solutions (capillary tubes) of folic acid. The system included a 30W Genix 3D x-ray generator with a Cu anode ($\lambda = 1.54$ Å) x-ray source and Dectris Eiger R 1M detector. The diffraction patterns were recorded between 4−30°

2θ using an increment of 0.02° 2θ. Folic acid was tested in both DI and a 0.75 M NaOH solution, pH = 13.5, at concentrations of 5.0 mg/mL, 0.5 mg/mL, and 0.05 mg/mL. The NaOH solution was used to determine the effect of a highly alkaline environment on the ability of folic acid to self-assemble into disk-like tetramers and columnar rod-like structures.

6.2.4 Cement Paste Sample Preparation

Cement paste samples were made with a water to cement ratio (w/c) of 0.42. Folic acid was added to the mixing water and stirred until dissolved. After a 3 min hand mix, cement paste samples were cast into cylindrical polyethylene molds 32 mm in height and 16 mm in diameter and cured for 14 days in a 99% relative humidity chamber according to ASTM C192 at 20°C ±2°C.[323] **Table 6.1** provides the cement paste sample compositions. The amount of folic acid chosen in the mix design was based on IRI results.[145]

Table 6.1. Cement Paste Mix Design

Sample	Cement (g)	w/c ratio	Folic acid concentration in mixing water (mg/mL)	Folic acid (wt.% of cement)
Control	100	0.42	-	-
FA-L	100	0.42	0.05	0.0021%
FA-M	100	0.42	0.5	0.021%
FA-H	100	0.42	1.0	0.042%

6.2.5 Isothermal Conduction Calorimetry

Isothermal conduction calorimetry (ICC) was performed to understand the impact of folic acid on both the heat of hydration and time of set. A TAM Air 8-Channel Isothermal Calorimeter (TA instruments) was set at 21°C and allowed to equilibrate for 24 hours. All samples were mixed for 3 minutes in glass ICC vials, with w/c=0.42, and immediately placed in the

calorimeter and allowed to equilibrate for 1 hour before the calorimeter signal was considered stable. Folic acid was tested at 0.00042%, 0.0021%, and 0.021% by weight of cement (*i.e.*, 0.01, 0.05, and 0.5 mg/mL in mixing water concentrations). Data was measured for 60 hours. The peak thermal power at 50% was used to approximate the time of set.[326]

6.2.6 Rapid Freeze-Thaw Testing

Freeze-thaw cycling of control, FA-L, FA-M, and FA-H paste samples was performed in a custom-built chamber. Details of the chamber may be found in **Appendix B**. All samples were tested in triplicate and exposed to a total of 30 cycles in which the freezing lasted for 1.5 h and thawing for 2.5 h, respectively. During freezing cycles, the temperature reached -15°C ± 2°C and thawing cycles 16.5°C ± 2°C. A water level that kept ~1/3 of the samples submerged was maintained in the sealed sample chamber to ensure the samples remained saturated.

Freeze-thaw damage was assessed by visual inspection for spalling of bulk samples and by scanning with micro X-ray computed tomography (MXCT) to observe internal microcracking. The MXCT (ZEISS Xradia 520 Versa) source voltage was set to 140 kV and the power to 10 W. An objective with an optical magnification of 0.4× was used. The source and detector locations were varied to obtain the desired resolution (voxel size) of approximately 5 µm. Dragonfly 2021.1 software (Object Research Systems) was used to generate reconstructions from MXCT scans that were analyzed for microcracking.

6.2.7 Hardened State Air Content

MXCT enabled 3D visualization of internal air void systems. The same MXCT parameters outlined in Section 6.2.6 were used and samples were scanned before freeze-thaw cycling.

Dragonfly 2021.1 software (Object Research Systems) was used to generate 3D reconstructions, to calculate the scanned volume of sample, and volume of all voids. The volume of air voids was determined from all voids with diameters greater than 14.8 μm. This diameter was chosen based on the accepted size range of air voids,[19] previous research,[327] and resolution capabilities of MXCT.

The MXCT data were first segmented within Dragonfly 2021.1 to identify voxels that are associated with air voids (*i.e.*, region of interest, ROI). Following segmentation, a multi-ROI analysis was performed. The multi-ROI analysis groups the labeled voxels and calculates a variety of properties including volume. The resulting volumes are exported and used to generate a histogram of air void sizes (diameters).

6.3 Results and Discussions

6.3.1 Antifreeze Properties

6.3.1.1 Ice Recrystallization Inhibition

Representative IRI assay micrographs of folic acid in DI, PBS, 0.41 mM NaCl, and 4.1 mM NaCl solutions at 0.01 mg/mL, 0.05 mg/ml, and 0.5 mg/mL can be found in **Figures 6.3-6.7**. **Figure 6.8** summarizes the IRI activity of folic acid in each solution, reported as the percent mean largest grain size (MLGS) of the corresponding control solution. As can be seen in all solutions, folic acid is moderately IRI active (MLGS <70%) at concentrations of 0.05 mg/mL and 0.5 mg/mL. The IRI activity in DI was screened to confirm that the compound has activity without the presence of Na^+. The mean largest grain size (n=10) was reduced by 29%, 44%, and 56% for 0.01 mg/mL, 0.05 mg/mL, and 0.5 mg/mL folic acid respectively when compared to DI water.

The NaCl solutions were chosen to determine the effect of Na$^+$ on the IRI activity of folic acid. Previous work has shown that Na$^+$ and K$^+$ can induce chirality in the self-assembled columnar structures.[364,366] Visually, this can be seen when the solutions display pearlescent coloring. None of the folic acid solutions tested for IRI display pearlescent coloring, but the 5 mg/mL and 10 mg/mL concentrations used for DIS testing did. The self-assembled structures appear to only result in multiple phases when the concentration of folic acid is greater than 1 mg/mL.[366] Representative splat assay micrographs of folic acid in 0.41 mM and 4.1 mM NaCl are provided in **Figures 6.5 and 6.6**. As can be seen in **Figure 6.8**, the IRI activity of folic acid in 0.41 mM and 4.1 mM NaCl is essentially the same at 0.05 mg/mL and 0.5 mg/mL. However, the IRI activity of 0.01 mg/mL folic acid in 4.1 mM NaCl is drastically higher than in 0.41 mM NaCl, 69% and 93% MLGS respectively.

Representative splat micrographs of folic acid in 0.86 mg/mL Ca(OH)$_2$ PBS solution are shown in **Figure 6.7**. No IRI activity was observed at a concentration of 0.5 mg/mL folic acid, therefore a higher concentration, 1.0 mg/mL, was tested. Negligible IRI activity was observed at 1.0 mg/mL folic acid in the Ca^{2+} containing solution. The Ca(OH)$_2$ solution was used to determine how Ca^{2+} would affect IRI activity. It is clear Ca(OH)$_2$ disrupted the ability of folic acid to inhibit ice recrystallization.
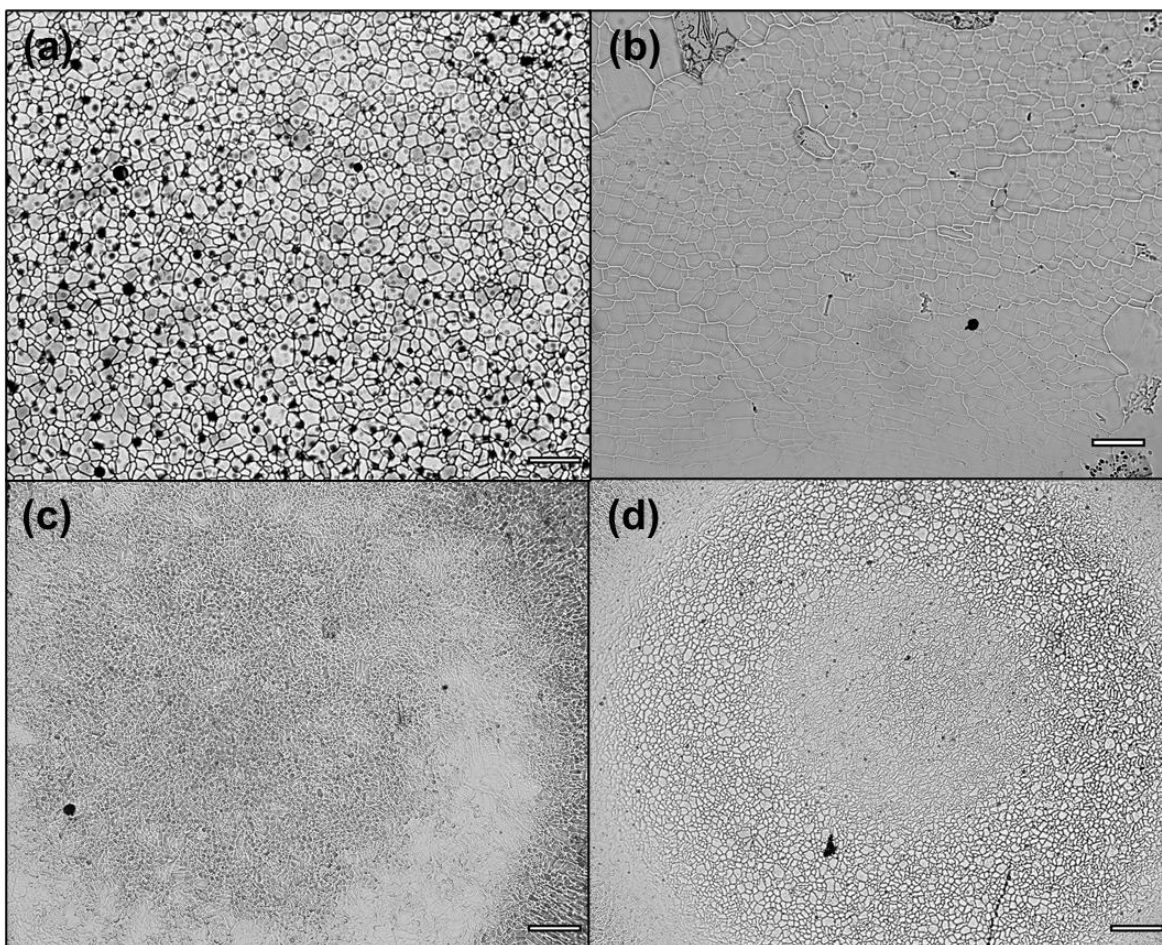
Figure 6.3. Representative micrographs of folic acid solutions in DI. (a) DI control, (b) 0.01 mg/mL folic acid, (c) 0.05 mg/mL folic acid, and (d) 0.5 mg/mL folic acid in DI after 30 min of annealing at -4°C. Scale bars are 100 µm.
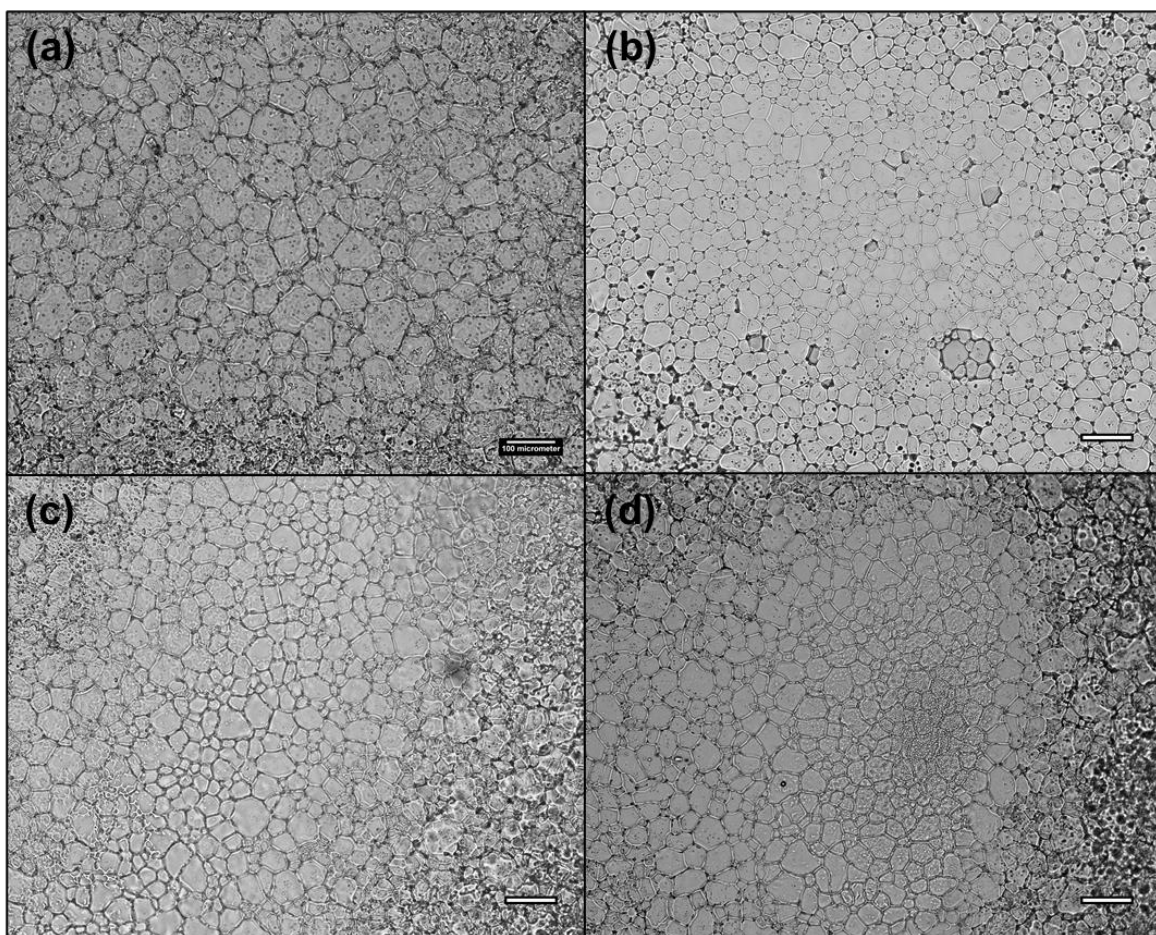
Figure 6.4. Representative micrographs of folic acid solutions in PBS. (a) PBS control solution and (b) 0.01 mg/mL folic acid, (c) 0.05 mg/mL folic acid, and (d) 0.5 mg/mL folic acid in PBS after 30 min of annealing at -4°C. Scale bars are 100 µm.
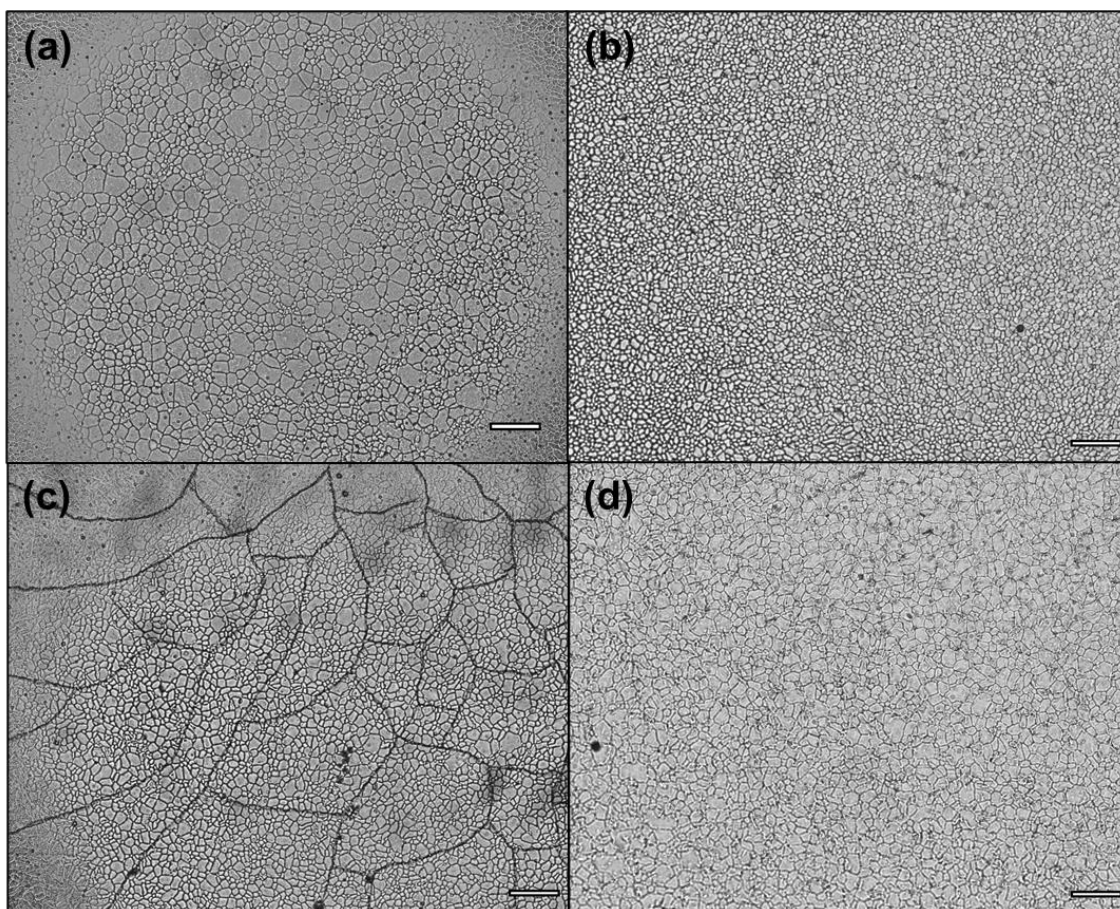
Figure 6.5. Representative micrographs of folic acid solutions in 0.41 mM NaCl. (a) 0.41 mM NaCl control solution and (b) 0.01 mg/mL folic acid, (c) 0.05 mg/mL folic acid, and (d) 0.5 mg/mL folic acid in 0.41 mM NaCl after 30 min of annealing at -4°C. Scale bars are 100 µm.
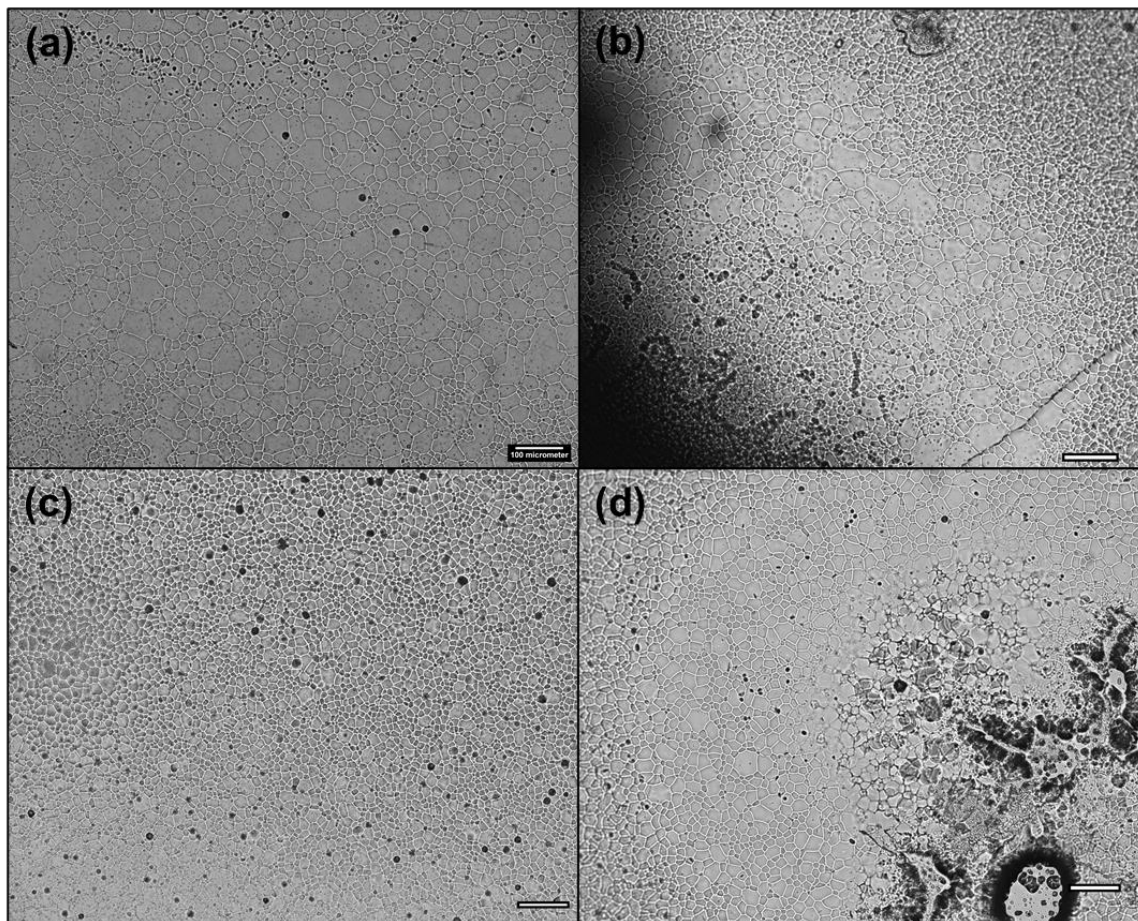
Figure 6.6. Representative micrographs of folic acid solutions in 4.1 mM NaCl. (a) 4.1 mM NaCl control solution and (b) 0.01 mg/mL folic acid, (c) 0.05 mg/mL folic acid, and (d) 0.5 mg/mL folic acid in 4.1 mM NaCl after 30 min of annealing at -4°C. Scale bars are 100 µm.
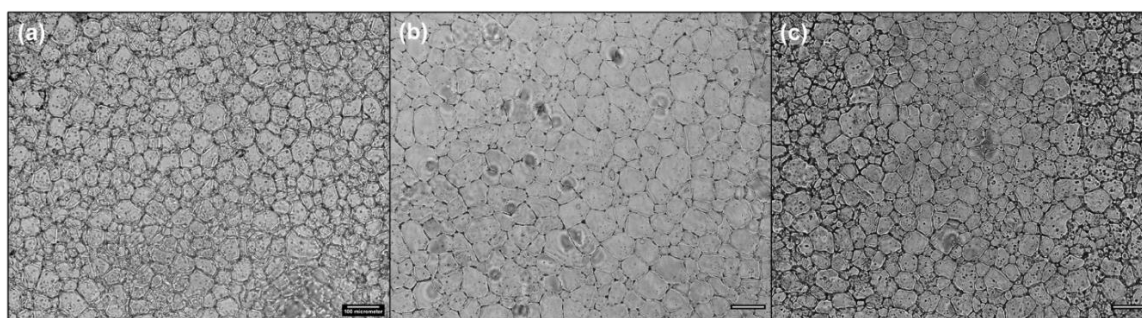
Figure 6.7. Representative micrographs of folic acid in 0.86 mg/mL Ca(OH)2 PBS solution. (a) 0.86 mg/mL Ca(OH)2 PBS solution and (b) 0.5 mg/mL folic acid, and (c) 1.0 mg/mL folic acid in 0.86 mg/mL Ca(OH)2 PBS after 30 min of annealing at -4°C. Scale bars are 100 µm.
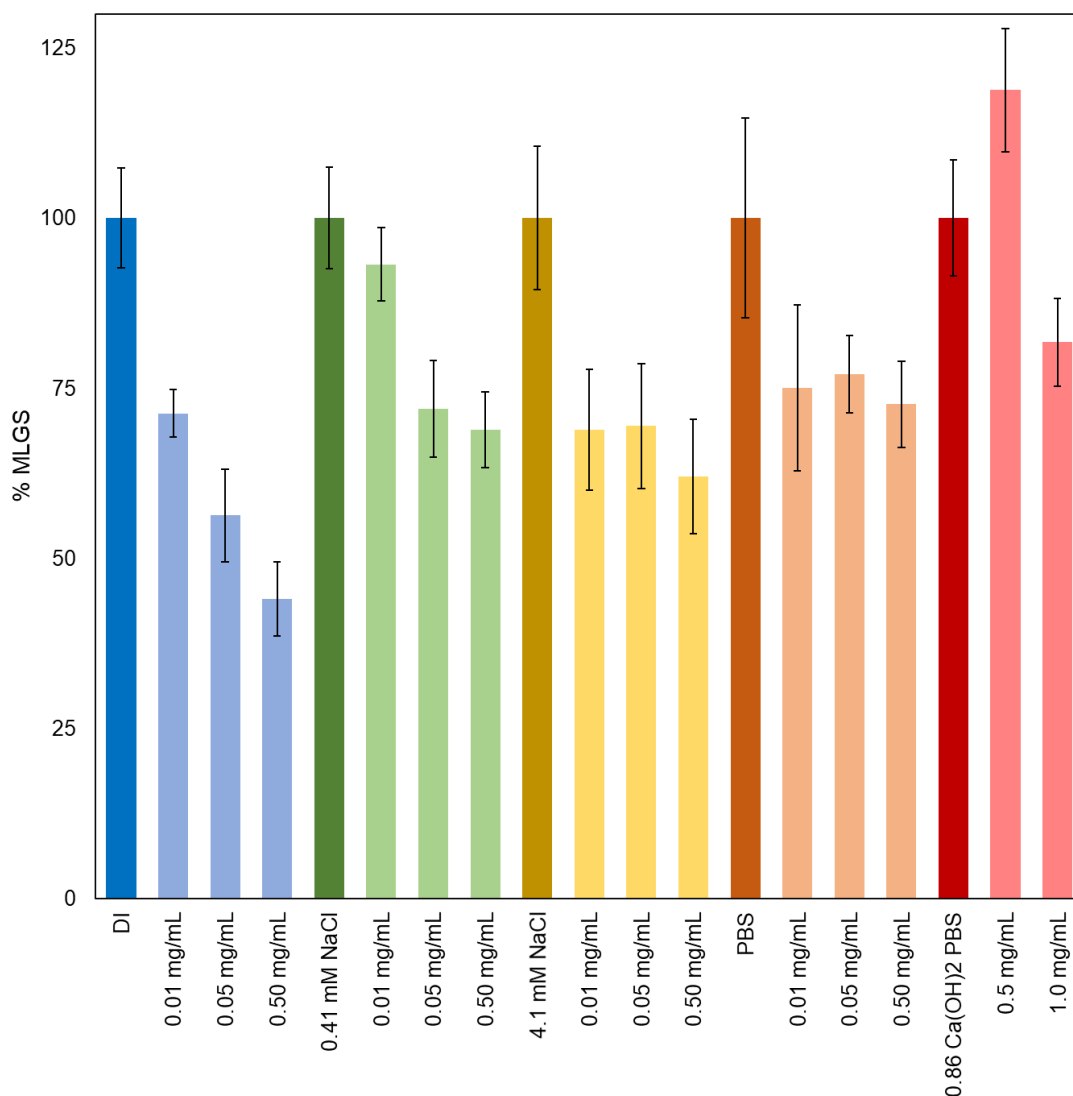
Figure 6.8. Ice recrystallization inhibition (IRI) activity results for folic acid. Results are reported as percent mean largest grain size (% MLGS) compared to solvent. Error bars represent one standard deviation. Solvents are deionized water (——), 0.41 mM NaCl (——), 4.1 mM NaCl (——), PBS (——), and 0.86 mg/mL Ca(OH)2 PBS (——).

The IRI activity of folic acid in PBS and NaCl solutions is promising as it parallels previously reported IRI active small molecules but at lower concentrations. For example, sugar molecules[290,292,293], surfactants,[290,294] and synthetic carbohydrate-based molecules[143,295] have been reported with MLGS of 50-72% compared to PBS and NaCl solutions but almost all at concentrations exceeding 1 mg/mL.

6.3.1.2 Thermal Hysteresis and Dynamic Ice Shaping

Folic acid did not display TH or DIS activity at any concentrations tested. **Figure 6.9** shows DIS micrographs of each folic acid concentration tested in DI. The DI control, 0.5 mg/mL folic acid, 5.0 mg/mL folic acid, and 10 mg/mL folic acid solutions displayed cylindrical shaping indicating no DIS activity. **Figure 6.10** shows the DIS micrographs of 5 mg/mL and 10 mg/mL folic acid in 0.75 M NaOH solution. Similar to folic acid in DI, folic acid in 0.75 M NaOH displayed no DIS activity. It is common for moderately IRI active materials (as opposed to highly active) not to display TH and DIS activity. Furthermore, the lack of TH and DIS activity would suggest that folic acid does not bind to ice to inhibit ice recrystallization like other small molecules.

Figure 6.11 provides an image showing folic acid fiber-like structures that formed at concentrations of 5 mg/mL and 10 mg/mL in 0.75 M NaOH. The fiber-like structures occurred during melting of the bulk ice but before a single ice crystal was obtained. The fiber structures have diameters that are approximately 4 to 5 µm which closely matches the folic acid based fiber diameters reported by Motkar *et al.*[366]
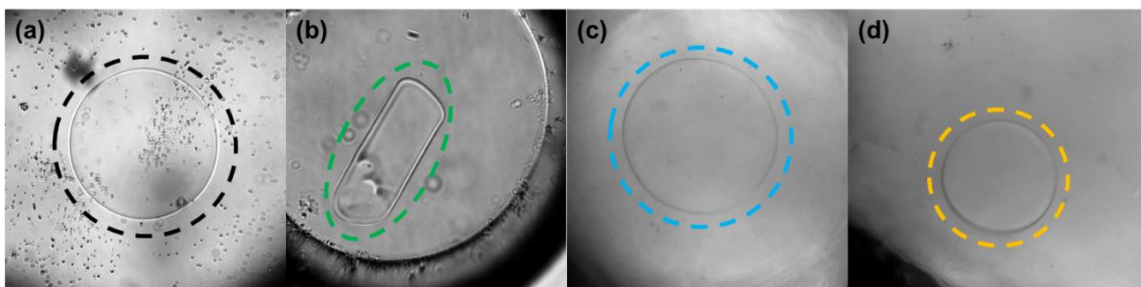
Figure 6.9. Dynamic ice shaping images. (a) DI control solution, (b) 0.5 mg/mL folic acid, (c) 5 mg/mL folic acid, and (d) 10 mg/mL folic acid in DI. Note that in (a), (c), and (d) the c-axis of the ice crystal is perpendicular to the plane of the image and in (b) it is in the plane of the image.
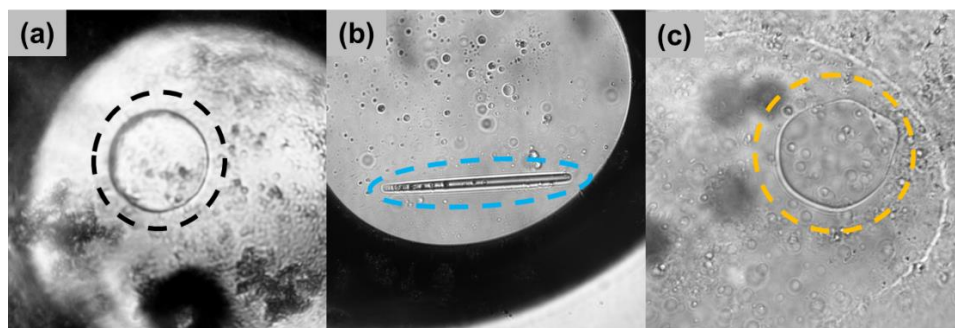
Figure 6.10. Dynamic ice shaping images of(a) 0.75 M NaOH solution, (b) 5 mg/mL folic acid, and (c) 10 mg/mL folic in 0.75 M NaOH. Note that in (a) and (c) the c-axis of the ice crystal is perpendicular to the plane of the image and in (b) it is in the plane of the image.
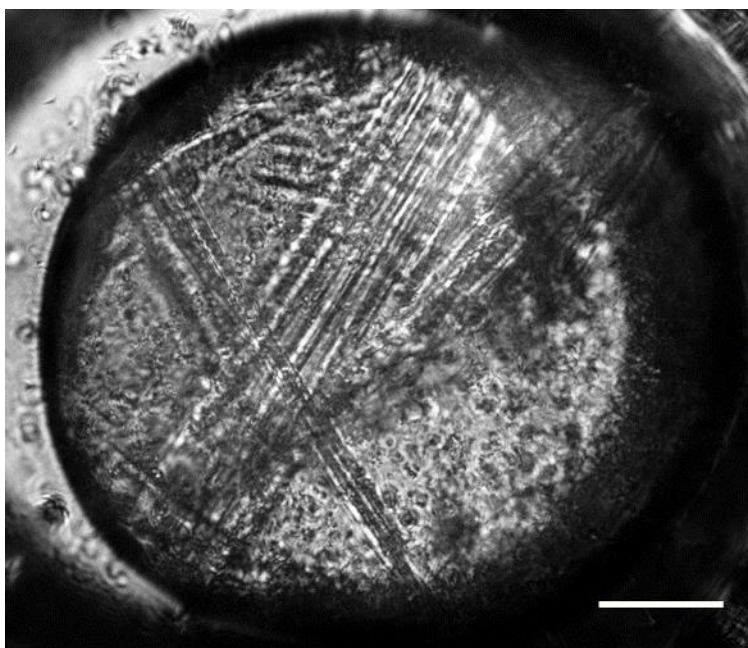
Figure 6.11. Micrograph of 5 mg/mL folic acid in 0.75 M NaOH. Interestingly, rod-like structures formed during TH and DIS testing. The rod-like structures have a diameter of ~ 4 to 5 µm. Scale bar is 50 µm.

6.3.2 X-Ray Diffraction

Figures 6.12 and 6.13 show XRD diffractograms of 0.05 mg/mL folic acid, 0.5 mg/mL folic acid, and 5 mg/mL folic acid in DI and 0.75 M NaOH. The peak centered at 15.6-16.0 Å is the most prominent and matches previously published values for the diameter of the folic acid

tetramers, 14.5-15.5 Å.[363–365] In both DI and 0.75 M NaOH, the diffractograms corresponding to 5 mg/mL concentrations do not display other distinguishable peaks. At 8.2-8.5 Å another peak is present for 0.05 mg/mL folic acid and 0.5 mg/mL folic acid in both DI and 0.75 M NaOH. In previous XRD studies of folic acid, peaks between 8-11 Å have been observed and attributed to the internal structure of folic acid assemblies[366] and the repeat distance between tetramer stacks.[365] Only 0.05 mg/mL folic acid in 0.75 M NaOH displays a peak at 4.2 Å, which agrees well with previously reported values for the distance between stacked tetramers.[363–365] The presences of peaks located at 15.6-16.0 Å and 8.2-8.5 Å indicate some level of folic acid tetramer self-assembly which is an interesting result as the self-assembly of folic acid has previously been studied at concentrations exceeding 1 mg/mL.[363–365]
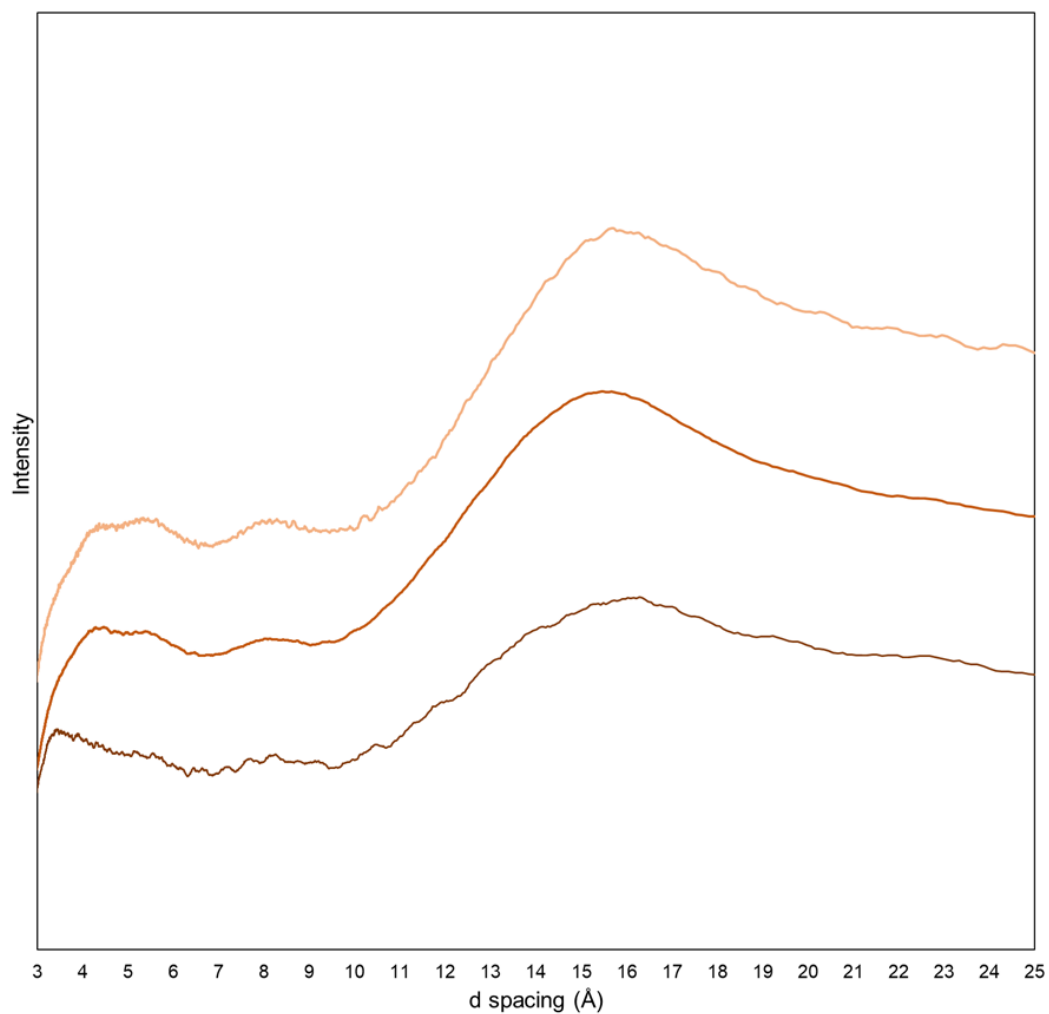
Figure 6.12. XRD diffractograms of folic acid solutions in DI. 5 mg/mL folic acid (——), 0.5 mg/mL folic acid (——), and 0.05 mg/mL folic acid (——) in DI.
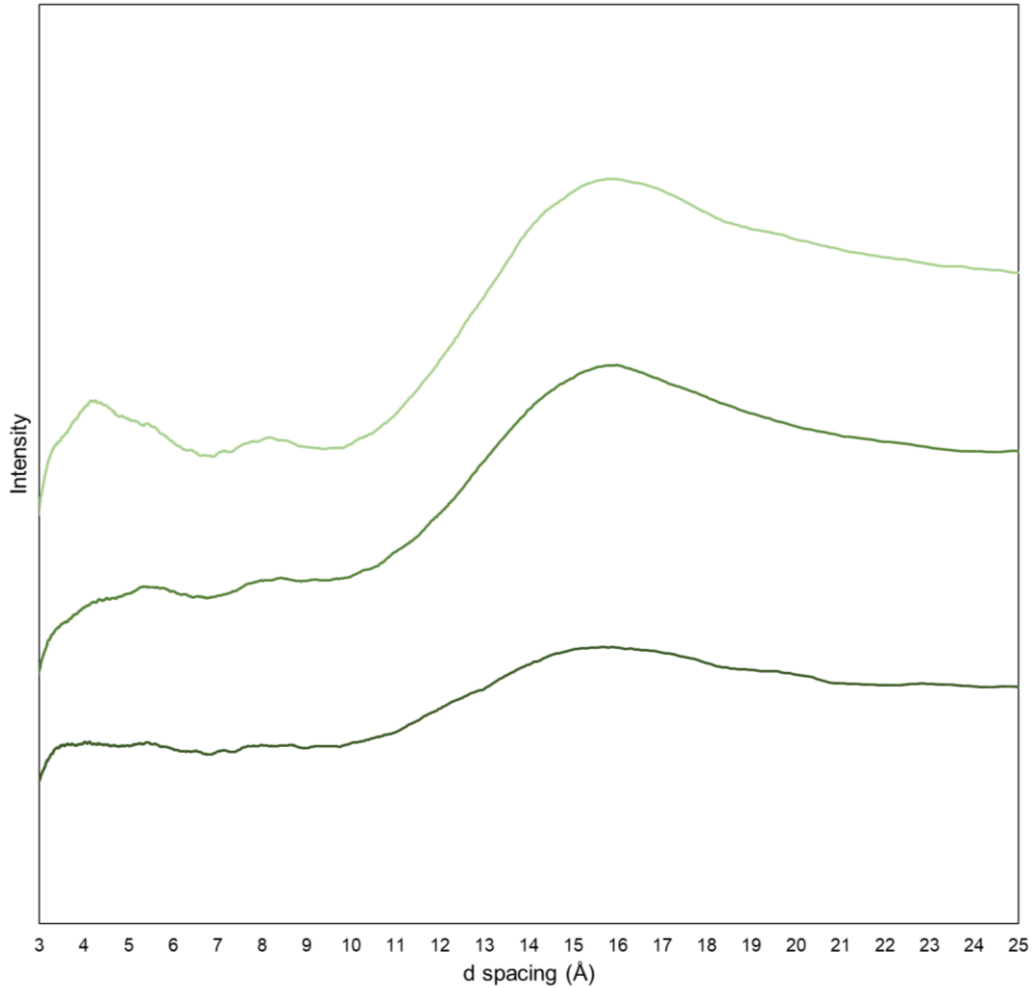
Figure 6.13. XRD diffractograms of folic acid solutions in 0.75 M NaOH solution (pH ~ 13.8). 5 mg/mL folic acid (━), 0.5 mg/mL folic acid (━), and 0.05 mg/mL folic acid (━) in 0.75 M NaOH solution.

6.3.3 Folic Acid as a Cement Additive

6.3.3.1 Isothermal Conduction Calorimetry

ICC results for folic acid modified pastes are shown in **Figures 6.14**. As can be seen in the normalized heat flow plot, the addition of folic acid at 0.01 mg/mL, 0.05 mg/mL, and 0.5 mg/mL resulted in a decrease of 6.9%, 4.8%, and 9.4% levels of peak thermal power compared to the control respectively. The approximate time of set was delayed by 48 mins, 33 mins, and 35 mins

for the 0.01 mg/mL, 0.05 mg/mL, and 0.5 mg/mL folic acid modified paste. The start of the acceleration period was delayed by 23 mins, 20 mins, and 22 mins for the 0.01 mg/mL, 0.05 mg/mL, and 0.5 mg/mL folic acid modified paste respectively.

Organic compounds containing carboxylic acid, such as polycarboxylic acid superplasticizers, are known to be retarding agents.[367,368] Citric acid is a small molecule that has carboxylic acid functional groups like that of the glutamic acid group of folic acid. Citric acid[369–371] and citrate[372] (deprotonated citric acid) have been previously studied as an additive to OPC paste, including its effect on cement hydration. Citric acid retards hydration at concentrations of 0.1-0.6% by wt. of cement similarly to the observations of folic acid herein. The retardation of hydration in the presence of citric acid was proposed to result from adsorption onto cement clinker grains which would retard dissolution.[369]
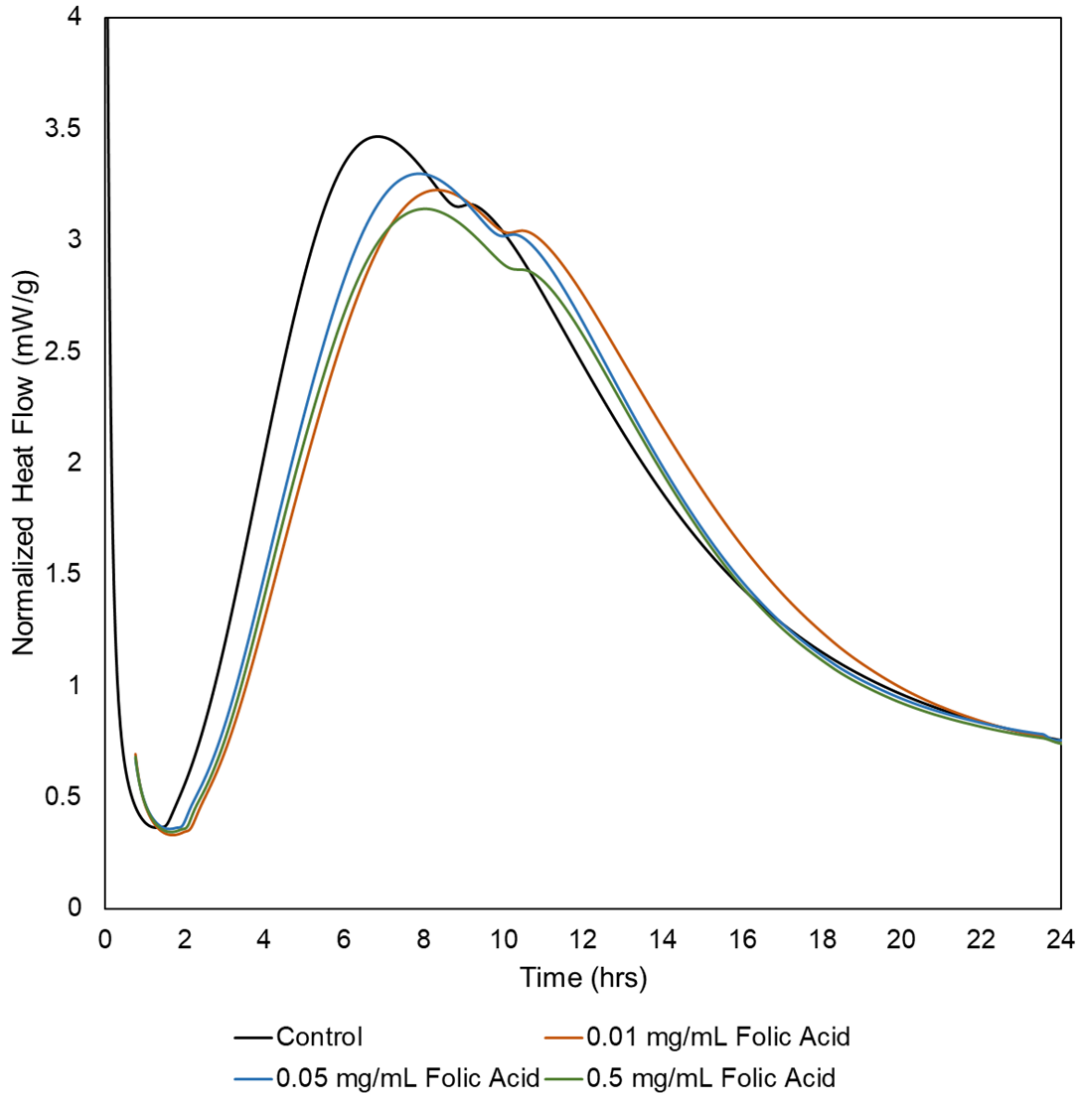
Figure 6.14. Isothermal conduction calorimetry normalized heat flow plots for control (—), 0.01 mg/mL folic acid (—), 0.05 mg/mL folic acid (—), 0.5 mg/mL folic acid (—).

6.3.3.2 Rapid Freeze-Thaw Cycling

Folic acid was tested as a water-soluble additive for freeze-thaw resistance in cement paste.

Figure 6.15 provides images of the control, FA-L (0.05 mg/mL folic acid), FA-M (0.5 mg/mL folic acid), and FA-H (1.0 mg/mL folic acid) modified pastes samples post 30 freeze-thaw cycles. The red arrows in **Figure 6.15** indicate spalling and scaling damage (*i.e.*, surface damage) in the control paste (2/2 replicates display damage), FA-M modified paste (2/2

137

replicates display damage), and FA-H modified paste (1/2 replicates display damage). The spalling and scaling are minimal in the FA-M replicates and occurs near the top of the sample. Thus, the spalling and scaling could be a result of poor settling and/or bleeding. The FA-L modified paste showed no surface damage.

Given the lack of surface damage, the FA-L modified paste was scanned with MXCT for the presence of internal microcracking. Representative 2D MXCT cross-sections of the control and FA-L modified paste samples can be found in **Figure 6.16**. The FA-L modified paste does display internal microcracking as indicated by the red arrows.

The presence of internal damage with no surface damage makes the FA-L modified pastes samples unique when compared to polyethylene glycol (PEG) and polyvinyl alcohol (PVA) modified pastes from **Chapter 4** that did not display freeze-thaw resistance. All the PEG and PVA modified pastes that displayed internal microcracking had apparent spalling and scaling. Previous studies of silica fume modified concrete have reported increased internal cracking with enhanced scaling resistance.[373] The propensity for resistance to surface damage *vs* internal freeze-thaw damage is likely a result of different mechanisms for the two types of damage.[374,375] Given the observations of surface damage resistance, further testing of folic acid as an additive for scaling resistance is recommended.

138
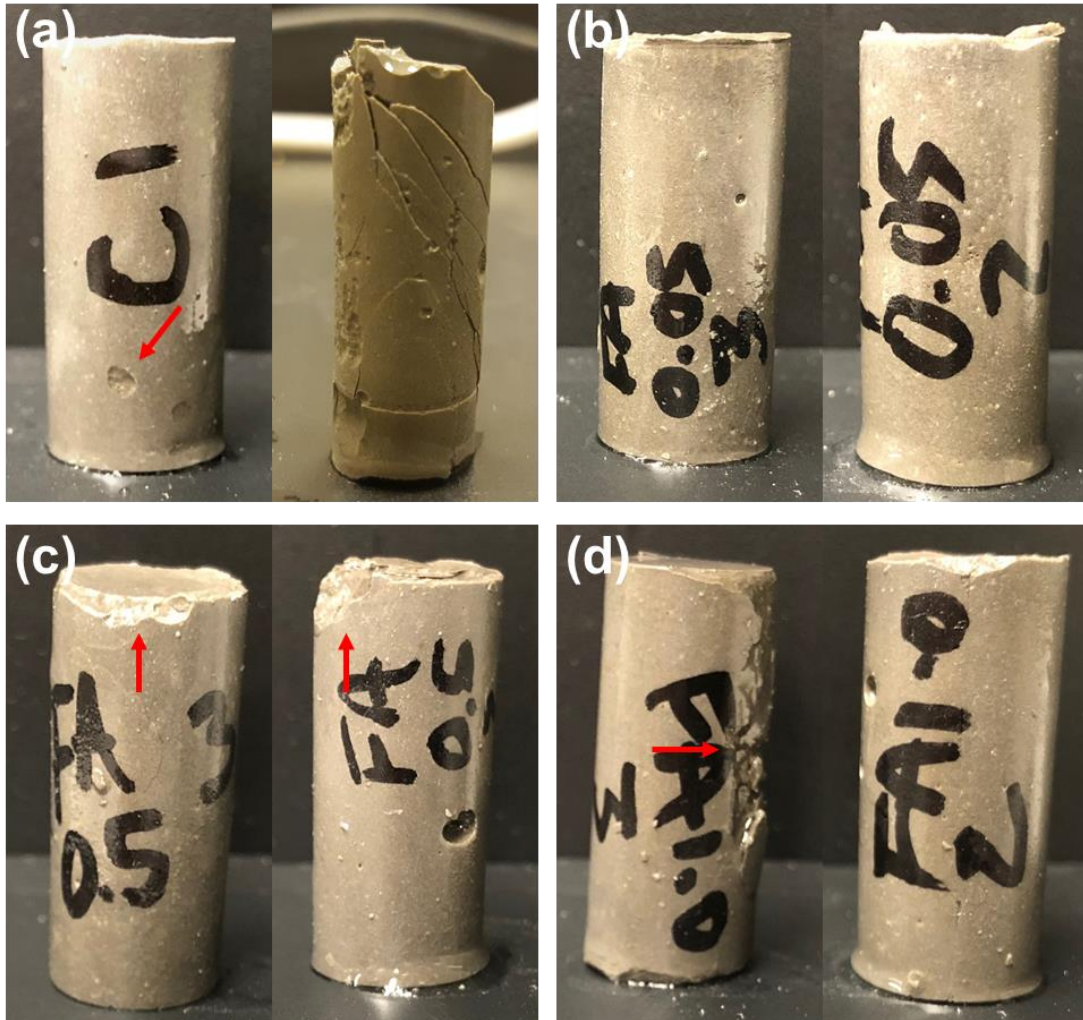
Figure 6.15. Images of bulk samples post 30 freeze-thaw cycles. Red arrows indicate areas of spalling. (a) control samples, (b) 0.05 mg/mL folic acid, (c) 0.5 mg/mL folic acid, and (d) 1.0 mg/mL folic acid modified paste.
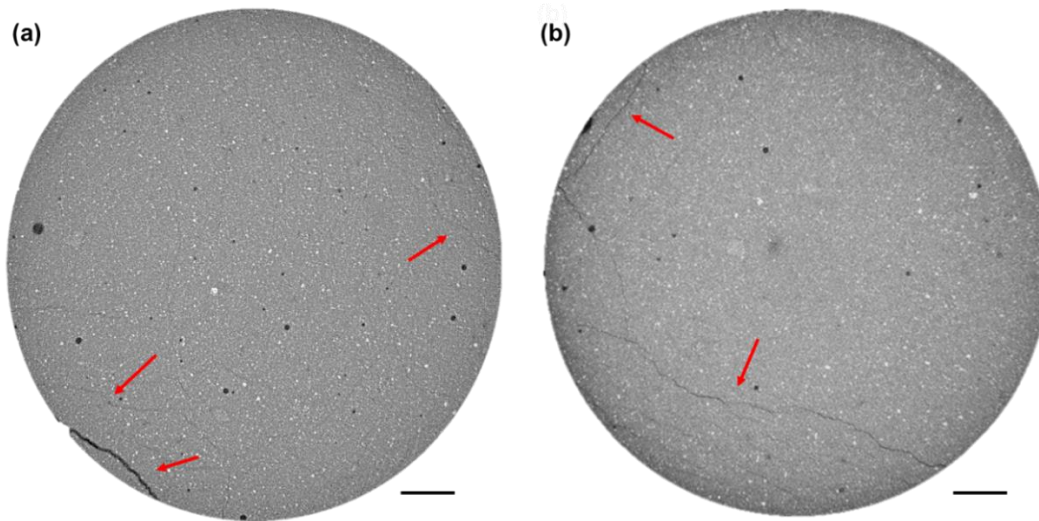
Figure 6.16. Post freeze-thaw MXCT 2D cross-sectional images of (a) control and (b) 0.05 mg/mL folic acid modified paste. Red arrows indicate microcracking. Scale bars are 1 mm.

6.3.3.3 Hardened State Air Content

The air content of the samples was determined by measuring the volume of pores with a diameter larger than 14.7 µm. This volume was determined from MXCT scans of samples after curing and before freeze-thaw cycling. **Table 6.2** summarizes the hardened state air content and the number of air voids detected in the scanned volumes. **Figure 6.17** provides representative 2D MXCT cross-sections with air voids colored pink for all samples.

FA-L, FA-M, and FA-H modified paste samples all contained less than 0.9% air while the control contained 0.41% air in the hardened state. These observed air contents are much lower than the industry accepted air contents of ~ 16 to 25% air by volume of cement paste,[163] or ~ 4 to 10% by volume of concrete.[163,168] However, it is worth noting that the air content is approximately double for the samples containing folic acid compared to the control. Additionally, the number of air voids with diameters between 15 µm and 60 µm are greater for FA-M and FA-H modified paste compared to the control, while FA-L has less. The air void size (diameter) distribution up to 60 µm for each sample is plotted in **Figure 6.18**. Taken together

with the freeze-thaw cycling results, the air content does not appear to affect the ability of folic

acid to provide freeze-thaw resistance (internal or surface). Additionally, the low hardened state

air contents taken together with the ICC results indicate that folic acid could be used as an

environmentally friendly, non-toxic retarding admixture.
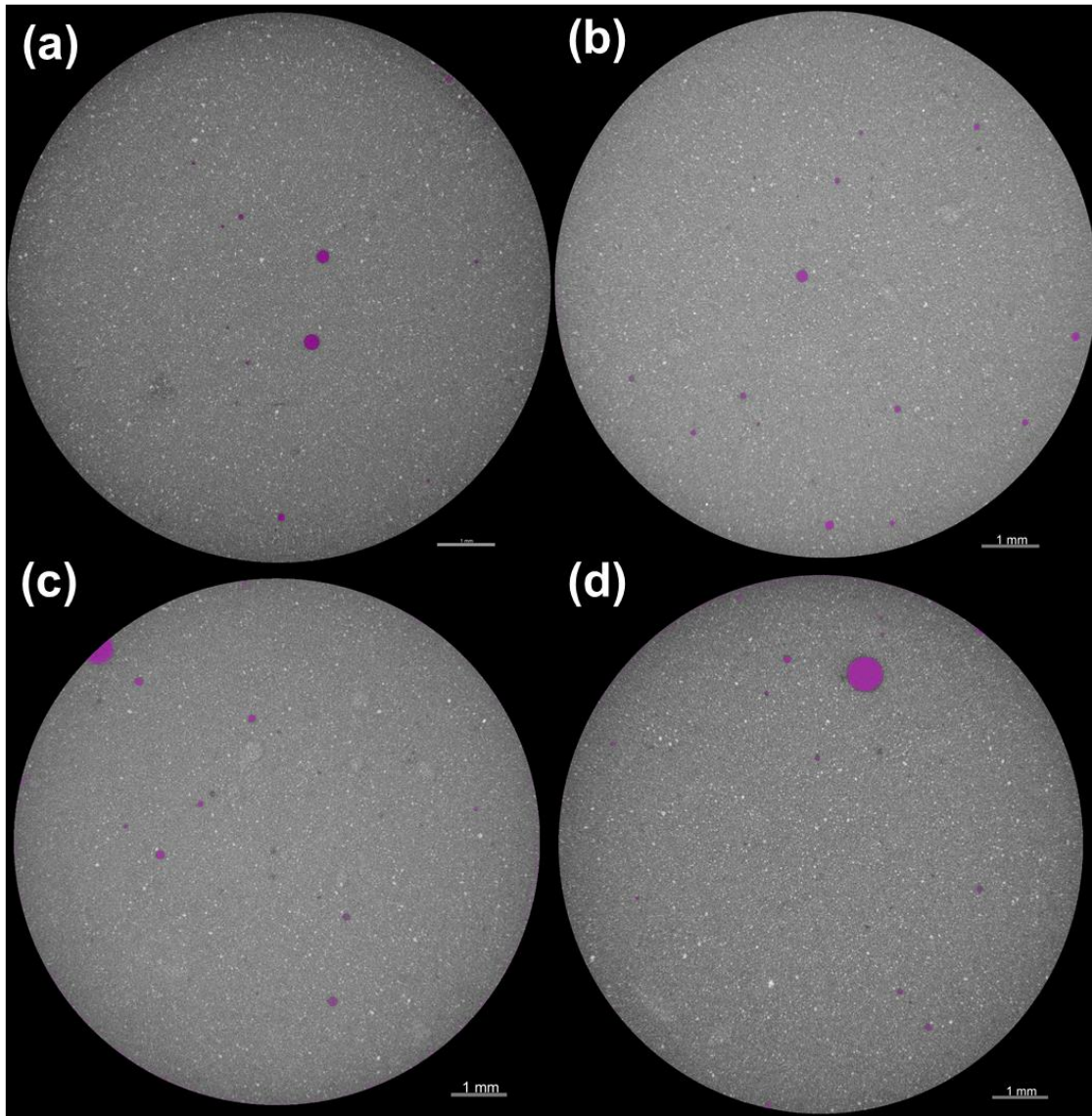
Figure 6.17. Representative 2D MXCT cross-sections with air voids highlighted in pink for (a) FA-L, (b) FA-M, and (c) FA-H. Scale bars are 1 mm.

Table 6.2. Hardened state air void parameters of control and folic acid modified hardened cement paste.

	Hardened state air content %	Number of voids
Control	0.41	572,975
FA-L	0.72	460,391
FA-M	0.85	763,544
FA-H	0.73	615,362
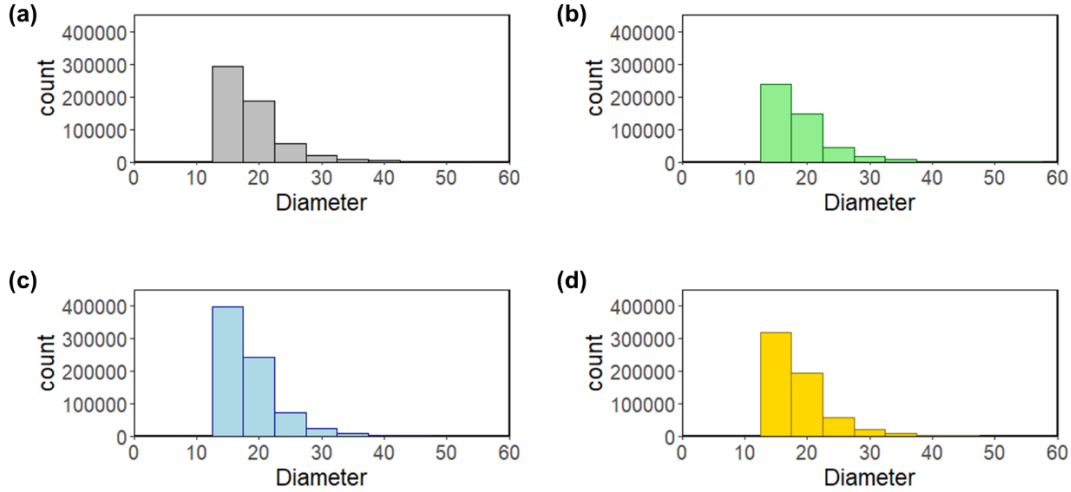
Figure 6.18. Histogram of air void diameters up to 60 µm. (a) control, (b) FA-L, (c) FA-M, and (d) FA-H.

6.5 Conclusions

This work presents, for the first time, experimental evidence that folic acid displays IRI activity. At concentrations as low as 0.01 mg/mL, folic acid was shown to reduce the MLGS by a minimum of 25% compared to DI, PBS, 0.41 mM NaCl, and 4.1 mM NaCl control solutions. Furthermore, an increase in the concentration of folic acid up to 0.5 mg/mL did not result in significantly higher IRI activity. The highest IRI activities achieved were 44% and 62% MLGS at 0.5 mg/mL in DI and 4.1 mM NaCl solution respectively. However, in the presence of 0.86 mg/mL $Ca(OH)_2$, folic acid displays negligible l IRI activity (~81% MLGS) up to concentrations of 1 mg/mL. XRD experiments indicate that self-assembly of folic acid into tetramers occurs at

concentrations as low as 0.05 mg/mL (0.005% wt). Although folic acid shows promise as an IRI active material, further investigation is required to fully explicate its use as an additive to cementitious materials. Samples modified with folic acid 0.0021% and 0.021% (FA-L and FA-M) by wt. of cement displayed resistance to surface freeze-thaw damage but did display internal microcracking. ICC results indicate that folic acid behaves as a retarding agent. Taken together, future research on folic acid as an additive to cement paste and concrete is merited, especially considering the non-toxic and environmentally friendly aspects of folic acid.

Chapter 7 Ice Recrystallization Inhibition Activity of Air Entraining Agents

7.1 Introduction

It is widely accepted that air entraining agents (AEAs) can be effective at providing freeze-thaw resistance when a high-quality air void system is created. However, a review of previously published results demonstrates variability in observed performance.[2,312] Our current understanding of air void systems suggests that performance can be predicted by a set of physical parameters, primarily fresh state air content and spacing factor.

Fresh state air content is a measure of all air present, including both entrained and entrapped air, within a freshly mixed cement paste, mortar, or concrete mixture. The recommend fresh state air content is 4-10% depending on the source, aggregate size, and exposure conditions.[163,168] The spacing factor is a measure that estimates the maximum distance from any point within the cement paste to an air void. The spacing factor is recommended to be below 0.2 mm.[50,168] For both fresh state air content and spacing factor, meeting these recommendations does not guarantee freeze-thaw durability and in some cases freeze-thaw performance is seen when these recommendations are not met.[157,158,376]

Figure 7.1 demonstrates this variability in performance from a selection of publications. **Figure 7.1** contains concrete freeze-thaw cycling results from previously published work.[155–158] For all of the data points, the samples are modified with AEA and ASTM C666 was followed. The red line indicates a durability factor of 60%, which is the minimum allowable durability factor to pass ASTM C666.[149] As can be seen in **Figure 7.1 (a)**, many concrete specimen, 21%, maintain a durability factor above 60% with a fresh state air content below the recommended 4-

10%. An even larger number of the concrete specimen, 46%, maintain a durability factor above

60% with a spacing factor > 0.2 mm as shown in **Figure 7.2 (b)**.
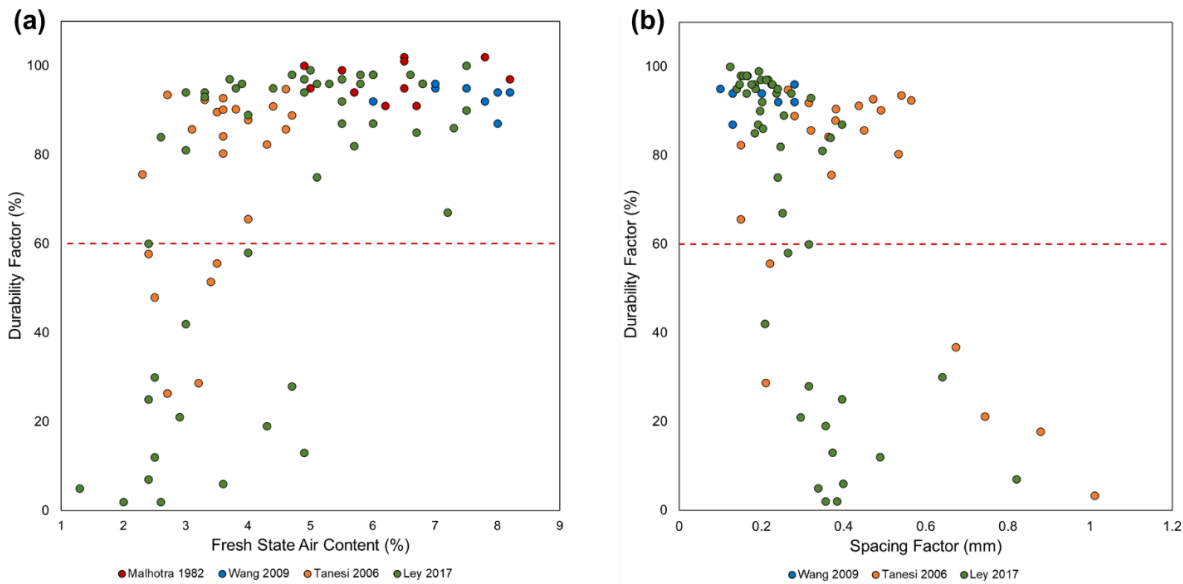
Figure 7.1. Reported freeze-thaw performance of AEA modified concrete. (a) The effect of fresh state air content on durability factor. (b) The effect of spacing factor on durability factor. The red line indicates a durability factor of 60% which is the point of failure in ASTM C666 freeze-thaw test. Data were taken from Malhotra (•),[155] Wang et al. (•),[156] Tanesi and Meininger (•),[157] and Ley et al. (•).[158]

The variability in performance could be due to an array of parameters that influence an AEAs ability to stabilize air voids including mix design, the mixing process itself, placement, finishing practices, and temperature.[377] However, some research has shown drastic variations in freeze-thaw performance when parameters (*i.e.*, mix design, air content, spacing factor, freeze-thaw conditions) were essentially identical for concrete samples modified with different AEAs.[163,378–380] It was suggested by Chatterji that some aspect of an AEA's chemical nature play an important role in performance.[163]

There are obvious chemical differences between the surfactants used as AEAs, which can be seen in how they are classified; 1) by the type of ionic compound: anionic, cationic, zwitterionic,

and non-ionic and 2) by their ability to coagulate in the presence of calcium (*i.e.*, insoluble vs. soluble). These chemical differences have been shown to affect the resulting air void system. For example, AEAs differing in ionic character have been shown to produce different size distributions and shapes of air voids in concrete.[381] Additionally, previous work has suggested that a minimum hydrocarbon chain length of 12 carbon atoms is required for effective air entrainment.

In the presence of AEAs, air voids have been shown to form with a shell around them.[160,162,382–384] The shell is a result of the surfactant molecules coagulating with calcium.[162] It is believed that the collection of these calcium salts forms a hydrophobic layer (*i.e.*, an insoluble calcium salt), which can reduce the amount of water that enters air voids.[2,163] A reduction in the amount of water that enters the air voids would lead to reduced ice formation within them.

When ice begins to form in the pores and air voids of cementitious materials, biomimetic antifreeze polymers are believed to interact with the ice-water interface and slow ice crystal growth. Biomimetic antifreeze polymers with ice recrystallization inhibition (IRI) activity have been shown to provide freeze-thaw resistance to hardened cement paste,[145] mortar,[311] and concrete.[145] In concrete, IRI-active polymers resulted in freeze-thaw resistance while having a marginal fresh state air content of 4.2%, a hardened state air content of 2.3%, and a spacing factor exceeding 0.390 mm.[145] IRI activity slows or prevents the thermodynamically driven process where smaller ice crystals grow into larger ice crystals (*i.e.*, Ostwald ripening).

Given that (1) variability in freeze-thaw performance is observed when different AEAs create similar air void systems (*i.e.*, physical parameters) in concrete, (2) microscopic imaging has shown ice forms on the surfaces of air voids (where surfactant molecules are located), (3)

enhanced freeze-thaw resistance observed with the use of biomimetic antifreeze polymers, it was

hypothesized that surfactants used in AEAs display varying levels of IRI activity.

7.2 Scope of Work

This study compared the IRI activity of sodium oleate, vinsol resin, sodium lauryl sulfate,

and a phenol ethoxylate (4-nonylphenol-polyethylene glycol) because of previously reported

side-by-side concrete freeze-thaw testing with each of these surfactants. Hewlett *et al*. reported

the results shown in **Table 7.1** where the air content of each sample is nearly identical.[385] The

freeze-thaw rating is reported to be an average of the measured modulus and compressive

strength after freeze-thaw cycling. It is clear from the results in **Table 7.1** that although the

AEAs resulted in similar air contents, they had considerably different freeze-thaw performances.

Chatterji pointed out that others have reported similar observations.[163,378,380]

Table 7.1. Freeze-thaw results of AEA modified concrete reported by Hewlett et al.

Surfactant	Air content (%)	Freeze-thaw rating
Sodium oleate	5.6	86
Vinsol resin	5.2	57
Sodium lauryl sulfate	5.8	46
Phenol ethoxylate	5.2	7
Control	2.0	5

In addition to the surfactants listed in **Table 7.1**, sodium dodecylbenzene sulfonate and

sodium octanoate were also screened for IRI activity. The structure of each surfactant studied

herein can be found in **Figure 7.2**. Beyond screening the surfactants for IRI activity, this work

explores the molecular properties that influence the IRI activity of surfactants and compares

them to other small molecules previously studied for IRI activity.
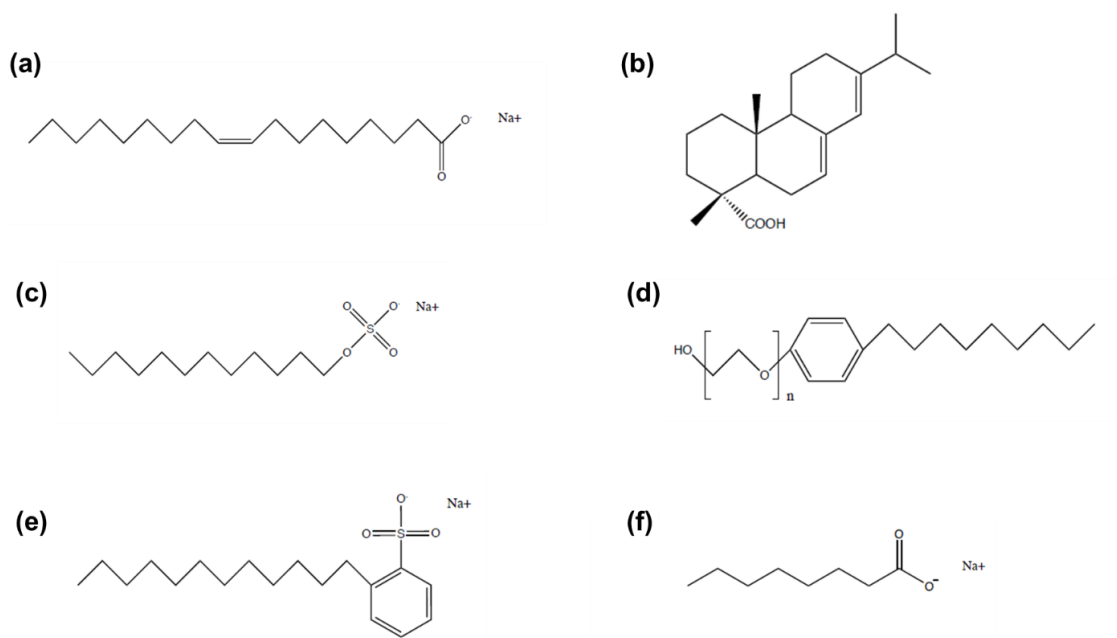
Figure 7.2. The chemical structure of surfactants used in this study. a-d were used in the work of Hewlett et al.[385] (a) sodium oleate, (b) abietic acid (major component of vinsol resin), (c) sodium lauryl sulfate, (d) 4-nonylphenol-polyethylene glycol (phenol ethoxylate), (e) sodium dodecylbenzene sulfonate, and (f) sodium octanoate.

7.2 Experimental Procedure

7.2.1 Materials

Sodium lauryl sulfate (SLS) (CAS # 151-21-3), sodium dodecylbenzene sulfonate (CAS # 25155-30-0), sodium octanoate (CAS # 1984-06-1), 4-nonylphenol-polyethylene glycol (CAS # 9016-45-9), and Ca(OH)$_2$ were purchased from Sigma-Aldrich and used without any modification. Sodium oleate (CAS # 143-19-1) was purchased from TCI and used without any modification. A commercially available vinsol resin based AEA was purchased and used without any modification.

7.2.2 Ice Recrystallization Inhibition

The IRI activity of each surfactant was tested at a concentration of 1.00 mg/mL in phosphate buffered saline (PBS). Sodium oleate, vinsol resin, sodium lauryl sulfate, and phenol ethoxylate were additionally tested in a 0.86 mg/mL Ca(OH)$_2$ PBS solution at a concentration of 1.00 mg/mL. A modified IRI assay was performed to observe IRI activity.[321] 10 μL of sample was dropped from 1.7 m onto a glass slide (thickness of 1 mm). The glass slide was pre-cooled on an aluminum block at −78°C. The slide was then immediately transferred to an Otago nanoliter osmometer cold stage and annealed at −4°C (air temperature) for 30 min. Images were collected immediately after the sample was placed on the cold stage and again at 30 min to observe ice recrystallization. For all samples, images were obtained using an Olympus BX41 microscope with ELWD U Plan 20×/0.45 objective and crossed polarizers, equipped with an OMAX A35140U camera on a 0.5× C-mount adaptor. ImageJ 1.48v software (National Institutes of Health) was used to measure the mean largest grain size (MLGS). The MLGS is the average size of the 10 largest grains in a micrograph. Reported MLGS values are the average of 3 replicates.

7.2.3 Molecular Properties

7.2.3.1 Hydrophobicity

The hydrophobicity of small molecules, including surfactants, has previously been shown to play an important role in IRI activity.[143,294,298] Given this, the relative hydrophobicity of the surfactants was compared using the partition coefficient, log P.[165] The partition coefficient is the log of the ratio of the concentration of a molecule in an aqueous phase and an organic phase at equilibrium. **Figure 7.3** provides a schematic representation of how the partition coefficient is measured. As log P increases in value so does the relative hydrophobicity of the molecule.

The measurement of log P in a laboratory setting is time intensive and difficult which led to the development of algorithms to predict log P.[386] Algorithms to predict the log P value are included in a variety of commercially available software packages including Molinspiration Cheminformatics (Slovensky Grob, Slovakia), which was used here. For each surfactant tested here, the log P values were calculated from the charged form where applicable.

organic phase
(octanol)

aqueous phase
(water)

$$\log P = \log \frac{[solute]_{organic}}{[solute]_{aqueous}}$$
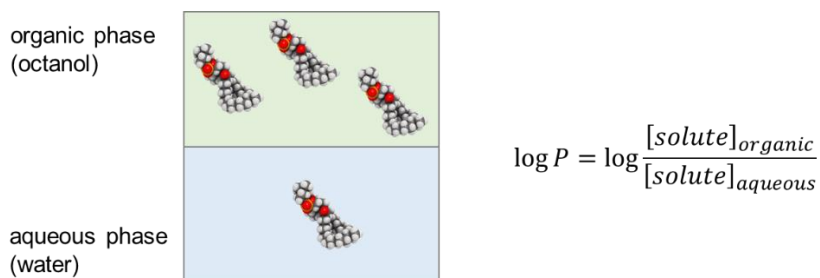
Figure 7.3. Schematic representation of how the partition coefficient, log P, is calculated. The concentration of a molecule is measured in two immiscible phases. In the example, the two phases are octanol and water.

7.2.3.2 Topological Polar Surface Area

Molecular polar surface area (PSA) is the surface area of polar atoms in a molecule. Topological polar surface area (tPSA) is a method of rapidly calculating the PSA based on surface contributions of polar fragments.[387] A variety of software packages are capable of calculating tPSA. Molinspiration Cheminformatics (Slovensky Grob, Slovakia) was used to calculate tPSA values used herein.[388]

7.2.3.3 Molecular Volume

Molecular volume influences the transport characteristics of molecules and is often used in models to correlate molecular properties to given activities. Molinspiration Cheminformatics (Slovensky Grob, Slovakia) was used to calculate molecular volumes.[388]

150

7.3 Results and Discussion

7.3.1 Ice Recrystallization Inhibition

Representative splat-assay micrographs showing the IRI activity of sodium oleate, vinsol resin, sodium lauryl sulfate, phenol ethoxylate, sodium dodecylbenzene sulfonate, and sodium octanoate at a concentration of 1 mg/mL in PBS solution are shown in **Figures 7.4**. The activity, reported as the % MLGS, of each surfactant compared to the PBS control solution is shown in **Figure 7.5**.

Sodium octanoate exhibited the highest level of IRI activity with an MLGS of 55% compared to the PBS control. Interestingly, sodium oleate exhibited the highest IRI activity, 74%, of the surfactants tested in the previously published side-by-side freeze-thaw study summarized in **Table 7.1**. Moreover, the trend in observed freeze-thaw performance matches that of IRI activity (*i.e.*, higher IRI activity, greater freeze-thaw performance). Sodium oleate, vinsol resin, and sodium lauryl sulfate all reported freeze-thaw performance in the side-by-side freeze-thaw cycling, while phenol ethoxylate which has no IRI activity performed nearly identical to the control in freeze-thaw cycling.

The observed IRI activities for the surfactants studied herein appear to agree well with the IRI activity of other previously studied hydrocarbon-containing surfactants. Fan *et al*. reported a MLGS of 70% for sodium lauryl sulfate at a concentration of ~0.05 mg/mL (0.2 mM)[291]. However, Capicciotti *et al*. previously reported no IRI activity for sodium lauryl sulfate at concentrations of ~ 0.1, 1.3, and 2.7 mg/mL (0.5, 5, and 10 mM respectively).[290] Additionally, Capiccotti *et al*. reported the IRI activity of Brij58 and Triton X-100 which are both commercially available surfactants. Brij 58 and Triton X-100 resulted in MLGS of 88% and 82%

compared to a PBS control at concentrations of ~ 5.6 and 3.1 mg/mL (5 mM) respectively.[290]

Balcerzak *et al*. reported IRI activities ranging from 5% to 95% for a series of anionic lysine

surfactants.[294]
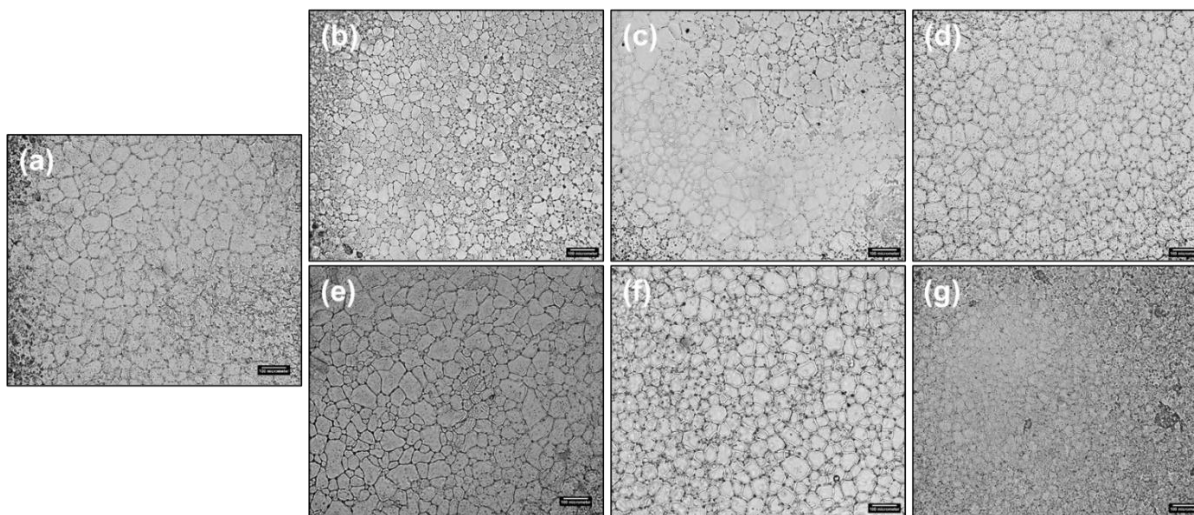
Figure 7.4. Optical Micrographs of IRI Splat Assay of sodium oleate, vinsol resin, sodium lauryl sulfate, phenol ethoxylate, sodium dodecylbenzene sulfonate, and sodium octanoate in PBS solution. Images show individual ice crystal grains that form in (a) PBS control solution, (b) 1 mg/mL sodium oleate, (c) 1mg/mL vinsol resin, (d) 1 mg/mL sodium lauryl sulfate, (e) 1 mg/mL phenol ethoxylate, (f) 1 mg/mL sodium dodecylbenzene sulfonate, and (g) 1 mg/mL sodium octanoate in PBS solution after 30 min of annealing at −4°C. Scale bars are 100 μm.
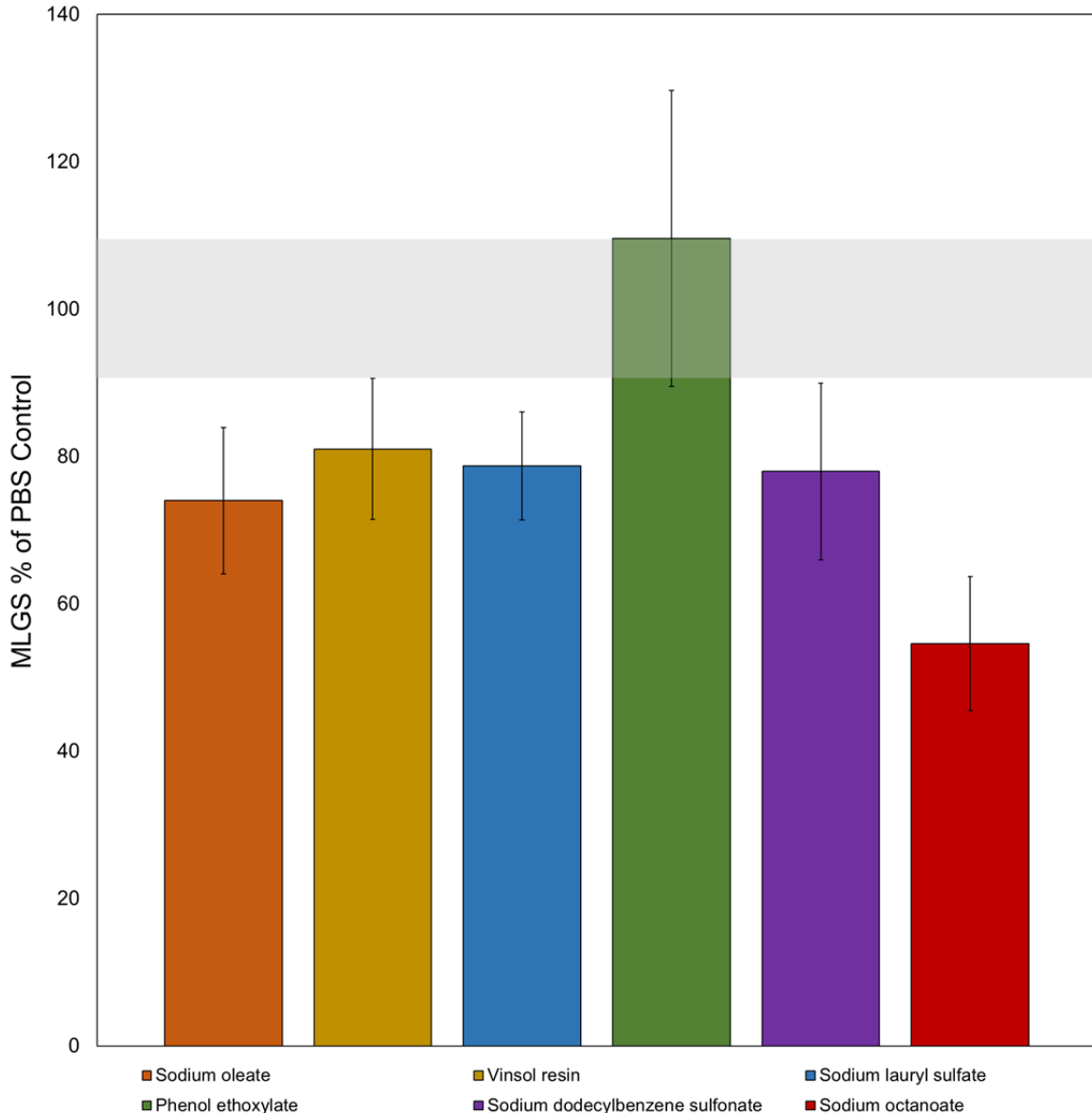
Figure 7.5. Summary of surfactant IRI activity in PBS. 1 mg/mL sodium oleate (■), 1 mg/mL vinsol resin (■), 1 mg/mL sodium lauryl sulfate (■), 1 mg/mL phenol ethoxylate (■), 1 mg/mL sodium dodecylbenzene sulfonate (■), and 1 mg/mL sodium octanoate (■) in PBS. IRI activity is reported as the percent mean largest grain size (% MLGS) compared to the control PBS solution. Error bars represent one standard deviation of 3 replicates. The grey area represents the control PBS solution MLGS.

Representative splat-assay micrographs showing the IRI activity of sodium oleate, vinsol resin, sodium lauryl sulfate, and phenol ethoxylate at a concentration of 1 mg/mL in 0.86 mg/mL $Ca(OH)_2$ PBS solution are shown in **Figure 7.6**. The pH of the 0.86 mg/mL $Ca(OH)_2$ PBS

solution was 12.5. The activity of each surfactant compared to the 0.86 mg/mL Ca(OH)$_2$ PBS control solution is shown in **Figure 7.7**.

The IRI activity of these surfactants was tested in the presence of Ca^{2+} because sodium oleate,[163] vinsol resin,[160,162,163] and sodium lauryl sulfate[389] are known to coagulate in the presence of Ca^{2+}. Additionally, these are the surfactants previously studied in a side-by-side cyclic freeze-thaw test in concrete. The MLGS compared to the 0.86 mg/mL Ca(OH)$_2$ PBS solution were 73%, 92%, 90%, and 96% for sodium oleate, vinsol resin, sodium lauryl sulfate, and phenol ethoxylate respectively at 1 mg/mL. Sodium oleate was the only surfactant that maintained or increased IRI activity in the presence of Ca^{2+}.
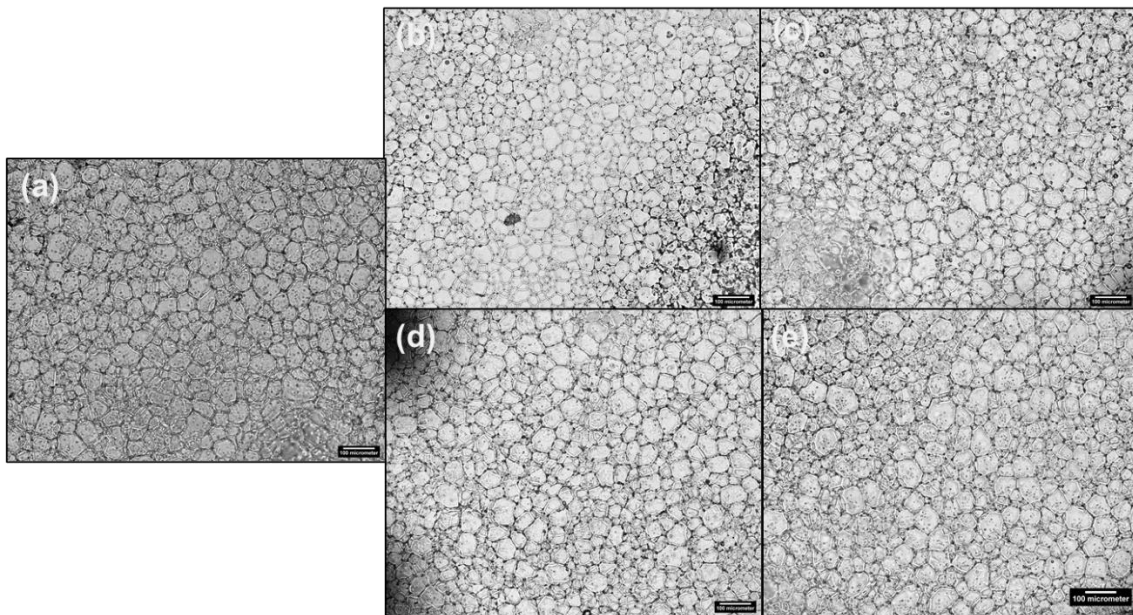
Figure 7.6. Optical Micrographs of IRI Splat Assay of sodium oleate, vinsol resin, sodium lauryl sulfate, and phenol ethoxylate in PBS solution. Images show individual ice crystal grains that form in (a) PBS control solution, (b) 1 mg/mL sodium oleate, (c) 1mg/mL vinsol resin, (d) 1 mg/mL sodium lauryl sulfate, and (e) 1 mg/mL phenol ethoxylate in PBS solution after 30 min of annealing at −4°C. Scale bars are 100 μm.
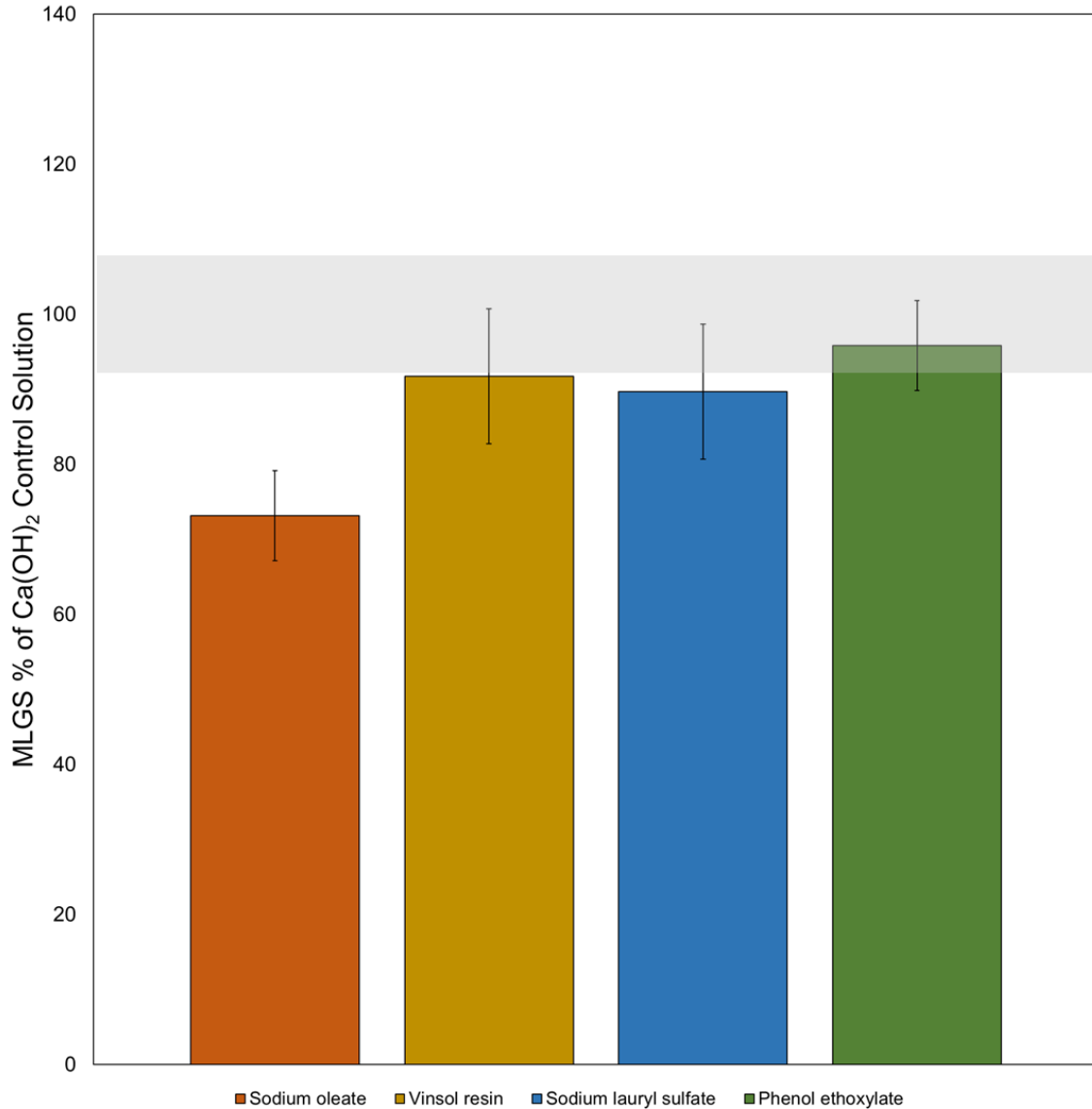
Figure 7.7. Summary of surfactant IRI activity in Ca(OH)$_2$ solution. 1 mg/mL sodium oleate (■), 1 mg/mL vinsol resin (■), 1 mg/mL sodium lauryl sulfate (■), and 1 mg/mL phenol ethoxylate (■). IRI activity is reported as the percent mean largest grain size (% MLGS) compared to the control 0.86 mg/mL Ca(OH)$_2$ in PBS solution. Error bars represent one standard deviation of 3 replicates. The grey area represents 0.86 mg/mL Ca(OH)$_2$ in PBS solution MLGS.

7.3.2 Molecular Properties

Table 7.2 summarizes the calculated log P, tPSA, and molecular volume for each surfactant. **Figure 7.8** shows the relationship between log P, tPSA, molecular volume, and molecular weight, and the IRI activity of each surfactant in PBS at 1 mg/mL.

The hydrophobicity of small molecules, including surfactants, has previously been shown to play an important role in IRI activity.[143,294,298] Given this, the relative hydrophobicity of the surfactants was compared using log P.[165] Large values of log P indicate higher relative hydrophobicity. As can be seen in **Figure 7.8 (a)**, there is no obvious relationship between log P and the IRI activity for the surfactants tested.

A lack of trend between hydrophobicity and IRI activity does not match the findings reported in literature. Balcerzak *et al*. showed that IRI activity is dependent upon the length of alkyl chains for anionic lysine surfactants, an indicator of hydrophobicity.[294] Trant *et al*. found that for alkylated galactose derivatives, hydrophobic chain lengths of appropriate length (n = 6 to 7) provided substantial IRI activity (*i.e.* >80% reduction).[143] The alkylated galactose derivatives did not show a general trend of increasing hydrophobicity, or chain length, leading to increasing IRI activity. For the anionic surfactants studied herein, the chain length does not appear to explain differences in IRI activity. This is evidenced by sodium lauryl sulfate, a C-12 alkane chain, having a lower IRI activity (*i.e.*, higher MLGS) than sodium octanoate, a C-7 alkane chain.

Table 7.2. Summary of calculated partition coefficients (log P), topological polar surface area (tPSA), molecular volumes, and molecular weights for surfactants.

Surfactant	log P	tPSA (Å^2)	Molecular volume (Å^3)	Molecular Weight (g/mol)
Sodium oleate	7.70	40.13	316.10	281.46
Vinsol resin	6.51	37.30	312.49	302.46
Sodium lauryl sulfate	5.39	66.43	259.71	265.39
Phenol ethoxylate	2.93	112.57	668.92	680.00
Sodium dodecylbenzene sulfonate	6.77	57.20	322.13	325.49
Sodium octanoate	2.90	40.13	154.26	143.20
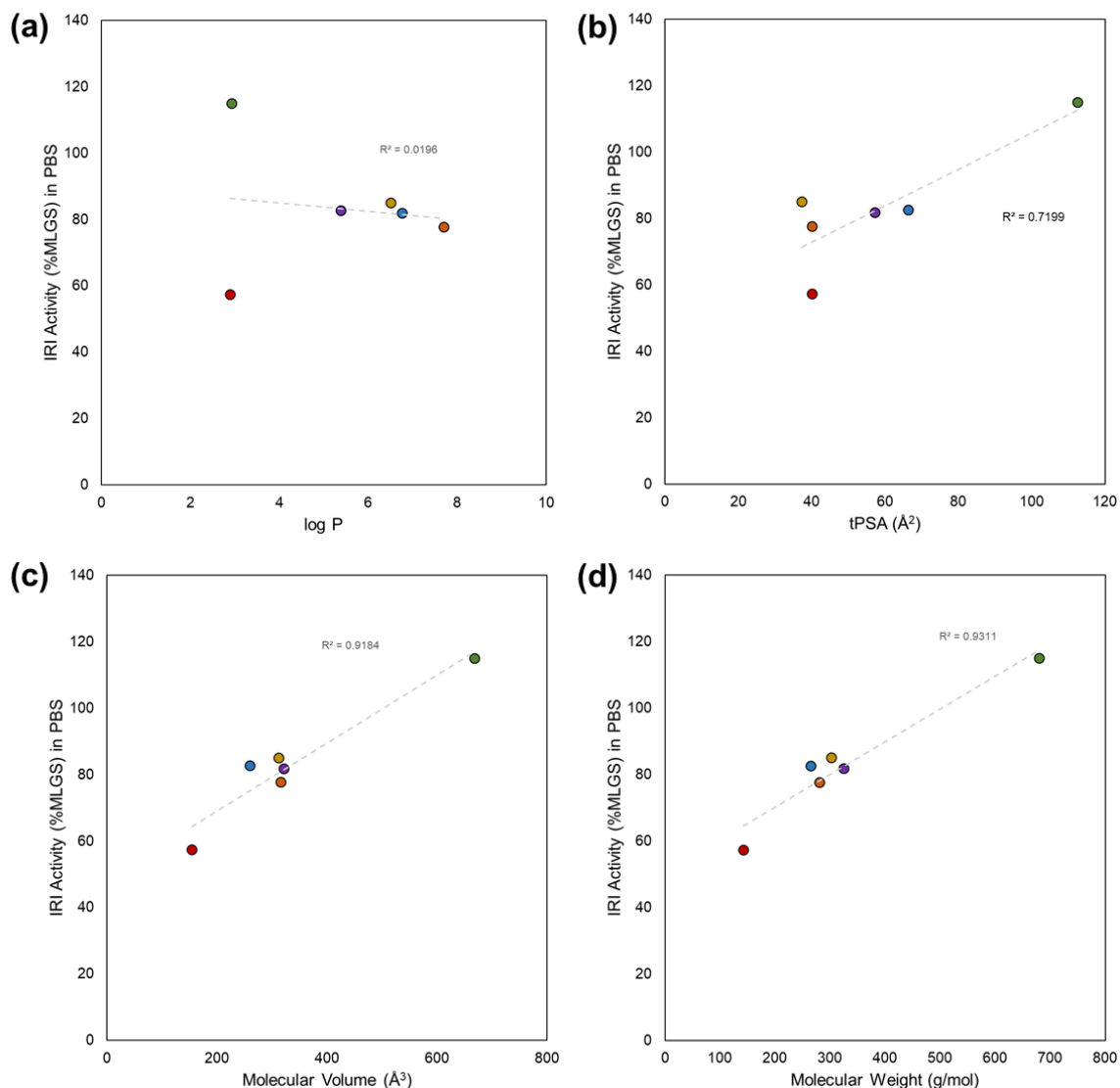
Figure 7.8. Relationship between molecular properties and IRI activity. (a) hydrophobicity (log P), (b) topological surface area (tPSA), (c) molecular volume, and (d) molecular weight. IRI activity is in PBS at a concentration of 1 mg/mL for each surfactant. Data points represent sodium oleate (●), vinsol resin (●), sodium lauryl sulfate (●), phenol ethoxylate (●), sodium dodecylbenzene sulfonate (●), and sodium octanoate (●).

Amphiphilicity has previously been shown to play a role in the function of AFPs, especially Type I AFPs.[234,390] Furthermore, amphiphilicity appears to be a factor contributing to the IRI activity of nanomaterials,[255,282] metallohelices,[284] polymers,[391] and small molecules.[294,392] Previously, the amphiphilicity of small molecules has been characterized by comparing the

158

content of CH groups in alkyl chains to hydroxyl groups, the ratio of polar surface area (PSA) to the molecular surface area, and general qualitative comparison of chemical structures when studying IRI activity.[294,392] When considering surfactants, they are inherently amphiphilic.

Topological polar surface area (tPSA) represents the surface area of polar atoms in a molecule. Previously, IRI activity was shown to decrease with increasing net polarity for N-alkyl aldonamides and N-alkyl-erythonamides derivatives (linear relationship with $R^2 = 0.8456$). The same general trend can be observed for the surfactants studied herein as shown in **Figure 7.8 (b)**, where greater polarity leads to decreased IRI activity.

For polymers and specifically PVA, IRI activity has been shown to depend on molecular weight.[266,345] Carbohydrate-based small molecules have been shown to display increasing IRI activity with increasing alkyl chain lengths and therefore increasing molecular weights.[294] The molecular weight of a molecule is closely related to the molecular volume. To the authors' knowledge, the molecular volume has not previously been studied as a parameter that influences the IRI activity of small molecules. The relationship between IRI activity and molecular volume and the molecular weight is shown in **Figures 7.8 (c)** and **7.8 (d)** respectively. For the surfactants studied herein, decreasing molecular weight and molecular volume led to increasing IRI activity. However, a majority of the surfactants (4 of 6) have similar molecular weights, 143-282 g/mol, and IRI activity, 77-83%.

Polar surface area, molecular volume, and molecular weight appear to have a linear relationship to the IRI activity of the surfactants studied here. When considering the effect of log P, tPSA, molecular volume, and molecular weight on IRI activity, caution should be taken extracting the results herein and applying them to non-surfactant small molecules. A review of the literature clearly shows that a unifying mechanism for explaining small molecule IRI activity

is still to be explicated. Furthermore, the molecular properties that influence IRI activity are still to be explicated. The small molecules that have been studied for IRI activity are almost exclusively polyols (*i.e.*, containing many hydroxyl groups) making their chemical structure significantly different than surfactants containing hydrocarbon chains and few to no hydroxyl groups (*i.e.*, sodium octanoate, sodium lauryl sulfate).

Figures 7.9-7.11 show the IRI activity of a variety of small molecules previously published and the results herein based on log P, tPSA, and molecular weight. log P data includes 71 molecules with 22 of them being non-polyols. tPSA data includes 48 molecules with 19 of them being non-polyols. Molecular weight data includes 112 molecules with 22 of them being non-polyols. When looking at the effect of tPSA on IRI activity in **Figure 7.9**, it appears that a tPSA > 100 Å^2 is required for high IRI activity (*i.e.*, MLGS < 20%) in combination with concentrations exceeding 7.5 mg/mL. A similar trend can be seen for the effect of molecular weight on IRI activity in **Figure 7.11**, where it appears that a molecular weight > 300 g/mol and concentrations exceeding 5 mg/mL are needed for high IRI activity. There does not appear to be a trend in the log P data shown in **Figure 7.10**.
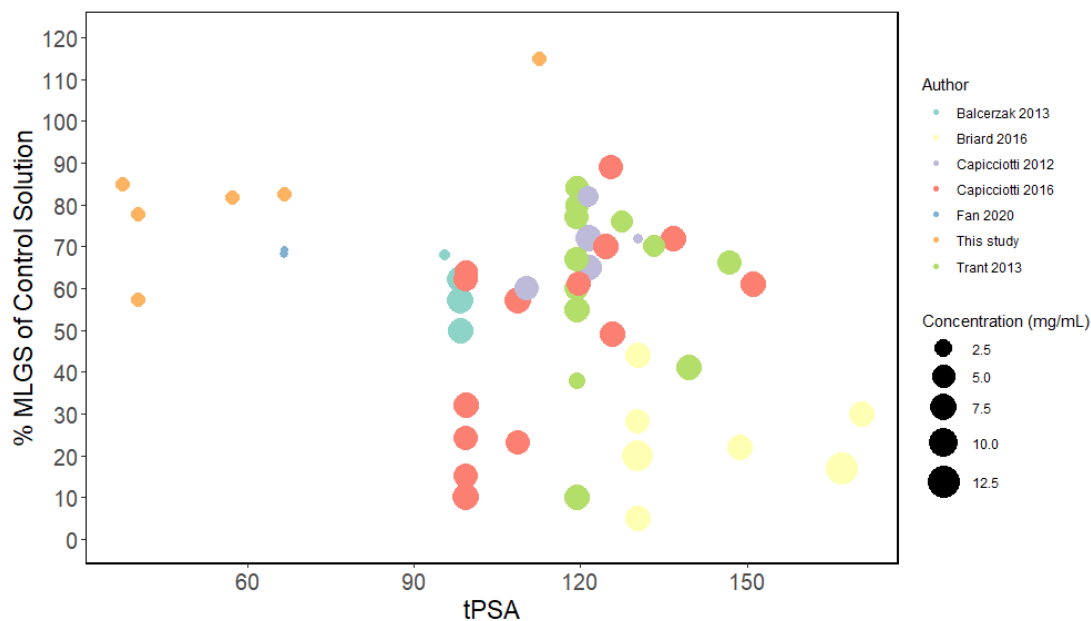
Figure 7.9. IRI activity of select small molecules based on tPSA (Å^2). Size of data point indicates concentration (mg/mL) tested at. Color of data point represents the source.[143,225,290,290,291,294]
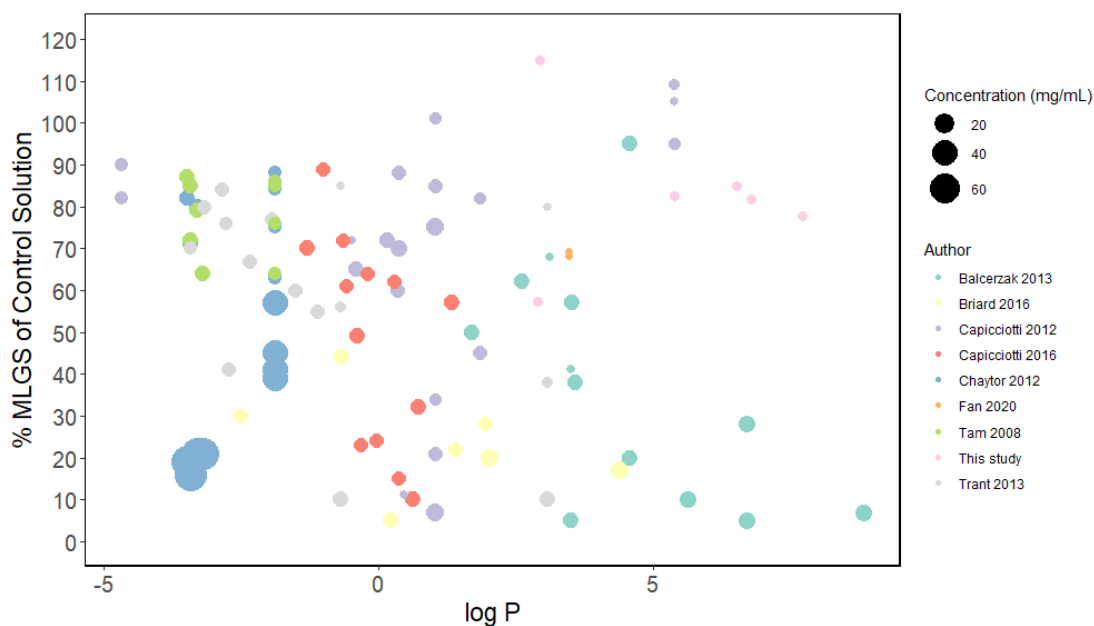
Figure 7.10. IRI activity of select small molecules based on log P. Size of data point indicates concentration (mg/mL) tested at. Color of data point represents the source.[143,225,290–295]
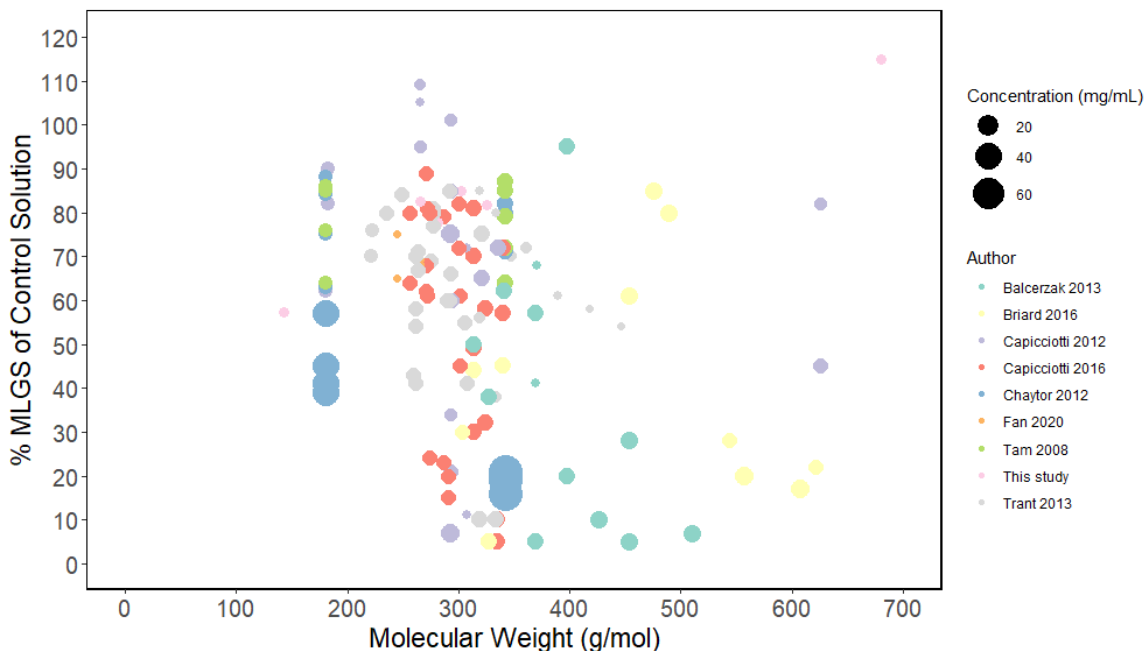
Figure 7.11. IRI activity of select small molecules based on molecular weight (g/mol). Size of data point indicates concentration (mg/mL) tested at. Color of data point represents the source.[143,225,290,290–294]

The molecular properties may explain surfactant IRI activity. It appears that decreasing molecular weight, decreasing molecular volume, and decreasing tPSA result in increasing IRI activity. This is evidenced by sodium octanoate having the highest IRI activity and lowest molecular weight, molecular volume, tPSA of the surfactants studied herein. However, when compared to the results of other small molecules previously studied for IRI activity, the effect of these molecular properties does not follow the same trends. The difference in the effect of the surfactants studied herein and the previously studied small molecules is likely because the vast majority of previously studied small molecules are polyols instead of amphiphilic surfactants.

The chemical and structural properties from a more extensive library of surfactants and small molecules could be utilized to develop correlations with IRI activity. This model could be used to assist in the prediction of small molecules with IRI activity and ultimately a better understanding of the chemical and structural parameters that contribute most significantly to IRI

activity. Briard *et al.* developed a quantitative structure-activity relationship (QSAR) model based on 83 previously studied small molecules.[225] However, all of the molecules used for the development, training, and testing of the model were polyols. The majority of small molecules studied for IRI activity are polyols because the primary intended application is cryopreservation. Small molecules with IRI activity are desirable for cryopreservation because IRI active materials with larger sizes such as PVA generally show poor cell recovery after cryopreservation.[294]

Although not including in the experimental work and analysis herein, it is important to discuss the critical micelle concentration (CMC). Surfactants undergo micelle formation at the CMC. Continued addition of surfactant molecule after the CMC results in increased micelle formation. Previous work has indicated that IRI activity is not affected at concentrations at or above the CMC for a given surfactant. The influence of micelle formation on the mechanism of IRI could be complex. Furthermore, CMC affects molecular properties such as the partition coefficient.[393]

7.4 Conclusions

The results presented herein demonstrate that surfactant molecules, including those commonly used as AEA admixtures, can display IRI activity. Interestingly, the IRI activity of 4 surfactants, namely sodium oleate, vinsol resin, sodium lauryl sulfate, and a phenol ethoxylate, displayed varying levels of IRI activity that correlate with previously reported freeze-thaw performance results (*i.e.*, higher IRI activity equates to better freeze-thaw performance). These initial results provide insight into new design parameters for effective AEAs.

The surfactants studied herein do not appear to follow the same structure-property relationships regarding IRI activity when compared to small molecule polyols. For polyol small

molecules it appears that a tPSA > 100 $Å^2$ and a molecular weight > 300 g/mol in combination with concentrations exceeding 5 mg/mL are required for high IRI activity (*i.e.*, MLGS < 20%). that a molecular weight > 300 g/mol and concentrations exceeding 5 mg/mL are need for high IRI activity. The results of the study highlight the need for future research focusing on understanding the underlying mechanisms that govern small molecule surfactant and polyol IRI activities in order to elucidate the likely differences in their governing structure-property relationships.

Chapter 8 Concluding Remarks

8.1 Summary of Contributions

The research presented herein advances the scientific understanding and technological application of IRI active materials for use as additives in cementitious materials for freeze-thaw resistance. The following provides a summary of the significant scientific contributions.

- The review of techniques used for freeze-thaw mitigation within cementitious materials provided an overview of the underlying mechanisms that allow for freeze-thaw resistance, materials used in each approach, and shortcomings of each method.

- The review of biomimetic antifreeze materials has provided an overview of the various materials reported to mimic the IRI activity of AFPs and AFGPS. The structure-property relationships that allow for IRI activity are presented.

- Polyvinyl alcohol-polyethylene glycol graft copolymer (PEG-PVA) was shown to display both IRI and DIS activity in neutral and pH 12.5 solutions.

- PEG-PVA and PVA maintain DIS activity in a saturated Ca^{2+} environment.

- PEG-PVA provides freeze-thaw resistance while minimally impacting fresh and hardened state properties of OPC paste (*i.e.*, hydration, mineralogy, compressive strength, and hardened state air content) at a dosage of 0.021% by wt. of cement.

- PVA of appropriate molecular weights (*i.e.*, >30,000 g/mol and < 214,500 g/mol) and degree of hydrolysis (*i.e.*, > 88%) provides freeze-thaw resistance to hardened OPC paste and result in lower amounts of ice during freezing temperatures as determined by DSC.

- Folic acid exhibits moderate IRI activity (*i.e.*, 45-70% MLGS) at concentrations down to 0.05 mg/mL in DI, PBS, and NaCl solutions, however, loses IRI activity in the presence of Ca^{2+}.

- Folic acid displays evidence of tetramer self-assembly in DI and 0.75 M NaOH at concentrations down to 0.05 mg/mL. Additionally, XRD results indicate that small columnar structures of the folic acid tetramers self-assemble at 0.05 mg/mL folic acid in 0.75 M NaOH.

- Folic acid retards cement hydration at dosages of 0.0021% to 0.042% by wt. of cement.

- Surfactants commonly used in AEAs display varying levels of IRI activity with sodium octanoate being the most active, 55% MLGS, surfactant studied at 1 mg/mL in PBS.

- Structure-property relationships describing the IRI activity of previously studied small molecules, which are almost exclusively polyols, do not appear to be accurate for the surfactants studied herein.

8.2 Future Research Directions

In this work, a new method for freeze-thaw mitigation of cementitious materials was introduced. The work focused on exploring the ability of PEG-PVA, PVA, and folic acid, all of which are IRI active, to enhance freeze-thaw resistance in OPC paste while entraining minimal air. The addition of these biomimetic antifreeze materials at appropriate IRI activity results in freeze-thaw mitigation and as evidence by DSC, lower amounts of ice development during freezing temperatures. However, further research is required to determine the performance of biomimetic antifreeze materials in concrete.

Future Research Direction #1. *Propensity of IRI Active Materials to Entrain Air.* A critical step for incorporation of IRI active materials in concrete and further mechanistic understanding will require knowledge of the propensity for IRI active materials to entrain air in concrete. For

example, PVA is known to entrain air in concrete but usually this is seen at dosages exceeding 1% by wt. of cement. Testing the ability for IRI active materials to entrain air should include a variety of doses and w/c ratios. Determination of the fresh state air content, hardened state air content, spacing factor, and specific surface, materials surface tension, and foaming capacity should all be included in these studies.

Future Research Direction #2. *IRI Active Polymers in Concrete.* Ultimately, these IRI active materials need to be placed in concrete and tested for freeze-thaw resistance. PEG-PVA has been tested in concrete and shown to provide freeze-thaw resistance.[145] PVA has been shown to provide scaling resistance in mortar.[311] However, these are both preliminary studies (for example only a single w/c ratio was tested). Freeze-thaw testing should be performed for a variety of mix compositions, sample ages, and water saturation levels. Additionally, the freeze-thaw testing would need to be performed with AEA modified concrete as a positive control. Lastly, during the freeze-thaw cycling, water used in the freeze-thaw chamber to maintain saturation should be tested for the presence of the IRI active materials to determine if and how much leeching occurs.

Future Research Direction #3. *Incorporation of IRI Active Material and AEA.* Given that an air void system can provide freeze-thaw resistance and increase the time till a critical degree of saturation (DOS_{cr}) is reached, the ability of IRI active materials to work synergistically with AEAs should be explored. Investigating the effect of the IRI active material on the ability of the AEA to create a high-quality air void network would be critical. Additionally, testing of the fresh- and hardened-state properties will be necessary.

Future Research Direction #4. *Interaction of Biomimetic Antifreeze Polymers with Other Concrete Additives*. Concrete almost always contains a variety of admixtures such as water reducing agents and superplasticizers. An investigation that explores the propensity of IRI active materials to interact with other concrete admixtures is critical for the application of these materials in the field. The investigations should ensure that no detrimental effects are seen for the IRI active materials, other concrete admixtures, and SCMs.

Future Research Direction #5. *Highly IRI Active Small Molecules*. Folic acid was the only IRI active small molecule tested for its ability to provide freeze-thaw resistance in this work. Highly IRI active (*i.e.*, MLGS <20%) small molecules should be tested as an additive for freeze-thaw resistance in both cement paste and concrete.

References

1. *2017 Report Card for America's Infrastructure*. (American Society of Civil Engineers, 2017). doi:10.1061/9780784478837.

2. Shah, H. A., Yuan, Q. & Zuo, S. Air entrainment in fresh concrete and its effects on hardened concrete-a review. *Constr. Build. Mater.* 121835 (2020) doi:10.1016/j.conbuildmat.2020.121835.

3. Sabir, B. B. Mechanical properties and frost resistance of silica fume concrete. *Cem. Concr. Compos.* **19**, 285–294 (1997).

4. Duan, P., Shui, Z., Chen, W. & Shen, C. Enhancing microstructure and durability of concrete from ground granulated blast furnace slag and metakaolin as cement replacement materials. *J. Mater. Res. Technol.* **2**, 52–59 (2013).

5. Behfarnia, K. & Salemi, N. The effects of nano-silica and nano-alumina on frost resistance of normal concrete. *Constr. Build. Mater.* **48**, 580–584 (2013).

6. Gonzalez, M., Tighe, S. L., Hui, K., Rahman, S. & de Oliveira Lima, A. Evaluation of freeze/thaw and scaling response of nanoconcrete for Portland Cement Concrete (PCC) pavements. *Constr. Build. Mater.* **120**, 465–472 (2016).

7. Laustsen, S., Hasholt, M. T. & Jensen, O. M. Void structure of concrete with superabsorbent polymers and its relation to frost resistance of concrete. *Mater. Struct.* **48**, 357–368 (2015).

8. Hasholt, M. T., Jensen, O. M. & Laustsen, S. Superabsorbent Polymers as a Means of Improving Frost Resistance of Concrete. *Adv. Civ. Eng. Mater.* **4**, 20150012 (2015).

9. Nam, J., Kim, G., Lee, B., Hasegawa, R. & Hama, Y. Frost resistance of polyvinyl alcohol fiber and polypropylene fiber reinforced cementitious composites under freeze thaw cycling. *Compos. Part B Eng.* **90**, 241–250 (2016).

10. Wang, S. & Li, V. C. Polyvinyl alcohol fiber reinforced engineered cementitious composites: material design and performances. in *Proceedings of International RILEM workshop on HPFRCC in structural applications* 65–73 (RILEM SARL, 2006).

11. Di Mundo, R., Labianca, C., Carbone, G. & Notarnicola, M. Recent Advances in Hydrophobic and Icephobic Surface Treatments of Concrete. *Coatings* **10**, 449 (2020).

12. Feng, Z. *et al.* Integral hydrophobic concrete without using silane. *Constr. Build. Mater.* **227**, 116678 (2019).

13. Monteiro, P. J. M., Miller, S. A. & Horvath, A. Towards sustainable concrete. *Nat. Mater.* **16**, 698–699 (2017).

14. Ready Mixed Concrete Volume & Price Trends. *Concrete Financial Insights* https://concretefinancialinsights.com/us-concrete-industry-data.

15. Concrete Price Considerations - Cost of Concrete: How much does concrete cost? *ConcreteNetwork.com* https://www.concretenetwork.com/concrete-prices.html (2020).

16. Cement & Concrete: Products. *Portland Cement Association* https://www.cement.org/cement-concrete/products.

17. How Concrete is Made. *Portland Cement Association* https://www.cement.org/cement-concrete/how-concrete-is-made.

18. C09 Committee. *Specification for Concrete Aggregates*. http://www.astm.org/cgi-bin/resolver.cgi?C33C33M-18 (2018) doi:10.1520/C0033_C0033M-18.

19. Mehta, P. Kumar & Monteiro, Paulo J. M. *Concrete: Microstructure, properties, and materials*. (McGraw-Hill, 2006).

20. Cachim, P. B. Mechanical properties of brick aggregate concrete. *Constr. Build. Mater.* **23**, 1292–1297 (2009).

21. Davis, S. J. *et al.* Net-zero emissions energy systems. *Science* **360**, eaas9793 (2018).

22. Andrew, R. M. Global CO2 emissions from cement production. *Open Access* 52 (2017).

23. Miller, S. A., Horvath, A. & Monteiro, P. J. M. Readily implementable techniques can cut annual CO $_2$ emissions from the production of concrete by over 20%. *Environ. Res. Lett.* **11**, 074029 (2016).

24. Miller, S. A., Horvath, A. & Monteiro, P. J. M. Impacts of booming concrete production on water resources worldwide. *Nat. Sustain.* **1**, 69–76 (2018).

25. P. Kumar Mehta and Ben C. Gerwick, Jr. Cracking-Corrosion Interaction in Concrete Exposed to Marine Environment. *Concr. Int.* **4**, (1982).

26. Emmons, P. H. & Sordyl, D. J. The State of the Concrete Repair Industry, and a Vision for its Future. *Concrete Repair Bulletin* vol. July-August 2006 7–14 (2006).

27. Kumar, R. & Bhattacharjee, B. Porosity, pore size distribution and in situ strength of concrete. *Cem. Concr. Res.* **33**, 155–164 (2003).

28. Aligizaki, K. K. *Pore structure of cement-based materials: testing, interpretation and requirements*. (Taylor & Francis, 2006).

29. Berodier, E., Bizzozero, J. & Muller, A. C. A. Mercury intrusion porosimetry. in *A Practical Guide to Microstructural Analysis of Cementitious Materials* (eds. Scrivener, K., Snellings, R., Lothenbach, B.) 419-444 (CRC Press, 2016).

30. Sant, G., Bentz, D. & Weiss, J. Capillary porosity depercolation in cement-based materials: Measurement techniques and factors which influence their interpretation. *Cem. Concr. Res.* **41**, 854–864 (2011).

31. Aligizak, K. K. Introduction. in *Pore Structure of Cement-Based Materials: Testing, Interpretation and Requirements.* 1–33 (CRC Press, 2014).

32. Seong, H. Effect of entrained air voids. 21.

33. Atahan, H. N., Carlos, C., Chae, S., Monteiro, P. J. M. & Bastacky, J. The morphology of entrained air voids in hardened cement paste generated with different anionic surfactants. *Cem. Concr. Compos.* **30**, 566–575 (2008).

34. Chen, X. & Wu, S. Influence of water-to-cement ratio and curing period on pore structure of cement mortar. *Constr. Build. Mater.* **38**, 804–812 (2013).

35. Cook, R. A. & Hover, K. C. Mercury porosimetry of hardened cement pastes. *Cem. Concr. Res.* **29**, 933–943 (1999).

36. Powers, T. C. Structure and Physical Properties of Hardened Portland Cement Paste. *J. Am. Ceram. Soc.* **41**, 1–6 (1958).

37. Zhang, J. & Taylor, P. C. Pore Size Distribution in Cement Pastes in Relation to Freeze-Thaw Distress. *J. Mater. Civ. Eng.* **27**, 04014123 (2015).

38. Neville, A. M. *Properties of concrete*. (Pearson, 2011).

39. Feldman, R. F. & Sereda, P. J. A model for hydrated Portland cement paste as deduced from sorption-length change and mechanical properties. *Matér. Constr.* **1**, 509–520 (1968).

40. Meng, K. R., B. & Müller, U. Investigating the original water content of concrete. in *Non-Destructive Evaluation of Reinforced Concrete Structures* 217–241 (Elsevier, 2010). doi:10.1533/9781845699536.2.217.

41. Sellevold, E. J. & Bjøntegaard, Ø. Coefficient of thermal expansion of cement paste and concrete: Mechanisms of moisture interaction. *Mater. Struct.* **39**, 809–815 (2006).

42. Jennings, H. M. A model for the microstructure of calcium silicate hydrate in cement paste. *Cem. Concr. Res.* **30**, 101–116 (2000).

43. Powers, T. C. Void Spacing as a Basis for Producing Air-Entrained Concrete. *J. Am. Concr. Inst.* **25**, 741–760 (1954).

44. Powers, T. C. The air requirement of frost-resistant concrete. *Highw. Res. Board Proc.* **29**, 184–211 (1949).

45. Powers, T. C. Freezing Effects In Concrete. *ACI Symposium Publication.* **47**, 1–12 (1975).

46. Litvan, G. G. Frost action in cement paste. *Matér. Constr.* **6**, 293–298 (1973).

47. Litvan, G. G. Frost action in cement in the presence of De-Icers. *Cem. Concr. Res.* **6**, 351–356 (1976).

48. Litvan, G. Freeze-Thaw Durability of Porous Building Materials. in *Durability of Building Materials and Components* (eds. Sereda, P. & Litvan, G.) 455-455–9 (ASTM International, 1980). doi:10.1520/STP36080S.

49. Scherer, G. W. & Valenza, J. J. Mechanisms of Frost Damage. in *Materials Science of Concrete, Vol. VIII* (eds. Skalny, J. & Young, F.) (American Ceramic Society, 2005).

50. Pigeon, M. & Pleau, R. *Durability of concrete in cold climates*. (Spon, 1995).

51. T. C. Powers. A Working Hypothesis for Further Studies of Frost Resistance of Concrete. *ACI J. Proc.* **41**, (1945).

52. Whitaker, S. Flow in porous media I: A theoretical derivation of Darcy's law. *Transp. Porous Media* **1**, 3–25 (1986).

53. Darcy, H. (1803-1858). Les fontaines publiques de la ville de Dijon : exposition et application des principes à suivre et des formules à employer dans les questions de distribution d'eau. / par Henry Darcy. (1856).

54. C09 Committee. *Test Method for Microscopical Determination of Parameters of the Air-Void System in Hardened Concrete*. http://www.astm.org/cgi-bin/resolver.cgi?C457C457M-16 (2016) doi:10.1520/C0457_C0457M-16.

55. Powers, T. C. & Helmuth, R. A. Theory of volume changes in hardened portland cement paste during freezing. *Highw. Res. Board Proc.* **32**, 285–297 (1953).

56. Lindmark, S. Mechanisms of salt frost scaling of Portland cement-bound materials: studies and hypothesis. (1998).

57. Michel Pigeon, B. Z. & Marchand, J. Freeze/thaw resistance. in *Advanced Concrete Technology* 1–17 (Elsevier, 2003). doi:10.1016/B978-075065686-3/50258-5.

58. Litvan, G. G. Phase Transitions of Adsorbates: IV, Mechanism of Frost Action in Hardened Cement Paste. *J. Am. Ceram. Soc.* **55**, 38–42 (1972).

59. Litvan, G. G. Phase Transitions of Adsorbates: VI, Effect of Deicing Agents on the Freezing of Cement Paste. *J. Am. Ceram. Soc.* **58**, 26–30 (1975).

60. Scherer, G. W. Crystallization in pores. *Cem. Concr. Res.* **29**, 1347–1358 (1999).

61. Israelachvili, J. N. *Intermolecular and surface forces*. (Academic Press London, 1991).

62. Pigeon, M., Prevost, J. & Simard, J.-M. Freeze-Thaw Durability Versus Freezing Rate. 9 (1985).

63. Fagerlund, G. Effect of the freezing rate on the frost resistance of concrete. *Nordic Concrete Research Publication No. 11*. 20-36 (1992).

64. Ge, X., Lu, C. & Mei, G. Study on frost resistance durability and bubble parameters of high air content concrete under different freezing rate. *IOP Conf. Ser. Mater. Sci. Eng.* **490**, 032030 (2019).

65. Jacobsen, S., Sœther, D. H. & Sellevold, E. J. Frost testing of high strength concrete: Frost/salt scaling at different cooling rates. *Mater. Struct.* **30**, 33–42 (1997).

66. Beaudoin, J. J. & MacInnis, C. Dimensional changes of hydrated portland cement paste during slow cooling and warming. *Cem. Concr. Res.* **2**, 225–240 (1972).

67. Bentz, D. P., Ehlen, M. A., Ferraris, C. F. & Garboczi, E. J. Sorptivity-based service life predictions for concrete pavements. in *7th Int. Conf. on Concrete Pavements* 181–193 (NIST, 2001).

68. Li, W., Pour-Ghaz, M., Castro, J. & Weiss, J. Water Absorption and Critical Degree of Saturation Relating to Freeze-Thaw Damage in Concrete Pavement Joints. *J. Mater. Civ. Eng.* **24**, 299–307 (2012).

69. Fagerlund, G. Criticdal degrees of saturation at freezing of porous and brittle materials. 11.

70. Fagerlund, G. The international cooperative test of the critical degree of saturation method of assessing the freeze/thaw resistance of concrete. *Matér. Constr.* **10**, 231–253 (1977).

71. Ghantous, R. M., Moradllo, M. K., Becker, H. H., Ley, M. T. & Weiss, W. J. Determining the freeze-thaw performance of mortar samples using length change measurements during freezing. *Cem. Concr. Compos.* **116**, 103869 (2021).

72. Todak, H., Lucero, C. & Weiss, J. W. Why is the air there? Thinking about freeze-thaw in terms of saturation. *Concrete InFocus* 3–7 (2015).

73. Liu, Z. & Hansen, W. A geometrical model for void saturation in air-entrained concrete under continuous water exposure. *Constr. Build. Mater.* **124**, 475–484 (2016).

74. Weiss, J. W. Relating Transport Properties to Performance in Concrete Pavements. (2014).

75. Eisenberg, D. & Kauzmann, W. *The structure and properties of water*. (Oxford University Press on Demand, 2005).

76. Structure and energy of ordinary ice. in *The Chemical Physics of Ice* (ed. Fletcher, N. H.) 23–48 (Cambridge University Press, 1970). doi:10.1017/CBO9780511735639.004.

77. Budke, C. & Koop, T. Ice Recrystallization Inhibition and Molecular Recognition of Ice Faces by Poly(vinyl alcohol). *ChemPhysChem* **7**, 2601–2606 (2006).

78. Momma, K. & Izumi, F. ıt VESTA3 for three-dimensional visualization of crystal, volumetric and morphology data. *J. Appl. Crystallogr.* **44**, 1272–1276 (2011).

79. Tanaka, K. K. & Kimura, Y. Theoretical analysis of crystallization by homogeneous nucleation of water droplets. *Phys. Chem. Chem. Phys.* **21**, 2410–2418 (2019).

80. Zhang, Z. & Liu, X.-Y. Control of ice nucleation: freezing and antifreeze strategies. *Chem. Soc. Rev.* **47**, 7116–7139 (2018).

81. Mitchell, D. E., Lovett, J. R., Armes, S. P. & Gibson, M. I. Combining Biomimetic Block Copolymer Worms with an Ice-Inhibiting Polymer for the Solvent-Free Cryopreservation of Red Blood Cells. *Angew. Chem. Int. Ed.* **55**, 2801–2804 (2016).

82. Knight, C. A. & Duman, J. G. Inhibition of recrystallization of ice by insect thermal hysteresis proteins: A possible cryoprotective role. *Cryobiology* **23**, 256–262 (1986).

83. Mitchell, D. E. *et al.* Ice-recrystallization inhibiting polymers protect proteins against freeze-stress and enable glycerol-free cryostorage. *Mater. Horiz.* **6**, 364–368 (2019).

84. Regand, A. & Goff, H. D. Ice Recrystallization Inhibition in Ice Cream as Affected by Ice Structuring Proteins from Winter Wheat Grass. *J. Dairy Sci.* **89**, 49–57 (2006).

85. Regand, A. & Goff, H. D. Structure and ice recrystallization in frozen stabilized ice cream model systems. *Food Hydrocoll.* **17**, 95–102 (2003).

86. Petzold, G. & Aguilera, J. M. Ice Morphology: Fundamentals and Technological Applications in Foods. *Food Biophys.* **4**, 378–396 (2009).

87. Alley, R. B., Perepezko, J. H. & Bentley, C. R. Grain Growth in Polar Ice: I. Theory. *J. Glaciol.* **32**, 415–424 (1986).

88. Duval, P. *et al.* Creep and plasticity of glacier ice: a material science perspective. *J. Glaciol.* **56**, 1059–1068 (2010).

89. Rempel, A. W., Waddington, E. D., Wettlaufer, J. S. & Worster, M. G. Possible displacement of the climate signal in ancient ice by premelting and anomalous diffusion. *Nature* **411**, 568–571 (2001).

90. *Antifreeze Proteins Volume 2: Biochemistry, Molecular Biology and Applications*. (Springer International Publishing, 2020). doi:10.1007/978-3-030-41948-6.

91. Sibley, D. N., Llombart, P., Noya, E. G., Archer, A. J. & MacDowell, L. G. How ice grows from premelting films and water droplets. *Nat. Commun.* **12**, 239 (2021).

92. Qiu, Y. & Molinero, V. Why Is It So Difficult to Identify the Onset of Ice Premelting? *J. Phys. Chem. Lett.* **9**, 5179–5182 (2018).

93. Benet, J., Llombart, P., Sanz, E. & MacDowell, L. G. Premelting-Induced Smoothening of the Ice-Vapor Interface. *Phys Rev Lett* **117**, 096101 (2016).

94. Chen, J., Maki, T., Nagashima, K., Murata, K. & Sazaki, G. Quasi-liquid Layers in Grooves of Grain Boundaries and on Grain Surfaces of Polycrystalline Ice Thin Films. *Cryst. Growth Des.* **20**, 7188–7196 (2020).

95. Kling, T., Kling, F. & Donadio, D. Structure and Dynamics of the Quasi-Liquid Layer at the Surface of Ice from Molecular Simulations. *J. Phys. Chem. C* **122**, 24780–24787 (2018).

96. Elbaum, M., Lipson, S. G. & Dash, J. G. Optical study of surface melting on ice. *J. Cryst. Growth* **129**, 491–505 (1993).

97. Wei, X., Miranda, P. B. & Shen, Y. R. Surface Vibrational Spectroscopic Study of Surface Melting of Ice. *Phys Rev Lett* **86**, 1554–1557 (2001).

98. Bluhm, H., Ogletree, D. F., Fadley, C. S., Hussain, Z. & Salmeron, M. The premelting of ice studied with photoelectron spectroscopy. *J. Phys. Condens. Matter* **14**, L227–L233 (2002).

99. Li, C. *et al.* Amphiphilic Antifogging/Anti-Icing Coatings Containing POSS-PDMAEMA- *b* -PSBMA. *ACS Appl. Mater. Interfaces* **9**, 22959–22969 (2017).

100. Chen, D., Gelenter, M. D., Hong, M., Cohen, R. E. & McKinley, G. H. Icephobic Surfaces Induced by Interfacial Nonfrozen Water. *ACS Appl. Mater. Interfaces* **9**, 4202–4214 (2017).

101. Bar Dolev, M., Braslavsky, I. & Davies, P. L. Ice-Binding Proteins and Their Function. *Annu. Rev. Biochem.* **85**, 515–542 (2016).

102. Duman, J. G., Bennett, V., Sformo, T., Hochstrasser, R. & Barnes, B. M. Antifreeze proteins in Alaskan insects and spiders. *J. Insect Physiol.* **50**, 259–266 (2004).

103. Graham, L. A., Liou, Y.-C., Walker, V. K. & Davies, P. L. Hyperactive antifreeze protein from beetles. *Nature* **388**, 727–728 (1997).

104. Tyshenko', M. G., Doucet', D., Davies, P. L. & Walker', V. K. The antifreeze potential of the spruce budworn1 thern1al hysteresis protein. **15**, 4 (1997).

105. Duman, J. G. Animal ice-binding (antifreeze) proteins and glycolipids: an overview with emphasis on physiological function. *J. Exp. Biol.* **218**, 1846–1855 (2015).

106. Griffith, M. & Yaish, M. W. F. Antifreeze proteins in overwintering plants: a tale of two activities. *Trends Plant Sci.* **9**, 399–405 (2004).

107. Raymond, J. A., Fritsen, C. & Shen, K. An ice-binding protein from an Antarctic sea ice bacterium: Bacterial ice-binding protein. *FEMS Microbiol. Ecol.* **61**, 214–221 (2007).

108.   Guo, S., Garnham, C. P., Whitney, J. C., Graham, L. A. & Davies, P. L. Re-Evaluation of a Bacterial Antifreeze Protein as an Adhesin with Ice-Binding Activity. *PLoS ONE* **7**, e48805 (2012).

109.   Guo, S. *et al.* Role of Ca $^{2+}$ in folding the tandem β-sandwich extender domains of a bacterial ice-binding adhesin. *FEBS J.* **280**, 5919–5932 (2013).

110.   Bar Dolev, M., Bernheim, R., Guo, S., Davies, P. L. & Braslavsky, I. Putting life on ice: bacteria that bind to frozen water. *J. R. Soc. Interface* **13**, 20160210 (2016).

111.   Raymond, J. A., Janech, M. G. & Fritsen, C. H. Novel Ice-Binding Proteins from a Psychrophilic Antarctic Alga (Chlamydomonadaceae, Chlorophyceae). *J. Phycol.* **45**, 130–136 (2009).

112.   Raymond, J. A., Christner, B. C. & Schuster, S. C. A bacterial ice-binding protein from the Vostok ice core. *Extremophiles* **12**, 713–717 (2008).

113.   Wilson, S. L., Kelley, D. L. & Walker, V. K. Ice-active characteristics of soil bacteria selected by ice-affinity. *Environ. Microbiol.* **8**, 1816–1824 (2006).

114.   Green, R. L. & Warren, G. J. Physical and functional repetition in a bacterial ice nucleation gene. *Nature* **317**, 645–648 (1985).

115.   Garnham, C. P., Campbell, R. L., Walker, V. K. & Davies, P. L. Novel dimeric β-helical model of an ice nucleation protein with bridged active sites. *BMC Struct. Biol.* **11**, 36 (2011).

116.   Davies, P. L. Ice-binding proteins: a remarkable diversity of structures for stopping and starting ice growth. *Trends Biochem. Sci.* **39**, 548–555 (2014).

117.   Duman, J. G. & Olsen, T. M. Thermal Hysteresis Protein Activity in Bacteria, Fungi, and Phylogenetically Diverse Plants. *Cryobiology* **30**, 322–328 (1993).

118. Moffatt, B., Ewart, V. & Eastman, A. Cold comfort: plant antifreeze proteins. *Physiol. Plant.* **126**, 5–16 (2006).

119. Atıcı, Ö. & Nalbantoğlu, B. Antifreeze proteins in higher plants. *Phytochemistry* **64**, 1187–1196 (2003).

120. Ewart, K. V. & Hew, C. L. *Fish antifreeze proteins*. vol. 1. (World Scientific, 2002).

121. Fletcher, G. L., Hew, C. L. & Davies, P. L. Antifreeze Proteins of Teleost Fishes. *Annu. Rev. Physiol.* **63**, 359–390 (2001).

122. DeVries, A. L. Fish Antifreeze Proteins. in *Antifreeze Proteins Volume 1* (eds. Ramløv, H. & Friis, D. S.) 85–129 (Springer International Publishing, 2020). doi:10.1007/978-3-030-41929-5_5.

123. Duman, J. G. & Newton, S. S. Insect Antifreeze Proteins. in *Antifreeze Proteins Volume 1: Environment, Systematics and Evolution* (eds. Ramløv, H. & Friis, D. S.) 131–187 (Springer International Publishing, 2020). doi:10.1007/978-3-030-41929-5_6.

124. Hoshino, T. *et al.* Antifreeze proteins from snow mold fungi. *Can. J. Bot.* **81**, 1175–1181 (2003).

125. Ruisi, S., Barreca, D., Selbmann, L., Zucconi, L. & Onofri, S. Fungi in Antarctica. *Rev. Environ. Sci. Biotechnol.* **6**, 127–141 (2007).

126. Gwak, I. G., sic Jung, W., Kim, H. J., Kang, S.-H. & Jin, E. Antifreeze Protein in Antarctic Marine Diatom, Chaetoceros neogracile. *Mar. Biotechnol.* **12**, 630–639 (2010).

127. Bayer-Giraldi, M., Weikusat, I., Besir, H. & Dieckmann, G. Characterization of an antifreeze protein from the polar diatom Fragilariopsis cylindrus and its relevance in sea ice. *Cryobiology* **63**, 210–219 (2011).

128. Wisniewski, M., Willick, I. R., Duman, J. G., Livingston, D. & Newton, S. S. Plant Antifreeze Proteins. in *Antifreeze Proteins Volume 1* (eds. Ramløv, H. & Friis, D. S.) 189–226 (Springer International Publishing, 2020). doi:10.1007/978-3-030-41929-5_7.

129. Gilbert, J. A., Hill, P. J., Dodd, C. E. R. & Laybourn-Parry, J. Demonstration of antifreeze protein activity in Antarctic lake bacteria. *Microbiology* **150**, 171–180 (2004).

130. Wang, C., Pakhomova, S., Newcomer, M. E., Christner, B. C. & Luo, B.-H. Structural basis of antifreeze activity of a bacterial multi-domain antifreeze protein. *PLOS ONE* **12**, e0187169 (2017).

131. Garnham, C. P. *et al.* A Ca2+-dependent bacterial antifreeze protein domain has a novel β-helical ice-binding fold. *Biochem. J.* **411**, 171–180 (2008).

132. Voets, I. K. From ice-binding proteins to bio-inspired antifreeze materials. *Soft Matter* **13**, 4808–4823 (2017).

133. Hudait, A. *et al.* Preordering of water is not needed for ice recognition by hyperactive antifreeze proteins. *Proc. Natl. Acad. Sci.* **115**, 8266–8271 (2018).

134. Hudait, A., Odendahl, N., Qiu, Y., Paesani, F. & Molinero, V. Ice-Nucleating and Antifreeze Proteins Recognize Ice through a Diversity of Anchored Clathrate and Ice-like Motifs. *J. Am. Chem. Soc.* **140**, 4905–4912 (2018).

135. Marks, S. M. & Patel, A. J. Antifreeze protein hydration waters: Unstructured unless bound to ice. *Proc. Natl. Acad. Sci.* **115**, 8244–8246 (2018).

136. Venketesh, S. & Dayananda, C. Properties, Potentials, and Prospects of Antifreeze Proteins. *Crit. Rev. Biotechnol.* **28**, 57–82 (2008).

137.   Eskandari, A., Leow, T. C., Rahman, M. B. A. & Oslan, S. N. Antifreeze Proteins and Their Practical Utilization in Industry, Medicine, and Agriculture. *Biomolecules* **10**, 1649 (2020).

138.   Ptitsyn, OlegB. Protein folding: Hypotheses and experiments. *J. Protein Chem.* **6**, (1987).

139.   Delesky, E. *et al.* Ice-Binding Protein from Shewanella frigidimarinas Inhibits Ice Crystal Growth in Highly Alkaline Solutions. *Polymers* **11**, 299 (2019).

140.   Congdon, T., Notman, R. & Gibson, M. I. Antifreeze (Glyco)protein Mimetic Behavior of Poly(vinyl alcohol): Detailed Structure Ice Recrystallization Inhibition Activity Study. *Biomacromolecules* **14**, 1578–1586 (2013).

141.   Bai, G. *et al.* Oxidized Quasi-Carbon Nitride Quantum Dots Inhibit Ice Growth. *Adv. Mater.* **29**, 1606843 (2017).

142.   Drori, R. *et al.* A Supramolecular Ice Growth Inhibitor. *J. Am. Chem. Soc.* **138**, 13396–13401 (2016).

143.   Trant, J. F., Biggs, R. A., Capicciotti, C. J. & Ben, R. N. Developing highly active small molecule ice recrystallization inhibitors based upon C-linked antifreeze glycoprotein analogues. *RSC Adv.* 5 (2013).

144.   Surís-Valls & Voets. Peptidic Antifreeze Materials: Prospects and Challenges. *Int. J. Mol. Sci.* **20**, 5149 (2019).

145.   Frazier, S. D. *et al.* Inhibiting Freeze-Thaw Damage in Cement Paste and Concrete by Mimicking Nature's Antifreeze. *Cell Rep. Phys. Sci.* **1**, 100060 (2020).

146.   Muzenski, S., Flores-Vivian, I. & Sobolev, K. Durability of superhydrophobic engineered cementitious composites. *Constr. Build. Mater.* **81**, 291–297 (2015).

147. Falchi, L., Zendri, E., Müller, U. & Fontana, P. The influence of water-repellent admixtures on the behaviour and the effectiveness of Portland limestone cement mortars. *Cem. Concr. Compos.* **59**, 107–118 (2015).

148. Liu, Z. & Hansen, W. Effect of hydrophobic surface treatment on freeze-thaw durability of concrete. *Cem. Concr. Compos.* **69**, 49–60 (2016).

149. C09 Committee. *Test Method for Resistance of Concrete to Rapid Freezing and Thawing*. http://www.astm.org/cgi-bin/resolver.cgi?C666C666M-15 doi:10.1520/C0666_C0666M-15.

150. AASHTO T 161. *Standard Method of Test for Resistance of Concrete to Rapid Freezing and Thawing*. (2017).

151. Kuosa, H., Ferreria, M. & Leivo, M. *Freeze-thaw testing CSLA Project - Task 1. Literature Review*. (2013).

152. Riyazi, S. Entrained Air-void System for Durable Highway Concrete. (ProQuest Dissertations Publishing, 2020).

153. Jones, W. & Weiss, W. J. Freeze Thaw Durability of Internally Cured Concrete Made Using Superabsorbent Polymers. in *Proceedings of the 4th International Conference on the Durability of Concrete Structures* 3–11 (Purdue University Libraries Scholarly Publishing Services, 2014). doi:10.5703/1288284315376.

154. Al Rikabi, F. T., Sargand, S. M., Khoury, I. & Hussein, H. H. Material Properties of Synthetic Fiber–Reinforced Concrete under Freeze-Thaw Conditions. *J. Mater. Civ. Eng.* **30**, 04018090 (2018).

155. Wedding, P. & Malhotra, V. Mechanical Properties and Freezing and Thawing Resistance of Non-Air-Entrained, Air-Entrained, and Air-Entrained Superplasticized Concrete Using ASTM Test C 666, Procedures A and B. *Cem. Concr. Aggreg.* **4**, 3 (1982).

156.   Wang, K., Lomboy, G. & Steffes, R. Investigation into Freezing-Thawing Durability of Low-Permeability Concrete with and without Air Entraining Agent. 45.

157.   Tanesi, J. & Meininger, R. Freeze-Thaw Resistance of Concrete with Marginal Air Content. *Transp. Res. Rec.* **2020**, 61–66 (2007).

158.   Ley, M. T., Welchel, D., Peery, J., Khatibmasjedi, S. & LeFlore, J. Determining the air-void distribution in fresh concrete with the Sequential Air Method. *Constr. Build. Mater.* **150**, 723–737 (2017).

159.   Hover, K. C. Air Content and Density of Hardened Concrete. in *Significance of Tests and Properties of Concrete and Concrete-Making Materials* (eds. Lamond, J. & Pielert, J.) 288–308 (ASTM International, 2006). doi:10.1520/STP169D-EB.

160.   Ley, M. T., Chancey, R., Juenger, M. C. G. & Folliard, K. J. The physical and chemical characteristics of the shell of air-entrained bubbles in cement paste. *Cem. Concr. Res.* **39**, 417–425 (2009).

161.   Microscopic Characterization of Ice Morphology in Entrained Air Voids. *ACI Mater. J.* **99**, (2002).

162.   Tunstall, L. E., Scherer, G. W. & Prud'homme, R. K. Studying AEA interaction in cement systems using tensiometry. *Cem. Concr. Res.* 8 (2017).

163.   Chatterji, S. Freezing of air-entrained cement-based materials and specific actions of air-entraining agents. *Cem. Concr. Compos.* **25**, 759–765 (2003).

164.   Cannon, R. C. New technologies for the improvement of concrete properties with application in catalysis and homeland security. (ProQuest Dissertations Publishing, 2014).

165. Cannon, C., Tepper, J., Apblett, A. & Ley, M. T. Investigation of the Effectiveness of Surfactants with Different Partition Coefficients to Entrain Air in Cement Paste. *Adv. Civ. Eng. Mater.* **5**, 20150025 (2016).

166. Chen, J. *et al.* Cationic oligomeric surfactants as novel air entraining agents for concrete. *Colloids Surf. Physicochem. Eng. Asp.* **538**, 686–693 (2018).

167. C09 Committee. *Test Method for Air Content of Freshly Mixed Concrete by the Pressure Method*. http://www.astm.org/cgi-bin/resolver.cgi?C231C231M-17A doi:10.1520/C0231_C0231M-17A.

168. ACI Committee 201. *Guide to Durable Concrete*. (American Concrete Institute, 2016).

169. Lu, H., Peterson, K. & Chernoloz, O. Measurement of entrained air-void parameters in Portland cement concrete using micro X-ray computed tomography. *Int. J. Pavement Eng.* **19**, 109–121 (2018).

170. Koenig, A. Analysis of air voids in cementitious materials using micro X-ray computed tomography (μXCT). *Constr. Build. Mater.* **244**, 118313 (2020).

171. Mehta, P., Khayat, K. & Nasser, K. Comparison of Air Contents in Fresh and Hardened Concretes Using Different Airmeters. *Cem. Concr. Aggreg.* **13**, 18 (1991).

172. Gagné, R. Air entraining agents. in *Science and Technology of Concrete Admixtures* 379–391 (Elsevier, 2016). doi:10.1016/B978-0-08-100693-1.00017-5.

173. Pigeon, M., Marchand, J. & Pleau, R. Frost resistant concrete. *Durab. Reinf. Concr. Struct.* **10**, 339–348 (1996).

174. Taylor, P. *et al. Entrained Air-Void Systems for Durable Highway Concrete*. 26071 (Transportation Research Board, 2021). doi:10.17226/26071.

175.   Wang, K. Improving Variability and Precision of Air-Void Analyzer (AVA) Test Results and Developing Rational Specification Limits. 100 (2008).

176.   Wong, H. S., Pappas, A. M., Zimmerman, R. W. & Buenfeld, N. R. Effect of entrained air voids on the microstructure and mass transport properties of concrete. *Cem. Concr. Res.* **41**, 1067–1077 (2011).

177.   Kalhori, H., Bagherzadeh, B., Bagherpour, R. & Akhlaghi, M. A. Experimental study on the influence of the different percentage of nanoparticles on strength and freeze–thaw durability of shotcrete. *Constr. Build. Mater.* **256**, 119470 (2020).

178.   Funk, B. *et al.* Impact of freeze–thaw weathering on integrity, internal structure and particle release from micro- and nanostructured cement composites. *Environ. Sci. Nano* **6**, 1443–1456 (2019).

179.   Rashad, A. M. Effect of carbon nanotubes (CNTs) on the properties of traditional cementitious materials. *Constr. Build. Mater.* **153**, 81–101 (2017).

180.   Tian, W. & Gao, F. Effect of Carbon Nanotubes' Diameter on Freeze-Thaw Resistance of Cement Paste. *J. Mech.* **36**, 437–449 (2020).

181.   Li, W.-W. *et al.* Investigation on the Mechanical Properties of a Cement-Based Material Containing Carbon Nanotube under Drying and Freeze-Thaw Conditions. *Materials* **8**, 8780–8792 (2015).

182.   Qing, Y., Zenan, Z., Li, S. & Rongshen, C. A comparative study on the pozzolanic activity between nano-SiO2 and silica fume. *J. Wuhan Univ. Technol.-Mater Sci Ed* **21**, 153–157 (2006).

183.   Li, H., Xiao, H., Yuan, J. & Ou, J. Microstructure of cement mortar with nano-particles. *Compos. Part B Eng.* **35**, 185–189 (2004).

184.   Stefanidou, M. & Papayianni, I. Influence of nano-SiO2 on the Portland cement pastes. *Compos. Part B Eng.* **43**, 2706–2710 (2012).

185.   Jo, B.-W., Kim, C.-H., Tae, G. & Park, J.-B. Characteristics of cement mortar with nano-SiO2 particles. *Constr. Build. Mater.* **21**, 1351–1355 (2007).

186.   *Nanotechnology in Construction 3*. (Springer Berlin Heidelberg, 2009). doi:10.1007/978-3-642-00980-8.

187.   Sáez de Ibarra, Y., Gaitero, J. J., Erkizia, E. & Campillo, I. Atomic force microscopy and nanoindentation of cement pastes with nanotube dispersions. *Phys. Status Solidi A* **203**, 1076–1081 (2006).

188.   Konsta-Gdoutos, M. S., Metaxa, Z. S. & Shah, S. P. Highly dispersed carbon nanotube reinforced cement based materials. *Cem. Concr. Res.* **40**, 1052–1059 (2010).

189.   *Nanotechnology in Construction: Proceedings of NICOM5*. (Springer International Publishing, 2015). doi:10.1007/978-3-319-17088-6.

190.   Konsta-Gdoutos, M. S., Metaxa, Z. S. & Shah, S. P. Multi-scale mechanical and fracture characteristics and early-age strain capacity of high performance carbon nanotube/cement nanocomposites. *Cem. Concr. Compos.* **32**, 110–115 (2010).

191.   Xu, S., Liu, J. & Li, Q. Mechanical properties and microstructure of multi-walled carbon nanotube-reinforced cement paste. *Constr. Build. Mater.* **76**, 16–23 (2015).

192.   Collins, F., Lambert, J. & Duan, W. H. The influences of admixtures on the dispersion, workability, and strength of carbon nanotube–OPC paste mixtures. *Cem. Concr. Compos.* **34**, 201–207 (2012).

193.   Mardani-Aghabaglou, A., İnan Sezer, G. & Ramyar, K. Comparison of fly ash, silica fume and metakaolin from mechanical properties and durability performance of mortar mixtures view point. *Constr. Build. Mater.* **70**, 17–25 (2014).

194.   Mardani-Aghabaglou, A., Andiç-Çakir, Ö. & Ramyar, K. Freeze–thaw resistance and transport properties of high-volume fly ash roller compacted concrete designed by maximum density method. *Cem. Concr. Compos.* **37**, 259–266 (2013).

195.   Hooton, R. D. Influence of Silica Fume Replacement of Cement on Physical Properties and Resistance to Sulfate Attack, Freezing and Thawing, and Alkali-Silica Reactivity. *ACI Mater. J.* **90**, (1993).

196.   Toutanji, H., Delatte, N., Aggoun, S., Duval, R. & Danson, A. Effect of supplementary cementitious materials on the compressive strength and durability of short-term cured concrete. *Cem. Concr. Res.* **34**, 311–319 (2004).

197.   Panesar, D. K. Supplementary cementing materials. in *Developments in the Formulation and Reinforcement of Concrete* 55–85 (Elsevier, 2019). doi:10.1016/B978-0-08-102616-8.00003-4.

198.   Ebrahimi, K., Daiezadeh, M. J., Zakertabrizi, M., Zahmatkesh, F. & Habibnejad Korayem, A. A review of the impact of micro- and nanoparticles on freeze-thaw durability of hardened concrete: Mechanism perspective. *Constr. Build. Mater.* **186**, 1105–1113 (2018).

199.   Duval, R. & Kadri, E. H. Influence of Silica Fume on the Workability and the Compressive Strength of High-Performance Concretes. *Cem. Concr. Res.* **28**, 533–547 (1998).

200. Diaz-Loya, I., Juenger, M., Seraj, S. & Minkara, R. Extending supplementary cementitious material resources: Reclaimed and remediated fly ash and natural pozzolans. *Cem. Concr. Compos.* **101**, 44–51 (2019).

201. Juenger, M. C. G., Snellings, R. & Bernal, S. A. Supplementary cementitious materials: New sources, characterization, and performance insights. *Cem. Concr. Res.* **122**, 257–273 (2019).

202. Kim, I. S., Choi, S. Y., Choi, Y. S. & Yang, E. I. An experimental study on absorptivity measurement of superabsorbent polymers (SAP) and effect of SAP on freeze-thaw resistance in mortar specimen. *Constr. Build. Mater.* **267**, 120974 (2021).

203. Craeye, B., Tielemans, T., Lauwereijssens, G. & Stoop, J. Effect of super absorbing polymers on the freeze–thaw resistance of coloured concrete roads. *Road Mater. Pavement Des.* **14**, 90–106 (2013).

204. Assmann, A. Physical properties of concrete modified with superabsorbent polymers.

205. Mechtcherine, V. Effect of superabsorbent polymers (SAP) on the freeze–thaw resistance of concrete: results of a RILEM interlaboratory study. *Mater. Struct.* 19 (2017).

206. Mobasher, B. *et al.* Guide to Design with Fiber-Reinforced Concrete. 4.

207. Richardson, A. E., Coventry, K. A. & Wilkinson, S. Freeze/thaw durability of concrete with synthetic fibre additions. *Cold Reg. Sci. Technol.* **83–84**, 49–56 (2012).

208. Çavdar, A. Investigation of freeze–thaw effects on mechanical properties of fiber reinforced cement mortars. *Compos. Part B Eng.* **58**, 463–472 (2014).

209. Şahmaran, M., Özbay, E., Yücel, H. E., Lachemi, M. & Li, V. C. Frost resistance and microstructure of Engineered Cementitious Composites: Influence of fly ash and micro poly-vinyl-alcohol fiber. *Cem. Concr. Compos.* **34**, 156–165 (2012).

210. Yun, H.-D. & Rokugo, K. Freeze-thaw influence on the flexural properties of ductile fiber-reinforced cementitious composites (DFRCCs) for durable infrastructures. *Cold Reg. Sci. Technol.* 7 (2012) doi:https://doi.org/10.1016/j.coldregions.2012.02.002.

211. Balaguru, P. N. & Ramakrishnan, V. Freeze-Thaw Durability of Fiber Reinforced Concrete. 9 (1986).

212. Basheer, L. & Cleland, D. J. Freeze–thaw resistance of concretes treated with pore liners. *Constr. Build. Mater.* **20**, 990–998 (2006).

213. Pan, X., Shi, Z., Shi, C., Ling, T.-C. & Li, N. A review on surface treatment for concrete – Part 2: Performance. *Constr. Build. Mater.* **133**, 81–90 (2017).

214. Basheer, P. A. M., Basheer, L., Cleland, D. J. & Long, A. E. Surface treatments for concrete: assessment methods and reported performance. *Constr. Build. Mater.* **11**, 413–429 (1997).

215. Sobolev, K. G. & Batrakov, V. G. Effect of a Polyethylhydrosiloxane Admixture on the Durability of Concrete with Supplementary Cementitious Materials. *J. Mater. Civ. Eng.* **19**, 809–819 (2007).

216. Ma, Z., Zhu, F. & Zhao, T. Effects of surface modification of silane coupling agent on the properties of concrete with freeze-thaw damage. *KSCE J. Civ. Eng.* **22**, 657–669 (2018).

217. Ma, Z., Wittmann, F. H., Xiao, J. & Zhao, T. Influence of freeze-thaw cycles on properties of Integral Water Repellent Concrete. *J. Wuhan Univ. Technol.-Mater Sci Ed* **31**, 851–856 (2016).

218. Medeiros, M. H. F. *et al.* Reducing Water and Chloride Penetration Through Silicate Treatments for Concrete as a Mean to Control Corrosion Kinetics. *Int J Electrochem Sci* **7**, 16 (2012).

219.   Dang, Y. *et al.* Accelerated laboratory evaluation of surface treatments for protecting concrete bridge decks from salt scaling. *Constr. Build. Mater.* **55**, 128–135 (2014).

220.   Marshall, C. B., Chakrabartty, A. & Davies, P. L. Hyperactive Antifreeze Protein from Winter Flounder Is a Very Long Rod-like Dimer of α-Helices*. *J. Biol. Chem.* **280**, 17920–17929 (2005).

221.   Naullage, P. M. & Molinero, V. Slow Propagation of Ice Binding Limits the Ice-Recrystallization Inhibition Efficiency of PVA and Other Flexible Polymers. *J. Am. Chem. Soc.* **142**, 4356–4366 (2020).

222.   Budke, C. & Koop, T. Inhibition of Recrystallization. in *Antifreeze Proteins Volume 2: Biochemistry, Molecular Biology and Applications* (eds. Ramløv, H. & Friis, D. S.) 159–184 (Springer International Publishing, 2020). doi:10.1007/978-3-030-41948-6_7.

223.   Raymond, J. A. & DeVries, A. L. Adsorption inhibition as a mechanism of freezing resistance in polar fishes. *Proc. Natl. Acad. Sci.* **74**, 2589–2593 (1977).

224.   Biggs, C. I. *et al.* Mimicking the Ice Recrystallization Activity of Biological Antifreezes. When is a New Polymer "Active"? *Macromol. Biosci.* 1900082 (2019) doi:10.1002/mabi.201900082.

225.   Briard, J. G., Fernandez, M., De Luna, P., Woo, Tom. K. & Ben, R. N. QSAR Accelerated Discovery of Potent Ice Recrystallization Inhibitors. *Sci. Rep.* **6**, 26403 (2016).

226.   Delesky, E. A. Ice Recrystallization Inhibition of Ice-Binding Proteins and Bioinspired Synthetic Mimics in Non-Physiological Environments. *ProQuest Dissertations and Theses* (University of Colorado at Boulder, 2020).

227.   Kuiper, M. J., Morton, C. J., Abraham, S. E. & Gray-Weale, A. The biological function of an insect antifreeze protein simulated by molecular dynamics. *eLife* **4**, e05142 (2015).

228.   Knight, C. A. Adding to the antifreeze agenda. *Nature* **406**, 249–251 (2000).

229.   Crevel, R. W. R., Fedyk, J. K. & Spurgeon, M. J. Antifreeze proteins: characteristics, occurrence and human exposure. *Food Chem. Toxicol.* **40**, 899–903 (2002).

230.   Ustun, N. S. & Turhan, S. Antifreeze Proteins: Characteristics, Function, Mechanism of Action, Sources and Application to Foods: Antifreeze Proteins. *J. Food Process. Preserv.* **39**, 3189–3197 (2015).

231.   Davies, P. L. & Sykes, B. D. Antifreeze proteins. *Curr. Opin. Struct. Biol.* **7**, 828–834 (1997).

232.   Ramløv, H. & Johnsen, J. L. Controlling the Freezing Process with Antifreeze Proteins. in *Emerging Technologies for Food Processing* 539–562 (Elsevier, 2014). doi:10.1016/B978-0-12-411479-1.00029-2.

233.   Davies, P. L. & Hew, C. L. Biochemistry of fish antifreeze proteins. *FASEB J.* **4**, 2460–2468 (1990).

234.   Sicheri, F. & Yang, D. S. C. Ice-binding structure and mechanism of an antifreeze protein from winter flounder. *Nature* **375**, 427–431 (1995).

235.   Nishimiya, Y. *et al.* Crystal Structure and Mutational Analysis of Ca2+-Independent Type II Antifreeze Protein from Longsnout Poacher, Brachyopsis rostratus. *J. Mol. Biol.* **382**, 734–746 (2008).

236.   Ye, Q., Leinala, E. & Jia, Z. Structure of type III antifreeze protein at 277K. *Acta Crystallogr. Sect. D* **54**, 700–702 (1998).

237.   Breiter, D. R. *et al.* Molecular structure of an apolipoprotein determined at 2.5-.ANG. resolution. *Biochemistry* **30**, 603–608 (1991).

238.   Graether, S. P. *et al.* β-Helix structure and ice-binding properties of a hyperactive antifreeze protein from an insect. **406**, 4 (2000).

239.   Liou, Y.-C., Tocilj, A., Davies, P. L. & Jia, Z. Mimicry of ice structure by surface hydroxyls and water of a b-helix antifreeze protein. **406**, 3 (2000).

240.   Marshall, C. B., Daley, M. E., Graham, L. A., Sykes, B. D. & Davies, P. L. Identification of the ice-binding face of antifreeze protein from Tenebrio molitor. *FEBS Lett.* 7 (2002).

241.   Graether, S. P. & Sykes, B. D. Cold survival in freeze-intolerant insects: The structure and function of β-helical antifreeze proteins. *Eur. J. Biochem.* **271**, 3285–3296 (2004).

242.   Harding, M. M., Anderberg, P. I. & Haymet, A. D. J. 'Antifreeze' glycoproteins from polar fish. *Eur. J. Biochem.* **270**, 1381–1392 (2003).

243.   Gibson, M. I., Barker, C. A., Spain, S. G., Albertin, L. & Cameron, N. R. Inhibition of Ice Crystal Growth by Synthetic Glycopolymers: Implications for the Rational Design of Antifreeze Glycoprotein Mimics. *Biomacromolecules* **10**, 328–333 (2009).

244.   Tsvetkova, N. M. *et al.* Dynamics of Antifreeze Glycoproteins in the Presence of Ice. *Biophys. J.* **82**, 464–473 (2002).

245.   Mochizuki, K. & Molinero, V. Antifreeze Glycoproteins Bind Reversibly to Ice via Hydrophobic Groups. *J. Am. Chem. Soc.* **140**, 4803–4811 (2018).

246.   DeVries, A. L., Komatsu, S. K. & Feeney, R. E. Chemical and Physical Properties of Freezing Point-depressing Glycoproteins from Antarctic Fishes. *J. Biol. Chem.* **245**, 2901–2908 (1970).

247.   Brown, R. A., Yeh, Y., Burcham, T. S. & Feeney, R. E. Direct evidence for antifreeze glycoprotein adsorption onto an ice surface. *Biopolymers* **24**, 1265–1270 (1985).

248.	Knight, C. A., Driggers, E. & DeVries, A. L. Adsorption to ice of fish antifreeze glycopeptides 7 and 8. *Biophys. J.* **64**, 252–259 (1993).

249.	Furukawa, Y. *et al.* Oscillations and accelerations of ice crystal growth rates in microgravity in presence of antifreeze glycoprotein impurity in supercooled water. *Sci. Rep.* **7**, 43157 (2017).

250.	Meister, K., DeVries, A. L., Bakker, H. J. & Drori, R. Antifreeze Glycoproteins Bind Irreversibly to Ice. *J. Am. Chem. Soc.* **140**, 9365–9368 (2018).

251.	Tachibana, Y. *et al.* Antifreeze Glycoproteins: Elucidation of the Structural Motifs That Are Essential for Antifreeze Activity. *Angew. Chem. Int. Ed.* **43**, 856–862 (2004).

252.	Budke, C. *et al.* Quantitative Efficacy Classification of Ice Recrystallization Inhibition Agents. *Cryst. Growth Des.* **14**, 4285–4294 (2014).

253.	Raymond, J. A. & Remias, D. Ice-Binding Proteins in a Chrysophycean Snow Alga: Acquisition of an Essential Gene by Horizontal Gene Transfer. *Front. Microbiol.* **10**, 2697 (2019).

254.	Lee, J. K. *et al.* An extracellular ice-binding glycoprotein from an Arctic psychrophilic yeast. *Cryobiology* **60**, 222–228 (2010).

255.	Li, T., Zhao, Y., Zhong, Q. & Wu, T. Inhibiting Ice Recrystallization by Nanocelluloses. *Biomacromolecules* **20**, 1667–1674 (2019).

256.	Mitchell, D. E., Lilliman, M., Spain, S. G. & Gibson, M. I. Quantitative study on the antifreeze protein mimetic ice growth inhibition properties of poly(ampholytes) derived from vinyl-based polymers. *Biomater. Sci.* 10 (2014).

257.   Stubbs, C., Bailey, T. L., Murray, K. & Gibson, M. I. Polyampholytes as Emerging

Macromolecular Cryoprotectants. *Biomacromolecules* acs.biomac.9b01053 (2019)

doi:10.1021/acs.biomac.9b01053.

258.   MacDonald, M. J., Cornejo, N. R. & Gellman, S. H. Inhibition of Ice Recrystallization by

Nylon-3 Polymers. *ACS Macro Lett.* 5 (2017).

259.   Ishibe, T. *et al.* Enhancement of Macromolecular Ice Recrystallization Inhibition Activity

by Exploiting Depletion Forces. *ACS Macro Lett.* **8**, 1063–1067 (2019).

260.   Inada, T. & Modak, P. R. Growth control of ice crystals by poly(vinyl alcohol) and

antifreeze protein in ice slurries. *Chem. Eng. Sci.* **61**, 3149–3158 (2006).

261.   Olijve, L. L. C., Hendrix, M. M. R. M. & Voets, I. K. Influence of Polymer Chain

Architecture of Poly(vinyl alcohol) on the Inhibition of Ice Recrystallization. *Macromol.*

Chem. Phys. **217**, 951–958 (2016).

262.   Lu, S.-S., Inada, T., Yabe, A., Zhang, X. & Grandum, S. Microscale study of poly(vinyl

alcohol) as an effective additive for inhibiting recrystallization in ice slurries. *Int. J. Refrig.*

25, 562–568 (2002).

263.   Weng, L., Stott, S. L. & Toner, M. Molecular Dynamics at the Interface between Ice and

Poly(vinyl alcohol) and Ice Recrystallization Inhibition. *Langmuir* **34**, 5116–5123 (2018).

264.   Naullage, P. M., Lupi, L. & Molinero, V. Molecular Recognition of Ice by Fully Flexible

Molecules. *J. Phys. Chem. C* **121**, 26949–26957 (2017).

265.   Deller, R. C., Vatish, M., Mitchell, D. A. & Gibson, M. I. Synthetic polymers enable non-

vitreous cellular cryopreservation by reducing ice crystal growth during thawing. *Nat.*

Commun. **5**, 3244 (2014).

266. Burkey, A. A., Riley, C. L., Wang, L. K., Hatridge, T. A. & Lynd, N. A. Understanding Poly(vinyl alcohol)-Mediated Ice Recrystallization Inhibition through Ice Adsorption Measurement and pH Effects. *Biomacromolecules* **19**, 248–255 (2018).

267. Naullage, P. M., Qiu, Y. & Molinero, V. What Controls the Limit of Supercooling and Superheating of Pinned Ice Surfaces? *J. Phys. Chem. Lett.* **9**, 1712–1720 (2018).

268. Congdon, T. R., Notman, R. & Gibson, M. I. Synthesis of star-branched poly(vinyl alcohol) and ice recrystallization inhibition activity. *Eur. Polym. J.* **88**, 320–327 (2017).

269. Mitchell, D. E., Cameron, N. R. & Gibson, M. I. Rational, yet simple, design and synthesis of an antifreeze-protein inspired polymer for cellular cryopreservation. *Chem. Commun.* **51**, 12977–12980 (2015).

270. Matsumura, K. & Hyon, S.-H. Polyampholytes as low toxic efficient cryoprotective agents with antifreeze protein properties. *Biomaterials* **30**, 4842–4849 (2009).

271. Inada, T. & Lu, S.-S. Thermal hysteresis caused by non-equilibrium antifreeze activity of poly(vinyl alcohol). *Chem. Phys. Lett.* **394**, 361–365 (2004).

272. Stubbs, C., Lipecki, J. & Gibson, M. I. Regioregular Alternating Polyampholytes Have Enhanced Biomimetic Ice Recrystallization Activity Compared to Random Copolymers and the Role of Side Chain versus Main Chain Hydrophobicity. *Biomacromolecules* **18**, 295–302 (2017).

273. Wierzbicki, A. *et al.* Structure−Function Relationship in the Antifreeze Activity of Synthetic Alanine−Lysine Antifreeze Polypeptides. *Biomacromolecules* **1**, 268–274 (2000).

274. Zhang, W. & Laursen, R. A. Artificial antifreeze polypeptides: K-helical peptides with KAAK motifs have antifreeze and ice crystal morphology modifying properties. *FEBS Lett.* 5 (1999).

275.   Tsuda, T. & Nishimura, S.-I. Synthesis of an antifreeze glycoprotein analogue: efficient preparation of sequential glycopeptide polymers. *Chem. Commun.* 2779 (1996) doi:10.1039/cc9960002779.

276.   Hachisu, M. *et al.* One-pot synthesis of cyclic antifreeze glycopeptides. *Chem. Commun.* 1641 (2009) doi:10.1039/b815917c.

277.   Tachibana, Y., Monde, K. & Nishimura, S.-I. Sequential Glycoproteins: Practical Method for the Synthesis of Antifreeze Glycoprotein Models Containing Base Labile Groups. *Macromolecules* **37**, 6771–6779 (2004).

278.   Wilkinson, B. L. *et al.* Total Synthesis of Homogeneous Antifreeze Glycopeptides and Glycoproteins. *Angew. Chem. Int. Ed.* **51**, 3606–3610 (2012).

279.   Kao, M. H., Fletcher, G. L., Wang, N. C. & Hew, C. L. The relationship between molecular weight and antifreeze polypeptide activity in marine fish. *Can. J. Zool.* **64**, 578–582 (1986).

280.   Burcham, T. S., Knauf, M. J. & Feeney, R. E. Antifreeze glycoproteins: Influence of polymer length and ice crystal habit on activity. 17.

281.   Stubbs, C., Wilkins, L. E., Fayter, A. E. R., Walker, M. & Gibson, M. I. Multivalent Presentation of Ice Recrystallization Inhibiting Polymers on Nanoparticles Retains Activity. 7 (2019).

282.   Geng, H. *et al.* Graphene Oxide Restricts Growth and Recrystallization of Ice Crystals. *Angew. Chem. Int. Ed.* **56**, 997–1001 (2017).

283.   Adam, M. K. *et al.* 1D Self-Assembly and Ice Recrystallization Inhibition Activity of Antifreeze Glycopeptide-Functionalized Perylene Bisimides. *Chem. - Eur. J.* **24**, 7834–7839 (2018).

284. Mitchell, D. E. *et al.* Antifreeze Protein Mimetic Metallohelices with Potent Ice Recrystallization Inhibition Activity. *J. Am. Chem. Soc.* **139**, 9835–9838 (2017).

285. Brotzakis, Z. F. Stability and growth mechanism of self-assembling putative antifreeze cyclic peptides. 11 (2017).

286. Mizrahy, O., Bar-Dolev, M., Guy, S. & Braslavsky, I. Inhibition of Ice Growth and Recrystallization by Zirconium Acetate and Zirconium Acetate Hydroxide. *PLoS ONE* **8**, e59540 (2013).

287. Deville, S., Viazzi, C. & Guizard, C. An Ice-Structuring Mechanism for Zirconium Acetate. 17.

288. Howson, S. E. & Scott, P. Approaches to the synthesis of optically pure helicates. *Dalton Trans.* **40**, 10268 (2011).

289. Lehn, J. M. *et al.* Spontaneous assembly of double-stranded helicates from oligobipyridine ligands and copper(I) cations: structure of an inorganic double helix. *Proc. Natl. Acad. Sci.* **84**, 2565–2569 (1987).

290. Capicciotti, C. J. *et al.* Potent inhibition of ice recrystallization by low molecular weight carbohydrate-based surfactants and hydrogelators. *Chem. Sci.* **3**, 1408 (2012).

291. Fan, Q. *et al.* Unraveling Molecular Mechanism on Dilute Surfactant Solution Controlled Ice Recrystallization. *Langmuir* **36**, 1691–1698 (2020).

292. Chaytor, J. L. *et al.* Inhibiting ice recrystallization and optimization of cell viability after cryopreservation. *Glycobiology* **22**, 123–133 (2012).

293. Tam, R. Y., Ferreira, S. S., Czechura, P., Chaytor, J. L. & Ben, R. N. Hydration Index—A Better Parameter for Explaining Small Molecule Hydration in Inhibition of Ice Recrystallization. 8.

294. Balcerzak, A. K., Febbraro, M. & Ben, R. N. The importance of hydrophobic moieties in ice recrystallization inhibitors. *RSC Adv.* **3**, 3232 (2013).

295. Capicciotti, C. J. *et al. O* -Aryl-Glycoside Ice Recrystallization Inhibitors as Novel Cryoprotectants: A Structure–Function Study. *ACS Omega* **1**, 656–662 (2016).

296. Czechura, P., Tam, R. Y., Dimitrijevic, E., Murphy, A. V. & Ben, R. N. The Importance of Hydration for Inhibiting Ice Recrystallization with C-Linked Antifreeze Glycoproteins. *J. Am. Chem. Soc.* **130**, 2928–2929 (2008).

297. Capicciotti, C. J., Doshi, M. & N., R. Ice Recrystallization Inhibitors: From Biological Antifreezes to Small Molecules. in *Recent Developments in the Study of Recrystallization* (ed. Wilson, P.) (InTech, 2013). doi:10.5772/54992.

298. Adam, M. K. *et al.* Carbohydrate-based surfactants as photocontrollable inhibitors of ice recrystallization. *RSC Adv.* **6**, 39240–39244 (2016).

299. Fliegl, H., Köhn, A., Hättig, C. & Ahlrichs, R. Ab Initio Calculation of the Vibrational and Electronic Spectra of *trans* - and *cis* -Azobenzene. *J. Am. Chem. Soc.* **125**, 9821–9827 (2003).

300. Capicciotti, C. J. *et al.* Small Molecule Ice Recrystallization Inhibitors Enable Freezing of Human Red Blood Cells with Reduced Glycerol Concentrations. *Sci. Rep.* **5**, 9692 (2015).

301. Ghobadloo, S. M. *et al.* Carbohydrate-Based Ice Recrystallization Inhibitors Increase Infectivity and Thermostability of Viral Vectors. *Sci. Rep.* **6**.

302. Amir, G. *et al.* Subzero nonfreezing cryopresevation of rat hearts using antifreeze protein I and antifreeze protein III. **48**, 273-282 (2004).

303. Makarevich, A. V. *et al.* Several aspects of animal embryo cryopreservation: anti-freeze protein (AFP) as a potential cryoprotectant. *Zygote Camb.* **18**, 145–153 (2010).

304.   Chang, T. & Zhao, G. Ice Inhibition for Cryopreservation: Materials, Strategies, and

Challenges. *Adv. Sci.* **8**, 2002425 (2021).

305.   Gao, D. & Critser, J. K. Mechanisms of Cryoinjury in Living Cells. *ILAR J.* **41**, 187–196

(2000).

306.   Boonsupthip, W. & Lee, T.-C. Application of Antifreeze Protein for Food Preservation:

Effect of Type III Antifreeze Protein for Preservation of Gel-forming of Frozen and Chilled

Actomyosin. *J. Food Sci.* **68**, 1804–1809 (2003).

307.   Zhang, C., Zhang, H., Wang, L. & Guo, X. Effect of carrot (Daucus carota) antifreeze

proteins on texture properties of frozen dough and volatile compounds of crumb. *LWT -

Food Sci. Technol.* **41**, 1029–1036 (2008).

308.   Kaleda, A., Tsanev, R., Klesment, T., Vilu, R. & Laos, K. Ice cream structure

modification by ice-binding proteins. *Food Chem.* **246**, 164–171 (2018).

309.   Wu, S. *et al.* Ion-specific ice recrystallization provides a facile approach for the

fabrication of porous materials. *Nat. Commun.* **8**, 15154 (2017).

310.   Peko, C., Groth, B. & Nettleship, I. The Effect of Polyvinyl Alcohol on the

Microstructure and Permeability of Freeze-Cast Alumina. *J. Am. Ceram. Soc.* **93**, 115–120

(2010).

311.   Qu, Z. *et al.* Enhancing the Freeze-Thaw Durability of Concrete Through Ice

Recrystallization Inhibition by Poly(vinyl Alcohol). (2019)

doi:10.26434/chemrxiv.11363843.v1.

312.   Du, L. & Folliard, K. J. Mechanisms of air entrainment in concrete. *Cem. Concr. Res.* **35**,

1463–1471 (2005).

313.   Chen, X., Wu, S. & Zhou, J. Influence of porosity on compressive and tensile strength of cement mortar. *Constr. Build. Mater.* **40**, 869–874 (2013).

314.   Xiang, H., Yang, X., Ke, L. & Hu, Y. The properties, biotechnologies, and applications of antifreeze proteins. *Int. J. Biol. Macromol.* **153**, 661–675 (2020).

315.   Chandra, S. & Aavik, J. Influence of proteins on some properties of portland cement mortar. *Int. J. Cem. Compos. Lightweight Concr.* **9**, 91–94 (1987).

316.   Jasiczak, J. & Zielinski, K. Effect of protein additive on properties of mortar. *Cem. Concr. Compos.* **28**, 451–457 (2006).

317.   Hassan, C.M. & Peppas, N.A.. Structure and Applications of Polyv(vinyl alcohol) Hydrogels Produced by Conventional Crosslinking or by Freezing/Thawing Methods. in *Biopolymers, PVA hydrogels, anionic polymerisation, nanocomposites*. 37-65 (Springer, 2000).

318.   Lozinsky, V. I. Cryotropic gelation of poly(vinyl alcohol) solutions. *Russ. Chem. Rev.* **67**, 573–586 (1998).

319.   Fouad, E. A., El-Badry, M., Neau, S. H., Alanazi, F. K. & Alsarra, I. A. Technology evaluation: Kollicoat IR. *Expert Opin. Drug Deliv.* **8**, 693–703 (2011).

320.   C01 Committee. *Specification for Portland Cement*. http://www.astm.org/cgi-bin/resolver.cgi?C150C150M-20 doi:10.1520/C0150_C0150M-20.

321.   Knight, C. A., Hallett, J. & DeVries, A. L. Solute effects on ice recrystallization: An assessment technique. *Cryobiology* **25**, 55–60 (1988).

322.   Gibson, M. I. Slowing the growth of ice with synthetic macromolecules: beyond antifreeze(glyco) proteins. 13 (2010).

323. C09 Committee. *Practice for Making and Curing Concrete Test Specimens in the Laboratory*. http://www.astm.org/cgi-bin/resolver.cgi?C192C192M-16A (2016) doi:10.1520/C0192_C0192M-16A.

324. C09 Committee. *Test Method for Compressive Strength of Cylindrical Concrete Specimens*. http://www.astm.org/cgi-bin/resolver.cgi?C39C39M-18 doi:10.1520/C0039_C0039M-18.

325. Wedding, P. & Kantro, D. Influence of Water-Reducing Admixtures on Properties of Cement Paste—A Miniature Slump Test. *Cem. Concr. Aggreg.* **2**, 95 (1980).

326. C09 Committee. *Practice for Measuring Hydration Kinetics of Hydraulic Cementitious Mixtures Using Isothermal Calorimetry*. http://www.astm.org/cgi-bin/resolver.cgi?C1679-17 (2017) doi:10.1520/C1679-17.

327. Batool, F. & Bindiganavile, V. Air-void size distribution of cement based foam and its effect on thermal conductivity. *Constr. Build. Mater.* **149**, 17–28 (2017).

328. Mitchell, D. E. & Gibson, M. I. Latent Ice Recrystallization Inhibition Activity in Nonantifreeze Proteins: Ca^{2+} -Activated Plant Lectins and Cation-Activated Antimicrobial Peptides. *Biomacromolecules* **16**, 3411–3416 (2015).

329. Knapen, E. & Van Gemert, D. Cement hydration and microstructure formation in the presence of water-soluble polymers. *Cem. Concr. Res.* **39**, 6–13 (2009).

330. Singh, N. B. & Rai, S. Effect of polyvinyl alcohol on the hydration of cement with rice husk ash. *Cem. Concr. Res.* **31**, 239–243 (2001).

331. Roussel, N., Lemaître, A., Flatt, R. J. & Coussot, P. Steady state flow of cement suspensions: A micromechanical state of the art. *Cem. Concr. Res.* **40**, 77–84 (2010).

332. Zingg, A. *et al.* The microstructure of dispersed and non-dispersed fresh cement pastes — New insight by cryo-microscopy. *Cem. Concr. Res.* **38**, 522–529 (2008).

333. Singh, N. B. & Rai, S. Effect of polyvinyl alcohol on the hydration of cement with rice husk ash. *Cem. Concr. Res.* **31**, 239–243 (2001).

334. Alonso, C. & Fernandez, L. Dehydration and rehydration processes of cement paste exposed to high temperature environments. *J. Mater. Sci.* **39**, 3015–3024 (2004).

335. Snellings, R. X-ray powder diffraction applied to cement. in *A Practical Guide to Microstructural Analysis of Cementitious Materials*. (eds. Scrivener, K., Snellings, R., Lothenbach, B.) 107-176 (CRC Press, 2016). doi:10.1201/b19074.

336. Castellote, M., Fernandez, L., Andrade, C. & Alonso, C. Chemical changes and phase analysis of OPC pastes carbonated at different CO2 concentrations. *Mater. Struct.* **42**, 515–525 (2009).

337. Ramlochan, T., Zacarias, P., Thomas, M. D. A. & Hooton, R. D. The effect of pozzolans and slag on the expansion of mortars cured at elevated temperature. *Cem. Concr. Res.* **33**, 807–814 (2003).

338. Bertron, A., Duchesne, J. & Escadeillas, G. Degradation of cement pastes by organic acids. *Mater. Struct.* **40**, 341–354 (2007).

339. Schneider, J., Cincotto, M. A. & Panepucci, H. 29Si and 27Al high-resolution NMR characterization of calcium silicate hydrate phases in activated blast-furnace slag pastes. *Cem. Concr. Res.* **31**, 993–1001 (2001).

340. Mendes, A., Gates, W. P., Sanjayan, J. G. & Collins, F. NMR, XRD, IR and synchrotron NEXAFS spectroscopic studies of OPC and OPC/slag cement paste hydrates. *Mater. Struct.* **44**, 1773–1791 (2011).

341.   Thong, C. C., Teo, D. C. L. & Ng, C. K. Application of polyvinyl alcohol (PVA) in cement-based composite materials: A review of its engineering properties and microstructure behavior. *Constr. Build. Mater.* **107**, 172–180 (2016).

342.   Singh, V. K., Khatri, S. D. & Singh, R. K. Hydration and Some Other Properties of Polyethylene Glycol Modified Cement Products. *Trans. Indian Ceram. Soc.* **61**, 152–161 (2002).

343.   Fagerlund, G. The critical degree of saturation method of assessing the freeze/thaw resistance of concrete. *Mater. Constr.* **10**, 217–229 (1977).

344.   Mönnig, S. & Lura, P. Superabsorbent Polymers — An Additive to Increase the Freeze-Thaw Resistance of High Strength Concrete. in *Advances in Construction Materials 2007* (ed. Grosse, C. U.) 351–358 (Springer Berlin Heidelberg, 2007).

345.   Inada, T. & Lu, S.-S. Inhibition of Recrystallization of Ice Grains by Adsorption of Poly(Vinyl Alcohol) onto Ice Surfaces. *Cryst. Growth Des.* **3**, 747–752 (2003).

346.   Kim, J.-H. & Robertson, R. E. Effects of Polyvinyl Alcohol on Aggregate-Paste Bond Strength and the Interfacial Transition Zone. *Adv. Cem. Based Mater.* **8**, 66–76 (1998).

347.   Kim, J.-H., Robertson, R. E. & Naaman, A. E. Structure and properties of poly(vinyl alcohol)-modified mortar and concrete. *Cem. Concr. Res.* 9 (1999).

348.   Yaowarat, T., Horpibulsuk, S., Arulrajah, A., Mirzababaei, M. & A Rashid, A. S. Compressive and Flexural Strength of Polyvinyl Alcohol–Modified Pavement Concrete Using Recycled Concrete Aggregates. *J. Mater. Civ. Eng.* **30**, 04018046 (2018).

349.   Ohama, Y. Polymer-based admixtures. *Cem. Concr. Compos.* **20**, 189–212 (1998).

350. C01 Committee. *Specification for Mixing Rooms, Moist Cabinets, Moist Rooms, and Water Storage Tanks Used in the Testing of Hydraulic Cements and Concretes*. http://www.astm.org/cgi-bin/resolver.cgi?C511-19 (2019) doi:10.1520/C0511-19.

351. Gates-Rector, S. & Blanton, T. The Powder Diffraction File: a quality materials characterization database. *Powder Diffr.* **34**, 352–360 (2019).

352. Beddoe, R. E. & Setzer, M. J. A low-temperature DSC investigation of hardened cement paste subjected to chloride action. *Cement and Concrete Research* **18**, 249–256 (1988).

353. Bednarska, D. & Koniorczyk, M. Freezing of partly saturated cementitious materials – Insight into properties of pore confined solution and microstructure. *Constr. Build. Mater.* **251**, 118895 (2020).

354. Sun, Z. & Scherer, G. W. Measurement and simulation of dendritic growth of ice in cement paste. *Cem. Concr. Res.* **40**, 1393–1402 (2010).

355. Brun, M., Lallemand, A., Quinson, J.-F. & Eyraud, C. A new method for the simultaneous determination of the size and shape of pores: the thermoporometry. *Thermochim. Acta* **21**, 59–88 (1977).

356. Kim, K. Y., Yun, T. S., Choo, J., Kang, D. H. & Shin, H. S. Determination of air-void parameters of hardened cement-based materials using X-ray computed tomography. *Constr. Build. Mater.* **37**, 93–101 (2012).

357. Selvol^{TM} Polyvinyl Alcohol Product Information. *Sekisui Specialty Chemicals America* https://www.sekisui-sc.com/products/polyvinyl-alcohol/.

358. Kim, J.-H. & Robertson, R. E. Prevention of air void formation in polymer-modified cement mortar by pre-wetting. *Cem. Concr. Res.* **27**, 171–176 (1997).

359.   Nguyen, D. D., Devlin, L. P., Koshy, P. & Sorrell, C. C. Effects of chemical nature of polyvinyl alcohol on early hydration of Portland cement. *J. Therm. Anal. Calorim.* **123**, 1439–1450 (2016).

360.   Knapen, E. & Van Gemert, D. Polymer film formation in cement mortars modified with water-soluble polymers. *Cem. Concr. Compos.* **58**, 23–28 (2015).

361.   Deng, G. Amino acid sequence of a new type of antifreeze protein, from the longhorn sculpin Myoxocephalus octodecimspinosis. 4 (1997).

362.   Lock, L. L. *et al.* Self-assembly of natural and synthetic drug amphiphiles into discrete supramolecular nanostructures. *Faraday Discuss.* **166**, 285 (2013).

363.   Ciuchi, F. *et al.* Self-Recognition and Self-Assembly of Folic Acid Salts: Columnar Liquid Crystalline Polymorphism and the Column Growth Process. *J. Am. Chem. Soc.* **116**, 7064–7071 (1994).

364.   Bonazzi, S., DeMorais, M. M., Gottarelli, G., Mariani, P. & Spada, G. P. Self-Assembly and Liquid Crystal Formation of Folic Acid Salts. *Angew. Chem. Int. Ed. Engl.* **32**, 248–250 (1993).

365.   Atluri, R. *et al.* Self-Assembly Mechanism of Folate-Templated Mesoporous Silica. *Langmuir* **29**, 12003–12012 (2013).

366.   Motkar, G., Lonare, M., Patil, O. & Mohanty, S. Self-assembly of folic acid in aqueous media. *AIChE J.* **59**, 1360–1368 (2013).

367.   Darweesh, H. H. M. 6 - Black liquor waste as a cement admixture or cement and concrete admixtures. 32.

368.   Xun, W. *et al.* Effect of Functional Polycarboxylic Acid Superplasticizers on Mechanical and Rheological Properties of Cement Paste and Mortar. *Appl. Sci.* **10**, 5418 (2020).

369.   Möschner, G., Lothenbach, B., Figi, R. & Kretzschmar, R. Influence of citric acid on the hydration of Portland cement. *Cem. Concr. Res.* 8 (2009).

370.   Singh, N. B., Singh, A. K. & Prabha Singh, S. Effect of citric acid on the hydration of portland cement. *Cem. Concr. Res.* **16**, 911–920 (1986).

371.   Wildlng, C. R., Walter, A. & Double, D. D. A classification of inorganic and organic admixtures by conduction calorimetry. **14**, 10 (1984).

372.   Ramachandran, V. Conduction calorimetric investigation of the effect of retarders on the hydration of Portland cement. 15.

373.   Pigeon, M., Pleau, R. & Aitcin, P. Freeze-Thaw Durability of Concrete With and Without Silica Fume in ASTM C666 (Procedure A) Test Method: Internal Cracking Versus Scaling. *Cem. Concr. Aggreg.* **8**, 76–85 (1986).

374.   Sun, Z. Mechanism of frost damage to concrete. 24.

375.   Valenza, J. J. & Scherer, G. W. A review of salt scaling: II. Mechanisms. *Cem. Concr. Res.* **37**, 1022–1034 (2007).

376.   Khanzadeh Moradllo, M. *et al.* Quantifying the freeze-thaw performance of air-entrained concrete using the time to reach critical saturation modelling approach. *Cem. Concr. Compos.* **106**, 103479 (2020).

377.   Integrated Materials and Construction Practices for Concrete Pavement: A State-of-the-Practice Manual. 338.

378.   Chatterji, S. Freezing of aqueous solutions in a porous medium Part I. Freezing of air-entraining agent solutions. *Cem. Concr. Res.* **15**, 13–20 (1985).

379.   Edmeades, R. M. & Hewlett, P. C. Cement Admixtures. in *Lea's Chemistry of Cement and Concrete* 841–905 (Elsevier, 1998). doi:10.1016/B978-075066256-7/50027-8.

380. Mielenz, R. C. Use of surface-active agents in concrete. in *Proceedings of the fifth International Symposium on the Chemistry of Cement* vol. IV 1–35 (Cement Association of Japan, 1969).

381. Zhang, X., Zhang, H., Gao, H., He, Y. & Jiang, M. Effect of bubble feature parameters on rheological properties of fresh concrete. *Constr. Build. Mater.* **196**, 245–255 (2019).

382. Corr, D. J., Lebourgeois, J., Monteiro, P. J. M., Bastacky, S. J. & Gartner, E. M. Air void morphology in fresh cement pastes. *Cem. Concr. Res.* **32**, 1025–1031 (2002).

383. Rashed, A. I. & Williamson, R. B. Microstructure of entrained air voids in concrete, Part I. *J. Mater. Res.* **6**, 2004–2012 (1991).

384. Rashed, A. I. & Williamson, R. B. Microstructure of entrained air voids in concrete, Part II. *J. Mater. Res.* **6**, 2474–2483 (1991).

385. Hewlett, P. C., Justnes, H. & Edmeades, R. M. Cement and Concrete Admixtures. in *Lea's Chemistry of Cement and Concrete* 641–698 (Elsevier, 2019). doi:10.1016/B978-0-08-100773-0.00014-9.

386. Petrauskas, A. A. & Kolovanov, E. A. ACD/Log P method description. 18.

387. Ertl, P., Rohde, B. & Selzer, P. Fast Calculation of Molecular Polar Surface Area as a Sum of Fragment-Based Contributions and Its Application to the Prediction of Drug Transport Properties. *J. Med. Chem.* **43**, 3714–3717 (2000).

388. *Molinspiration Cheminformatics free web services*.

389. Baviere, M., Bazin, B. & Aude, R. Calcium effect on the solubility of sodium dodecyl sulfate in sodium chloride solutions. *J. Colloid Interface Sci.* **92**, 580–583 (1983).

390. Yang, D. S. C., Sax, M., Chakrabartty, A. & Hew, C. L. Crystal structure of an antifreeze polypeptide and its mechanistic implications. *Nature* **333**, 232–237 (1988).

391. Graham, B., Fayter, A. E. R., Houston, J. E., Evans, R. C. & Gibson, M. I. Facially Amphipathic Glycopolymers Inhibit Ice Recrystallization. *J. Am. Chem. Soc.* **140**, 5682–5685 (2018).

392. Ampaw, A., Charlton, T. A., Briard, J. G. & Ben, R. N. Designing the next generation of cryoprotectants - From proteins to small molecules. *Pept. Sci.* **111**, e24086 (2019).

393. Abbott, S. *Surfactant science: principles & practice*. (DEStech Publications, Inc, 2017).

Appendix A Chemical Composition of Ordinary Portland Cement (OPC) Paste

Quantitative X-Ray Fluorescence (XRF) was performed on Type I/II OPC to determine the chemical composition. The XRF results, including oxide content, can be found in **Table A1**.

Table A1. Chemical Composition of Type I/II OPC

Composition	Percentage
Al_2O_3	4.38
CaO	62
Fe_2O_3	3.33
K_2O	0.757
MgO	1.38
MnO	0.21
Na_2O	0.19
P_2O_5	0.183
SiO_2	19.7
SO_3	3.32
TiO_2	0.18
LOI	2.96

Appendix B Freeze-Thaw Chamber for Cement Paste

A schematic of the custom-built freeze-thaw chamber can be found in **Figure B1 (a)**. All parts used to make the chamber were commercially available. The sample chamber was a 3-in x 3-in x 1.5-in (L x W x H) sealable plastic container. Ice water was kept cold in a refrigerator and pumped through an aluminum block to act as a heat sink for stacked Peltier plates, which provided the source for cold temperatures. The Peltier plates were stacked and wired to a benchtop power board (SparkFun), as shown in **Figure B1 (b)**, to achieve the desired cooling temperature. The temperature within the chamber was monitored with a DHT-22 temperature sensor (SparkFun). The temperature sensor was connected to a Raspberry Pi Zero W for data collection. The temperature profile can be found in **Figure B2**.
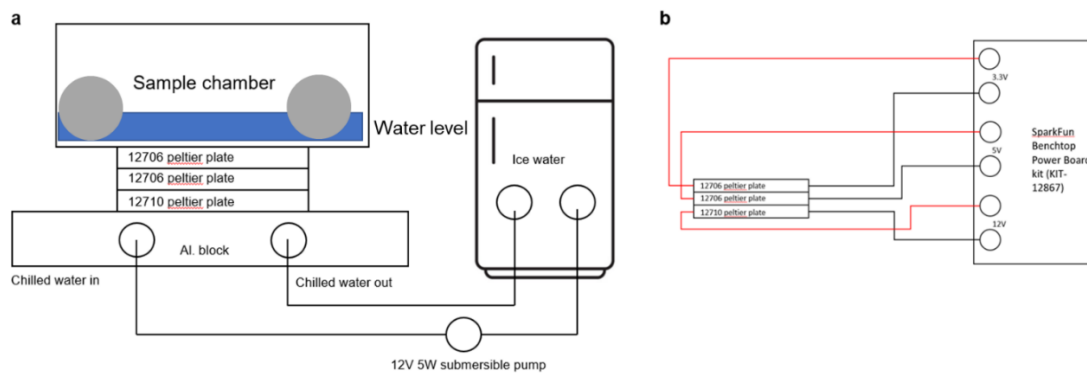

Figure B1. Layout of the custom-built freeze-thaw chamber. (**a**) Schematic diagram of the freeze-thaw chamber and (**b**) wiring diagram of Peltier plates to 12V, 5V, and 3.3V power supply.
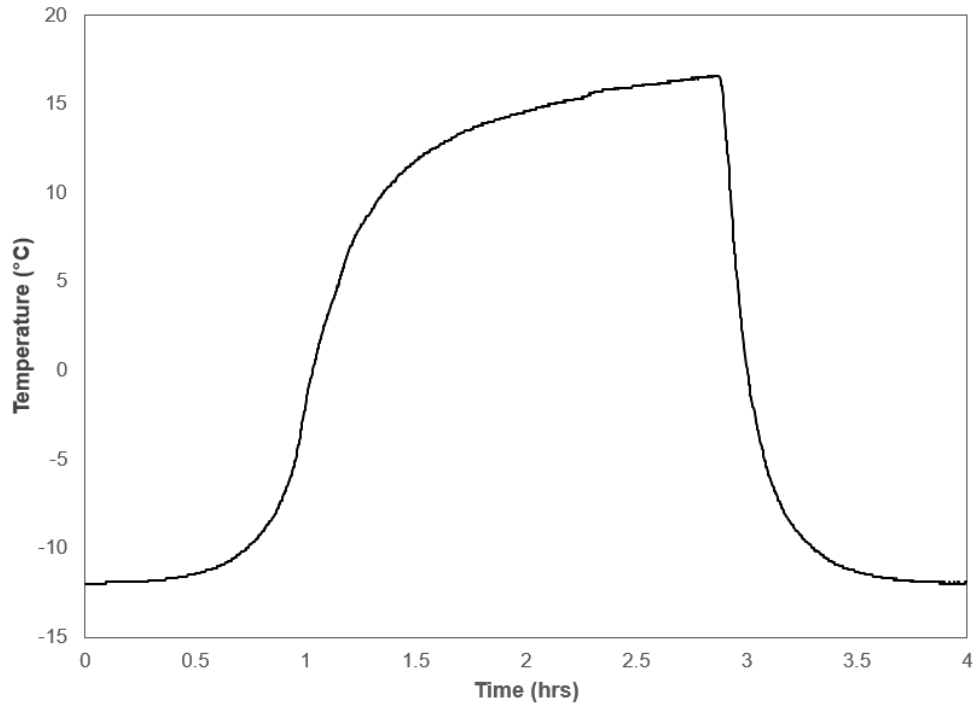
Figure B2. Temperature profile of the custom-built freeze-thaw chamber. The temperature profile showing the maximum and minimum temperatures, rate of heating and cooling, and length of a single cycle.

Appendix C Air Entraining Agent Dosage in Cement Paste

The fresh state air content of 0.45 w/c and AEA modified paste was measured according to ASTM C231. The fresh state air content was determined using a Humboldt H-2783 concrete air meter. Batches of AEA modified paste were mixed and fresh state air content was measured until a desired fresh state air content of ~18% was achieved. 18% fresh state air was chosen as the target to meet industry accepted air contents of ~ 16 to 25% air by volume of cement paste, or ~ 4 to 10% by volume of concrete.[163,312] A commercially available AEA with active ingredients of sulfonic acids (1-3%) and rosin (<1%) was purchased and the surfactant 4-nonylphenol-polyethylene glycol, phenol ethoxylate, (CAS # 9016-45-9) was purchased from Sigma-Aldrich.

Micro X-ray computed tomography (MXCT) enabled 3D visualization of internal air void systems. Samples were scanned using MXCT before freeze-thaw cycling. The MXCT (ZEISS Xradia 520 Versa) source voltage was set to 140 kV and the power to 10 W. An objective with an optical magnification of 0.4× was used. The source and detector locations were varied to obtain the desired resolution (voxel size) of approximately 5 µm. Dragonfly 2021.1 software (Object Research Systems) was used to generate 3D reconstructions, to calculate the scanned volume of sample, and volume of all voids. The volume of air voids was determined from all voids with diameters greater than 15 µm. This diameter was chosen based on the accepted size range of air voids,[19] previous research,[327] and resolution capabilities of MXCT.

The MXCT data were first segmented in Dragonfly 2021.1 to identify voxels that are associated with air voids (*i.e.*, region of interest, ROI). Following segmentation, a multi-ROI analysis was performed. The multi-ROI analysis groups the labeled voxels and calculates a variety of properties including volume.

Table C.1 summarizes the fresh and hardened state air contents of the control and AEA

modified OPC paste. Additionally, the AEA dosages used to entrain ~18% fresh state air are

provided in **Table C.1**. **Figure C.1** provides representative MXCT 2D cross-sections of the

control, phenol ethoxylate, and commercially available AEA modified hardened pastes where the

air void system can be visualized.

Table C.1. Measured fresh and hardened state air content of control and AEA modified OPC
paste samples at w/c=0.45.

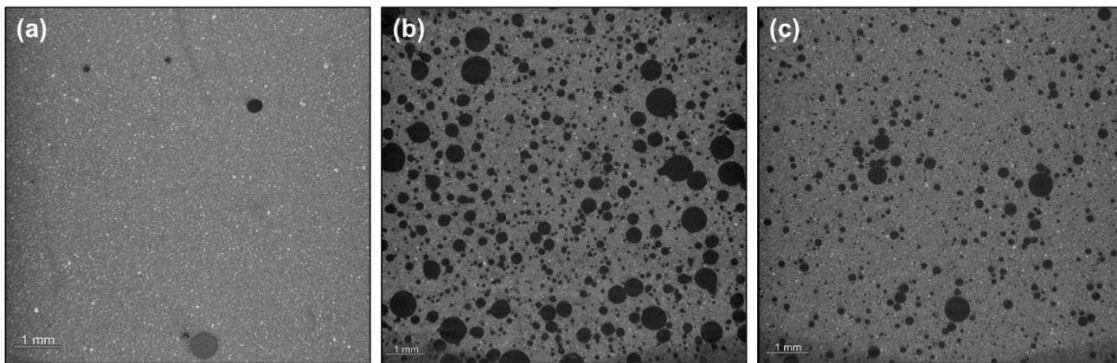| Sample	AEA dosage (wt. % of cement)	Fresh state air content (%)	Hardened state air content(%)
Control	-	4.6	0.41
Phenol ethoxylate	0.8	18.0	17.4
Commercial AEA	1.4	18.5	9.0

Figure C.1. Representative MXCT 2D cross-sections of air void system of (a) control, (b) 0.8
wt% phenol ethoxylate, and (c) 1.4 wt% commercial AEA modified hardened OPC paste. Scale
bars are 1 mm.